Rationalization of the contractile behavior of light-sensitive polymeric materials based on synthetic molecular motors

Alexis Perrot

UNIVERSITÉ DE STRASBOURG

ÉCOLE DOCTORALE DES SCIENCES CHIMIQUES

Institut Charles Sadron, UPR22-CNRS

THÈSE présentée par :

Alexis PERROT

soutenue le : **30 septembre 2021**

pour obtenir le grade de : **Docteur de l'Université de Strasbourg**

Discipline/ Spécialité : Chimie

Rationalisation du comportement contractile de matériaux polymériques photosensibles fondés sur des moteurs moléculaires synthétiques

THÈSE dirigée par :

Mme MOULIN Émilie	Directrice de Recherche, CNRS
M. GIUSEPPONE Nicolas	Professeur, Université de Strasbourg

RAPPORTEURS :

M. COLOMBANI Olivier	Maître de conférences HDR, Université du Mans
Mme KATSONIS Nathalie	Professeure, Rijksuniversiteit Groningen

Rationalization of the contractile behavior of light-sensitive polymeric materials based on synthetic molecular motors

Alexis PERROT

Table of contents

Acknowledgments

> "Je me suis aussi fait enlever les canaux lacrymaux. Je ne les utilisais jamais."
>
> —Sue Sylvester

I would like to thank first my thesis co-directors, Dr Émilie Moulin and Prof. Nicolas Giuseppone. I learnt a lot during these last four years, mainly thanks to the both of you. Our scientific discussions pushed me to do my best, and I appreciated our informal discussions as well. I wish you a future full of personal and professional successes, even though I do not doubt it will be the case. I thank you for the opportunity to do this thesis with you.

Then, I thank Dr Gad Fuks, whose advice were precious when I arrived in the SAMS team. You always had kind words, which helped me to begin and pursue my thesis in good conditions. I do hope I will become a mentor like you are during my career. I also thank Dr Andreas Vargas-Jentzsch, who taught me a lot about how research works, and helped me to step back on my successes and failures. I thank Dr Pierre Lutz, who has always been kind to me, and whose knowledge in polymer science was valuable for this thesis.

I thank Odile Gavat for her daily support. Our morning talks gave me a boost for the rest of the day. I thank Marie-Céline Samy-Arlaye, whose mood and support helps us all to be more efficient every day. I thank Julie Lemoine, who greatly facilitated my integration with the team and the institute in general, I am grateful for what you have done for me.

Importantly, I want to thank Damien Dattler. I believe that the amount of time we spent together already gave you my complete opinion about you, but our common passion for written proofs of what we say, and what we bet, pushes me to write it once more here. Our relationship evolved significantly during these last four, almost five, years, where you started as a simple 'beauf' to an emotional mystery to my eyes, and where you finally ended up as one of the people to whom I am the closest. I admire you for your honesty, your integrity, your devotion to your loved ones and for your scientific skills, and I will probably never thank you enough for all your personal and professional support. My dear Louloutre, I wish you a successful, happy life, because I do believe you deserve it. With a bit of luck, this life will lead you to a chatelaine brewery, with your friends and family by your side.

I also thank Claire Counil. You are a loving, devoted, funny and smart woman, and I am proud to have you as a friend. You helped in ways that not so many people would have done, and I am truly

grateful. Your life as a traveler led you relatively far away, but I am convinced that we will meet often in the future.

I thank Raphaël Pauchet; our Kaamelott times during these last months were a landmark of the day, and our scientific and personal discussions helped me to feel less lonely in this laboratory full of organic chemists. I thank Jean-Rémy Colard-Itté, whose teaching skills and kindness helped me to start my thesis with serenity. I thank Flavio Picini; I will remember your well-built body, as well as your humor and kindness in general.

My years as a member of the SAMS team led me to meet a significant amount of people, and I cannot thank all of them individually; I hope I am honest enough everyday so that it is not necessary. Nevertheless, all of them contributed in their own ways in this thesis. Therefore, I thank, without specific order, Mounir, Lara, Erol, Frédéric, Shoichi, Maria Jesus, Nicolas, Christian, Cristian, Alessandro, Dania, Sergio, Philippe, Thiebault, Melodie, Vasyl, Xuyang, Xiaoqin, Manick, Junjun, Yali, Simon, Artem, Antoine, Chloé, Nathan, Andreï, Andres, Cyprien, Martin, Cristina, and I wish them a successful life. I specifically thank Joakim, Wenzhi and Chuan, who shared my life of 'motorist'.

I also wish to thank all the staff from the Charles Sadron institute, both permanent and non-permanent. I thank the administrative staff, specifically Odile Lemblé, for her general good mood and her participation in the 'Cafés vITaminés', Nadia Barkani, for our formal and informal discussions, and Jean-Marc Chauvelot, who did his best to make me like football and music. I thank the staff from the characterization platform, especially Catherine Foussat and Mélanie Legros, whose scientific and moral support was of great value. I also thank Wiebke Drenckhan and Laure Biniek, with whom I had the occasion to participate in science communication events that mattered to me, I appreciated the opportunity to take part in them.

I thank Prof. Éric Buhler, whose teaching skills greatly improved my understanding of small-angle neutron scattering, and whose help and kindness was valuable for the writing of this manuscript. I also thank the different local contacts that I met for these analysis, Dr Fabrice Cousin and Dr Sylvain Prévost. I thank Dr Jésus Raya for our discussions on HRMAS RMN analysis.

I would also like to thank my friends, who were by my side these last years, without any specific order. Alex, our common love for board and video games probably contributed to our relationship but I do believe it is not limited to that. Marion, we have met at the beginning of my undergraduate studies; your honesty, good mood, and your secret love of spying on people are part of the reason why I am happy to say that you are a close friend of mine. Nadia, even though these last years were not the best for you, you have always been there for your friends. You are one of the kindest and strongest persons I have ever met, and I am also proud to be your friend. Valérie, your legendary combo "rosé-petite-clope" will stay in my mind forever, and our board games sessions and holidays greatly contributed to our friendship. Genya, meeting you during our master's degree made my arrival in Strasbourg a lot better, and your energy always pushed me to be a better version of myself. I probably forget some of my friends here, but I hope they know enough about what I think of them that they will not hold a grudge.

I thank my family, grandparents, uncles and aunts, and cousins. I thank my parents, who taught me values that gave me the strength to finish this work. Mom, Dad, you always supported me during

my studies and pushed me to live life as I wanted. My sisters, Julie and Mélody, who became strong women over these last years, the love we have for each other made me the person I am today.

Kéryann, our history may have had a complicated beginning, we have today a strong and intense relationship. I am happy to share my life with you, and I hope the years to come will be by your side. I thank you for our life, your support, and your love.

I thank Kepler and Ouden, whose presence was comforting during my thesis, and whose purrs were significantly relaxing. I thank Alexandra Elbakyan for her contribution for open scientific research.

Finally, I thank Dr Olivier Colombani and Prof Nathalie Katsonis for accepting to examine this work.

Remerciements

> "I'm grieving. And I grieve by insulting those who mean the most to me. It's just a coincidence that it's also what I do when I'm not grieving."
>
> —Sue Sylvester

Je tiens tout d'abord à remercier mes co-directeurs de thèse, Dr. Émilie Moulin et Pr. Nicolas Giuseppone. J'ai beaucoup appris pendant ces quatre dernières années en grande partie grâce à vous. Nos discussions scientifiques m'ont poussé à toujours donner le meilleur de moi-même et j'ai tout autant apprécié nos conversations plus informelles. Je vous souhaite à tous les deux un avenir rempli de réussites professionnelles et personnelles, bien que je ne doute pas un instant que cela sera le cas. Je vous remercie de m'avoir donné l'opportunité de faire une thèse à vos côtés.

Je remercie ensuite Dr. Gad Fuks dont les conseils furent précieux à mes débuts au sein de l'équipe. Tu as toujours eu des mots bienveillants qui m'ont permis d'appréhender mes premières années, et plus généralement ma thèse, de manière plus sereine. J'espère sincèrement devenir un enseignant et un encadrant tel que tu es au cours de ma carrière. Je remercie également Dr. Andreas Vargas-Jentzsch qui m'a permis de relativiser mon travail au sein de l'équipe, aussi bien dans les réussites que dans les échecs, et dont les discussions m'ont permis de bien mieux comprendre le monde de la recherche. Je remercie Dr. Pierre Lutz, dont la gentillesse n'a d'égale que l'étendue de sa connaissance en polymères. J'ai également beaucoup appris à vos côtés.

Je remercie Odile Gavat pour son soutien au quotidien. Nos discussions matinales m'ont souvent permis de commencer la journée dans de meilleures dispositions. Je remercie Marie-Céline Samy-Arlaye, dont la bonne humeur et l'aide au quotidien nous permettent à tous de travailler dans de meilleures conditions. Je remercie Julie Lemoine qui a beaucoup facilité mon intégration au sein de l'équipe et de l'institut à mon arrivée, je t'en suis extrêmement reconnaissant.

Je tiens tout particulièrement à remercier Damien Dattler. Je pense que le temps qu'on passe au quotidien ensemble m'a déjà permis de te dire tout ce que je pense de toi, mais notre appréciation commune pour les traces écrites de nos discussions et paris me pousse à laisser une preuve supplémentaire de l'importance de notre relation dans ces remerciements. Notre relation a beaucoup évolué durant ces quatre, presque cinq, dernières années, où tu es passé d'un simple beauf' à un mystère émotionnel, pour finalement terminer comme une des personnes dont je suis le plus proche. Je t'admire pour ton honnêteté, ton intégrité, ton dévouement à tes proches et pour tes compétences

scientifiques, et je ne te remercierai probablement jamais assez du soutien professionnel et personnel dont tu as fait preuve envers moi. Je te souhaite, ma Louloutre, une vie remplie de réussites et de bonheur, car tu fais partie des quelques personnes qui, je pense, le méritent réellement. Avec un peu de chance, cette vie te mènera vers une brasserie châtelaine, avec tes amis et ta famille à tes côtés.

Je remercie aussi tout particulièrement Claire Counil. J'ai trouvé en toi une personne aimante, dévouée, drôle et intelligente, et je suis fier de pouvoir te compter parmi mes amis. Tu as fait pour moi des choses que peu de personnes auraient pu faire, et je t'en suis reconnaissant. Ta vie de globe-trotteuse t'a, pour le moment, éloignée géographiquement mais je suis convaincu qu'on se recroisera souvent à l'avenir.

Je remercie Raphaël Pauchet ; les sessions Kaamelott pendant ces derniers mois de thèse étaient un rendez-vous incontournable qui me donnaient la force de tenir jusqu'au goûter, et nos discussions scientifiques et personnelles m'ont souvent permis de me sentir moins seul dans ce laboratoire d'organiciens. Je remercie Jean-Rémy Colard-Itté, dont la pédagogie et la gentillesse m'ont permis de commencer ma thèse avec sérénité. Je remercie Flavio Picini ; je me souviendrai avec émotions de ton corps sculpté avec soin, ainsi que de ton humour et de ta gentillesse en général.

Mes années au sein de l'équipe SAMS m'ont fait croiser un certain nombre de personnes, et je ne peux pas toutes les remercier individuellement ; j'espère être assez honnête au quotidien pour que ce ne soit pas indispensable. Quoiqu'il en soit, toutes ces personnes ont certainement participé à faire de ma thèse ce qu'elle est, et elles ont chacune contribué à leur manière à me laisser ce souvenir impérissable qu'est cette aventure. Je remercie donc, sans ordre particulier, Mounir, Lara, Erol, Frédéric, Shoichi, Maria Jesus, Nicolas, Christian, Cristian, Alessandro, Dania, Sergio, Philippe, Thiebault, Melodie, Vasyl, Xuyang, Xiaoqin, Manick, Junjun, Yali, Simon, Artem, Antoine, Chloé, Nathan, Andreï, Andres, Cyprien, Martin, Cristina, et je leur souhaite à tous un avenir radieux, en espérant n'en avoir oublié aucun. Je tiens cependant à donner une mention spéciale à Joakim, Wenzhi et Chuan, qui ont partagé mon quotidien de « motoriste ».

Je tiens également à remercier l'ensemble du personnel de l'institut Charles Sadron, permanents et non-permanents. Je remercie le personnel administratif, tout particulièrement Odile Lemblé, pour sa bonne humeur générale et pour sa contribution aux « Cafés vITaminés », Nadia Barkani, pour nos discussions formelles et informelles, et Jean-Marc Chauvelot, qui, malgré tous ses efforts, ne m'a pas fait davantage aimer le football ou la musique. Je remercie l'ensemble du personnel des plateformes de caractérisation, dont la plupart des analyses sont présentées dans cette thèse, avec une mention particulière pour Catherine Foussat et Mélanie Legros, pour leur aide scientifique et leur soutien moral en général pendant nos discussions. Je remercie également particulièrement Wiebke Drenckhan et Laure Biniek, avec qui j'ai eu l'occasion de participer à plusieurs activités de vulgarisation scientifique qui me tiennent à cœur, j'ai apprécié l'opportunité qu'elles m'ont laissée d'y contribuer.

Je remercie Pr. Éric Buhler, dont la pédagogie a permis de me faire comprendre (relativement) clairement les analyses de diffusion de neutrons aux petits angles, et dont la bienveillance générale fut précieuse pour l'écriture de ce manuscrit sur cet aspect. Je remercie également les différents contacts locaux auxquels j'ai eu affaire pour ces analyses, Dr. Fabrice Cousin et Dr. Sylvain Prévost. Je remercie également Dr. Jésus Raya pour nos discussions sur les analyses RMN HRMAS.

Il est important pour moi de remercier tous mes amis qui m'ont accompagné ces dernières années, encore une fois sans ordre particulier. Alex, notre passion commune pour les jeux vidéo ou de société nous a certainement rapprochés mais j'ose espérer que nous partageons une relation bien plus profonde que ça. Marion, tu es à mes côtés depuis les débuts de mes études universitaires ; ton franc-parler, ta bonne humeur, ton honnêteté (et ton amour du « chouettage ») sont autant d'aspects de ta personnalité qui font que je suis heureux de te compter parmi mes amies proches aujourd'hui. Nadia, tu as surmonté un certain nombre d'obstacles ces dernières années, mais tu as toujours su rester disponible pour tes amis. Tu es une des personnes les plus fortes et bienveillantes que je connaisse et je suis également fier de t'avoir à mes côtés. Valérie, ton amour légendaire du combo « rosé-petite-clope » restera probablement gravé dans ma mémoire, et bien que nous nous connaissions que depuis plus récemment, nos sessions jeux de société et nos vacances me font te compter parmi mes amis proches. Genya, ta présence pendant le master a été essentielle à mon épanouissement lors de mon arrivée en Alsace, et bien que nos thèses respectives aient espacé nos interactions, ta bonne humeur et ton énergie m'ont toujours poussé à être une meilleure version de moi-même. Gaël, on se connaît depuis longtemps et la distance géographique a certainement changé la nature de notre relation, mais nos retrouvailles sont toujours une source de plaisir. J'oublie probablement des personnes et j'espère qu'elles ne m'en tiendront pas rigueur, et j'ose également espérer que je suis assez honnête au quotidien pour qu'elles sachent qu'elles comptent pour moi malgré cet oubli.

Je remercie également ma famille, grands-parents, oncles et tantes, cousins et cousines. Je remercie mes parents, qui m'ont inculqué des valeurs m'ayant donné la possibilité de terminer cette thèse. Maman, Papa, vous m'avez toujours soutenu tout au long de mes études et m'avez poussé à vivre ma vie telle que je la souhaitais. Mes sœurs, Julie et Mélody, qui sont devenues des femmes épanouies au cours de ces dernières années, et l'amour que l'on se porte a fait de moi la personne que je suis aujourd'hui.

Kéryann, bien que nos débuts aient pu être agités, nous vivons aujourd'hui une relation forte et intense. Je suis heureux de partager ma vie avec la tienne, et j'espère que les années à venir seront également à tes côtés. Je te remercie pour notre quotidien, ton soutien, et ton amour.

Je remercie Kepler et Ouden, dont la présence fut d'un grand réconfort pendant toute la durée de cette thèse, et dont les ronronnements m'ont souvent apaisé. Je remercie Alexandra Elbakyan pour sa contribution à la recherche scientifique ouverte.

Pour finir, je remercie Dr. Olivier Colombani et Pr. Nathalie Katsonis pour avoir accepté d'examiner ce travail.

Résumé de la thèse (français)

Les matériaux organiques sensibles à leur environnement sont de plus en plus étudiés depuis ces dernières décennies. Leurs propriétés mécaniques sont davantage adaptées pour une utilisation à l'interface avec les systèmes biologiques que leurs homologues métalliques rigides. Leur capacité à répondre aux conditions environnementales permet aussi de s'affranchir d'un système informatique, voire d'un utilisateur actif, pour leur fonctionnement. Par conséquent, ces matériaux trouvent de plus en plus d'applications dans les domaines biomédicaux, dans le stockage et traitement de l'information, ou en tant qu'actionneurs mécaniques quand leurs dimensions changent.[1,2]

L'utilisation de molécules sensibles aux stimuli externes dans des matrices molles est une stratégie majeure pour le développement d'actionneurs macroscopiques. Par exemple, l'azobenzène est couramment utilisé comme dopant dans les élastomères cristaux liquides. La photoisomérisation *trans*- vers *cis*- de la molécule perturbe localement l'ordre du matériau, causant ainsi sa déformation macroscopique quand il est irradié. Le spiropyrane est souvent incorporé dans des gels polymériques, puisque sa photoisomérisation entre sa forme neutre et sa forme chargée permet de changer l'équilibre de gonflement du matériau et, ainsi, entraîne une expansion ou contraction du réseau. Les cristaux de diaryléthène peuvent également se déformer sous irradiation lumineuse puisque les changements de conformation de la molécule dans la maille cristalline s'amplifient jusqu'à l'échelle macroscopique.[1]

Les moteurs moléculaires sont une classe particulière de molécules sensibles à leur environnement. Contrairement aux commutateurs moléculaires, comme l'azobenzène ou le spiropyrane, les moteurs moléculaires s'isomérisent de façon directionnelle. Par conséquent, ils dissipent de l'énergie dans l'environnement au fur et à mesure de leur fonctionnement. Cependant, ces systèmes ont été développés plus récemment que les commutateurs et, par conséquent, les exemples de leur utilisation dans des matrices molles sont plus rares.

Dans cette thèse, nous utilisons des moteurs moléculaires fondés sur des alcènes encombrés. Ce type de moteurs a été développé par Pr. Feringa, et a été considérablement optimisé par la même équipe depuis.[3–5] Il existe quelques exemples de l'utilisation de cette structure dans des matrices molles où le changement de géométrie pendant le cycle de fonctionnement du moteur mène à des changements macroscopiques de propriétés.[6–8] Cependant, le mouvement unidirectionnel du moteur moléculaire n'est pas exploité en tant que tel.

Notre équipe a présenté en 2015 l'utilisation de moteurs moléculaires comme agents de réticulation dans des gels polymériques.[9] Dans ces réseaux, la rotation unidirectionnelle des moteurs enroulent

les chaînes polymériques entre elles ; la création de nouveaux nœuds de réticulation entraîne une contraction macroscopique du gel sous irradiation lumineuse. Par conséquent, le caractère unidirectionnel du mouvement est primordial pour le changement de volume du matériau. Cependant, la déformation était irréversible, puisque les moteurs tournent seulement dans un sens. Ces premiers systèmes ont donc été améliorés avec l'incorporation de diaryléthènes comme agents de réticulation, qui permettent de relâcher la tension mécanique du matériau avec le stimulus lumineux approprié.[10]

L'objectif de cette thèse est d'étudier davantage ces réseaux polymériques intégrant des moteurs moléculaires. L'étude de nos premiers systèmes était tournée vers les conséquences des rotations nanoscopiques des moteurs sur la matrice. Ici, nous voulons plutôt observer l'influence du réseau lui-même sur le fonctionnement des moteurs moléculaires et, ainsi, les changements qui en découlent sur la contraction du gel. Notre étude est portée par trois axes : d'abord, la modification de paramètres environnementaux et topologiques ; ensuite, le changement de la nature chimique des polymères ; enfin, le développement de systèmes contractiles anisotropes.

Ce résumé suit une structure similaire à celle du manuscrit principal. La première partie permet de présenter le contexte général de nos travaux avec une description des moteurs moléculaires et des réseaux polymériques. La deuxième partie développe la synthèse de plusieurs grammes de moteurs moléculaires multifonctionnels utilisés comme agents de réticulation. Ensuite, la troisième partie présente nos résultats sur la variation de paramètres structuraux sur la contraction de gels de poly(éthylène glycol) réticulés avec des moteurs moléculaires. La synthèse, la réticulation et le comportement photosensible de matériaux fondés sur d'autres chaînes polymères sont détaillés dans la quatrième partie. Enfin, nous terminons avec la préparation d'élastomères cristaux liquides réticulés avec des moteurs moléculaires.

1.1 Moteurs moléculaires synthétiques et réseaux de polymères

Les systèmes biologiques vivants sont tous dépendants du fonctionnement de moteurs moléculaires afin d'être constamment « hors-équilibre », c'est-à-dire consommer et dissiper de l'énergie en accomplissant une tâche. Par exemple, le complexe protéique F_1F_0-ATP synthase consomme l'énergie de l'hydrolyse de l'adénosine triphosphate (ATP) pour déplacer des protons contre des gradients de concentration ; selon les conditions, il peut également exploiter un flux de protons pour synthétiser de l'ATP.[11]

Le développement de machines moléculaires synthétiques s'inscrit donc dans une démarche biomimétique pour la création de nouveaux systèmes « intelligents ». Dans le cadre de cette thèse, nous nous intéressons seulement aux moteurs moléculaires fondés sur des alcènes encombrés, développés par Pr. Feringa et son équipe depuis 1999.[3] Dans son premier rapport, la molécule consiste en deux parties identiques connectées par une double liaison. La présence de substituants à base de naphtalènes proches de la double liaison impose une hélicité à la molécule. Des carbones asymétriques sont également proches de la double liaison et favorisent une hélicité par rapport à l'autre (Figure R.1.A). Ainsi, à l'état initial, la molécule est dans sa conformation *(P,P)-trans* la plus

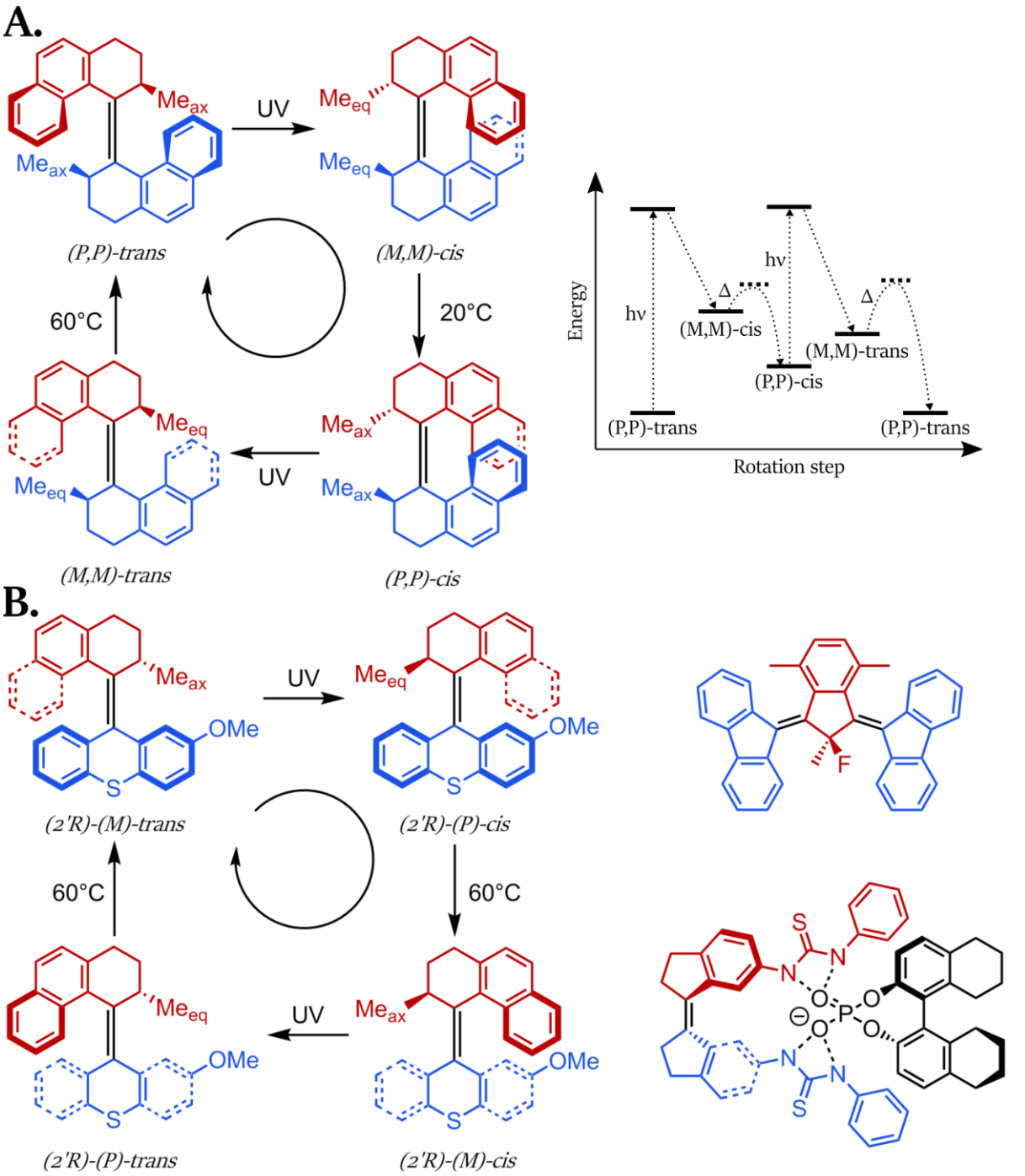

Figure R.1. Moteurs moléculaires fondés sur des alcènes encombrés. **A.** À gauche, mécanisme de la rotation unidirectionnelle du rotor (rouge) par rapport au stator (bleu) pour des moteurs moléculaires de première génération. L'encombrement stérique proche de la double liaison impose une hélicité, et les carbones asymétriques favorisent la conformation *(P,P)-trans* à l'état initial. Sous irradiation UV, le molécule se photoisomérise avec inversion d'hélicité pour former l'isomère *(M,M)-cis*. Les groupements méthyles sont alors pseudo-équatoriaux et cette conformation est métastable. La molécule s'isomérise donc par inversion thermique d'hélice pour former l'isomère *(P,P)-cis*, plus stable, et le rotor a tourné de 180° par rapport au stator. La répétition de l'étape de photoisomérisation et de l'inversion thermique d'hélice complète la rotation à 360°. À droite, diagramme énergétique des différents isomères. **B.** Différentes générations de moteurs moléculaires. À gauche, moteur moléculaire de deuxième génération avec un seul carbone asymétrique, qui suit un mécanisme identique à ceux de première génération. À droite, haut, moteur moléculaire de troisième génération avec un carbone pseudo-asymétrique ; bas, moteur moléculaire de quatrième génération où un auxiliaire chiral favorise un isomère par rapport à l'autre.

stable. Sous irradiation UV, il y a photoisomérisation de la double liaison, entraînant l'inversion de

l'hélicité du moteur pour former l'isomère (*M,M)-cis*. Cependant, cette configuration n'est pas la plus stable puisque les méthyles portés par les carbones sont alors en position pseudo-équatoriale, et interagissent alors fortement avec la moitié de la molécule de l'autre côté de la double liaison. Par conséquent, la molécule se relaxe par inversion thermique d'hélice pour former l'isomère *(P,P)-cis* ; dans ce cas, les méthyles sont en position pseudo-axiale, ce qui minimise l'interaction stérique avec l'autre partie du moteur. Après ces deux étapes, photoisomérisation et inversion thermique d'hélice, la partie « haute » du moteur a donc effectué une rotation de 180° par rapport à la partie basse. La rotation à 360° est complétée après une nouvelle photoisomérisation suivie de l'inversion d'hélice (Figure R.1.A). La rotation est unidirectionnelle car la photoisomérisation forme exclusivement l'isomère avec l'hélicité opposée à cause de l'encombrement proche de la double liaison, et car l'isomère d'hélicité *(P,P)* est thermodynamiquement favorisé. Par conséquent, deux moteurs moléculaires énantiomères ont un sens de rotation opposé.

Ces premiers moteurs ont été optimisés en diminuant l'information chirale nécessaire à l'unidirectionnalité de mouvement de rotation (Figure R.1.B). Dans les moteurs de deuxième génération, la partie « basse », qualifiée de « stator », est symétrique et ne porte pas de centre chiral ; seule la partie « haute », le « rotor », porte un carbone asymétrique. Le mécanisme de rotation est identique aux moteurs de première génération mais les deux inversions thermiques d'hélice sont, dans ce cas, identiques.[4] Les moteurs de troisième génération correspondent à deux moteurs de deuxième génération partageant le même rotor et, par conséquent, le carbone contrôlant la direction de rotation est seulement pseudo-asymétrique.[12] Dans les moteurs de quatrième génération, la molécule elle-même ne porte pas de centre chiral ; un auxiliaire asymétrique favorise un isomère par rapport à l'autre.[13] Dans le cadre de ce manuscrit, nous utilisons des moteurs moléculaires de deuxième génération pouvant atteindre des fréquences de rotation de l'ordre du MHz.[14]

Les solutions de polymères ont un comportement différent des solutions de petites molécules organiques à cause de leur conformation en solution. Trois régimes de concentration peuvent être observés (Figure R.2).[15] Dans le régime dilué, les pelotes de polymères sont éloignées les unes des autres. Au-dessus d'une concentration critique, appelée la concentration de recouvrement c*, les

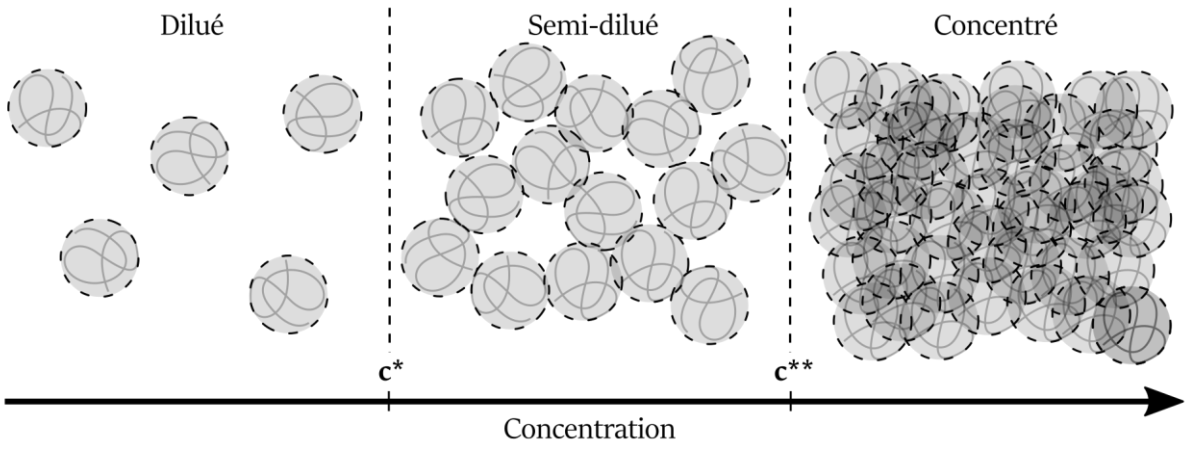

Figure R.2. Différents régimes de concentration pour les solutions de polymères.

pelotes sont en contact mais la concentration massique en polymères est toujours faible. Dans le régime concentré, au-dessus d'une seconde concentration critique c**, les pelotes sont interpénétrées avec une forte concentration massique en polymères dans la solution. Lors de nos précédentes études, nous avons déterminé que la concentration optimale pour former nos gels était c* car les pelotes sont assez proches pour avoir une réticulation quantitative, tout en limitant le nombre d'enchevêtrements initial.[16,17] Par conséquent, dans le cadre de cette thèse, nous avons déterminé c* pour nos systèmes en mesurant la viscosité intrinsèque [η] de nos solutions, grâce à la formule :

$$c^* \approx \frac{1}{[\eta]} \tag{R.1}$$

Par ailleurs, le volume d'un gel est relié à la masse moléculaire des chaînes entre nœuds de réticulation $\overline{M_c}$ par l'équation de Flory-Rehner :[18]

$$\frac{1}{\overline{M_c}} = \frac{2}{\overline{M_n}} - \frac{\ln\left(1 - \phi_{sw}\right) + \phi_{sw} + \chi\,\phi_{sw}^{\,2}}{V_1 \rho_d \left(\phi_{sw}^{\,1/3} - \frac{\phi_{sw}}{2}\right)} \tag{R.2}$$

avec $\overline{M_n}$ la masse moléculaire du polymère avant réticulation, ϕ_{sw} la fraction volumique du polymère dans le gel, χ le paramètre d'interaction de Flory, V_1 le volume molaire du solvent et ρ_d la densité du polymère sec. Cette équation montre que lorsque la masse des chaînes entre nœuds de réticulation diminue, alors la fraction volumique des polymères dans le gel augmente. Dans le cas de nos gels, la rotation du moteur crée de nouveaux enchevêtrements dans le réseau, soit des nouveaux nœuds de réticulation physiques. Par conséquent, la masse des chaînes entre ces nœuds diminue et la fraction volumique du polymère augmente, ce qui se traduit par une contraction macroscopique du matériau (Figure R.3).[9]

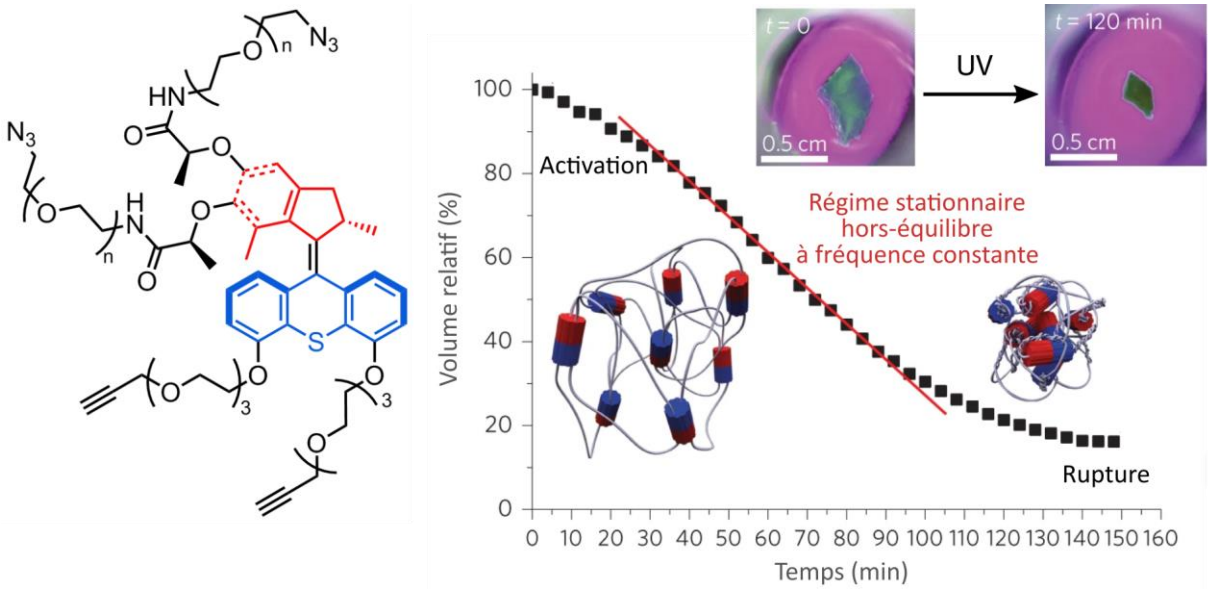

Figure R.3. À gauche, structure des moteurs moléculaires utilisés pour former nos réseaux photoactifs. À droite, évolution du volume du matériau en fonction du temps d'irradiation sous UV. Le volume diminue à cause de la création de nouveaux enchevêtrements (schémas avec cylindres rouges et bleus). Des photographies du gel avant et après irradiation sont montrées en haut à droite. Adapté de la référence [9].

Dans cette thèse, nous avons utilisé des matériaux de différentes masses moléculaires et de différentes structures chimiques. Pour tous ces systèmes, la concentration de recouvrement c* a été mesurée pour réticuler les gels dans les conditions optimales. Nous avons également modifié la voie de synthèse des réseaux, où nous réticulons désormais des chaînes téléchéliques avec des moteurs tétrafonctionnels par cycloaddition azoture-alcyne catalysée au cuivre(I). La synthèse de ces agents de réticulation est présentée dans la partie suivante.

1.2 Synthèse à l'échelle de plusieurs grammes de moteurs moléculaires tétrafonctionnels

Le moteur moléculaire utilisé comme agent de réticulation dans nos réseaux polymériques est obtenu par un couplage de Barton-Kellogg entre un indanethione et un thioxanthone diazoïque.

Le thioxanthone hydrazone **7** est obtenu après sept étapes de synthèse (Schéma R.1). L'étape majeure de cette voie de synthèse est l'orthométallation dirigée pour former le thioéther **4**, précurseur du thioxanthone **5**. À cette étape, les groupements méthoxy et amide dirigent la

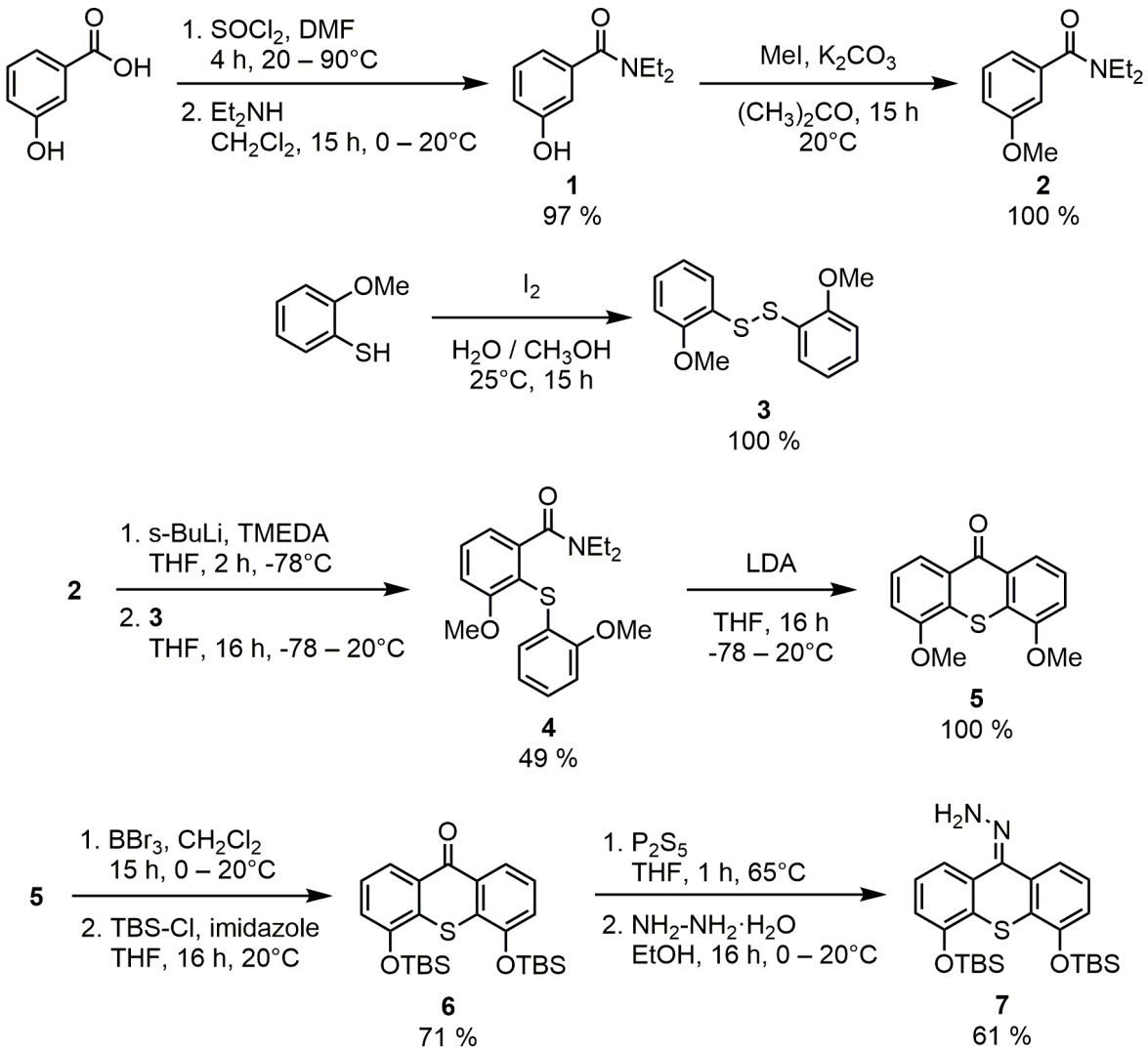

Schéma R.1. Synthèse du thioxanthone hydrazone **7**.

métallation du composé **2** en *ortho* pour la substitution avec le disulfure **3**. Le composé final **7** est obtenu après protection des phénols avec des groupements *tert*-butylsilyle (TBS) et activation du carbonyle avec l'hydrazine. Dans le cadre de cette thèse, nous avons obtenu 13 g de composé **7** au maximum en une fois, et la synthèse a été répétée plusieurs fois pour le couplage de Barton-Kellogg final.

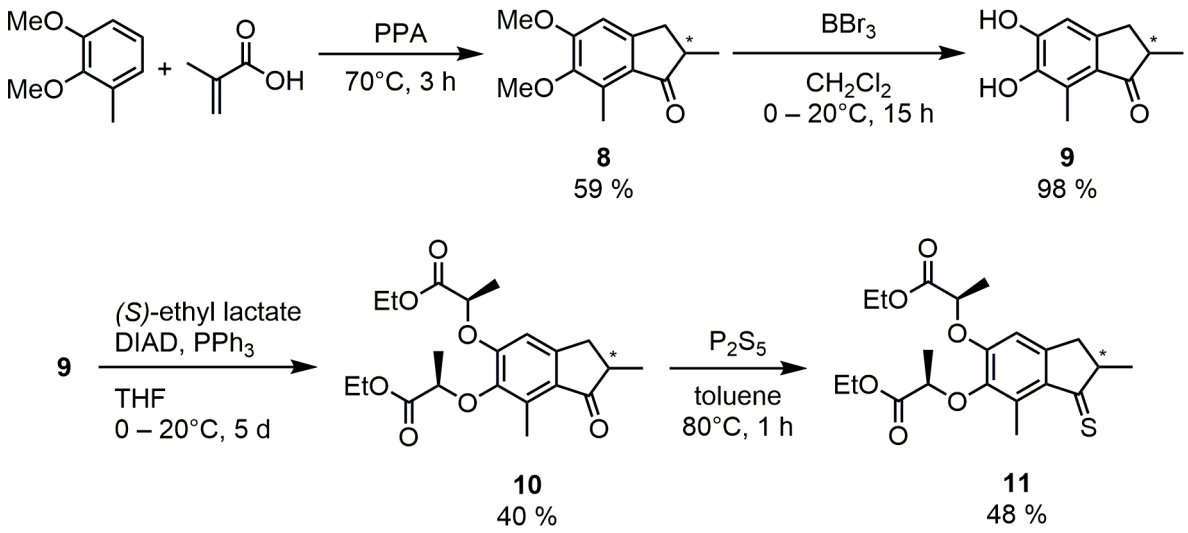

Schéma R.2. Synthèse de l'indanethione **11**.

L'indanethione **11** est obtenu après quatre étapes de synthèse (Schéma R.2). Ici, l'étape-clef est l'éthérification de Mitsunobu pour former le mélange racémique de diastéréoisomères **10**. Dans la section précédente, nous avons précisé qu'un énantiomère de moteur moléculaire tournait dans une seule direction ; par conséquent, il est nécessaire de séparer les deux énantiomères pour étudier leur impact sur le comportement de nos gels. Afin d'éviter une purification par chromatographie sur colonne chirale, qui peut être complexe et coûteuse, nous avons introduit sur le rotor des groupements chiraux. Les diastéréoisomères peuvent ainsi être séparés par chromatographie sur colonne standard. Cependant, à cette étape, la séparation des composés n'est pas idéale, et les diastéréoisomères sont donc séparés après la formation de l'épisulfure (*vide infra*). Nous avons réussi à obtenir 8 g d'indanethione **11** au maximum en une fois et, comme pour le thioxanthone **7**, nous avons répété plusieurs fois cette voie de synthèse pour atteindre les quantités désirées.

Le couplage de Barton-Kellogg se déroule en deux étapes (Schéma R.3). Tout d'abord, le thioxanthone hydrazone est oxydé pour former le composé diazoïque correspondant, puis l'indanethione **7** est ajouté. La condensation entre ces deux parties forme l'épisulfure **12** avec départ de diazote. C'est à cette étape que les diastéréoisomères sont séparés pour obtenir des moteurs moléculaires optiquement purs. C'est également à cette étape que la synthèse à l'échelle de plusieurs grammes est terminée, car les épisulfures semblent plus stables à long terme que les alcènes encombrés correspondants. En une fois, nous avons réussi à obtenir jusqu'à 3.7 g de composé **12**. La réduction avec la triphénylphosphine permet ensuite d'obtenir le moteur moléculaire protégé **13** à des échelles adaptées à notre utilisation.

Les moteurs tétrafonctionnels finaux sont obtenus après déprotection et fonctionnalisation des phénols du stator et des esters du rotor. Le détail de ces synthèses ne sera pas présenté dans ce

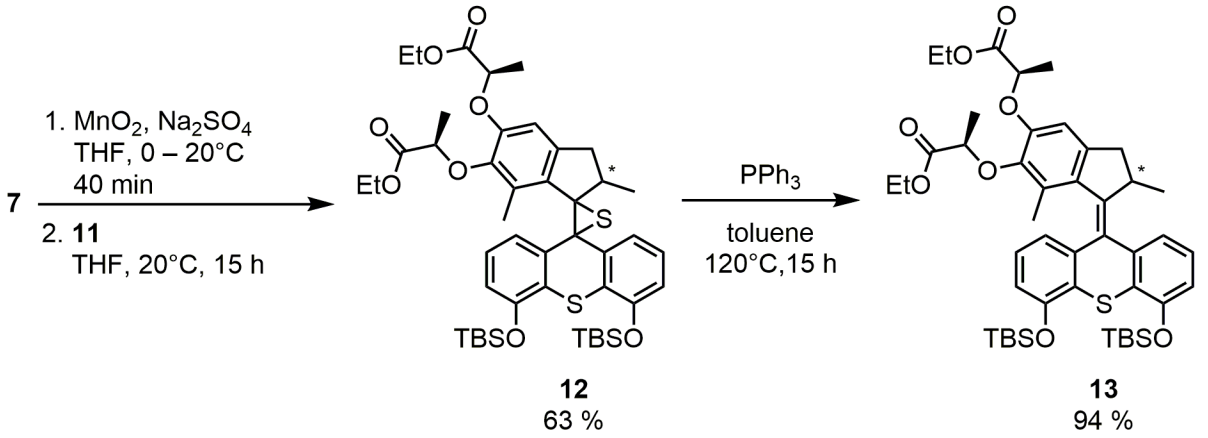

Schéma R.3. Couplage de Barton-Kellogg entre l'indanethione 11 et le thioxanthone 7 pour former le moteur moléculaire **13**.

résumé, mais des moteurs tétra-alcynes et tétra-azotures furent préparés pour la réticulation par cycloaddition azoture-alcyne catalysée au cuivre(I), et des moteurs tétra-acrylates et tétra-amines furent synthétisés pour leur intégration dans des élastomères cristaux liquides et pour la polymérisation de polypeptides, respectivement. Les matériaux formés à partir de ces moteurs sont présentés dans les sections suivantes.

1.3 Étude et optimisation des propriétés de contraction de gels de poly(éthylène glycol) réticulés par des moteurs moléculaires

La voie de synthèse initiale que nous avons présentée dans nos précédents travaux reposait sur la réticulation de moteurs moléculaires portant deux chaînes polymères.[9] Dans cette thèse, nous avons choisi de réticuler des polymères linéaires téléchéliques avec des moteurs tétrafonctionnels, la synthèse de ces derniers ayant été présentée dans la partie précédente.

Par conséquent, il est nécessaire de fonctionnaliser les groupements terminaux de poly(éthylène glycol) (PEG) avec des groupements azotures ou alcynes. À partir de α,ω-dihydroxy-PEG, nous avons préféré la préparation de α,ω-dipropargyl-PEG avec la formation d'alcoolates intermédiaires, puisque cette voie donne des polymères quantitativement fonctionnalisés pour une large de gamme de masses moléculaires (Schéma R.4). Nous avons ainsi préparé des polymères ayant des masses moléculaires de 3 000, 6 000, 10 000 et 20 000 g·mol^{-1}.

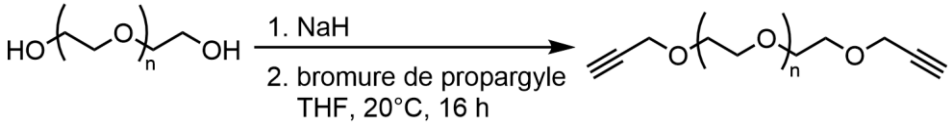

Schéma R.4. Synthèse de α,ω-dipropargyl-PEG à partir de α,ω-dihydroxy-PEG.

Pour former les gels dans des conditions de concentration optimales, c* a été déterminé par viscosimétrie pour ces chaînes polymères. Les gels ont été formés dans le diméthylformamide aux c* respectives de chacune des chaînes polymères, puis gonflés dans l'eau pour les études présentées dans les paragraphes suivants.

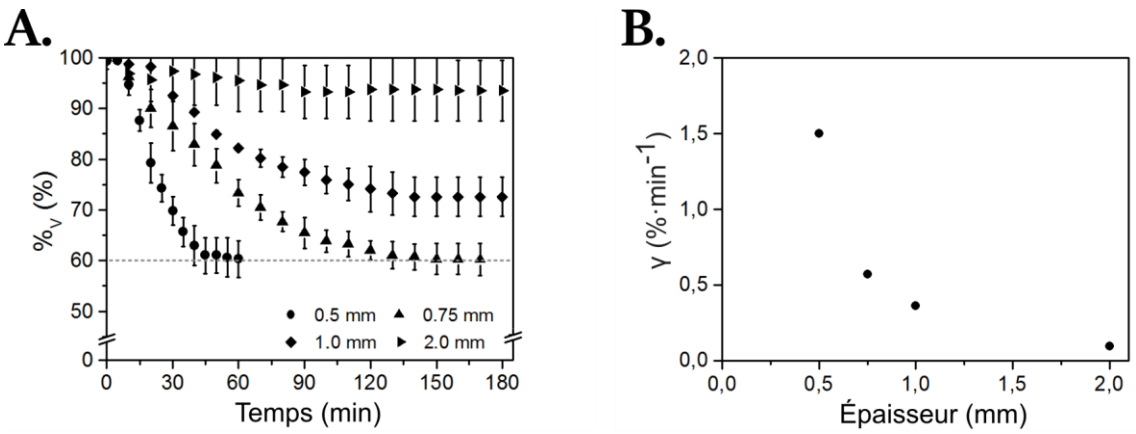

Figure R.4. A. Évolution du volume relatif $\%_V$ en fonction du temps d'irradiation pour des gels de PEG avec une masse moléculaire de 6 000 g·mol^{-1} ayant des épaisseurs différentes. Les gels sont irradiés à 365 nm à 80 mW·cm^{-2}. **B.** Vitesse de contraction maximale γ en fonction de l'épaisseur du gel.

Le premier paramètre étudié est l'épaisseur (Figure R.4). Des gels de PEG ayant une masse moléculaire de 6 000 g·mol^{-1} ont été préparés avec différentes épaisseurs. Les gels les plus fins (0.5 mm et 0.75 mm d'épaisseur) atteignent le même volume relatif $\%_V$ final sous irradiation lumineuse, proche de 60 % du volume initial, indiquant que ce paramètre dépend seulement de la taille des mailles du réseau, qui est indépendante de l'épaisseur puisque tous les gels sont formés à c*. Pour les gels les plus épais, le volume relatif final est plus élevé, et nous supposons que cet effet est dû à la dégradation du réseau sous lumière UV. En effet, pour ces gels, la cinétique de contraction est plus faible, alors que la cinétique d'oxydation sous UV est probablement indépendante de l'épaisseur. Les chaînes entre nœuds de réticulation sous donc dégradées avant que le matériau n'atteigne son volume final optimal.

La vitesse maximale de contraction γ, quant à elle, diminue quand le matériau est plus épais. Ce phénomène peut être attribué à l'atténuation de l'intensité lumineuse lors de sa pénétration dans le gel et, par conséquent, les moteurs moléculaires les plus éloignés de la source lumineuse tournent moins rapidement, ce qui entraîne une contraction plus lente.

L'influence de la puissance lumineuse sur la cinétique de contraction des gels fut ensuite étudiée (Figure R.5). Tous les gels atteignent un volume relatif final statistiquement identique, indiquant une nouvelle fois que ce paramètre dépend seulement de la taille des mailles du réseau. En revanche, la vitesse de contraction maximale γ augmente avec des sources lumineuses plus puissantes et semble atteindre un plateau proche de 2.7 %·min^{-1}. Ces résultats étaient attendus en considérant les études théoriques de l'équipe de Feringa, où les auteurs démontrent qu'à faibles intensités lumineuses, les moteurs sont dans un régime « photochimiquement limité ».[19] Dans ce cas, le nombre de photons par moteur est trop faible pour peupler de manière significative l'état métastable et, par conséquent, les moteurs se relaxent rapidement vers leur état stable par inversion thermique d'hélice. Au contraire, pour des intensités lumineuses plus élevées, la cinétique de relaxation est trop faible par rapport à la cinétique de photoisomérisation. Ainsi, des moteurs à l'état métastable peuvent être photoisomérisés vers leur état initial, ce qui entraîne une vitesse limite de rotation avec une perte de l'unidirectionnalité du mouvement.

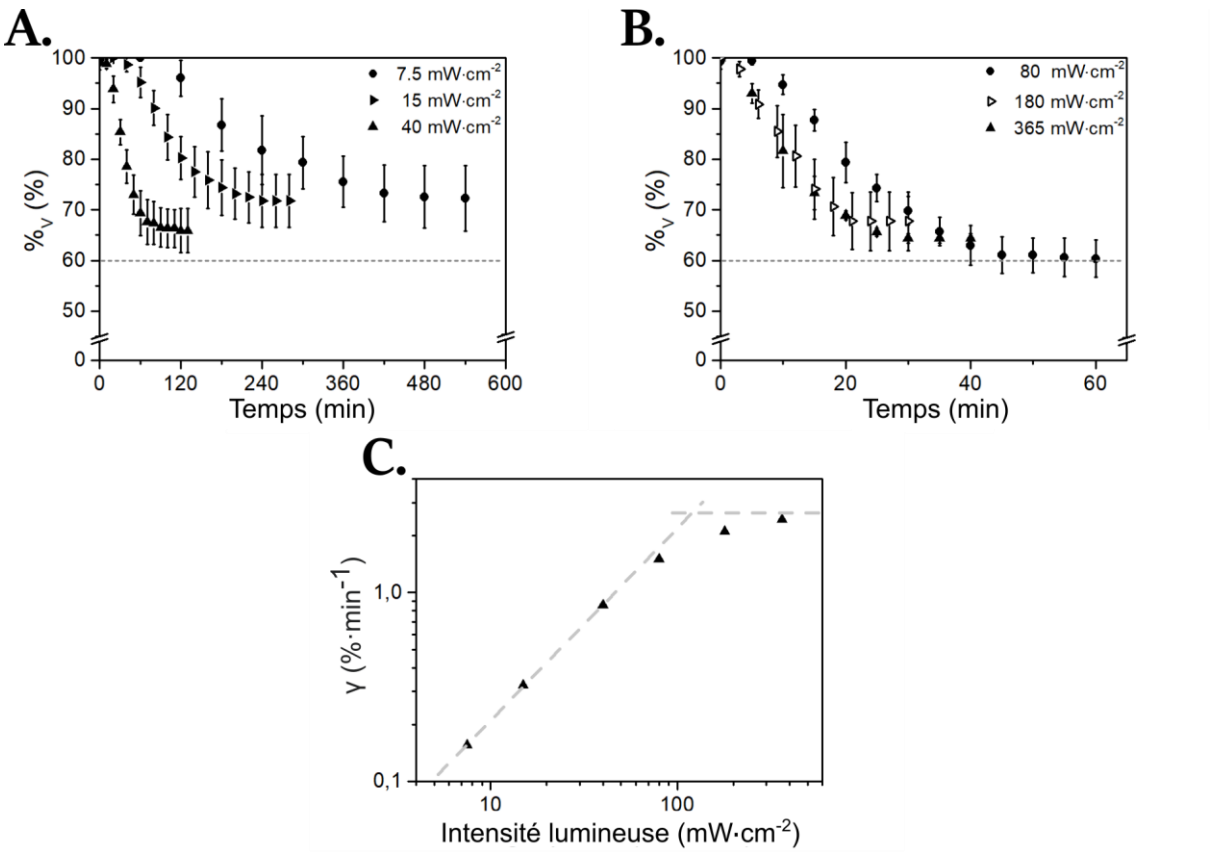

Figure R.5. A et B. Évolution du volume relatif $\%_V$ en fonction du temps d'irradiation pour des gels de PEG avec une masse moléculaire de 6 000 g·mol^{-1} à des intensités lumineuses différentes, à 365 nm. **C.** Vitesse de contraction maximale γ en fonction de l'intensité lumineuse.

Nous avons ensuite étudié les propriétés de contraction de nos gels en fonction de la température (Figure R.6). Dans un premier temps, les gels furent chauffés avant d'être irradiés (Figure R.6.A). Quand la température atteint 70°C, les gels se contractent à 55 ± 5 % de leur volume initial, ce qui est vraisemblablement causé par un déplacement de l'équilibre de gonflement du gel avec la température, et possiblement par la température critique inférieure de dissolution du PEG dans l'eau aux alentours de 100°C.[20] Sous lumière UV, les gels atteignent ensuite environ 25 ± 5 % de leur volume initial après 30 min. Dans un second temps, les gels furent d'abord irradiés avant d'être chauffés (Figure R.6.B). Après irradiation, les gels atteignent 67 ± 14 % de leur volume initial, puis l'augmentation de la température permet d'atteindre un volume relatif final de 39 ± 6 %.

En comparant les évolutions normalisées de $\%_V$ à différentes températures sous irradiation UV, il apparaît qu'il n'y ait pas de différence significative dans la cinétique de contraction lorsque les gels sont chauffés (Figure R.6.C). Ce résultat était attendu en considérant que les moteurs sont dans un régime photochimiquement limité, comme expliqué plus haut. Cependant, les écarts-type de ces mesures sont importants, et des conclusions claires ne peuvent donc pas être tirées sans études plus approfondies. De la même manière, les évolutions normalisées de $\%_V$ en fonction de la température, selon l'état étendu ou contracté du gel, ne montrent pas de différence significative. Il semble donc que les chaînes de polymères sont, dans les deux cas, gonflées dans un bon solvant, ce qui est corroboré par nos résultats obtenus par diffusion de neutrons aux petits angles.

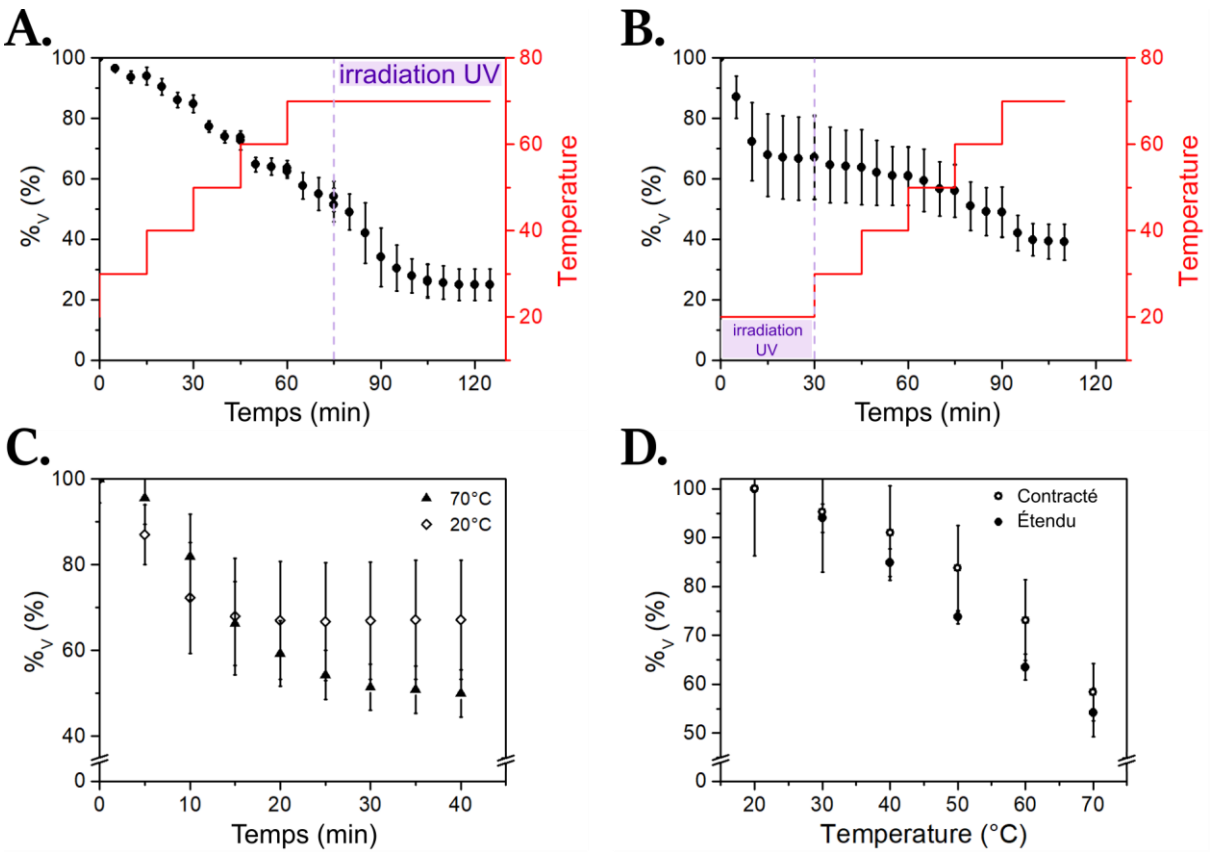

Figure R.6. Évolution du volume relatif $\%_V$ de gels de PEG ayant une masse moléculaire de 6 000 g·mol^{-1} irradiés à 365 nm à 80 mW·cm^{-2}. **A.** Les gels ont d'abord été chauffés avant d'être irradiés à 70°C. **B.** Les gels ont d'abord été irradiés à 20°C avant d'être chauffés jusqu'à 70°C. **C.** Évolution de $\%_V$ normalisé à deux températures différentes sous irradiation lumineuse. **D.** Évolution de $\%_V$ en fonction de la température normalisée, suivant l'état étendu ou contracté du gel.

Le dernier paramètre étudié est la masse moléculaire des chaînes entre nœuds de réticulation (Figure R.7). Tout d'abord, l'influence du dégazage a été étudiée car la présence d'oxygène a un impact significatif sur la contraction de gels formés à partir de PEG ayant une masse moléculaire de 10 000 g·mol^{-1} (Figure R.7.A). Cet effet n'est pas aussi important pour les gels formés avec des PEG plus courts, probablement car c* et, ainsi, la fraction volumique en polymères, est plus élevée dans ces gels. La rupture de certains maillons peut donc avoir un impact négligeable lorsque les chaînes sont plus courtes. Quoiqu'il en soit, les gels furent dégazés avant d'être irradiés (Figure R.7.B). Lorsque la masse moléculaire des PEG diminue, le volume relatif final $\%_{V,max}$ est plus élevé et la vitesse de contraction γ diminue. Comme indiqué plus tôt, la fraction volumique en polymère est plus élevée pour les chaînes courtes, ce qui peut expliquer ces résultats puisque les chaînes ont moins d'espace pour être enchevêtrées. De plus, les faibles γ peuvent également être expliquées par une concentration plus élevée en moteurs, diminuant le nombre de photons disponibles par molécule photo-active.

En conclusion, l'étude de nos gels de PEG ayant une topologie identique a permis d'identifier des tendances sur les propriétés de contraction de ces matériaux suivant plusieurs paramètres environnementaux ou structuraux. Ces résultats démontrent que la matrice influe le mouvement de

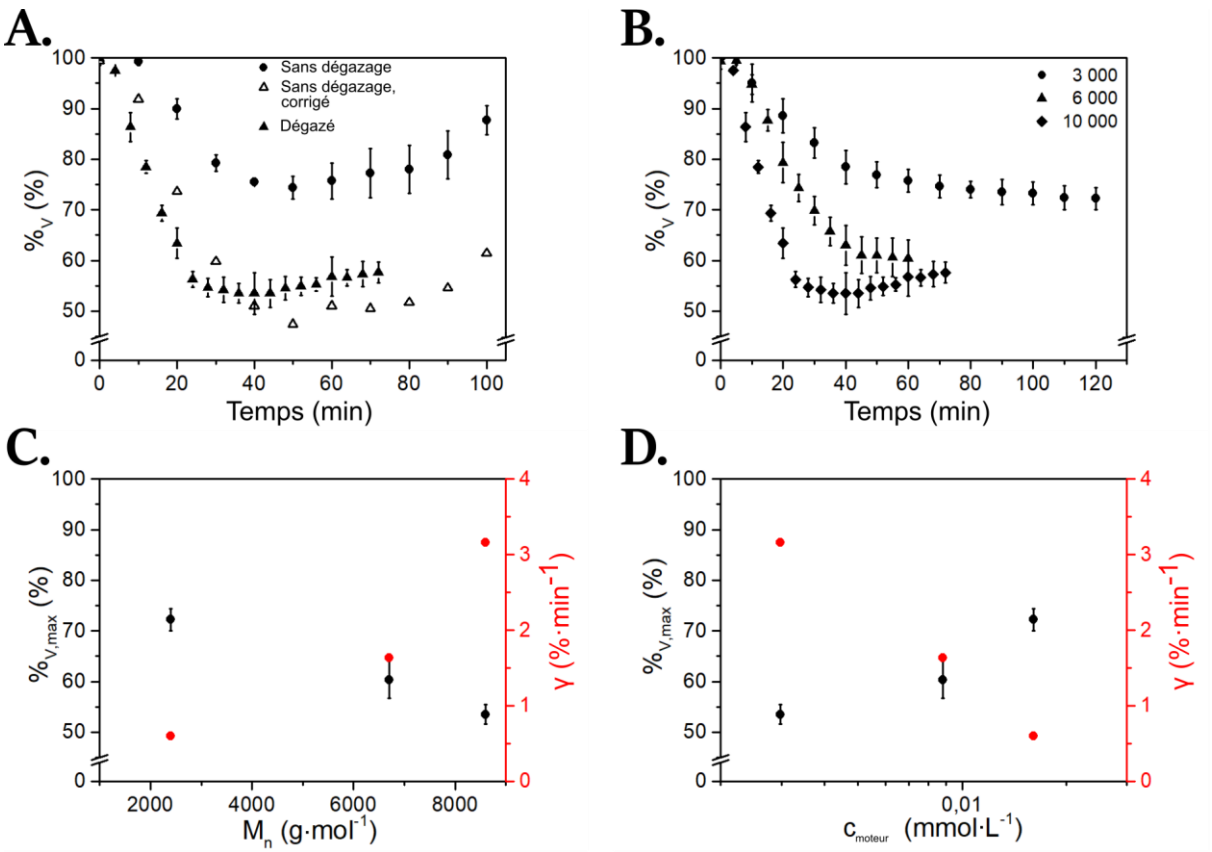

Figure R.7. A. Influence du dégazage sur la contraction des gels de PEG. **B.** Évolution du volume relatif $\%_V$ de gels de PEG ayant différentes masses moléculaires irradiés à 365 nm à 80 mW·cm^{-2}. **C et D.** Volume relatif final $\%_{V,max}$ et vitesse de contraction maximale en fonction de la masse moléculaire du PEG ou de la concentration en moteurs, respectivement.

rotation des moteurs, menant alors à différentes vitesses de contraction et à différents volumes finaux.

1.4 Synthèse d'autres polymères téléchéliques et formation des réseaux photoactifs correspondants

Plusieurs polymères ont été envisagés pour la préparation de réseaux réticulés avec des moteurs moléculaires. Tout d'abord, du poly(3-hexylthiophène) (P3HT) a été préparé par polymérisation par

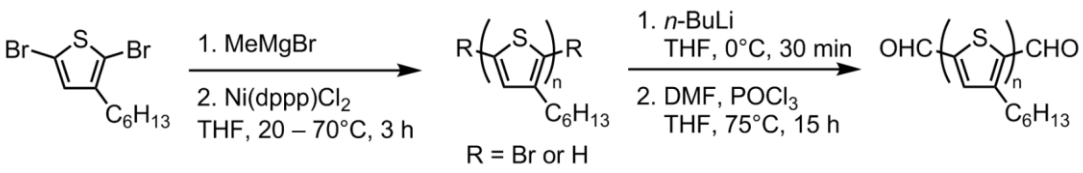

Schéma R.5. Synthèse de P3HT téléchélique par polymérisation par métathèse initiée par réactifs de Grignard.

métathèse initiée par réactifs de Grignard (Schéma R.5). Cette voie de synthèse a bien permis d'obtenir le polymère mais la fonctionnalisation n'a pas fonctionné quantitativement, donc ces dernières étapes doivent être optimisées.

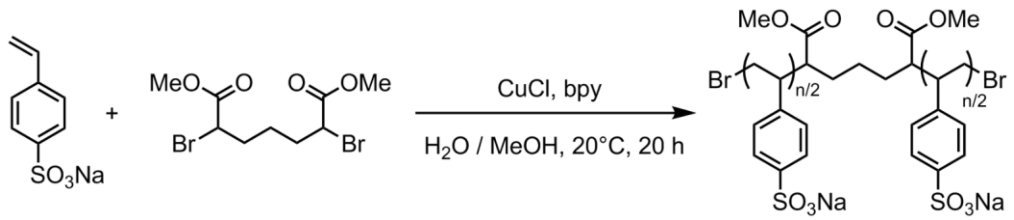

Schéma R.6. Synthèse de NaPSS téléchélique par polymérisation radicalaire à transfert d'atome.

Le second polymère dont la synthèse a été explorée est le poly(styrène sulfonate) de sodium (NaPSS). Dans ce cas, la macromolécule est formée par polymérisation radicalaire à transfert d'atome initiée par le 2,5-dibromoheptanedioate de diméthyle afin d'obtenir des halogénures terminaux pouvant être substitués (Schéma R.6). Cependant, nous n'avons pas obtenu de taux de conversion assez élevés pour pouvoir mener la fonctionnalisation des polymères pour leur intégration dans des matériaux. Cette voie de synthèse est également en cours d'optimisation.

Le poly(N-isopropylacrylamide) (PNIPAAm) a également été obtenu par polymérisation radicalaire à transfert d'atome (Schéma R.7). Contrairement au NaPSS, le taux de conversion de la

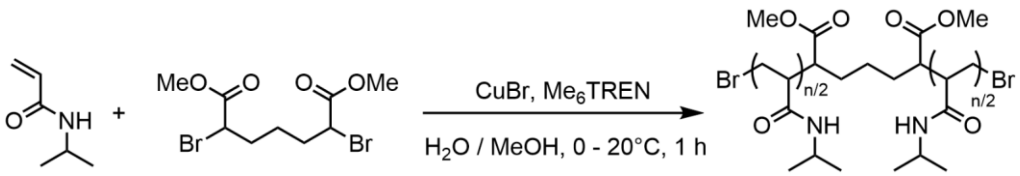

Schéma R.7. Synthèse de PNIPAAm téléchélique par polymérisation radicalaire à transfert d'atome.

polymérisation fut quantitatif. Cependant, les bromures terminaux sont significativement hydrolysés. Par conséquent, la fonctionnalisation n'est pas simplement possible par substitution nucléophile, mais elle peut être réalisée en suivant une stratégie similaire à celle utilisée par les PEG et est actuellement explorée.

Le poly(diméthylsiloxane) (PDMS) est, tout comme le PEG, disponible commercialement en tant que polymère linéaire téléchélique portant des groupements hydroxyles en bouts de chaîne. Par conséquent, sa fonctionnalisation a été effectuée en suivant la même voie de synthèse que celle utilisée pour les PEG. La concentration de recouvrement c* fut aussi déterminée afin de former les gels dans les conditions de concentration optimales dans le dichlorométhane.

Les gels de PDMS furent ensuite gonflés dans le tétrahydrofurane et irradiés sous UV (Figure R.8). Pour les deux puissances lumineuses testées, les gels atteignent le même volume relatif final de 64 ± 7 %. En outre, les gels contractent plus vite lorsque la puissance lumineuse est plus élevée ; pour le gel irradié à 365 $mW \cdot cm^{-2}$, la vitesse de contraction maximale est $\gamma = 8.5$ $\%\cdot min^{-1}$. Ces tendances sont identiques à celles observées pour les gels de PEG. Cependant, il est important de noter que la cinétique de contraction est plus rapide pour le PDMS que pour le PEG, alors que la fraction volumique en polymère dans le premier cas est bien plus élevée. Nous proposons donc que cet effet est dû à la plus faible longueur de persistance du PDMS, et donc sa plus grande flexibilité, par rapport au PEG, qui contrebalance l'effet de l'augmentation de la fraction volumique en polymères sur la contraction.

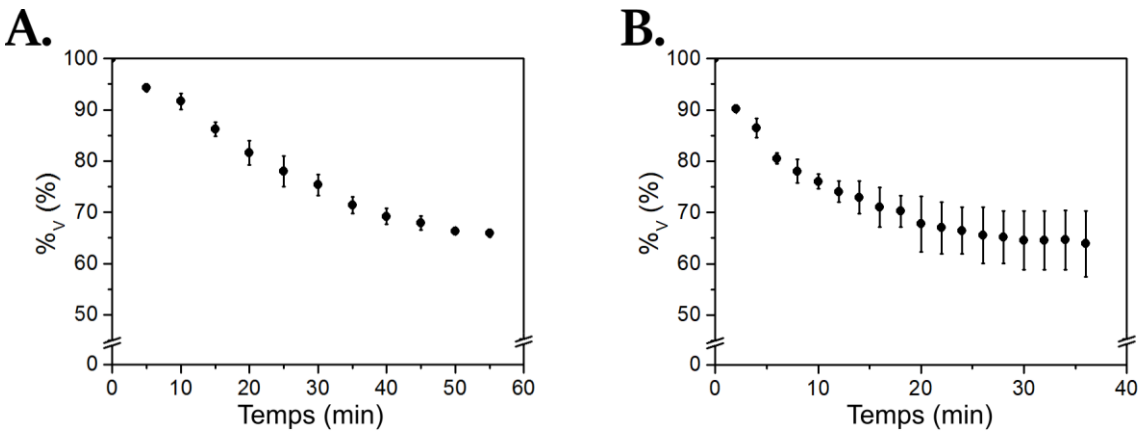

Figure R.9. Évolution du volume relatif $\%_V$ de gels de PDMS en fonction du temps d'irradiation à **A.** 80 mW·cm^{-2} et **B.** 365 mW·cm^{-2}.

La température de transition vitreuse et la température de fusion du PDMS est largement inférieure à la température ambiante[21] et, ainsi, les réseaux secs sont des élastomères souples. Par conséquent, les gels réticulés avec les moteurs moléculaires ont été séchés pour former des films et leur comportement sous irradiation UV fut observé (Figure R.9). Les films se déforment quand ils sont irradiés mais la quantification du changement de volume est délicate à cause de sa forme courbée. Il semble donc que les films atteignent un volume relatif final de 83 ± 10 % avec une vitesse de contraction maximale de 6.4 %·min^{-1}, seulement 24 % inférieure à celle obtenue pour les gels correspondants.

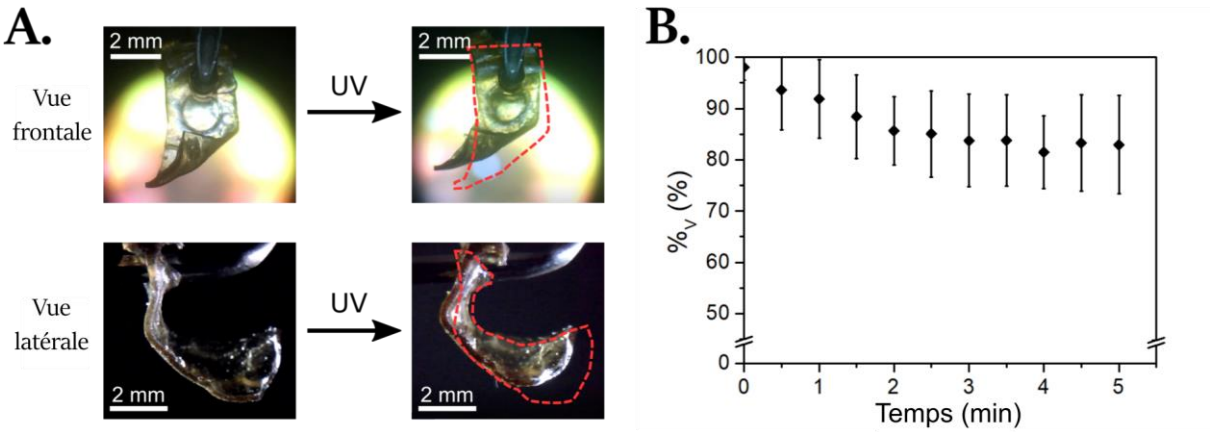

Figure R.8. A. Photographies des films de PDMS avant et après irradiation. **B.** Évolution du volume relatif $\%_V$ en fonction du temps d'irradiation pour les films de PDMS à 365 nm et à 365 mW·cm^{-2}.

Afin de comprendre le mécanisme responsable du changement de forme des films de PDMS, ils furent étudiés par analyse mécanique dynamique (Figure R.10.A et B). Le matériau semble se fluidifier réversiblement sous irradiation. Le module d'élasticité E' diminue significativement sous lumière UV et retourne à sa valeur initiale lorsque la source lumineuse est éteinte. Nous attribuons cette observation à l'effet photothermique du moteur moléculaire lorsqu'il est irradié, puisque l'augmentation de la température entraîne également une diminution du module d'élasticité du film. Cependant, l'effet photothermique seul ne peut pas expliquer le changement de volume de nos films puisqu'il est irréversible. Nous avons donc supposé que l'application d'une force pendant l'analyse mécanique dynamique change le mode de fonctionnement du moteur en empêchant la rotation. Par

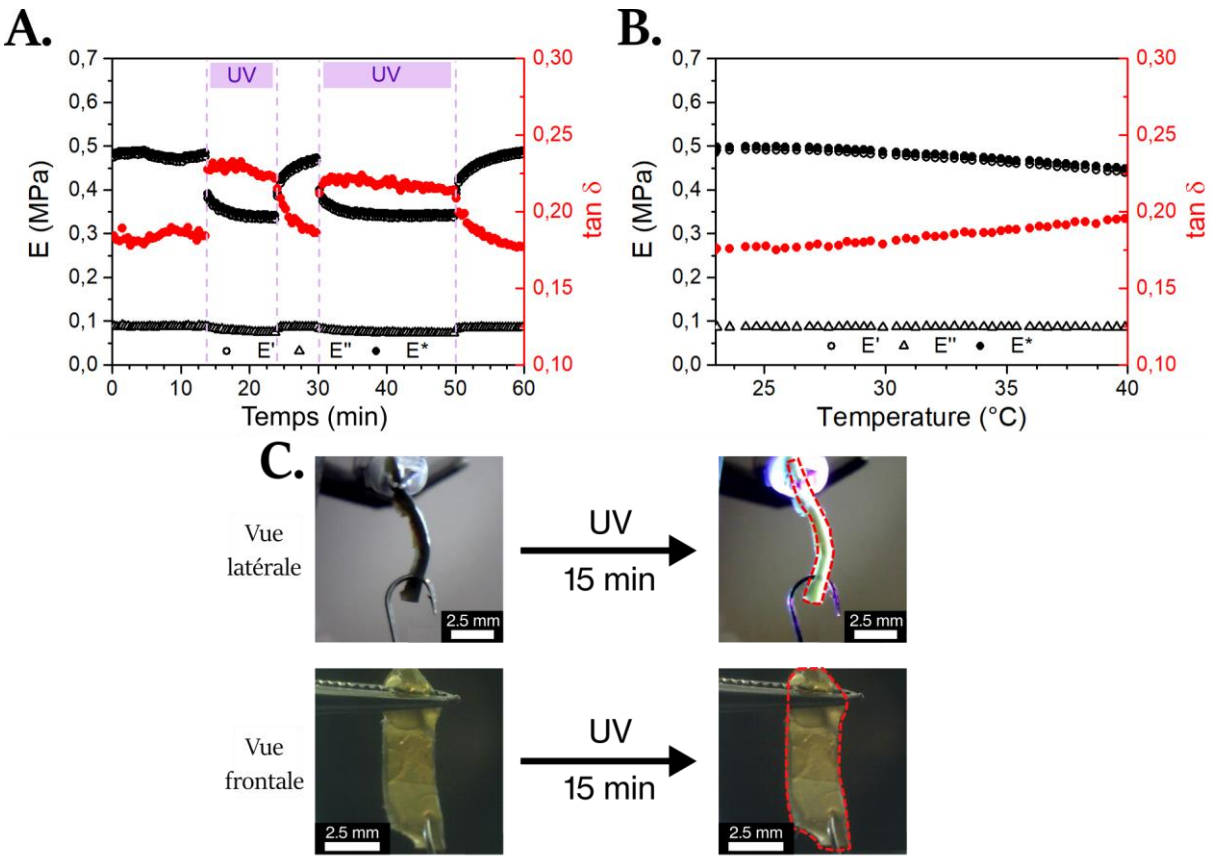

Figure R.10. A. Analyse mécanique dynamique d'un film de PDMS réticulé avec des moteurs moléculaires, avec et sans irradiation UV. **B.** Analyse mécanique dynamique d'un film de PDMS en fonction de la température. **C.** Photographies d'un film de PDMS avant et après irradiation UV lorsqu'un hameçon y est accroché.

conséquent, nous avons attaché une masse à nos films de PDMS pour voir un changement éventuel sur le comportement de contraction (Figure R..C) ; dans ce cas, aucune déformation n'a été observée. En conclusion, les contributions de l'effet photothermique et de l'éventuel effet de la rotation du moteur dans les élastomères de PDMS doivent être davantage étudiées pour comprendre la cause de la déformation sous lumière UV.

Le dernier système exploré est basé sur du poly(γ-benzyl-L-glutamate) (PBLG). Un polymère en étoile à quatre branches a été préparé par polymérisation par ouverture de cycle initiée par un moteur tétra-amine. Un gel physique fut préparé à partir de ces polymères dans le toluène et irradié sous UV (Figure R.11). Un effet de synérèse est observé, où le matériau expulse du solvant. Cette transformation n'est probablement pas seulement due à un effet photothermique car elle est irréversible. Le gel peut être reformé lorsque le système est chauffé, et une nouvelle irradiation UV mène une nouvelle fois à une synérèse. Ces systèmes prometteurs sont actuellement explorés plus en profondeur.

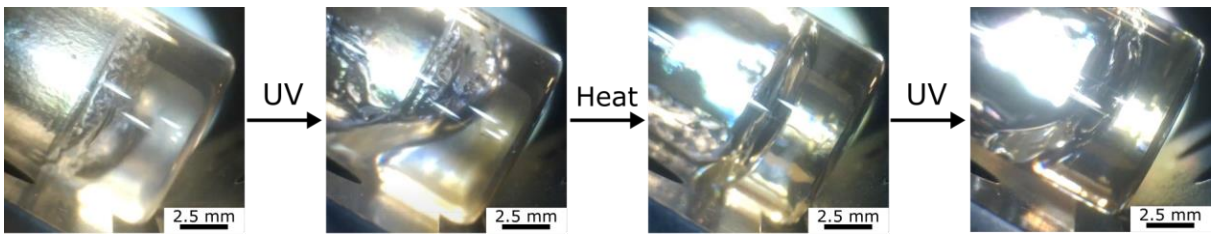

Figure R.11. Synérèse réversible pour les gels physiques de PBLG comportant des moteurs moléculaires.

En conclusion, plusieurs polymères ont été envisagés pour la formation de matériaux réticulés avec des moteurs moléculaires. Cependant, la plupart des synthèses n'ont pas mené à des polymères linéaires téléchéliques pouvant être utilisés pour la préparation de gels. Cela étant, des gels et des films secs de PDMS ont pu être obtenus. Leur comportement sous irradiation UV suit les mêmes tendances que pour les gels de PEG et peuvent ainsi permettre de confirmer nos premières conclusions. De plus, il semble que la plus faible longueur de persistance de ce polymère permet des cinétiques de contraction plus rapides. Ces premiers résultats montrent aussi le premier exemple de déformation macroscopique causée par des moteurs moléculaires dans une matrice molle amorphe, et des études supplémentaires doivent être conduites pour comprendre le mécanisme de ce changement de forme. Nous avons également réussi à former des gels physiques réversibles comportant des moteurs moléculaires à partir de PBLG, ce qui n'a jamais été présenté auparavant.

1.5 Intégration de moteurs moléculaires dans des élastomères cristaux liquides

Le dernier axe d'étude de cette thèse repose sur l'intégration de moteurs moléculaires dans des réseaux gonflés anisotropes. Nous avons repris la formulation d'élastomères cristaux liquides déjà utilisée précédemment dans la littérature en y incorporant nos moteurs moléculaires tétra-acrylate (Schéma R.8). Cependant, nous n'avons pas réussi à obtenir, pour le moment, de films pouvant être convenablement étudiés, et l'optimisation des conditions de préparation est en cours.

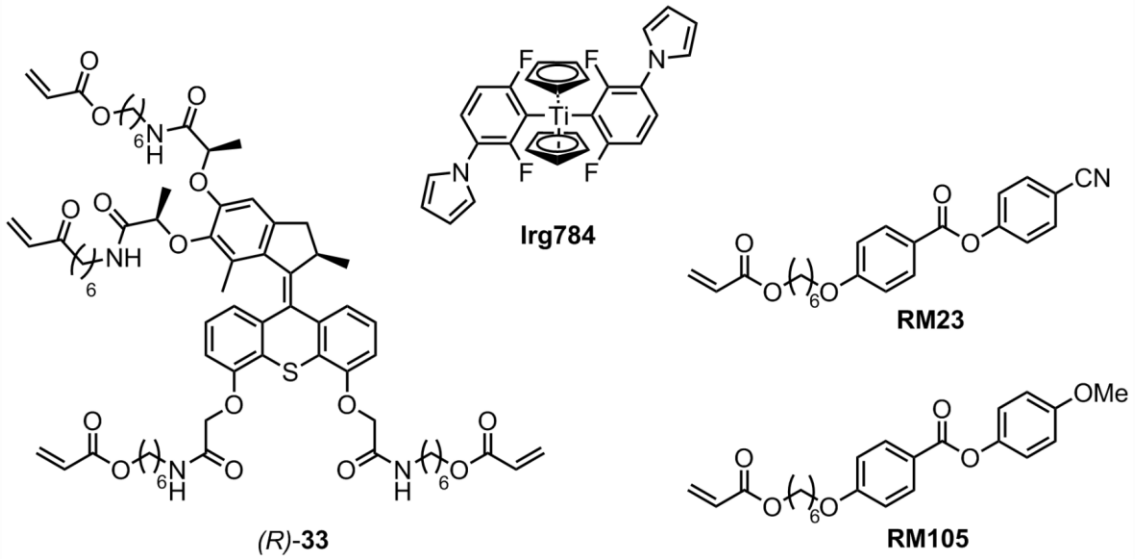

Schéma R.8. Formulation d'élastomères cristaux liquides incorporant des moteurs moléculaires comme nœuds de réticulation.

Conclusion et perspectives

Le premier objectif de cette thèse était l'étude de plusieurs paramètres environnementaux et structurels sur la rotation de moteurs moléculaires utilisés comme nœuds de réticulation dans des gels polymériques. Nous avons ainsi étudié l'impact de l'épaisseur du matériau, de la puissance

lumineuse, de la température et de la masse moléculaire entre nœuds de réticulation sur la cinétique de contraction. Plusieurs tendances se sont dégagées et doivent être confirmées pour des gels de différentes natures chimiques.

Par conséquent, le deuxième objectif de ce travail était d'utiliser d'autres polymères téléchéliques pour la préparation de gels. Nous avons réussi à obtenir des gels de PDMS qui semble suivre les mêmes tendances générales observées pour les gels de PEG. De plus, nous avons pu obtenir des élastomères de PDMS réticulés par des moteurs moléculaires, et nous avons observé pour la première fois un changement de forme causé par des moteurs moléculaires dans une matrice molle amorphe. Nous avons également préparé des gels physiques de PBLG à partir de polymères en étoile comportant des moteurs moléculaires. Lorsque ces matériaux sont irradiés, du solvent semble être expulsé de la matrice, et le gel peut être reformé en chauffant le système.

Le dernier objectif de ce projet était d'incorporer les moteurs moléculaires dans des gels anisotropes. Cependant, les formulations testées jusqu'à maintenant n'ont pas permis de former des matériaux qui peuvent être étudiés.

Ces résultats, présentés plus en détail dans le manuscrit, permettent ainsi de comprendre l'influence de la matrice sur le fonctionnement des moteurs moléculaires, et inversement. Bien que cette étude ne se soit seulement concentrée sur des matériaux synthétiques simples, nous espérons qu'elle puisse participer à la compréhension de réseaux plus complexes intégrant des machines moléculaires, comme les tissus biologiques.

Références

1. D. Dattler, G. Fuks, J. Heiser, E. Moulin, A. Perrot, X. Yao, N. Giuseppone, *Chem. Rev.* **2020**, *120*, 310–433.
2. F. Lancia, A. Ryabchun, N. Katsonis, *Nat. Rev. Chem.* **2019**, *3*, 536–551.
3. N. Koumura, R. W. J. Zijlstra, R. A. van Delden, N. Harada, B. L. Feringa, *Nature* **1999**, *401*, 152–155.
4. N. Koumura, E. M. Geertsema, A. Meetsma, B. L. Feringa, *J. Am. Chem. Soc.* **2000**, *122*, 12005–12006.
5. J. C. M. Kistemaker, P. Štacko, D. Roke, A. T. Wolters, G. H. Heideman, M.-C. Chang, P. van der Meulen, J. Visser, E. Otten, B. L. Feringa, *J. Am. Chem. Soc.* **2017**, *139*, 9650–9661.
6. J. Chen, F. K.-C. Leung, M. C. A. Stuart, T. Kajitani, T. Fukushima, E. van der Giessen, B. L. Feringa, *Nat. Chem.* **2017**, *10*, 132–138.
7. T. Orlova, F. Lancia, C. Loussert, S. Iamsaard, N. Katsonis, E. Brasselet, *Nat. Nanotechnol.* **2018**, *13*, 304–308.
8. R. Eelkema, M. M. Pollard, J. Vicario, N. Katsonis, B. S. Ramon, C. W. M. Bastiaansen, D. J. Broer, B. L. Feringa, *Nature* **2006**, *440*, 163–163.
9. Q. Li, G. Fuks, E. Moulin, M. Maaloum, M. Rawiso, I. Kulic, J. T. Foy, N. Giuseppone, *Nat. Nanotechnol.* **2015**, *10*, 161–165.
10. J. T. Foy, Q. Li, A. Goujon, J.-R. Colard-Itté, G. Fuks, E. Moulin, O. Schiffmann, D. Dattler, D. P. Funeriu, N. Giuseppone, *Nat. Nanotechnol.* **2017**, *12*, 540–545.
11. J. E. Walker, *Biochem. Soc. Trans.* **2013**, *41*, 1–16.
12. J. C. M. Kistemaker, P. Štacko, J. Visser, B. L. Feringa, *Nat. Chem.* **2015**, *7*, 890–896.

13. S. J. Wezenberg, B. L. Feringa, *Nat. Commun.* **2018**, *9*, 1984.
14. M. Klok, N. Boyle, M. T. Pryce, A. Meetsma, W. R. Browne, B. L. Feringa, *J. Am. Chem. Soc.* **2008**, *130*, 10484–10485.
15. I. Teraoka, *Polymer Solutions*, John Wiley & Sons, Inc., **2002**.
16. J.-R. Colard-Itté, Q. Li, D. Collin, G. Mariani, G. Fuks, E. Moulin, E. Buhler, N. Giuseppone, *Nanoscale* **2019**, *11*, 5197–5202.
17. G. Mariani, J.-R. Colard-Itté, E. Moulin, N. Giuseppone, E. Buhler, *Soft Matter* **2020**, *16*, 4008–4023.
18. N. R. Richbourg, N. A. Peppas, *Prog. Polym. Sci.* **2020**, *105*, 101243.
19. M. Klok, W. R. Browne, B. L. Feringa, *Phys. Chem. Chem. Phys.* **2009**, *11*, 9124.
20. S. Saeki, N. Kuwahara, M. Nakata, M. Kaneko, *Polymer* **1976**, *17*, 685–689.
21. A. C. M. Kuo, in *Polymer Data Handbook* (Ed.: J.E. Mark), Oxford University Press, **1999**, pp. 411–435.

List of tables and illustrations

List of units, symbols and abbreviations

°C	degree Celsius
%	percent
$\%_V$	relative volume
δ	phase lag
γ	maximum contraction rate
ε	strain
σ	stress
ω	angular frequency
[η]	intrinsic viscosity
η_{red}	reduced viscosity
η_{sp}	specific viscosity
μ	kinematic viscosity
μm	micrometer
μs	microsecond
χ	polymer-solvent interaction parameter
Å	Ångstrom
ATRP	Atom-Transfer Radical Polymerization
Bn	benzyl
Boc	*tert*-butoxycarbonyl
bpy	2,2'-bipyridyl
BTG	1,4-butanediol bis(thioglycolate)
n-Bu	butyl
s-Bu	butan-2-yl
t-Bu	2-methylpropan-2-yl

cm	centimeter
CuAAC	Cu(I)-catalyzed Azide-Alkyne Cycloaddition
d	day
Da	Dalton
DBHD	dimethyl 2,6-dibromoheptanedioate
DBU	*1,8*-diazabicyclo[5.4.0]undec-7-ene
DCC	dicyclohexylcarbodiimide
DIAD	diisopropyl azodicarboxylate
DMA	Dynamic Mechanical Analysis
DMAP	dimethylaminopyridine
DMF	dimethylformamide
DMPA	2,2-dimethoxy-2-phenylacetophenone
DNA	deoxyribonucleic acid
DPMK	diphenylmethyl potassium
dppp	1,3-bis(diphenylphosphino)propane
DSC	Differential Scanning Calorimetry
DTT	D,L-dithiothreitol
EDC	1-ethyl-3-(3-dimethylaminopropyl)carbodiimide
eq	equivalent
ESI	Electrospray Ionization
Et	ethyl
Fmoc	fluorenylmethoxycarbonyl
fps	frame per second
g	gram
GPC	Gel Permeation Chromatography
GRIM	Grignard metathesis
h	hour
HOBt	hydroxybenzotriazole
HPLC	High Pressure Liquid Chromatography
HRMAS	High-Resolution Magic-Angle Spinning
HRMS	High-Resolution Mass Spectrometry

HTP	Helical Twisting Power
Hz	Hertz
IUPAC	International Union of Pure and Applied Chemistry
k_B	Boltzmann constant
L	liter
L_C	contour length
LCE	Liquid Crystalline Elastomer
LCP	Liquid-Crystalline Polymer
LCST	Lower Critical Solution Temperature
LED	Light-Emitting Diode
M	$mol \cdot L^{-1}$
m	meter
MALDI	Matrix-Assisted Laser Desorption Ionization
MALS	Multi-Angle Light Scattering
Me	methyl
Me_6TREN	tris[2-(dimethylamino)ethyl]amine
mg	milligram
MHz	megahertz
min	minute
mL	milliliter
mm	millimeter
mmol	millimole
mol	mole
MOM	methoxymethyl
MPa	megapascal
MS	Mass Spectrometry
mW	milliwatt
$\mathcal{N}_A$	Avogadro constant
NaPSS	sodium poly(styrene sulfonate)
nm	nanometer
ns	nanosecond

NMR	Nuclear Magnetic Resonance
P3HT	poly(3-hexylthiophene)
Pa	Pascal
PBLG	poly(γ-benzyl-L-glutamate)
PDA	photodiode array
PDB	Protein Data Bank
PDMS	poly(dimethylsiloxane)
PEG	poly(ethylene glycol)
PET	poly(ethylene terephthalate)
PGA	poly(L-glutamic acid)
Ph	phenyl
PMB	*para*-methoxyphenyl
PMDETA	*N,N,N′,N″,N‴*-pentamethyldiethylenetriamine
PNIPAAm	poly(*N*-isopropylacrylamide)
PPA	polyphosphoric acid
ppm	parts per million
Q	swelling ratio
R_f	retardation factor
R_F	end-to-end distance
R_G	radius of gyration
R_H	hydrodynamic radius
RDRP	Reversible-Deactivation Radical Polymerization
ROP	Ring-Opening Polymerization
s	second
SANS	Small-Angle Neutron Scattering
SET	Single-Electron Transfer
SQD	Single Quadrupole Detection
t	time
T	temperature
T_g	glass transition temperature
TBAF	tetra-*n*-butylammonium fluoride

TBS	*tert*-butyldimethylsilyl
TEG	tri(ethylene glycol)
TFA	Trifluoroacetic Acid
THF	tetrahydrofuran
THI	Thermal Helix Inversion
TLC	Thin Layer Chromatography
TMEDA	tetramethylethylenediamine
TOF	Time of Flight
Ts	4-methylbenzenesulfonyl, tosyl
UPLC	Ultra-Performance Liquid Chromatography
USB	Universal Serial Bus
UV	ultraviolet
V	volume
W	Watt
WLC	Worm-Like Chain

Introduction

Actuating materials based on synthetic molecular machines have gained tremendous interest over the last decades. The use of stimuli-sensitive organic molecules in materials science allowed the design of a new generation of responsive soft matrices that are more adapted to function with biological systems than their hard counterparts based on metallic assemblies, and, hence, can be applied in the fields of medicine, information processing or soft robotics, for instance. Moreover, they rely on the operation of nanoscopic molecular assemblies that are sensitive to their environment and may, therefore, operate at a scale that may be hardly accessible by miniaturization of existing machines, and without the need of user input.

Synthetic molecular machines can be divided in two main categories: molecular switches and molecular motors. The formers have been widely investigated as the active units in a wide array of soft matrices. For instance, azobenzene is commonly used as a photosensitive dopant in liquid-crystalline system. Its shape change occurring during light irradiation may disrupt the ordered, liquid-crystalline phase and may, hence, trigger deformations up to the macroscale. Spiropyran, on the other hand, is commonly used in swollen networks because the difference in polarity between its two states may lead to different swelling equilibria of the material. Finally, actuating crystals of diarylethenes were designed where the small geometry changes occurring during stimulation led to large deformation modes.

Synthetic molecular motors, however, have been designed more recently and, consequently, fewer reports describe their use in actuating system. The main difference between this class of molecules and molecular switches is their ability to perform directional motion under appropriate input on energy, like biological machineries using ATP to continuously accomplish their task out of equilibrium. The most studied synthetic molecular motors are based on overcrowded alkenes, which have been integrated in soft systems such as supramolecular assemblies and liquid-crystalline phases. While some of these systems may operate out-of-equilibrium because molecular motors continuously alternate between several states, none of them truly exploit the directional motion produced during the operation cycle.

We reported the design of polymeric gels crosslinked with synthetic molecular motors based on overcrowded alkenes, where the unidirectional motion triggers macroscopic actuation. The polymer strands composing the network are continuously intertwined upon the operation of the active crosslinkers under light irradiation, and the creation of new entanglements results in the contraction of the material over time. Since the rotation from the motors is unidirectional, the shape change was

irreversible; the introduction of complementary crosslinkers based on diarylethenes, acting as 'stress releasers', led to the full reversibility of the actuation upon orthogonal stimulation. Moreover, these initial systems were carefully investigated by mechanical analysis and scattering techniques to link the nanoscopic motion to the resulting macroscopic properties.

So far, however, our studies were only focused on gels of poly(ethylene glycol) in only one set of optimal conditions. Several molecular weights were investigated but only one of the corresponding gels was formed at its overlap concentration, which was determined to be the concentration where the gels have the best performance. Therefore, a deeper understanding of the mechanism of operation of our photoactive gels may be achieved by investigating the materials when they are prepared at their respective optimal concentrations. In these conditions, we can then alter parameters that change the structure of the network, regardless of its topology, and isolate their effects on the contraction performance of the gels.

Moreover, changing the chemical nature of the polymer strands has not yet been investigated. When the gels are formed at the overlap concentration and, hence, the topology is identical, we expect that the persistence length of the chains has an influence on the contractile behavior of the materials. The crosslinking units braid the polymers together, so their rigidity or flexibility should alter the process and, consequently, different macroscopic responses may rise. Changing the chemical nature of the strands may give additional properties to our systems as well, such as thermoresponsiveness or conductivity, by crosslinking the adequate polymer chains.

Finally, we reported so far isotropic polymer gels and we hypothesized that the integration of molecular motors inside anisotropic swollen polymer networks may also give different properties than the ones we previously observed. In liquid-crystalline systems, the polymer chains adopt long-range conformational order and, hence, the braiding of the strands might be direction-dependent; consequently, the shape change at the macroscopic scale might be anisotropic.

The present thesis is therefore divided into two parts. The first part is a literature review containing the recent advances in the field and the concepts necessary to understand the operation of our materials and consists of two chapters. Chapter 1 presents the design principles of molecular motors, their mechanism of operation and focuses on recent applications of molecular motors in the field of materials science. Chapter 2 provides an overview of physicochemical properties of polymer networks, as well as the main properties of the polymers used in this work. The second part of this thesis is focused on our advances on the topics that we stated in the previous paragraphs and consists of four chapters. Chapter 3 is devoted to the multigram-scale synthesis of tetra-functional molecular motors based on overcrowded alkenes, which were used as crosslinking agents for all the following chapters. Chapter 4 is focused on photoactive gels of poly(ethylene glycol) and our systematic variation of parameters to understand their impact on the contractile properties. Chapter 5 presents our investigations on the alteration of the chemical nature of the strands by synthesizing and crosslinking different polymers with molecular motors. Chapter 6 is devoted to our attempts to form liquid-crystalline elastomers and gels crosslinked with molecular motors. We end this manuscript by

providing a short overview of the results obtained and perspectives for future research on the mutual effect of soft matrices and molecular motors.

Part I
Bibliography

Chapter 1
Synthetic molecular motors and amplification of their motion

Macroscopic and nanoscopic motors do not follow the same operation principles because of the scale at which they operate. The Reynolds number represents the ratio of inertial forces over viscous forces acting on an object immersed in a fluid. It scales with the size of the object in question; therefore, a macroscopic object usually moves in an environment of high Reynolds number and its motion is mostly governed by inertial forces described by classical mechanics. Conversely, nanoscopic objects evolve in environments of low Reynolds number where motion is mainly controlled by viscous forces.[1] In that scenario, the trajectory of the particle is not determined by its inertia but rather subjected to Brownian motion described by statistical physics.[2]

Even though controlling their motion is not as straightforward as for their macroscopic counterparts, exploiting the mechanical motion of nanomotors to perform macroscopic tasks presents advantages. For instance, they allow the design of functional materials from a bottom-up approach[3] and, therefore, overcome the issues associated with the miniaturization of existing technologies. They can also be incorporated into soft robotic systems based on organic materials. Finally, they can be operated by a wide array of stimuli, including light, chemical potential, or electric fields. The main challenge resides in amplifying their nanoscopic motion to the macroscopic world by a proper design of the system.

The present chapter consists in three parts. The first one gives definitions and basis on the thermodynamic framework that are necessary to understand how molecular motors operate. Examples of synthetic molecular motors are then presented in a second section. Finally, the chapter ends with the presentation of systems where controlled nanoscopic motion was successfully amplified at the macroscopic scale in ‘smart’ materials.

1.1 Definitions and thermodynamic considerations

As stated in the introduction, the underlying principles governing the mechanisms of operation of active molecular systems are different from the ones explaining the operation of macroscopic machines. Therefore, a specific terminology must be used, and important terms are defined in the

following paragraphs. Some of these definitions are still discussed in the scientific community but the ones used in this thesis follow what seems to be a general consensus.[4]

The principle of **microscopic reversibility** states, according to IUPAC, that 'in a reversible reaction, the mechanism in one direction is exactly the reverse of the mechanism in the other direction. This does not apply to reactions that begin with a photochemical excitation.'[5] Notably, as will be further discussed later, photochemical processes do not follow the principle of microscopic reversibility because they are not thermal processes occurring at the ground energy level of the molecule.

Detailed balance is tightly related to microscopic reversibility. Again, the IUPAC definition states that 'when equilibrium is reached in a reaction system, [...] as many atoms, in their respective molecular entities will pass forward, as well as backwards, along each individual path in a given finite time interval. Accordingly, the reaction path in the reverse direction must in every detail be the reverse of the reaction path in the forward direction [...].'[6] In other words, at equilibrium, there is no net flux of molecules going from one state to another and, consequently, no energy can be harnessed from a system at equilibrium.

In the context of this thesis, any molecular assembly that can perform a function in a controlled manner is considered as a molecular machine. It includes molecular switches, molecular motors, and any combination of the two, eventually correlated to each other with molecular gears.

Molecular switches are stimuli-sensitive molecules that can change their state depending on their environment. Specifically, **chemical molecular switches** have different energy landscapes depending on their chemical environment, for instance by modulating the pH or the redox potential (Figure 1.1.A). The stimulation is reversible and, following the principle of microscopic reversibility, the backward path is exactly the reverse of the forward path. In other words, any work performed

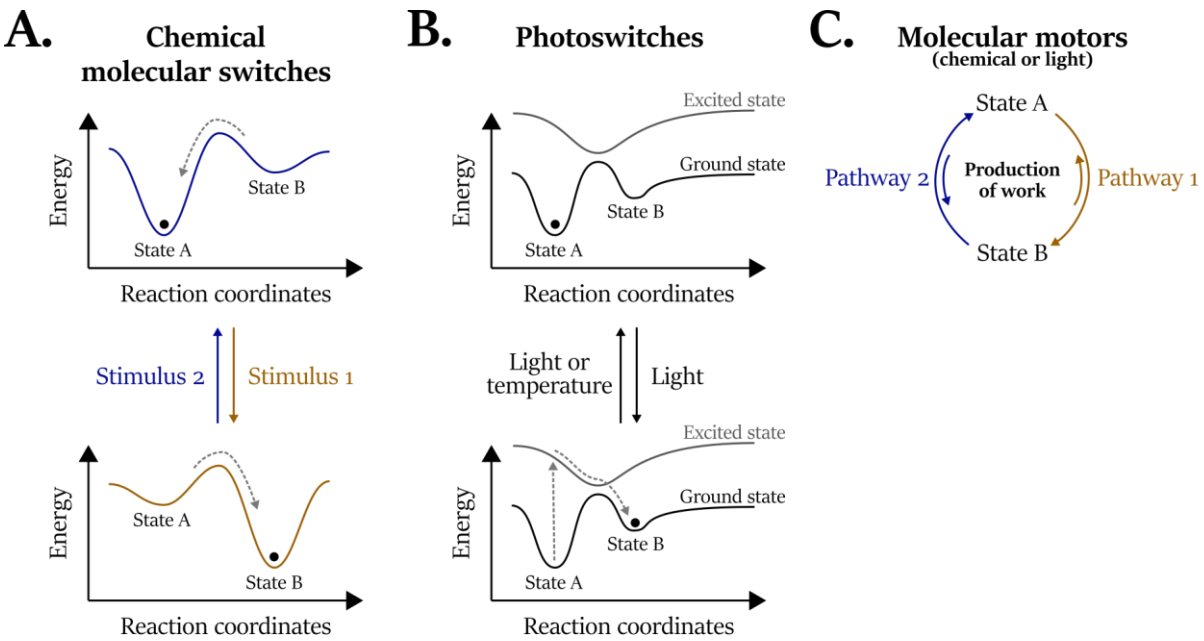

Figure 1.1. General mechanisms of molecular switches and motors. **A.** Chemical molecular switches have different energy profiles depending on their environment. The molecule (black dot) adopts the most stable state depending on which stimulus is applied. **B.** Photoswitches can populate a higher energy state upon light irradiation. They return to the initial state either by light irradiation or thermal relaxation. **C.** Molecular motors can produce work if the direction of its motion is controlled and do not follow the same pathway between the forward motion and the backward motion.

when going from state A to state B is cancelled out when going back from state B to state A. **Photoswitches**, on the other hand, absorb photons to reach their photoexcited state. Relaxation back to their ground energy profile may lead to the population of a state of higher energy than the initial one. The initial state can be recovered upon light irradiation or by thermal relaxation (Figure 1.1.B). Since photochemical processes do not follow the principle of microscopic reversibility, photoswitches 'break' detailed balance and may be out-of-equilibrium;[7] however, energy cannot be continuously extracted from these systems because there is no directionality in their motion and, consequently, any work that may be performed averages to zero over time.

Molecular motors differ from molecular switches because they perform directional motion that can produce work, which can be released to their environment. As for molecular switches, they can be powered by chemical energy or light energy and follow different mechanistic principles accordingly. Regardless of the stimuli, the molecule must break detailed balance during its operation cycle by following different pathways to return to its initial state. Moreover, its motion must be controlled in one specific direction so that work can be performed (Figure 1.1.C). Unidirectionality may be achieved with irreversible steps called '**energy ratchets**' that, just as macroscopic ones, favor motion in one direction.[8]

Quantitative analysis of molecular motors cannot be described by 'classical' thermodynamics, which deals with systems at equilibrium. Instead, stochastic thermodynamics frameworks have been developed in the last few decades to characterize the mechanisms of work production of these machines and have notably been used for biological molecular motors.[9,10] The exact thermodynamic description of out-of-equilibrium systems are beyond the scope of this thesis; however, a few general aspects are presented.

Molecular motors, as explained earlier, are molecules capable of producing mechanical work during their operation cycle. The fact that their motion is controlled implies that their entropy decreases and, consequently, there must be an energy input in order not to break the second law of thermodynamics. Therefore, the operation of molecular motors, and out-of-equilibrium systems in general, must be conducted in an open system; energy is absorbed by the molecular machine and is then dissipated in its environment.[11] The energy dissipation of molecular motors can be characterized by their entropy production rate.[10]

Mechanisms for energy conversion to mechanical work are usually separated in two extreme models: the power stroke and the Brownian ratchet.[11,12] In the **power stroke** model, the energy input is used by the molecule to adopt a high-energy state that will relax to its most stable state after directional motion of large amplitude. In the **Brownian ratchet** model, in reference to Feynman's thought experiment 'Ratchet and pawl',[13] the molecule is subjected to Brownian motion and the energy input is used to favor the forward direction over the backward direction, hence leading to directional motion. From these mechanisms, it has been derived that power strokes should move faster and work against loads better than Brownian ratchets.[14] Real systems, however, follow mechanisms between those two extremes, sometimes depending on the step of their operation cycle,[12] and theoretical analysis have been conducted to determine the contributions of each.[15] Light-driven molecular motors, as will be discussed later, seem to follow a power stroke mechanism.

Molecular motors are ubiquitous in biology because they are the active units driving living systems out-of-equilibrium. Contrariwise to molecular switches, which impact their environment depending on their state, molecular motors impact their environment depending on their trajectories. From a thermodynamic viewpoint, these machines 'simply' convert energy from one form to another, like macroscopic motors. The next sections provide a few examples of molecular motors.

1.2 Examples of synthetic molecular motors

Before discussing examples of artificial molecular motors, we will introduce a few examples of biological ones to highlight their differences and similarities. Living systems are constantly being driven out-of-equilibrium by supramolecular machineries, for instance to transport cargos,[16] achieve muscle contraction[17] or pump ions against concentration gradients.[18] In this introduction, we will only focus on F_0F_1-ATP synthase, a rotary motor, and kinesins on microtubules, which are linear motors. More detailed descriptions of these machines can be found in recent reviews.[11,12]

Kinesins are a wide family of proteins with transport functions in living cells.[19] The motorized part of these molecules is composed of two heads linked by a neck, which are connected to cargos with longer coils (Figure 1.2).[20,21] While the exact mechanism depends on the kinesin and is still under debate,[22] the general mechanism is described as the ATP-powered processive rotation of one head past the other along the microtubule chain, resulting in a translating motion of the protein along its track.

F_0F_1-ATP synthase is a supramolecular complex of proteins capable of synthesizing ATP from a transmembrane proton gradient or, depending on the conditions, pump protons against a concentration gradient by hydrolyzing ATP.[23] It consists of two units, connected to each other with a 'stator': the F_0 unit, embedded in the membrane and sensitive to proton flow, and the F_1 unit, responsible for the processing of ATP (Figure 1.2).[24] This latter is composed of a hexagonal arrangement of three alternating pairs of α and β subunits inside which is inserted the γ subunit. The γ subunit rotates following three 120° steps, one for each β subunit processing one ATP molecule;[25] in other words, three molecules of ATP are necessary to complete a full 360° rotation.

Just as for these two examples, synthetic molecular motors have also been designed to produce either rotary or translational motion. The main difference, however, between artificial motors and biological ones resides in their complexity; the latter consists of heavy supramolecular assemblies that were designed over the course of evolution to perform precise tasks with excellent yields, while lab-made machineries are smaller systems that may be more easily understood.

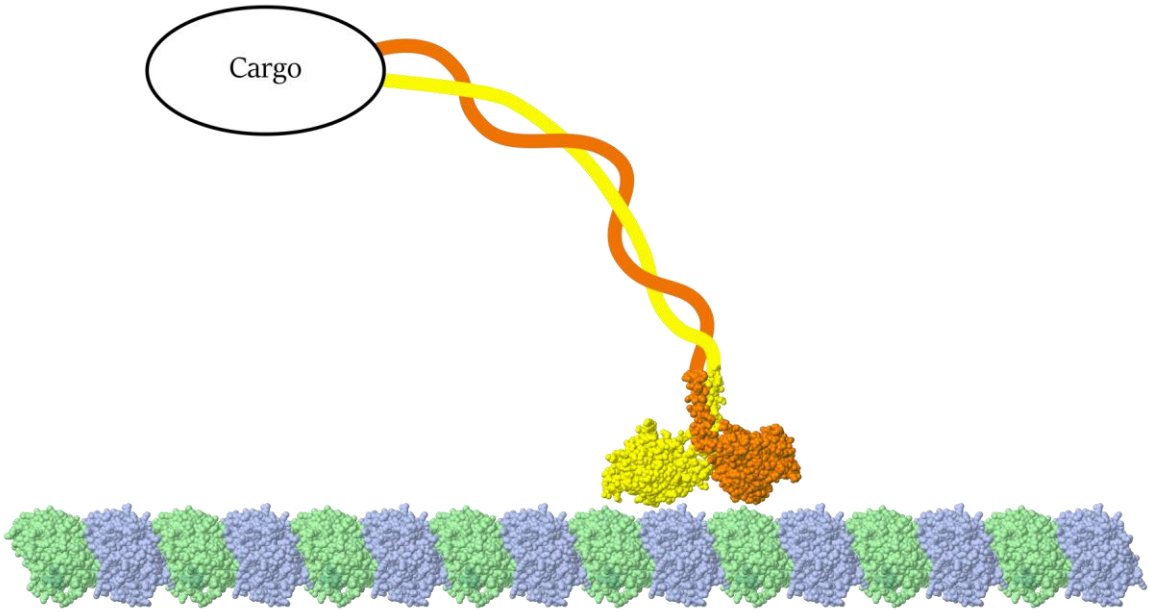

Figure 1.2. Structure of a kinesin head from *Rattus norvegicus*[20] on microtubules. The microtubule dimer (blue and green) is from *Sus scrofa*.[21] The exact assembly between the kinesin head and the microtubule is not shown. The kinesin head is composed of two heads (yellow and orange) linked together with a neck and connected to a cargo. The continuous repetition of the rotation of one head past the other along the track results in a translational motion.

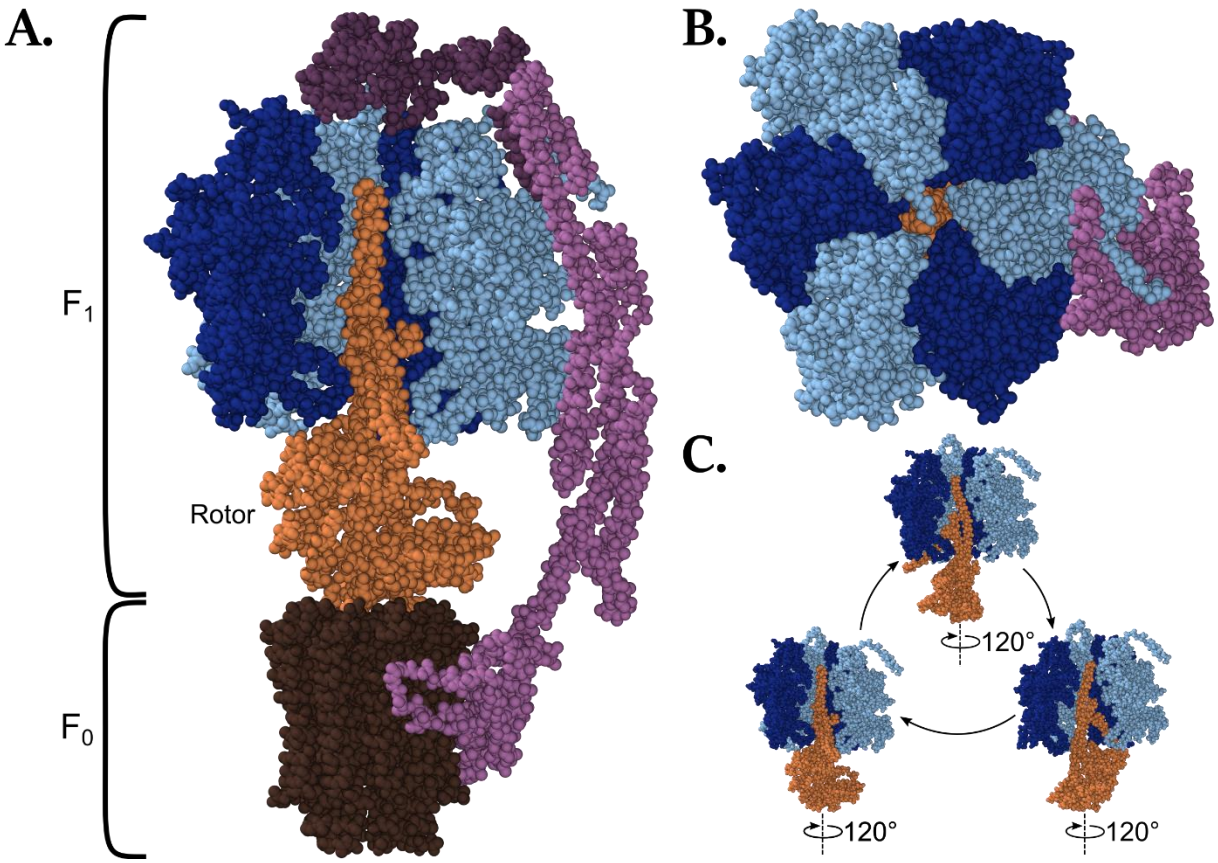

Figure 1.3. Structure of F_oF_1-ATP synthase from *Pichia Angusta*.[24] The F_o unit (in dark brown) is embedded in the membrane. The γ subunit (in orange), acting as a rotor, is partially inserted in a cavity composed of three α (light blue) and three β (dark blue) subunits and form together the F_1 unit. This cavity is immobilized by a stator (in purple) connected to F_o. **A.** Side view (one α and one β subunit were removed). **B.** Top view. **C.** Rotation of the γ subunit upon ATP hydrolysis. Overall, three molecules of ATP are necessary to achieve full 360° rotation.

This section begins with the description of mechanically interlocked molecular motors that can perform motion of large amplitude. The second part will introduce a few covalent motors that were not used in this thesis, while the last and most important part will describe molecular motors based on overcrowded alkenes that were at the core of this work.

1.2.1 Mechanically interlocked molecular motors

Mechanically interlocked molecules are a class of compounds whose parts are connected topologically through mechanical bonds. Even though these parts are not covalently linked, their separation requires the breakage of covalent bonds. There are two main categories of mechanically interlocked molecules: rotaxanes, where an axle is threaded through a macrocycle, and catenanes, where macrocycles interpenetrate each other (Figure 1.4). Since they are not restrained by covalent bonds, the different parts of these molecules perform large amplitude motion related to each other and controlling this motion may lead to molecular motors.

Figure 1.4. Two families of mechanically interlocked molecules: rotaxanes, where a macrocycle surrounds an axle, and catenanes, where macrocycles interpenetrate each other.

Leigh, Wong and coworkers reported the unidirectional motion of two macrocycles around a third one in a [3]catenane.[26] The main macrocycle is composed of four stations to which the two other ones bind by hydrogen bonding (Figure 1.5.A). The first two stations A and B are light-sensitive fumaramide motifs. A benzophenone moiety is next to station A to trigger its photoisomerization at a different wavelength than station B, and station B is methylated to slightly reduce its affinity to the macrocycles. Station C is a succinimic amide ester and station D is an amide group. The two secondary macrocycles are based on benzylic amides. The relative affinity of these macrocycles to the different stations is A > B > C > D; therefore, at the initial state, they bind stations A and B. Irradiation with UV light at 350 nm sensitizes the benzophenone, which triggers the isomerization of station A to its *Z* isomer and greatly reduces its affinity to the macrocycle. The latter will therefore bind station C following a (relative) counterclockwise rotation around the main macrocycle since station B is occupied by the other secondary macrocycle, which provides a steric barrier against (relative) clockwise rotation. This step is followed by irradiation with UV light at 254 nm, which isomerizes station B to its *Z* isomer and, following a similar mechanism, triggers the binding of the other secondary macrocycle to station D following a counterclockwise motion. Finally, stations A and B are reinitialized, either by thermal or chemical means, and the two secondary macrocycles return to these stations but with their initial positions inverted. Repetition of these three steps results in an overall 360° counterclockwise rotation of the two secondary macrocycles around the main macrocycle (Figure 1.5.A, right). In this design, microscopic reversibility is broken by coupling different equilibria that act as energy ratchets upon another; the position of one macrocycle affects the directionality of motion of the other one by steric hindrance. Therefore, this system acts as a molecular motor powered by (photo)chemical energy. One year later, Leigh and coworkers reported a similar system where, this time, the direction of rotation could be controlled by changing the sequence of chemical inputs.[27]

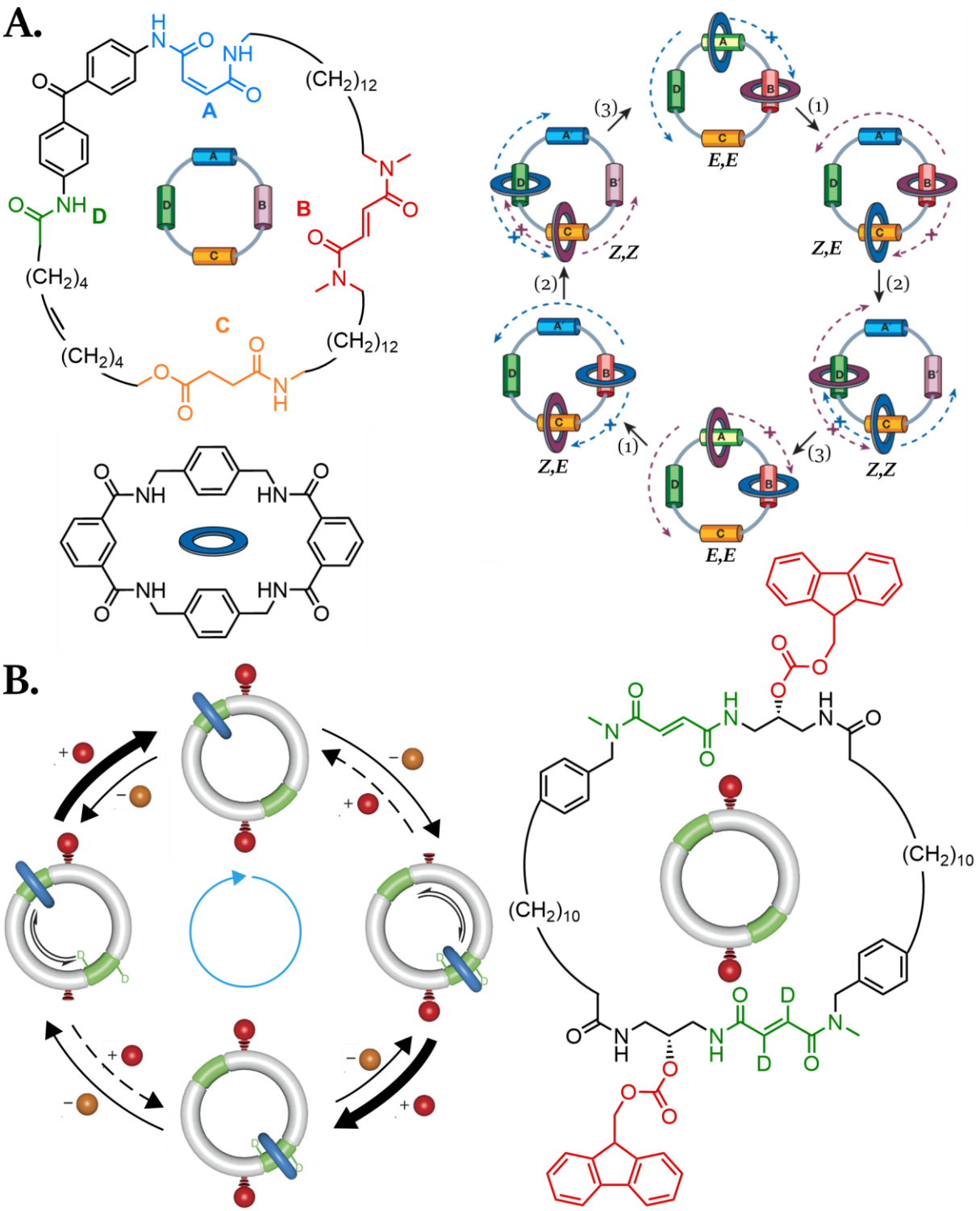

Figure 1.5. Catenane-based molecular motors. **A.** Left, chemical structures and corresponding schematic representations of the components of a [3]catenane-based molecular motor. Right, mechanism of unidirectional motion of the two secondary macrocycles around the third main one. Conditions (1): light irradiation at 350 nm; conditions (2): light irradiation at 254 nm; conditions (3): heating at 100°C, or ethylenediamine, or Br_2 with blue light. The relative affinity of binding is changed and triggers the motion of one macrocycle to different stations while the position of the other macrocycle induces unidirectional motion (see main text for further details), hence leading to a 360°C anticlockwise motion of the secondary macrocycles around the third main one. Adapted from reference [26]. **B.** Left, mechanism of unidirectional motion an autonomous [2]catenane-based molecular motor. The cleavage rate of Fmoc (producing waste, yellow sphere) does not depend on the position of the secondary macrocycle (blue ring), The rate of attachment of Fmoc-Cl (red sphere) is, on the other hand, position-dependant; the reaction occurs faster at a position far away from the station where the blue macrocycle identical to the one in panel A, is positioned. This kinetic bias drives the unidirectional motion of the secondary macrocycle. Right, chemical structure and corresponding schematic representations of the main macrocycle of an autonomous [2]catenane-based molecular motor. Adapted from reference [28].

Leigh and coworkers further optimized this system by designing an autonomous chemical molecular motor based on a [2]catenane.[28] The main macrocycle has two fumaramide stations, one of which being deuterated, that can bind a secondary macrocycle based on benzylic amides (Figure 1.5.B, right). Moreover, two bulky stoppers based on fluorenylmethoxycarbonyl (Fmoc) moieties, which can be reversibly cleaved, are present right next to each station. The authors reported that the rate of Fmoc cleavage does not depend on the position of the secondary macrocycle, while the rate of Fmoc coupling occurs faster at a position far away from the station bound to the secondary macrocycle. Consequently, they prepared a mixture containing the [2]catenane, triethylamine, which cleaves the Fmoc stopper, $KHCO_3$, which regenerates the amine from its ammonium salt after cleavage, and Fmoc-Cl, which acts as the chemical fuel consumed to regenerate the stoppers. In these conditions, the kinetic bias provided by the position-dependent rate of Fmoc attachment drives the unidirectional motion of the secondary macrocycle relative to the main one as long as the chemical fuel is present (Figure 1.5.B, left). Therefore, this molecule acts as a rotary molecular motor with an 'information ratchet', where the position of the particle modulates the energy profile of the system.[8]

While catenanes have been investigated as rotary molecular motors, rotaxanes have been used to develop synthetic linear molecular motors. For instance, Credi and coworkers reported a light-powered [2]pseudorotaxane capable of pumping macrocycles in one preferential direction.[29,30] They designed an axle bearing a dialkylammonium station, which can bind to a macrocycle based on crown ether, a light-sensitive azobenzene moiety at one side and a cyclopentadiene at the other one (Figure 1.6.A, top). In the *E* configuration, the macrocycle preferentially threads the axle *via* the azobenzene side because of steric constraints. In the *Z* configuration, the interaction between the dialkylammonium station and the macrocycle is destabilized and, also due to steric constraints, the macrocycle preferentially unthreads the axle *via* the cyclopentadiene end. Consequently, irradiation at a wavelength triggering both the *E* to *Z* and *Z* to *E* isomerizations autonomously drives the threading of the macrocycle at one end and its unthreading at the other, thereby linearly displacing it in one preferential direction (Figure 1.6.A, bottom).

Following their work on a chemically driven molecular pump,[31] Stoddard and coworkers went one step further by designing a system where the displaced macrocycles are stored in a thread, thereby exploiting the mechanical work to create a higher-energy state of lower entropy.[32] The active part of the molecule consists of a dicationic viologen station bearing a dimethylpyridinium at one side and an isopropylphenyl at the other, and is connected to a thread with a diisopropylphenyl stopper *via* a triazole unit. The viologen station can bind a macrocycle based on cyclobis(paraquat-*p*-phenylene) (Figure 1.6.B, top). Upon reduction, the station and the macrocycle are converted into their radical cation derivatives and form a triradical tricationic complex (Figure 1.6.B, bottom, state 1) after threading the macrocycle *via* the pyridinium end of the axle. Oxidation restores the initial state of the molecules, and the macrocycle unbinds the viologen *via* the isopropylphenyl side due to electrostatic repulsion with the pyridinium end (Figure 1.6.B, bottom, state 2). Therefore, the macrocycle is 'stored' on the thread against entropy (Figure 1.6.B, bottom, state 3). This linear molecular motor therefore acts as a pump displacing macrocycles against concentration gradients. The same team recently reported an enhanced system where two pumping units are connected to the same thread and could together pump up to ten macrocycles along the axle.[33]

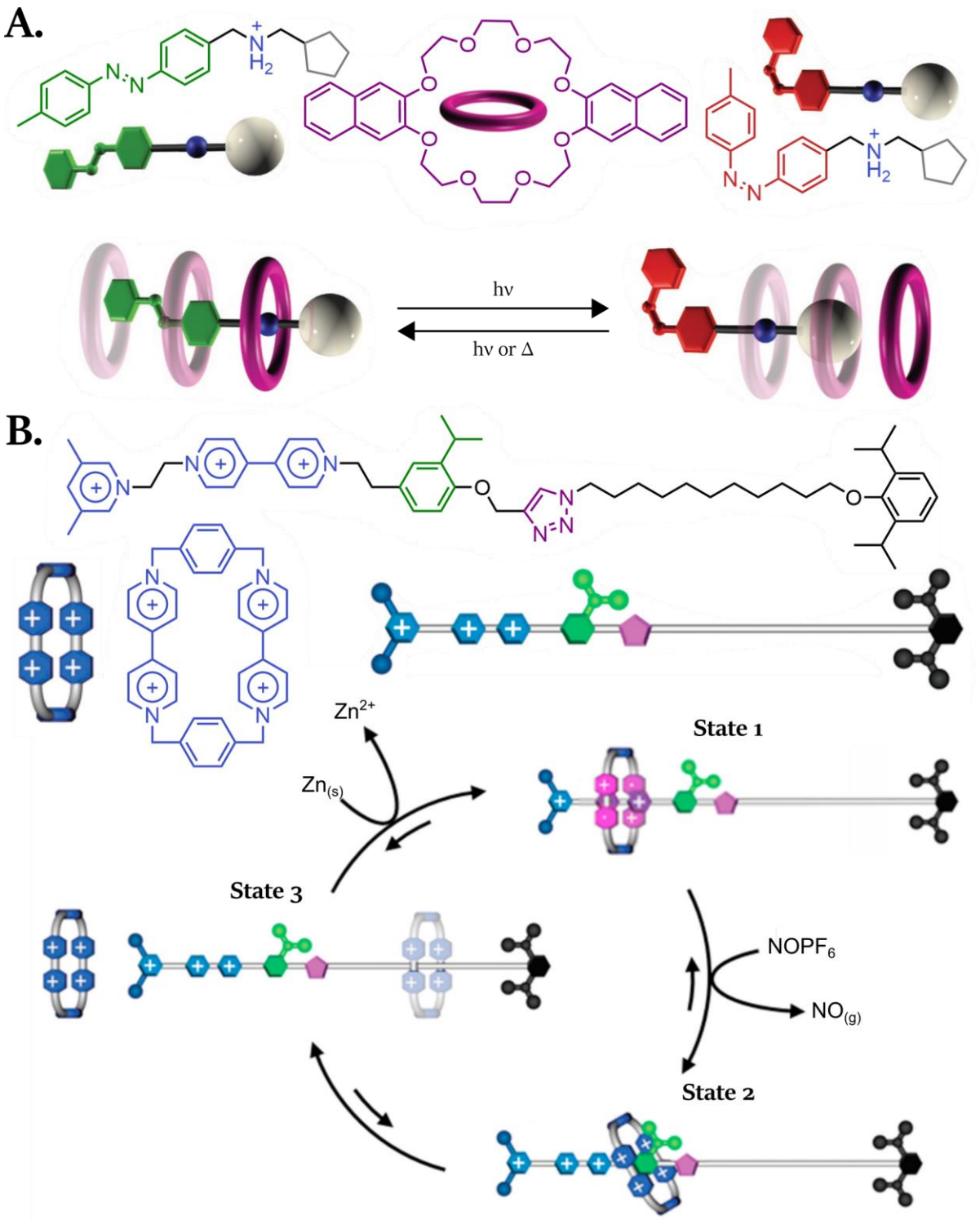

Figure 1.6. Rotaxane-based linear molecular motors. **A.** Top, chemical structures and corresponding schematic representations of a light-powered [2]pseudorotaxane-based molecular motor. Bottom, mechanism of the unidirectional translation of the macrocycle along the axle. In the *E* configuration, the macrocycle preferentially binds the station by threading the axle through the azobenzene end. In the *Z* configuration, the macrocycle is preferentially unthreaded through the cyclopentadiene end. Irradiation at a wavelength triggering both isomerizations therefore leads to unidirectional pumping of the macrocycle along the axle. Adapted from reference [29]. **B.** Top, chemical structures and corresponding schematic representations of a [2]rotaxane-based molecular motor acting as a macrocycle pump. Bottom, schematic representation of the pumping mechanism. Reduction of the macrocycle and of the viologen station triggers the formation of a triradical tricationic complex after threading the axle through the pyridinium end (state 1). Reoxydation of the system destabilizes the complex and the macrocycle is preferentially displaced through the isopropylphenyl side (state 2) and is therefore stored in the adjacent thread (state 3). In other words, the active unit pumps the macrocycle onto the thread against entropy. Adapted from reference [32].

Mechanically interlocked molecular motors present the advantage of producing large amplitude motion since their components are not covalently linked. Moreover, both light- and chemically powered motors have been developed to produce linear or rotary motion, so they can be potentially used for different applications. However, these systems involve the synthesis of several molecules resulting, most of the time, in large assemblies that can be complicated to characterize. Moreover, since they are usually based on supramolecular recognition motif, they function under a specific set of conditions. Covalent molecular motors, discussed in the next sections, avoid these drawbacks because they tend to be smaller molecules and are less sensitive to their environment, so their behavior is more easily studied and more robust towards external parameters.

1.2.2 Overview of covalent molecular motors

Different types of covalent molecular motors have been developed over the last few decades, which vary in their stimuli-responsiveness or the type of motion they produce. Before diving further in the systems based on overcrowded alkenes in the next section, which are the subject of this thesis, this section presents few different designs of other types of covalent molecular motors.

First, several chemically powered rotary molecular motors based on biaryls have been developed by Feringa and coworkers and they all follow the same general mechanism.[34] *o*-substituted biaryls may exist as different atropoisomers because free rotation around the central C—C bond does not take place, due to the presence of the substituents. The energetic barrier for atropisomerization is too high to occur at reasonable temperatures but the addition of reactant, acting as a chemical fuel, may lower the barrier enough for isomerization to take place. Moreover, the isomerization must be directional to obtain a molecular motor; the interaction between the biaryl and the chemical fuel must therefore be asymmetric and favor one atropisomer over the other (Figure 1.7.A).

The first reported design is based on a naphthalenic stator connected to a benzenic rotor (the rotor and stator parts are arbitrarily assigned) (Figure 1.7.B). The benzene ring has its two *ortho* positions substituted with protected alcohols and the naphthalene is *ortho*-substituted with a carboxylic acid. In the initial state, the rotor and stator are bridged by an ester bond, forming a lactone, and the remaining phenol is protected with a *para*-methoxyphenyl (PMB) group. Reduction of the lactone by an asymmetric reducing agent, *(S)*-2-methyl-oxazaborolidine, drives induces unidirectional rotation by forming mainly one atropisomer. The resulting phenol is protected with an allyl group and the benzylic alcohol is oxidized to the corresponding carboxylic acid. Deprotection of the former PMB-protected alcohol leads to the formation of a new lactone where the rotor has performed a 180° rotation around the stator. Repetition of these steps (asymmetric reduction, protection/oxidation, and deprotection/cyclization) completes the 360° rotation of this chemically driven molecular motor. In this case, the rotation is fully reversible by using the reducing agent of opposite configuration.[35]

The second design reported by Feringa and coworkers is based on a biaryl where two benzene rings are connected to each other (Figure 1.7.C). The stator is *o*-substituted with a fluorine on one side and a chiral sulfoxide on the other, and the rotor is *o*-substituted with a bromine. Addition of Pd(II) activates the *ortho* C—H bond of the rotor and the resulting intermediate has a lower energetic barrier for atropisomerization. The chiral information on the sulfoxide favors the atropisomer with

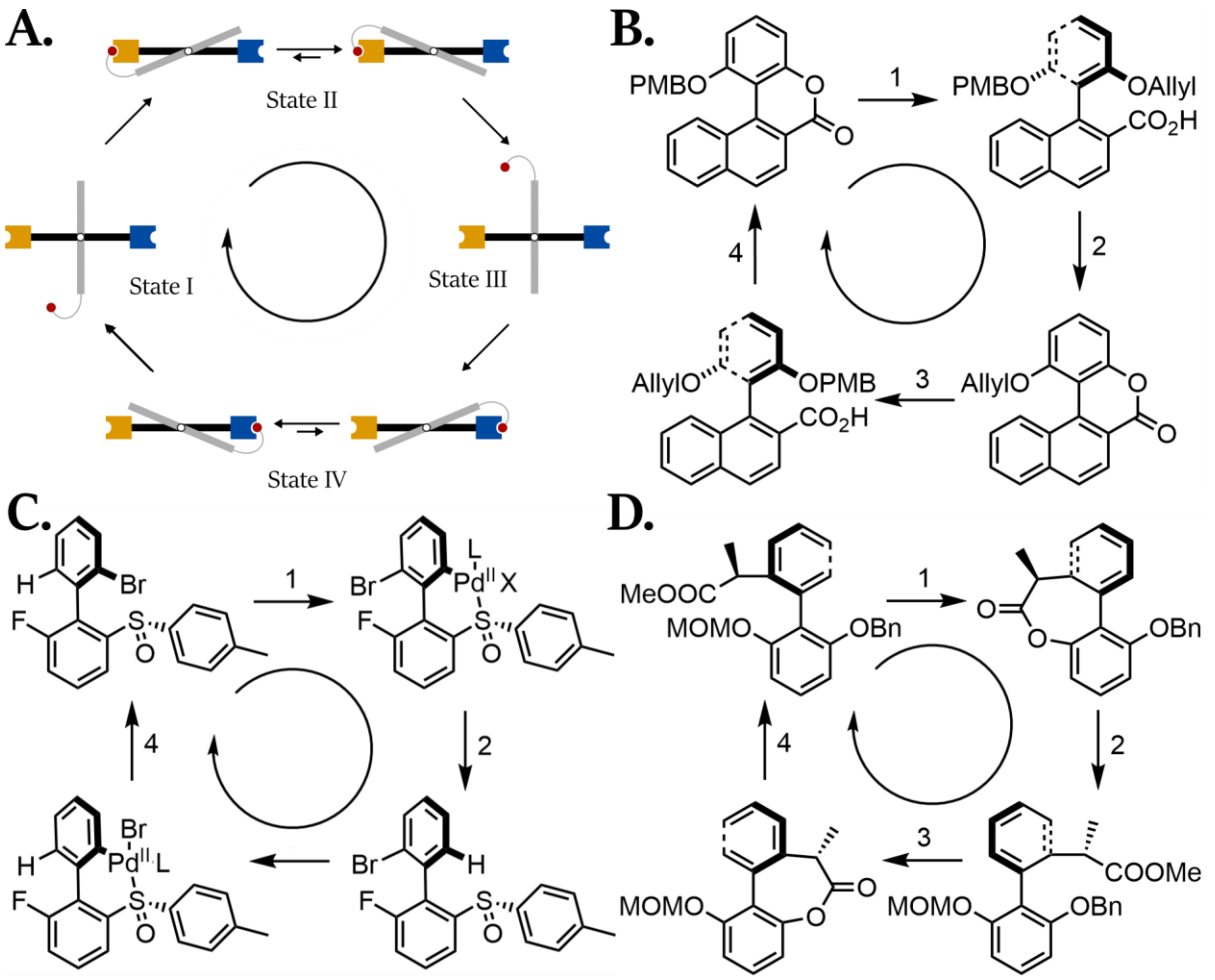

Figure 1.7. Chemically driven covalent rotary molecular motors based on biaryls. **A.** Schematic representation of the general mechanism of directional rotation in biaryl-based molecular motors (top view). Since the presence of substituents hinders the free rotation around the C—C bond (white dot), the rotor (grey line) cannot perform 360° rotation around the stator (black line) so state I cannot directly reach state III. Addition of a chemical fuel that bridges the two halves may lower the energy barrier for atropisomerization and a proper design of the system may favour the formation of one atropisomer over the other (states II and IV), leading to unidirectional rotation. Adapted from reference [34]. **B.** Chemical structures of the first biaryl-based chemical rotary molecular motor during its rotation cycle. In step 1, the lactone is reduced with a chiral reducing agent to mainly form one atropisomer, which drives unidirectional motion. The resulting phenol is protected with an allyl group and the benzylic alcohol is oxidized to a carboxylic acid. Deprotection of PMB (step 2) forms a new lactone where the rotor has performed a 180° rotation. After asymmetric reduction of the lactone, protection of the phenol, oxidation of the benzylic alcohol (step 3), deprotection of the allyl and cyclization (step 4), the 360° rotation is complete. Adapted from reference [35]. **C.** Chemical structures of the second design of a biaryl-based chemical rotary molecular motor during its rotation cycle. In step 1, C—H activation with Pd(II), directed by the sulfoxide, forms an intermediate where the helicity is inverted because of the configuration of the sulfoxide, thereby inducing directional rotation. In step 2, the C—H bond is reintroduced and oxidative addition of Pd(0) on the C—Br bond (step 3) forms back the initial helicity because of the configuration of the sulfoxide. The initial atropisomer is restored after reintroduction of the C—Br bond (step 4). Overall, the rotor has performed a 360° unidirectional rotation relative to the stator. Adapted from reference [36]. **D.** Chemical structures of the latest design of a biaryl-based chemical rotary molecular motor during its rotation cycle. In step 1, the MOM-protected phenol is deprotected, the ester is saponified, and addition of EDC·HCl forms the lactone. The configuration of the carbon next to the ester drives the helix inversion and, therefore, unidirectional rotation. After transesterification of the ester and reprotection of the phenol in step 2, the other atropisomer is formed after an overall 180° rotation. The repetition of these two steps (selective deprotection followed by lactonization, and transesterification followed by reprotection) forms the initial atropisomer back, where the stator has performed 360° unidirectional rotation. Adapted from reference [34].

opposite helicity and, therefore, drives the unidirectionality of the rotation. Subsequent reintroduction of the C—H bond leads to 180° rotation of the rotor around the stator. Then, oxidative

addition of Pd(0) on the C—Br bond forms a new intermediate where, once more, the chirality of the sulfoxide favors the formation of one preferential atropoisomer after helix inversion. After reintroducing the C—Br bond, the rotor has completed a 360° unidirectional rotation around the stator.[36]

The most recent design of a biaryl-based molecular motor also consists of two connected benzene rings (Figure 1.7.D). The rotor bears a chiral α-ester on one of its *ortho* position and the stator has two orthogonally protected alcohols on its *ortho* positions. First, the methoxymethyl-protected (MOM-protected) alcohol is selectively deprotected, leading to the concomitant saponification of the ester. Subsequent addition of 1-ethyl-3-(3-dimethylaminopropyl)carbodiimide hydrochloride (EDC·HCl) drives the lactonization between the carboxylic acid moiety and the free alcohol. The conformation of the stereocenter next to the ester drives the helix inversion and mainly forms the other atropisomer. Transesterification of the lactone and reprotection of the phenol with MOM restores the biaryl, where the rotor rotated 180° with respect to the stator. Selective deprotection of the other phenol bearing a benzyl group (Bn) and saponification of the ester, followed by addition of EDC·HCl, forms the other corresponding lactone. For the same reasons as before, namely the configuration of the carbon next to the ester, helix inversion occurs and the other atropisomer is formed back after transesterification of the lactone and reprotection with BnBr, completing 360° unidirectional rotation. The main advance of this system compared to the two previous ones is that the overall yield of the rotation cycle is higher with a better unidirectionality.[34]

Linear covalent molecular motors, usually qualified as 'molecular walkers', have been reported to mimic the function of transport proteins such as kinesins.[37] Many designs are based on DNA because of its highly selective binding motifs[37,38] but we will only focus here on fully synthetic directional molecular walkers, which have been developed by Leigh and coworkers.

Their first design is based on a bipedal 'walker' that can move along a 'track' composed of four stations with two orthogonal chemistries (Figure 1.8.A). The walker can bind the track with a hydrazone linkage at one end and a disulfide bridge at the other, both being dynamic covalent bonds under appropriate conditions. The track is composed two sets of alternating stations that can either form a hydrazone (stations 1 and 3) or a disulfide (stations 2 and 4) bond. Under acidic conditions, the disulfide bond is stable, but the hydrazone bond is labile; contrariwise, under basic conditions, the disulfide bond is labile, and the hydrazone bond is stable. Therefore, starting with the isomer where the walker binds stations 1 and 2 (1,2-isomer), addition of trifluoroacetic acid (TFA) leads to an equilibrium between the 1,2- and 2,3-isomers. Subsequent addition of *1,8*-diazabicyclo[5.4.0]undec-7-ene (DBU) as a strong base, along with D,L-dithiothreitol (DTT) to favor disulfide exchange and dimethyl *3,3'*-disulfanediyldipropanoate as a placeholder, then leads to equilibria between the 1,2- and 1,4-isomers, and 2,3- and 3,4-isomers. Cycling between these two sets of conditions eventually leads to an equilibrium distribution of isomers determined by the relative stabilities of the different macrocycles. However, reduction of the 2,3-isomer with DBU and DTT (without the disulfide placeholder) to form the ring-opened intermediate, followed by reoxidation with iodine, leads to the formation of the kinetically favored 3,4-isomer (Figure 1.8.A, bottom). The walker is then out-of-equilibrium, which is highlighted by the difference in relative

amount of the 3,4-isomer obtained after redox conditions or after basic conditions (43 % and 19 %, respectively).[39] This design was further investigated with different lengths for the walker, highlighting the impact of the size of the macrocycle on the directionality of the system.[40]

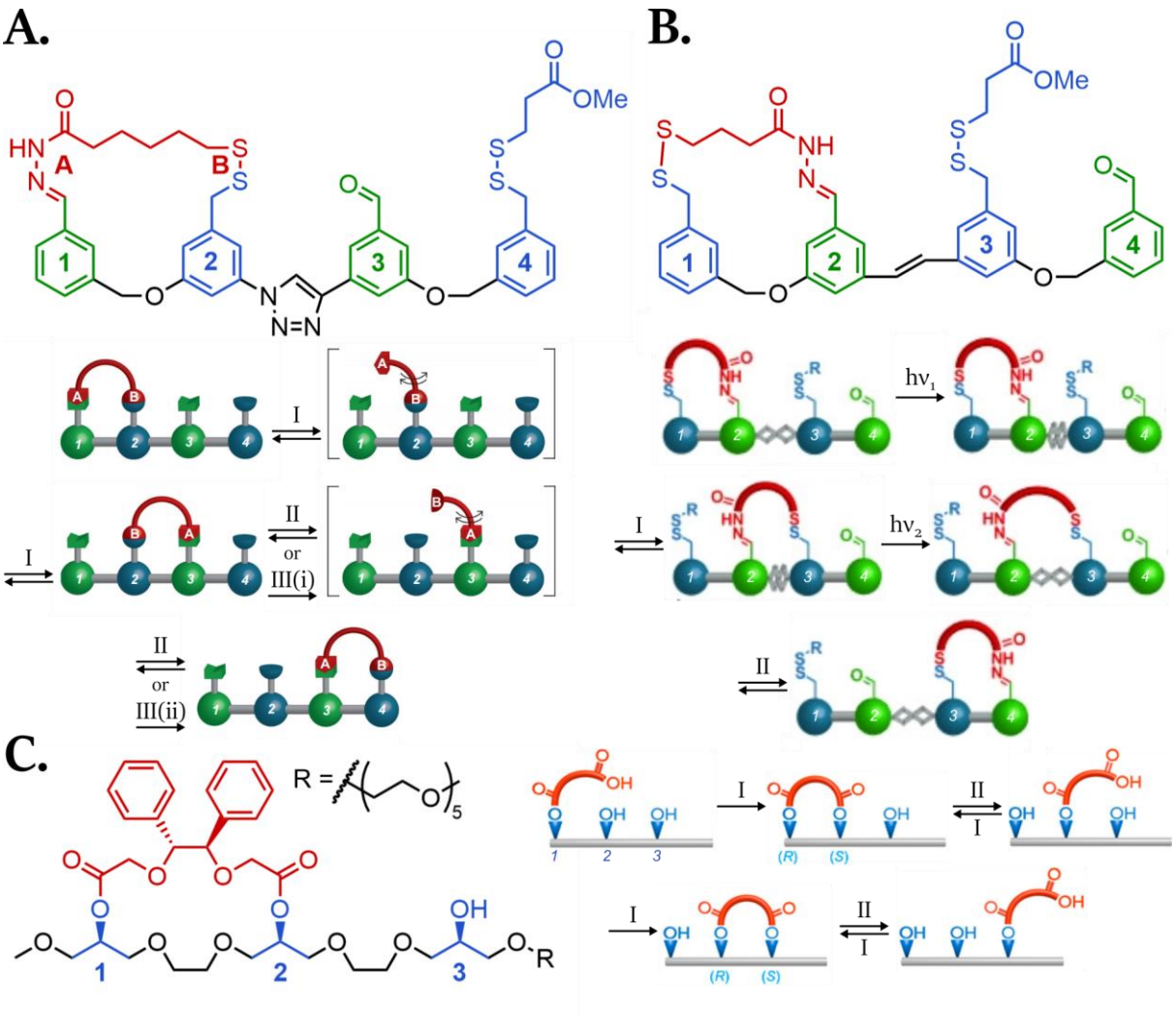

Figure 1.8. Covalent linear molecular motors or 'molecular walkers'. **A.** Top, chemical structure of the molecular walker (red) on its track composed of two pairs of alternating stations that can form hydrazone (green) or disulfide (blue) bonds. Bottom, schematic representation of the mechanism of directional motion of the walker. Under acidic conditions I, the hydrazone bond is labile and the disulfide bond is stable. Under basic conditions II, the disulfide bond is labile and the hydrazone bond is stable. Alternating between these conditions leads to an equilibrium distribution of isomers after a few cycles. However, applying a redox cycle III instead of basic conditions drives the system out-of-equilibrium by forming the kinetically favoured *3,4*-isomer. Adapted from reference [39]. **B.** Top, chemical structure of the molecular walker following the same general design as the previous one, with a stilbene unit between stations 2 and 3. Bottom, schematic representation of the mechanism of directional motion of the walker. Irradiation with light at 365 nm ($h\nu_1$) forms the *Z*-1,2-isomer. In this configuration, the *Z*-2,3-isomer is formed under basic conditions I. Subsequent irradiation with light at 500 nm ($h\nu_2$) forms the *E*-2,3-isomer where the strain of the macrocycle destabilizes the conformation. Consequently, under acidic conditions II, the *E*-3,4-isomer is mainly formed, thereby leading to an unidirectional motion of the walker along its track. Adapted from reference [41]. **C.** Left, chemical structure of the enzymatically driven molecular walker. Right, schematic representation of the mechanism of directional motion of the walker. Cyclization of the walker on the track (conditions I) is symmetric and the walker can either take a step forward or return to its initial position. Cleavage of one of the linkages between the walker and the track, however, occurs preferentially at the rear end because of the stereochemistry of the station. Since the configuration of the station changes depending on the position of the walker, the enzymatic cleavage acts as an information ratchet driving unidirectional motion. Adapted from reference [42].

This first system was then modified by replacing the triazole linkage between stations 2 and 3 with a light-sensitive stilbene unit (Figure 1.8.B, top). Hence, starting from the *E*-1,2-isomer, irradiation with light at 365 nm leads to the formation of the *Z*-1,2-isomer. In this configuration, stations 2 and 3 are in proximity and under basic conditions (DBU, DTT and placeholder), the *Z*-2,3-isomer is slightly favored. Irradiation with light at 500 nm isomerizes the stilbene back to form the *E*-2,3-isomer where the strain on the macrocycle destabilizes the conformation. Hence, in acidic conditions, the *E*-3,4-isomer is highly favored (Figure 1.8.B, bottom), while the *E*-1,2-isomer is formed under basic conditions.[41] The fact that the directionality of motion depends on the cycle of stimuli indicates that the walker works out-of-equilibrium and it is further proven by the fact that the relative distribution of isomers when light is involved in the cycle is different than when only acid/base cycles are applied. Therefore, light irradiation acts as an energy ratchet driving the directionality in this case while, in the previous system, the redox cycle acts as an information ratchet where the kinetically favored isomer depends on the position of the walker on its track.[39]

Leigh and coworkers recently reported an enzymatically driven molecular walker with chemically identical stations on the track (Figure 1.8.C). The walker forms two ester linkages with two stations of the track and the absolute configuration of the bound stations depends on the position of the macrocycle; the station binding the 'rear' end of the walker is *(R)*, while the station binding the 'front' end is *(S)* (Figure 1.8.C, left). Cyclization between the walker and the track is symmetric but hydrolysis of the ester bonds with an enzyme occurs preferentially on the rear end because of its stereochemistry. Moreover, the absolute configuration of the stations depends on the position of the macrocycle. A former *(S)* front station therefore becomes a *(R)* rear station once the walker takes a step forward. Consequently, application of several cyclization/hydrolysis cycles drives the unidirectional motion of the walker along the track (Figure 1.8.C, right). Since the enzymatic cleavage is position-dependent, this step acts as an information ratchet driving the unidirectionality.[42]

These chemically driven covalent rotary and linear molecular motors represent a significant advance in the design of synthetic bio-inspired nanomachineries where chemical fuels are used to trigger controlled mechanical motion, mimicking the operation of proteins described in the introduction of this section. Their main drawback, however, is the accumulation of waste over several operation cycles, which limit their application in materials where the elimination of products may not be straightforward; light-driven systems do not generate waste during their operation and, hence, overcome this limitation.

Most of the designs presented so far for covalent molecular motors are chemically powered; however, as stated earlier (see Section 1.1), photochemical processes are ideal to break detailed balance and, hence, fuel the unidirectional motion of these systems. For instance, Leigh and coworkers used a light-sensitive stilbene unit to drive the unidirectional translational motion of their molecular walker (*vide supra*)[41] and rotary molecular motors have also been designed to function under light irradiation.

Dube and coworkers reported light-driven molecular motors based on hemithioindigos. Their first design follows the general mechanism of molecular motors based on overcrowded alkenes, which is discussed in detail later (Section 1.2.3), because of their similar structures. The molecule consists of

an oxidized thioindigo stator connected to a stilbene rotor through a C=C double bond (Figure 1.9.A). Due to the steric hindrance close to the central double bond, the structure is not planar and adopts a helicity; moreover, the asymmetric sulfoxide group bears the chiral information driving unidirectionality. Under light irradiation, the initial stable isomer is photoisomerized to the isomer of opposite helicity. This isomer, however, has a metastable conformation and relaxes by thermal helix inversion, acting as the energy ratchet, to form the most stable one. The relative stability of the isomers before and after helix inversion is governed by the stereochemistry of the sulfoxide group. Therefore, after photoisomerization and thermal helix inversion, the rotor has performed a 180° unidirectional rotation around the central double bond relative to the stator. Repetition of these two steps completes the 360° rotation (Figure 1.9.A).[43] The main advantage of hemithioindigo-based molecular motors is that they operate with visible light instead of UV light used for molecular motors based on overcrowded alkenes. However, the quantum yields of photoisomerizations are lower, leading to slower rotation speeds.

These systems were further studied to optimize their operation. First, the same team reported hemithioindigo-based molecular motors based only on photochemical steps. Since no thermal helix inversion is involved, they can operate at low temperature. Moreover, the quantum yields of

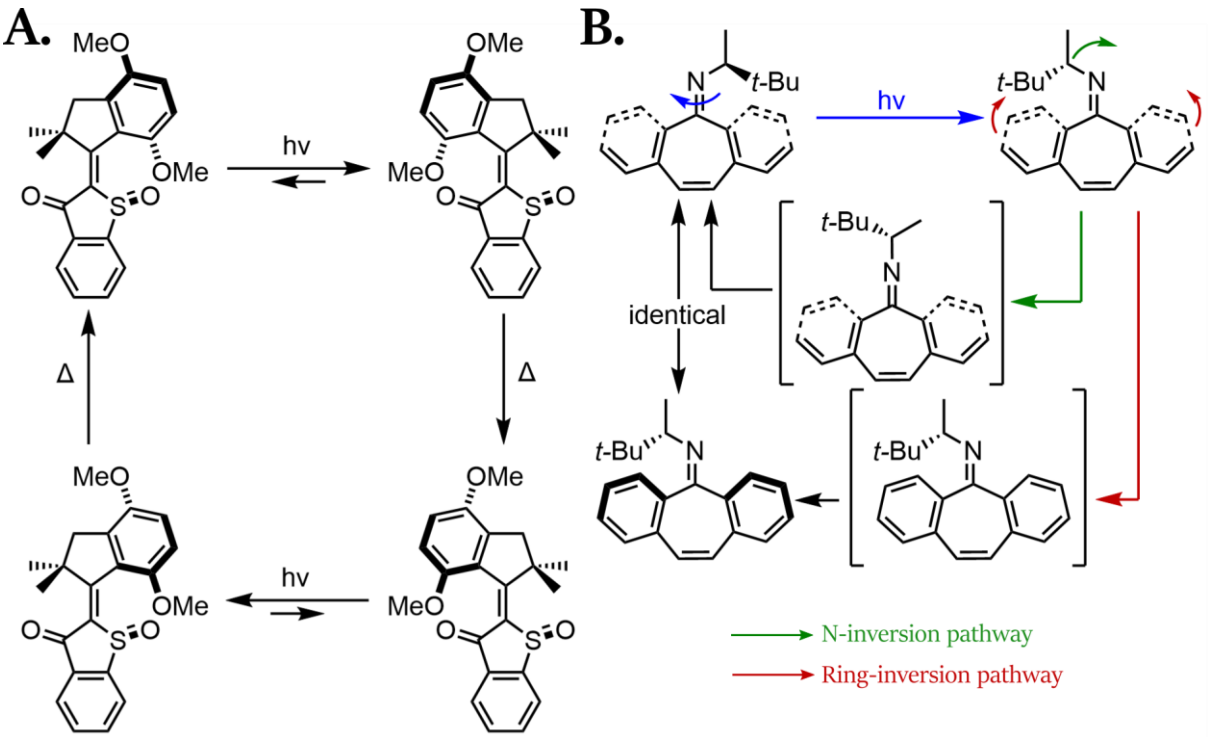

Figure 1.9. Hemithioindigo- and imine-based light-driven rotary molecular motors. **A.** Chemical structure and mechanism of rotation of an hemithioindigo-based motor. Photoisomerization with visible light drives the formation of the corresponding isomer of opposite helicity. This conformation is not the most stable and relaxes by thermal helix inversion to form the most stable one. The relative stability of these two isomers is caused by the stereochemistry of the sulfoxide group. Repetition of the photoisomerization and thermal helix inversion steps completes the unidirectional 360° rotation. Adapted from reference [43]. **B.** Chemical structure and mechanism of rotation of an imine-based motor. Isomerisation under irradiation drives the formation of an unstable isomer that can relax thermally following either one of two pathways. In the N-inversion pathway (green), the initial isomer is restored after N-inversion, thereby completing the rotation after two steps. In the ring-inversion pathway (red), the most stable isomer is formed after thermal helix inversion. Repetition of photoisomerization and thermal helix inversion steps completes the 360° unidirectional rotation after four steps. Adapted from reference [48].

photoisomerization tend to increase with decreasing temperatures so the motors rotate faster.[44] After optimization of their synthetic procedure to observe the unstable isomers of their initial design by increasing the steric hindrance around the double bond,[45] Dube and coworkers systematically investigated the influence of substituents close to the double bond on the rotation speed of their motors.[46]

After conjecturing the possibility to design imine-based molecular motors,[47] Lehn and coworkers reported the synthesis and operation of such systems. The 'stator' consists of a dibenzocycloheptene connected to different 'rotors' through a C=N double bond (Figure 1.9.B). The mechanism of rotation can follow two different pathways. In both cases, it starts with the photoisomerization of the double bond to form a metastable isomer after out-of-plane rotation of the rotor. In the N-inversion pathway, the most stable isomer is formed by an in-plane rotation of the rotor after N-inversion of the substituents, thereby completing the rotation in two steps. In the ring-inversion pathway, the most stable isomer is formed after thermal helix inversion and repetition of these two steps completes the 360° rotation in four steps in total.[48] In both cases, two directional orthogonal processes occur and, therefore, allow the operation of the molecular motor.

Hemithioindigo- and imine-based motors are promising systems for the design of new molecular motors. However, molecular motors based on overcrowded alkenes have been designed and studied for a longer time and are, consequently, more suitable for applications in materials. Many different structures have been reported, and the next section introduces the work that has been conducted on these systems.

1.2.3 Rotary covalent molecular motors based on overcrowded alkenes

The development of rotary molecular motors based on overcrowded alkenes followed the study of chiroptical switches. Chiroptical switches have different chiral states depending on the stimulus applied, for instance upon light irradiation. Overcrowded alkenes adopt a helical structure to avoid steric hindrance around the double bond and helicity can be switched by photoisomerization with light (Figure 1.10.A).[49] The introduction of asymmetric centers led to the development of molecular motors, which were classified into different generations depending on the number of stereocenters introduced in the molecule. Several reviews cover this topic more thoroughly than what will be discussed here.[50,51]

The first generation of molecular motors based on overcrowded alkenes was reported in 1999. It consists in two identical halves, the rotor and the stator, both bearing an asymmetric carbon center close to the central double bond (Figure 1.10.B, left). As for chiroptical switches, the molecule adopts a helicity because of the steric hindrance in the 'fjord' region —the region close to the double bond where the upper and lower halves interact through space. The most stable isomer has a conformation *(P,P)-trans* where both chiral methyl groups have a pseudoaxial conformation relative to the helices, thereby minimizing interaction between them and the opposite aromatic cycles in the fjord region. Under UV light, the double bond photoisomerizes to afford the *(M,M)-cis*-isomer of opposite helicity. Importantly, irradiation does not lead directly to the *(P,P)-cis*-isomer because of the steric hindrance in the fjord region. In the *(M,M)-cis* conformation, the methyl groups have a pseudo-equatorial conformation and are, consequently, metastable because they interact more with the aromatic core

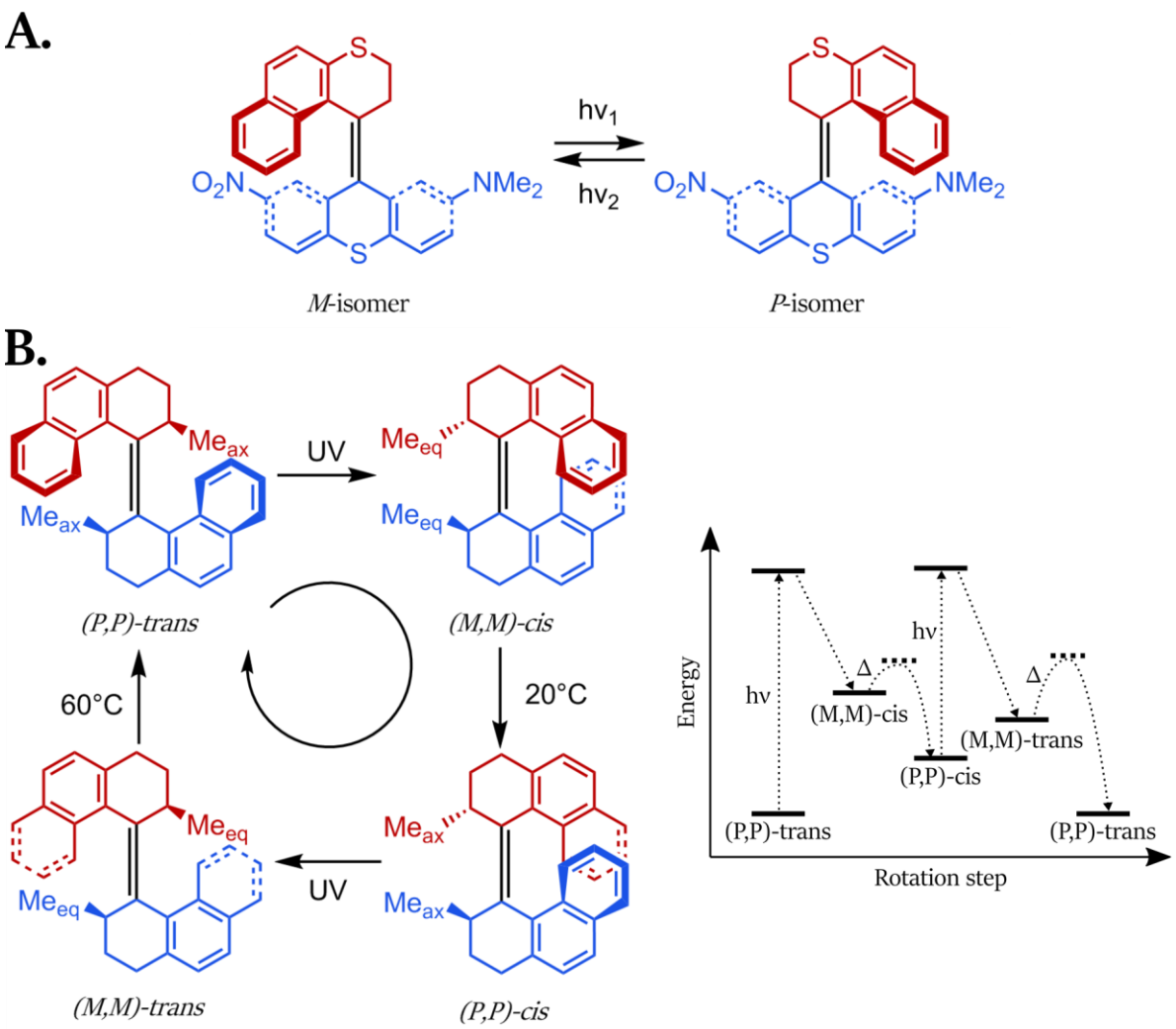

Figure 1.10. From chiroptical switches to molecular motors. **A.** Chemical structure and mechanism of switching of a chiroptical switch. Photoisomerization of the central double bond leads to an inversion of helicity of the molecule but steric hindrance close to the double bond prevents racemization. It can recover its initial conformation after irradiation at another wavelength. Adapted from reference [49]. **B.** Left, chemical structure and mechanism of rotation of a first-generation molecular motor based on overcrowded alkenes. It consists in identical rotor (red) and stator (blue) with two stereogenic centers connected through a double bond. The most stable isomer is *(P,P)-trans* with the methyl substituents in a pseudoaxial conformation. After photoisomerization, the *(M,M)-cis* molecule has an opposite helicity and the methyl groups adopt a pseudoequatorial conformation, destabilizing the isomer. Therefore, thermal helix inversion occurs to relax the steric strain to form the *(P,P)-cis* isomer where the methyl groups are pseudoaxial again. Repetition of these two steps completes the unidirectional 360° rotation of the rotor with respect to the stator. Since the stator is not symmetric, the two thermal helix inversions have different activation energies. Adapted from reference [52]. Right, schematic representation of an energy diagram corresponding to the mechanism of rotation. Adapted from reference [51].

of the other half of the motor. The molecule adopts the most stable *(P,P)-cis* conformation by thermal helix inversion where the aromatic moieties of the rotor and the stator 'slip' past each other; in this state, the methyl groups recover a pseudo-axial conformation. The thermal helix inversion therefore acts as the energy ratchet of the rotation cycle and the absolute configuration of the stereocenters control the unidirectionality of this step. Subsequent photoisomerization leads to the *(M,M)-trans*-isomer, which, for the same reasons, relaxes by thermal helix inversion to form the initial *(P,P)-trans*-isomer, thereby completing a 360° unidirectional rotation of the rotor, relative to the stator.[52] Overall, the rotation cycle consists in two photoisomerization steps that populate high-energy states and break detailed balance, and two thermal helix inversions that act as energy ratchets driving

unidirectionality (Figure 1.10.B, right). It is worth noticing that, in this design, the *cis* and *trans* isomers are not equivalent, so the two thermal helix inversions have different activation energies (Figure 1.10.B, right). Moreover, using the other enantiomer leads to the opposite rotation.

The second generation of molecular motors was reported one year later. Feringa and coworkers designed a molecule where only one stereocenter was present on the rotor, while the stator was symmetric (Figure 1.11.A). They showed that this chiral information was sufficient to induce a 360° unidirectional rotation, following the same mechanism as for the first-generation motors.[53] Moreover, since the stator is symmetric, both thermal helix inversions have the same activation energies and can be optimized jointly.

Following this exploration on the amount of chiral information needed for unidirectionality, the same team reported the third generation of molecular motors in 2015 with only one pseudo-asymmetric center controlling the direction of rotation. The design corresponds to two second-generation molecular motors 'fused' by their stators (Figure 1.11.B). Consequently, the molecule does not present any chiral center. Nevertheless, substituents on the pseudo-asymmetric carbon of the stator control the unidirectionality of motion of both rotors, which rotate in opposite directions relative to each other, like tires on an axle.[54]

Finally, Feringa and coworkers recently reported a fourth generation of molecular motors. Here, the molecule has neither chiral nor pseudo-asymmetric carbon centers. The directional motion is

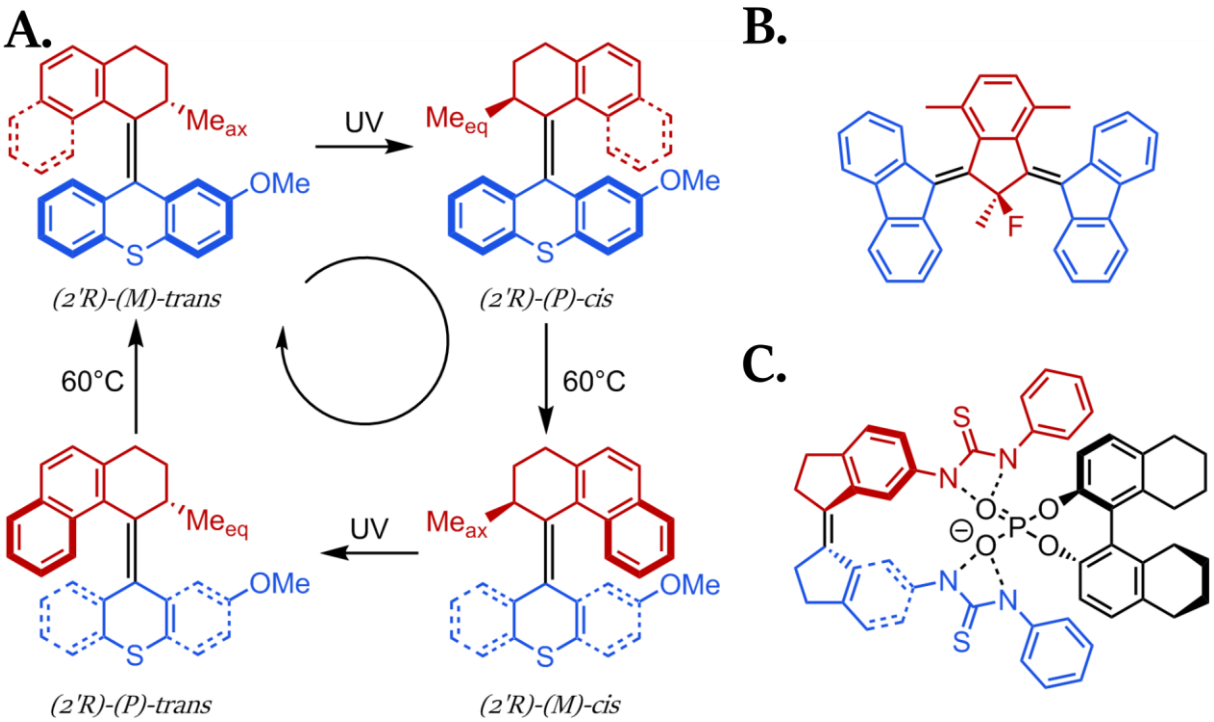

Figure 1.11. Next generations of molecular motors based on overcrowded alkenes. **A.** Chemical structure and mechanism of rotation of a second-generation molecular motor. Compared to the first generation, only one stereocenter is enough to induce unidirectionality. Moreover, the stator (blue) can be symmetric so the thermal helix inversions have the same activation energies. Adapted from reference [53]. **B.** Chemical structure of a third-generation molecular motor. Its structure corresponds to two second-generation molecular motors with the same stator (red). Therefore, the molecule does not have any stereocenters, but the pseudoasymmetric carbon on the stator drives the unidirectional motion. Adapted from reference [54]. **C.** Chemical structure of a fourth-generation molecular motor. The motor itself does not have any stereocenters. The unidirectionality of the thermal helix inversion is driven by the supramolecular interaction with a chiral auxiliary. Adapted from reference [55].

induced by the supramolecular interaction with a chiral auxiliary, which favors one isomer over the other to induce helix inversion (Figure 1.11.C).[55]

In this thesis, second-generation molecular motors have been used because their rotor and stator parts can be functionalized independently since they are not identical and, moreover, the two thermal helix inversions are identical and are therefore optimized at the same time. A complete review on the different investigations conducted to tune the rotation speed or the irradiation wavelength of such molecular motors has been reported elsewhere,[51,56] but few key aspects are discussed in the following paragraphs.

Since photoisomerization of molecular motors takes place in the picosecond timescale,[57] improving their rotation speed is achieved by increasing the rate of thermal helix inversion, the rate-limiting step. Two different strategies have been explored. The first one involves the destabilization of the ground energy of the metastable conformation. This is achieved by decreasing the conformational flexibility of the rotor part of the molecule bearing the stereocenter because the pseudoequatorial conformation is less accomodated. The second strategy consists in lowering the energy of the transition state during the thermal helix inversion. In that scenario, increasing the conformational flexibility of the lower part, as well as reducing the steric hindrance in the fjord region, allows for an easier 'slippage' between the two halves of the molecule during thermal relaxation.[51]

Feringa and coworkers thoroughly investigated the influence of the molecular structure on the rotation speed of molecular motors.[50] Decreasing the ring size of the upper cycle connected to the double bond reduces the flexibility of the rotor and, hence, accelerates the rotation speed. Going from a six-membered ring to a five-membered one led to a 2.5 × 10^5-fold decrease of the half-time of the THI, reducing it to 3 min (Figure 1.12, Entries 1 and 2).[56]

Contrariwise, increasing the ring size of the lower cycle connected to the double bond enhances the flexibility of the stator, which in turn increases the rate of THI. Using a six-membered ring instead

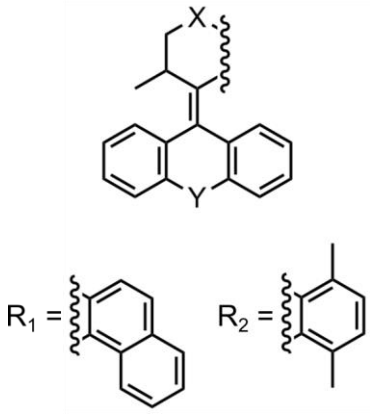

Entry	X	Y	R	$t_{1/2}$
1	CH_2	Ø	R_1	1.4 × 10^3 years
2	Ø	Ø	R_1	3 min
3	Ø	Ø	R_2	15 s
4	Ø	O	R_1	2.5 µs
5	Ø	S	R_1	200 ns

Figure 1.12. Structural modifications of second-generation molecular motors to tune their rotation speed. **Left:** general structure of second-generation molecular motors. **Right:** Different half-time $t_{1/2}$ values for the THI of the corresponding structures. Decreasing the flexibility of the upper part destabilizes the metastable conformation and, therefore, increases the rate of THI (Entries 1 and 2). Moreover, increasing the flexibility of the lower part lowers the energy barrier of the transition state of the THI and thereby increases its rate as well (Entries 1, 3, 4 and 5). Similarly, decreasing the steric hindrance in the fjord region increases the rate of THI (Entries 2 and 3).

of a five-membered one greatly reduces the half-time of thermal relaxation (Figure 1.12, Entries 2, 4 and 5).[58] Moreover, the nature of the atom used to increase the ring size also has an impact on the rotation speed; for instance, replacing an oxygen atom by a sulfur atom, which is larger, increases the flexibility of the stator and leads to a 10-fold acceleration of the rate of THI, thereby achieving a rotation in the MHz regime (Figure 1.12, Entries 4 and 5).[58]

Finally, modifying the aromatic group of the rotor alters the steric hindrance in the fjord region and, consequently, changes the rate of THI. This was demonstrated by changing a naphthalene side group to a *p*-xylene one on the rotor, leading to a 12-fold decrease of the half-time for THI, which reached 15 s at room temperature (Figure 1.12, Entries 2 and 3).[56]

The use of UV light as stimuli limits some applications of molecular motors in materials that are UV-sensitive, like polymers or living systems. Therefore, tuning the irradiation wavelength to shift it towards visible light has also been widely explored by Feringa and coworkers. This may be achieved by substituting the motor with donor and acceptor groups, or by extending the aromatic core of the molecule, for instance.[51] In another strategy, Feringa and coworkers reported the use of porphyrin as a triplet sensitizer to trigger photoisomerization of the motor under visible light (Figure 1.13.A). The triplet-triplet charge transfer could take place both inter- and intramolecularly and rotation of the motor occurred at 530 nm.[59] Incorporating the motor in a ruthenium(II) complex (Figure 1.13.B) also shifted the absorption wavelength of the motor to 450 nm because of metal-to-ligand charge transfer.[60]

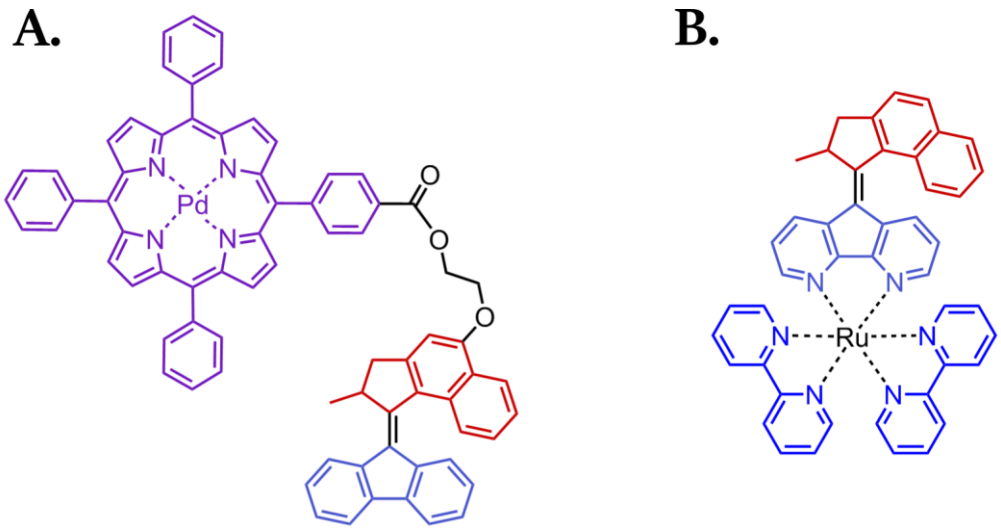

Figure 1.13. Structural modifications of second-generation molecular motors to tune their excitation wavelength. **A.** A porphyrin (purple) acts as a triplet sensitizer to activate the rotation of the molecular motor (red and blue). Light irradiation at 530 nm triggers a triplet-triplet charge transfer between the porphyrin and the motor, leading to its photoisomerization. **B.** The integration of the molecular motor in a complex with ruthenium(II) also shifts the absorption wavelength of the molecule to 450 nm because of metal-to-ligand charge transfer.

Molecular motors based on overcrowded alkenes have been thoroughly studied since their discovery to understand their mechanism of operation, to optimize their rotation speed or to tune their excitation wavelength. These studies also helped to design new molecular motors based on double bonds, like the hemithioindigo-based ones discussed earlier or oxindole-based ones that have been recently reported.[61] In the context of this work, we decided to use a structure close to the one

presented in Figure 1.12, Entry 5, because of its maximum rotation speed in the MHz range. Since our goal was to amplify the motion at the nanoscale up to a macroscopic material, the next section is devoted to the presentation of few examples where molecular motors have been used to trigger macroscopic changes in properties.

1.3 Amplification of the motion of synthetic molecular motors

The design of stimuli-responsive macroscopic systems from molecular switches has been widely explored, as it opens potential applications in sensing devices, catalytic systems or soft robotics, among others. For this purpose, they have been integrated, for instance, in liquid crystals, self-assembled systems or polymer networks, thereby triggering different macroscopic changes in properties, such as conductivity, optical or volume changes.[4] Since molecular motors exhibit unidirectional motion, and molecular switches do not, their incorporation may lead to new emergent properties at the macroscale. As for molecular switches, molecular motors have also been integrated in different types of systems to trigger macroscopic changes in properties. For instance, they have been used as dopants in liquid crystals to change their optical properties,[62–65] in self-assembled systems with switchable morphologies,[66,67] or to change the helicity of polymers.[68] The following paragraphs, however, will be focused only on systems where the molecular motion results in a macroscopic actuation of the material, since it is the main topic of this thesis.

Liquid crystals constitute a medium of choice for the amplification of molecular motion. The combination of their long-range organizational order with their liquid properties allows for the propagation of small changes in geometry up to the macroscopic scale. In an early example, Feringa and coworkers reported the incorporation of molecular motors as chiral dopants in a liquid-crystalline phase.[69] A fingerprint texture, typical of a cholesteric phase, with a surface relief of 20 nm appeared at the interface between the liquid crystal and air. When irradiated with UV light, the change in helical twisting power (HTP) of the motor, caused by the switching of its helicity, induced the rotation of the fingerprint texture that generated a torque capable of displacing a microobject deposited on the surface (Figure 1.14.A). Further investigations, elucidating the transduction mechanism from molecular motion to the fingerprint texture, showed that the unwinding of the cholesteric helix occurring during the photoisomerization of the motors was responsible for the rotational motion of the texture at the interface.[70]

Katsonis, Brasselet and coworkers also incorporated molecular motors as chiral dopants in a liquid crystalline medium to form a frustrated cholesteric phase.[71] The medium was placed between two glass slides spaced by a distance smaller than the helical pitch of the cholesteric phase; since the interface between the glass substrate and the liquid crystal promotes a perpendicular orientation of the mesogen relative to the surface, no helix was formed. This frustration can be released upon energy input. In this example, isomerization of the motor under UV light (used along with a co-dopant) triggered helix inversion of the cholesteric phase over time because of the change of HTP and, hence, generated patterns that could be observed under crossed polarizers. Above a critical light

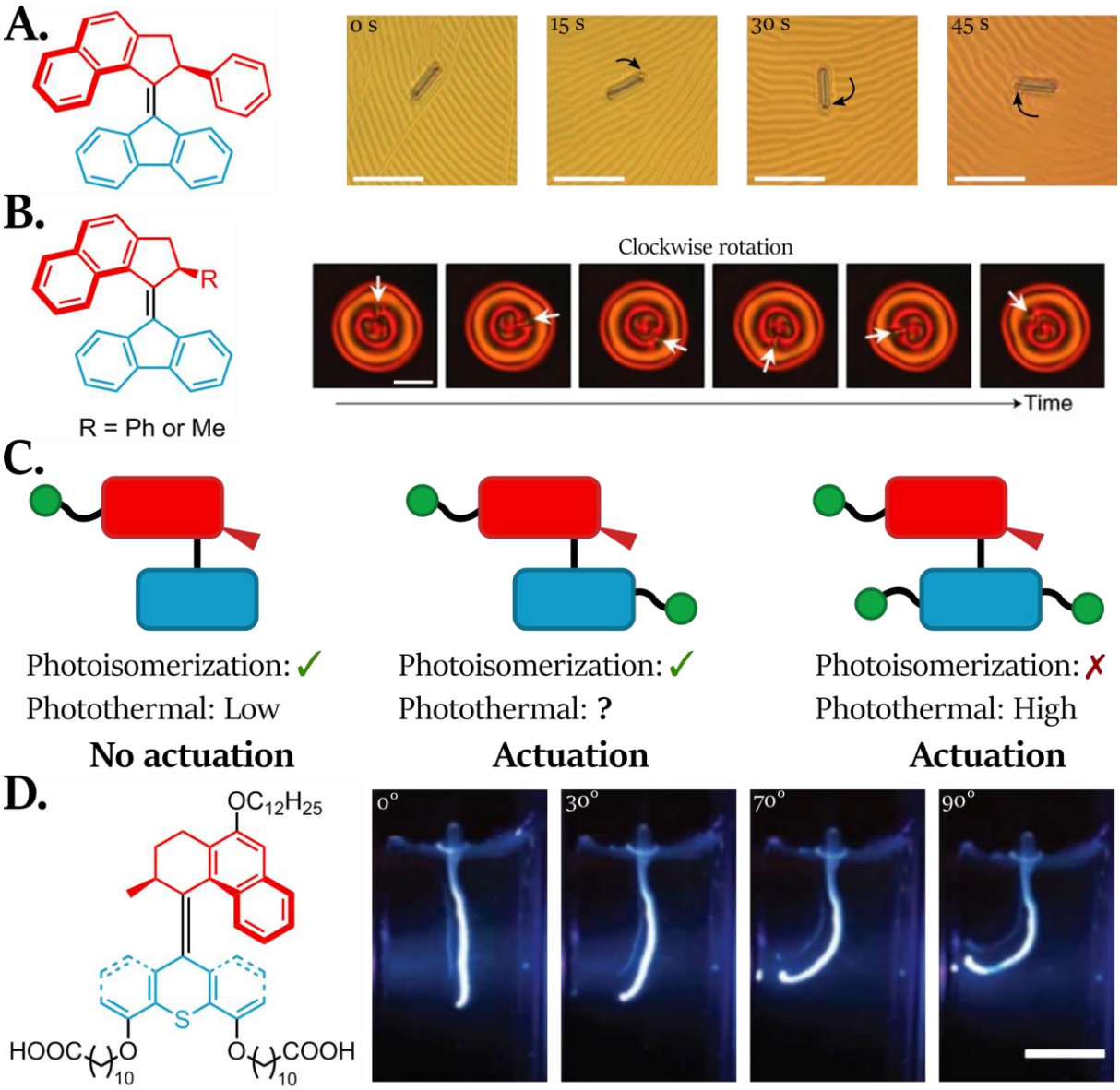

Figure 1.14. Amplification of the nanoscopic motion of molecular motors up to the macroscopic scale in ordered systems. **A.** A second-generation molecular motor (left) was used as a chiral dopant in a liquid crystal. Snapshots on the right show the rotation of a glass microrod deposited on the surface of the liquid at different times under UV light, as observed under crossed polarizers with an optical microscope. Isomerization of the motors triggers the unwinding of the helices in the cholesteric phase, which in turn lead to rotation of the fingerprint texture at the surface. It generates a torque that can move the microobject. Scale bars: 50 µm. Adapted from reference [70]. **B.** In another example where a molecular motor (left, red and blue) was used as a chiral dopant in a liquid crystalline phase, it was demonstrated that, above a certain irradiation power, isomerization of the motor led to the formation of continuously rotating supramolecular patterns that could be observed between crossed polarizers with an optical microscope (right). The emergence of this behaviour rises from a feedback mechanism between the diffusion of the motors, their influence on the chirality of the liquid crystalline phase and the resulting new chiral gradients in the material. Scale bar: 20 µm. Adapted from reference [71]. **C.** Two separate studies (see references [72] and [73]) used molecular motors (rotor in red, stator in blue) bearing varying number of acrylate groups (green circles) as comonomers in LCEs. When only one acrylate group is present, no actuation takes place, even though photoisomerization of the motor was observed. On the contrary, when three acrylate groups are present, there is no photoisomerization but the photothermal effect from the motors trigger actuation. When two acrylate groups are present, photoisomerization occurs and the LCE film bends but the exact contribution of the photothermal effect was not evaluated. **D.** An amphiphilic second-generation molecular motor (right) was used to form macroscopic supramolecular fibers. Under irradiation, the string bent towards the light source, because of a local shortening of the supramolecular packing due to the geometrical changes of the motor. Adapted from reference [75].

power, where full photoconversion was reached, the axial symmetry of the initial patterns was

broken, leading to the formation of larger and continuously rotating supramolecular structures as long as light irradiation was pursued (Figure 1.14.B). Careful modelling of this behavior showed that the emergence and rotation of these patterns arose from a feedback mechanism between the helicity of the motors, their impact on the helical twist of the liquid crystal and the resulting changes in diffusion rates of the motors inside the new chiral gradients.

The introduction of molecular motors inside liquid crystalline elastomers (LCEs) has been independently reported by Chen, Feringa and coworkers,[72] and Yang and colleagues.[73] In both studies, second-generation motors with different numbers of reactive acrylate groups were copolymerized with mesogens to form a material, which could eventually bend under light irradiation. While the structures of the motors used in both cases are not identical, they both follow the same actuation mechanism and, hence, these studies complete each other. First, Yang and colleagues prepared a molecular motor bearing three acrylate groups. When used as a crosslinking agent in the reactive liquid crystalline mixture, the resulting LCE bent under light irradiation. Since they observed no change in the UV absorption spectrum of the film under UV light and, hence, no photoisomerization, they concluded that the actuation resulted from a photothermal effect from the motor (see Chapter 2, section 2.2.2 for further explanations on the photothermal effect in LCE). On the other hand, when they used a molecular motor with only one acrylate group as a comonomer in the LCE, they observed that photoisomerization occurred because of a shift in the absorption maximum of the film, but no actuation took place. Therefore, they concluded that the nanoscopic motion was not sufficient to disrupt the liquid crystalline order and induce bending of the film, and that the photothermal effect, reduced because part of the light energy is used for photoisomerization, did not lead to a high enough increase in temperature to drive actuation.[73] Feringa and coworkers also used a molecular motor with only one acrylate group in their LCEs and similarly observed that no actuation took place under UV light. When they used a motor bearing two acrylate groups, however, light irradiation led to bending of the films. The absorption spectrum of the film showed that isomerization of the motors took place and the authors concluded that the nanoscopic actuation from the motors disrupted the molecular order, which, in turn, led to actuation of the material. They considered the photothermal effect as negligible, since no actuation was observed for the motor with one acrylate; contrariwise to Yang and coworkers, they did not consider that the photothermal effect might be dependent on the functionality of the motors.[72] Nevertheless, these two studies show that, similarly to many other stimuli-responsive molecules,[4] molecular motors can be embedded in LCEs to trigger their actuation and that precise contribution of both photomechanical and photothermal effects must be further investigated (Figure 1.14.C).

As for liquid crystalline systems, the high order in self-assemblies can be exploited to amplify the nanoscopic motion of molecular motors. For instance, Qu and coworkers synthesized a first-generation amphiphilic molecular motor that could self-assemble into nanovesicles in aqueous solutions. Under irradiation, the change in geometry of the motor led to a shrinkage of the vesicles and the actuation was reversible after heating the system.[74] Feringa and colleagues went one step further by preparing macroscopic supramolecular fibers based on amphiphilic molecular motors

(Figure 1.14.D). When irradiated with UV light sideways, the fiber bent towards the light source, both when it was immerged in water or in air, and its initial shape was recovered after heating. The authors suggested that the change in geometry of the molecule after photoisomerization led to an increase of the diameter of the assembly and, consequently, a shortening of its length to keep its volume constant. Considering the absorbance of the motor and the diameter of the string, the deformation occurs only at the irradiated side of the fiber and led to its bending.[75] They later improved their system by adding iron nanoparticles in the self-assemblies, which were then responsive to both light and magnetic fields.[76]

All previously described systems exploited the geometrical changes occurring during the operation cycle of the molecular motors under light irradiation. Since there is a change in helicity between the stable and metastable states after photoisomerization, the impact on ordered structures is important enough to generate macroscopic actuation. Moreover, thermal relaxation allows recovery of the initial state without the need for another light input. None of these systems, however, exploit the fact that the motion produced at the nanoscale is unidirectional; therefore, our team designed a system where this unique property could be used to trigger macroscopic actuation.

Our group reported the use of tetrafunctional molecular motors as crosslinking agents in the formation of poly(ethylene glycol) (PEG) networks. Chemical gels were formed by copper-catalyzed Huisgen 1,3-dipolar cycloaddition, a 'click' coupling reaction between terminal alkynes and azides, between molecular motors bearing two bifunctional PEG chains. Under UV irradiation, the unidirectional rotation of the molecular motors braids the polymer chains together, effectively creating new entanglements in the network acting as physical crosslinks. As the number of crosslinks increases, the volume of the gel decreases. After an activation time, probably caused by the heterogeneity of the material, a steady-state regime occurs where the material contracts linearly over time, before reaching its minimum volume of approximately 20 % of the initial one (Figure 1.15.A).[77]

This first system was not reversible because the direction of rotation of the motor is determined by its stereochemistry. Therefore, stress-releasing units were added as crosslinks in the network (Figure 1.15.B). These units are based on a diarylethene motif. Under UV light, the diarylethene is in its closed form and, as before, rotation of the motor creates new entanglements in the material, which then contracts. However, under visible light, the motor does not rotate anymore but diarylethene crosslinks isomerize to their open form. In this conformation, free rotation around σ bonds allows for the unbraiding of the polymer chains and the gel recovers its initial shape. Moreover, simultaneous irradiation with both UV and visible light allow to control the volume of the gel by controlling the distance to the visible light source. In this case, the gel is inherently dynamic and is constantly dissipating energy.[78]

The evolution of the mechanical properties of these materials was further investigated. This study showed that the best contraction efficiency, characterized by the higher ratio between the final and initial volumes, occurred when the gel was formed at the overlap concentration of the molecules (see Chapter 2, section 2.1.2, for further details). At this concentration, all chains are in contact with each other, allowing for a complete conversion of crosslinking, but there is little interpenetration between the chains and, hence, low amount of entanglements in the initial state, so the creation of new ones

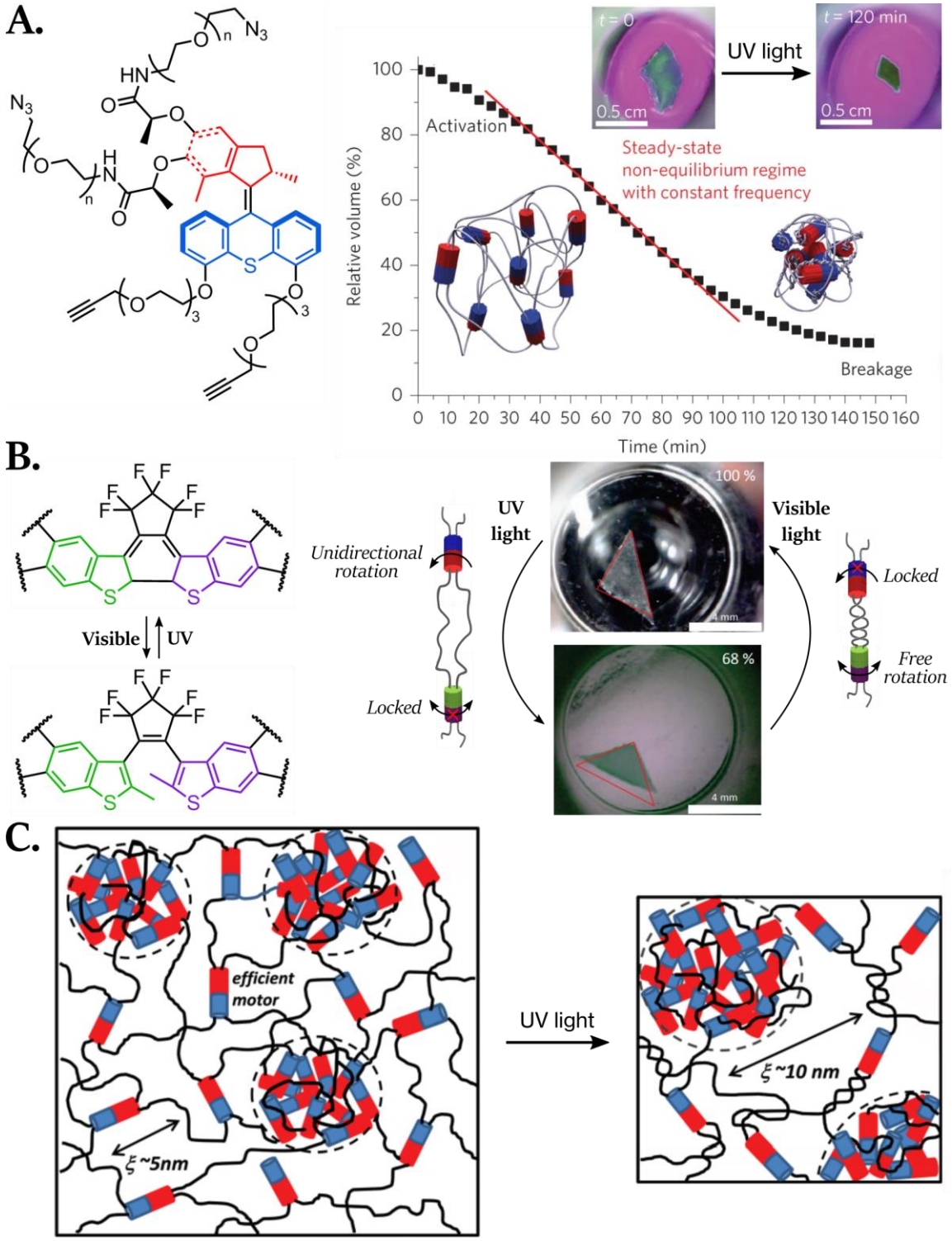

Figure 1.15. Amplification of the nanoscopic motion of molecular motors in amorphous polymer networks. **A.** Left, structure of the molecular motor bearing two PEG chains. Right, evolution of the relative volume of the gel under UV irradiation with the corresponding snapshots (upper right corner). Under UV irradiation, molecular motors (blue and red cylinders) braid polymer chains together (grey strings), which leads to contraction of the gel. Adapted from reference [77]. **B.** Addition of diarylethene-based crosslinks (chemical structure on the right, represented as green and purple cylinders) allows for the recovery of the initial volume of the gel. Under UV light, the diarylethene is in its closed form and new physical crosslinks are created. Contrariwise, under visible light, the motors do not rotate and the diarylethenes are in their open form; free rotation around the σ bonds untwist the chains and the gel swells. Adapted from reference [78]. **C.** Structural changes occurring during the contraction. As the polymer chains are twisted together, both the mesh size (characterized by ξ) and the size of heterogeneities (dashed circles) increase. Adapted from reference [80].

has more effect when the motors braid the chains together. It was also observed that the number of

monomers between crosslinks decreased after UV irradiation, proving that rotation of the motors indeed formed new physical crosslinking points.[79]

Thorough characterizations by neutron and X-ray scattering were conducted to elucidate the structure-property relationship of the gels. These studies confirmed the importance to form materials at the overlap concentration, for reasons stated previously. Counterintuitively, the mesh size of the network was found to increase after contraction, as well as the size of the heterogeneities of the network. Therefore, we proposed that intertwining the polymer chains into pairs led to an increased spacing between them, while increasing the number of entanglements tends to bring heterogeneities closer to each other, thereby increasing their size (Figure 1.15.C).[80]

Molecular motors have been incorporated into ordered systems, as their structural changes could be easily amplified to the macroscopic scale in such materials. However, to date, such designs did not exploit the unidirectional rotation of the molecule. In our team, the rotation and, hence, the continuous work performed on the environment were used to twist polymer chains together, leading to the formation of new entanglements that ultimately leads to a reduction of the volume over time under UV light. One of the goals of this thesis is to go one step further by investigating the influence of the polymer network itself on the contractile behavior of the material, for instance by changing the chemical nature of the polymer.

References

1. E. M. Purcell, *Am. J. Phys.* **1977**, *45*, 3–11.
2. A. Einstein, *Ann. Phys.* **1905**, *322*, 549–560.
3. V. Balzani, A. Credi, M. Venturi, *Chem. Eur. J.* **2002**, *8*, 5524–5532.
4. D. Dattler, G. Fuks, J. Heiser, E. Moulin, A. Perrot, X. Yao, N. Giuseppone, *Chem. Rev.* **2020**, *120*, 310–433.
5. In *IUPAC, Compendium of Chemical Terminology, 2nd Ed. (The "Gold Book")*, Principle Of Microscopic Reversibility, IUPAC, Research Triangle Park, NC, **2014**.
6. In *IUPAC, Compendium of Chemical Terminology, 2nd Ed. (The "Gold Book")*, Detailed Balancing (Principle Of), IUPAC, Research Triangle Park, NC, **2014**.
7. M. Kathan, S. Hecht, *Chem. Soc. Rev.* **2017**, *46*, 5536–5550.
8. S. Erbas-Cakmak, D. A. Leigh, C. T. McTernan, A. L. Nussbaumer, *Chem. Rev.* **2015**, *115*, 10081–10206.
9. U. Seifert, *Rep. Prog. Phys.* **2012**, *75*, 126001.
10. X.-J. Zhang, H. Qian, M. Qian, *Phys. Rep.* **2012**, *510*, 1–86.
11. A. I. Brown, D. A. Sivak, *Chem. Rev.* **2020**, *120*, 434–459.
12. W. Hwang, M. Karplus, *Proc. Natl. Acad. Sci.* **2019**, *116*, 19777–19785.
13. R. P. Feynman, R. B. Leighton, M. Sands, in *The Feynman Lectures on Physics*, Addison-Wesley Publishing Company, **1963**, pp. 46,1-46,9.
14. J. A. Wagoner, K. A. Dill, *J. Phys. Chem. B* **2016**, *120*, 6327–6336.
15. H. Wang, G. Oster, *Appl. Phys. A* **2002**, *75*, 315–323.

16. S. L. Reck-Peterson, W. B. Redwine, R. D. Vale, A. P. Carter, *Nat. Rev. Mol. Cell Biol.* **2018**, *19*, 382–398.
17. J. R. Sellers, *Biochim. Biophys. Acta Mol. Cell Res.* **2000**, *1496*, 3–22.
18. P. L. Jorgensen, K. O. Håkansson, S. J. D. Karlish, *Annu. Rev. Physiol.* **2003**, *65*, 817–849.
19. N. Hirokawa, Y. Noda, Y. Tanaka, S. Niwa, *Nat. Rev. Mol. Cell Biol.* **2009**, *10*, 682–696.
20. F. Kozielski, S. Sack, A. Marx, M. Thormählen, E. Schönbrunn, V. Biou, A. Thompson, E.-M. Mandelkow, E. Mandelkow, *Cell* **1997**, *91*, 985–994.
21. E. Nogales, S. G. Wolf, K. H. Downing, *Nature* **1998**, *391*, 199–203.
22. W. O. Hancock, *Biophys. J.* **2016**, *110*, 1216–1225.
23. J. E. Walker, *Biochem. Soc Trans.* **2013**, *41*, 1–16.
24. K. R. Vinothkumar, M. G. Montgomery, S. Liu, J. E. Walker, *Proc. Natl. Acad. Sci.* **2016**, *113*, 12709–12714.
25. R. Yasuda, H. Noji, K. Kinosita, M. Yoshida, *Cell* **1998**, *93*, 1117–1124.
26. D. A. Leigh, J. K. Y. Wong, F. Dehez, F. Zerbetto, *Nature* **2003**, *424*, 174–179.
27. J. V. Hernandez, *Science* **2004**, *306*, 1532–1537.
28. M. R. Wilson, J. Solà, A. Carlone, S. M. Goldup, N. Lebrasseur, D. A. Leigh, *Nature* **2016**, *534*, 235–240.
29. G. Ragazzon, M. Baroncini, S. Silvi, M. Venturi, A. Credi, *Nat. Nanotechnol.* **2015**, *10*, 70–75.
30. S. Corra, L. Casimiro, M. Baroncini, J. Groppi, M. La Rosa, M. Tranfic Bakic, S. Silvi, A. Credi, *Chem. Eur. J.* **2021**, chem.202101163.
31. H. Li, C. Cheng, P. R. McGonigal, A. C. Fahrenbach, M. Frasconi, W.-G. Liu, Z. Zhu, Y. Zhao, C. Ke, J. Lei, et al., *J. Am. Chem. Soc.* **2013**, *135*, 18609–18620.
32. C. Pezzato, M. T. Nguyen, C. Cheng, D. J. Kim, M. T. Otley, J. F. Stoddart, *Tetrahedron* **2017**, *73*, 4849–4857.
33. Y. Qiu, B. Song, C. Pezzato, D. Shen, W. Liu, L. Zhang, Y. Feng, Q.-H. Guo, K. Cai, W. Li, et al., *Science* **2020**, *368*, 1247–1253.
34. Y. Zhang, Z. Chang, H. Zhao, S. Crespi, B. L. Feringa, D. Zhao, *Chem* **2020**, *6*, 2420–2429.
35. S. P. Fletcher, F. Dumur, M. M. Pollard, B. L. Feringa, *Science* **2005**, *310*, 80–82.
36. B. S. L. Collins, J. C. M. Kistemaker, E. Otten, B. L. Feringa, *Nat. Chem.* **2016**, *8*, 860–866.
37. D. A. Leigh, U. Lewandowska, B. Lewandowski, M. R. Wilson, in *Molecular Machines and Motors* (Eds.: A. Credi, S. Silvi, M. Venturi), Springer, **2014**, pp. 111–138.
38. J. Valero, M. Škugor, *ChemPhysChem* **2020**, *21*, 1971–1988.
39. M. von Delius, E. M. Geertsema, D. A. Leigh, *Nat. Chem.* **2010**, *2*, 96–101.
40. M. von Delius, E. M. Geertsema, D. A. Leigh, D.-T. D. Tang, *J. Am. Chem. Soc.* **2010**, *132*, 16134–16145.
41. M. J. Barrell, A. G. Campaña, M. von Delius, E. M. Geertsema, D. A. Leigh, *Angew. Chem. Int. Ed.* **2011**, *50*, 285–290.
42. C. J. Martin, A. T. L. Lee, R. W. Adams, D. A. Leigh, *J. Am. Chem. Soc.* **2017**, *139*, 11998–12002.
43. M. Guentner, M. Schildhauer, S. Thumser, P. J. Mayer, D. Stephenson, P. J. Mayer, H. Dube, *Nat. Commun.* **2015**, *6*, 8406.
44. A. Gerwien, P. Mayer, H. Dube, *J. Am. Chem. Soc.* **2018**, *140*, 16442–16445.
45. L. A. Huber, K. Hoffmann, S. Thumser, N. Böcher, P. Mayer, H. Dube, *Angew. Chem. Int. Ed.* **2017**, *56*, 14536–14539.
46. L. A. Huber, S. Thumser, K. Grill, D. Voßiek, N. N. Bach, P. Mayer, H. Dube, *Chem. Eur. J.* **2021**, chem.202100950.

47. J.-M. Lehn, *Chem. Eur. J.* **2006**, *12*, 5910–5915.
48. L. Greb, J.-M. Lehn, *J. Am. Chem. Soc.* **2014**, *136*, 13114–13117.
49. B. L. Feringa, A. Schoevaars, W. F. Jager, B. de Lange, N. P. M. Huck, *Enantiomer* **1996**, *273*, 325–335.
50. D. Roke, S. J. Wezenberg, B. L. Feringa, *Proc. Natl. Acad. Sci.* **2018**, *115*, 9423–9431.
51. V. García-López, D. Liu, J. M. Tour, *Chem. Rev.* **2020**, *120*, 79–124.
52. N. Koumura, R. W. J. Zijlstra, R. A. van Delden, N. Harada, B. L. Feringa, *Nature* **1999**, *401*, 152–155.
53. N. Koumura, E. M. Geertsema, A. Meetsma, B. L. Feringa, *J. Am. Chem. Soc.* **2000**, *122*, 12005–12006.
54. J. C. M. Kistemaker, P. Štacko, J. Visser, B. L. Feringa, *Nat. Chem.* **2015**, *7*, 890–896.
55. S. J. Wezenberg, B. L. Feringa, *Nat. Commun.* **2018**, *9*, 1984.
56. J. Bauer, L. Hou, J. C. M. Kistemaker, B. L. Feringa, *J. Org. Chem.* **2014**, *79*, 4446–4455.
57. C. R. Hall, J. Conyard, I. A. Heisler, G. Jones, J. Frost, W. R. Browne, B. L. Feringa, S. R. Meech, *J. Am. Chem. Soc.* **2017**, *139*, 7408–7414.
58. M. Klok, N. Boyle, M. T. Pryce, A. Meetsma, W. R. Browne, B. L. Feringa, *J. Am. Chem. Soc.* **2008**, *130*, 10484–10485.
59. A. Cnossen, L. Hou, M. M. Pollard, P. V. Wesenhagen, W. R. Browne, B. L. Feringa, *J. Am. Chem. Soc.* **2012**, *134*, 17613–17619.
60. S. J. Wezenberg, K.-Y. Chen, B. L. Feringa, *Angew. Chem. Int. Ed.* **2015**, *54*, 11457–11461.
61. D. Roke, M. Sen, W. Danowski, S. J. Wezenberg, B. L. Feringa, *J. Am. Chem. Soc.* **2019**, *141*, 7622–7627.
62. R. A. van Delden, N. Koumura, N. Harada, B. L. Feringa, *Proc. Natl. Acad. Sci.* **2002**, *99*, 4945–4949.
63. R. Eelkema, B. L. Feringa, *Chem. Asian J.* **2006**, *1*, 367–369.
64. C. Loussert, S. Iamsaard, N. Katsonis, E. Brasselet, *Adv. Mater.* **2014**, *26*, 4242–4246.
65. J. Sun, R. Lan, Y. Gao, M. Wang, W. Zhang, L. Wang, L. Zhang, Z. Yang, H. Yang, *Adv. Sci.* **2018**, *5*, 1700613.
66. C. Poloni, M. C. A. Stuart, P. van der Meulen, W. Szymanski, B. L. Feringa, *Chem. Sci.* **2015**, *6*, 7311–7318.
67. D. J. van Dijken, J. Chen, M. C. A. Stuart, L. Hou, B. L. Feringa, *J. Am. Chem. Soc.* **2016**, *138*, 660–669.
68. T. van Leeuwen, G. H. Heideman, D. Zhao, S. J. Wezenberg, B. L. Feringa, *Chem. Commun.* **2017**, *53*, 6393–6396.
69. R. Eelkema, M. M. Pollard, J. Vicario, N. Katsonis, B. S. Ramon, C. W. M. Bastiaansen, D. J. Broer, B. L. Feringa, *Nature* **2006**, *440*, 163–163.
70. A. Bosco, M. G. M. Jongejan, R. Eelkema, N. Katsonis, E. Lacaze, A. Ferrarini, B. L. Feringa, *J. Am. Chem. Soc.* **2008**, *130*, 14615–14624.
71. T. Orlova, F. Lancia, C. Loussert, S. Iamsaard, N. Katsonis, E. Brasselet, *Nat. Nanotechnol.* **2018**, *13*, 304–308.
72. J. Hou, A. Mondal, G. Long, L. Haan, W. Zhao, G. Zhou, D. Liu, D. J. Broer, J. Chen, B. L. Feringa, *Angew. Chem. Int. Ed.* **2021**, anie.202016254.
73. R. Lan, J. Sun, C. Shen, R. Huang, Z. Zhang, C. Ma, J. Bao, L. Zhang, L. Wang, D. Yang, et al., *Adv. Funct. Mater.* **2020**, 2000252.
74. J.-J. Yu, Z.-Q. Cao, Q. Zhang, S. Yang, D.-H. Qu, H. Tian, *Chem. Commun.* **2016**, *52*, 12056–12059.

75. J. Chen, F. K.-C. Leung, M. C. A. Stuart, T. Kajitani, T. Fukushima, E. van der Giessen, B. L. Feringa, *Nat. Chem.* **2018**, *10*, 132–138.

76. F. K. Leung, T. Kajitani, M. C. A. Stuart, T. Fukushima, B. L. Feringa, *Angew. Chem. Int. Ed.* **2019**, *58*, 10985–10989.

77. Q. Li, G. Fuks, E. Moulin, M. Maaloum, M. Rawiso, I. Kulic, J. T. Foy, N. Giuseppone, *Nat. Nanotechnol.* **2015**, *10*, 161–165.

78. J. T. Foy, Q. Li, A. Goujon, J.-R. Colard-Itté, G. Fuks, E. Moulin, O. Schiffmann, D. Dattler, D. P. Funeriu, N. Giuseppone, *Nat. Nanotechnol.* **2017**, *12*, 540–545.

79. J.-R. Colard-Itté, Q. Li, D. Collin, G. Mariani, G. Fuks, E. Moulin, E. Buhler, N. Giuseppone, *Nanoscale* **2019**, *11*, 5197–5202.

80. G. Mariani, J.-R. Colard-Itté, E. Moulin, N. Giuseppone, E. Buhler, *Soft Matter* **2020**, *16*, 4008–4023.

PDB IDs: for F_1F_o ATP synthase, see 5LQX, 5LQY and 5LQZ.

for microtubule, see 1TUB.

for kinesin, see 3KIN.

Chapter 2
Physicochemical properties of polymer chains and networks

The previous chapter introduced the concept of molecular motors and the amplification of their nanoscopic motion to the macroscopic scale. In our team, and as it is further explored in this manuscript, the unidirectional rotary motion of overcrowded alkenes is used to induce the macroscopic contraction of polymeric gels because the photoactive molecules are topologically linked to each other *via* macromolecules.

While molecular motors induce the contraction of our material, the material itself probably has an impact on the rotation of the motors as well. For instance, Feringa and coworkers explored the impact of the surrounding solvent on the rotation of molecular motors,[1] and Yang and coworkers reported different dissipative pathways of their molecular motors depending on their crosslinking functionality *f* inside liquid crystalline networks.[2] We can therefore safely expect that the nature of polymer chains in our gels also have an impact on the rotation of our molecular motor and, hence, on the contractile behaviour of the material.

Polymers chains do not, indeed, all have the same physicochemical properties. Their conformation in solution depends on the chemical nature of the monomers, the solvent, and the temperature, for instance. Therefore, when they are crosslinked, the resulting swollen networks are also dependent on the same set of parameters. The elucidation of the structure-property relationship of our materials therefore implies an understanding of the behaviour of the macromolecules in solution.

The present chapter is divided into three parts. On the one hand, the first two sections introduce relevant concepts to understand the conformation of polymer chains in solution and the resulting properties of polymer networks respectively, with an emphasis on gels and liquid crystalline elastomers. It includes definitions of the different dimensions used to describe a polymer chain and various models developed over the years to predict the macroscopic properties that are experimentally observed. On the other hand, the third section presents the polymers used in this thesis, with a short discussion on their uses, mechanical properties, and synthesis.

The first sections of this chapter, concerning the statistical physics of macromolecules, can be found in textbooks of polymer science. We will not provide thorough demonstration for all equations that will be discussed; hence, we refer the reader to relevant books for a more comprehensive approach on the conformation of polymers in solution.[3–6]

2.1 Conformation of polymer chains in solution

Polymers are molecules composed of many (*poly-*) repeating units (*-mers*), called monomers, that are linked to each other. This term has been reserved for classical, covalently linked polymers for many years, but the development of supramolecular chemistry and the concurrent design of polymers where the monomers are linked to each other *via* supramolecular interactions (H-bonding, π–π interaction, host-guest complexes, among others) led to the emergence of the corresponding 'supramolecular polymers'. Note that the main difference between these polymers and colloidal assemblies like micelles or vesicles, which also hold because of weak interactions, resides in the strong directionality of supramolecular bonds. This manuscript focuses exclusively on covalent polymers.

Since Staudinger pioneered the field of polymer sciences a century ago,[7–9] polymers have become ubiquitous in our daily lives, but they were widely used even before scientists coined the term 'macromolecule' on them. Wood, for instance, is mainly composed of cellulose, hemicellulose and lignin, three polymers that are mainly responsible for its mechanical properties[10] and, hence, its use for construction since the beginning of humankind. As far as we know, all living matter is based on polymers like proteins (polymers of amino acids) or DNA (polymer of nucleotides). The industrial use of synthetic plastics also started before the publication of the seminal papers from Staudinger, for example with phenolic resins like Bakelite.[11] This latter marked the dawn of our modern Plastics Age —plastics in strata are one indicator of the Anthropocene[12]— and plastics can now be found in almost everything around us, in various fields like transportation, packaging, health or electronics.[13,14]

Polymers can have various chemical and topological structures. When they are composed of a single type of monomers, they are called homopolymers; they are otherwise called copolymers. Moreover, copolymers can be further classified depending on how the different types of monomers are arranged along the chain and can therefore be random, alternating, gradient or block copolymers, for instance. The topology of polymers can be linear, with only two chain ends, or branched, with more than two chain ends. Furthermore, branched polymers can also be divided in more specific subsections, like dendrimers or brushes. When chain ends bear functional groups with which further chemical reactions can take place, the polymers are said to be telechelic. The work presented here focuses in telechelic linear homopolymers that are crosslinked through end-linking.

The main difference between small molecules and polymers is their conformation. The conformation of a small molecule often has little to no impact on its physicochemical behaviour, unless very specific interactions come at play. On the other hand, the conformation of polymer chains is the foundation of their viscoelastic properties. Monomers tend to diffuse in solution, like any other small molecule, but their motion is impaired in polymers due to their connection to neighbouring monomers. It results that polymers adopt a statistical conformation in solution resembling a coil. While the conformation of a single chain at a specific moment cannot be exactly determined, it is possible to model the average behaviour of many chains in solution.

We discuss in this section the relevant aspects of the behaviour of polymer chains in solution in two parts. First, we present the characteristic lengths used to describe the conformation of single

polymer chains in solution. In the second subsection, the different concentration regimes of polymer solutions are introduced and we highlight the overlap concentration, since we previously determined its importance for the formation of our molecular-motor-containing gels.[15,16]

2.1.1 Conformation of single chains in solution

Several lengths are commonly used to describe the coiled conformation of polymers in solution: the end-to-end distance R_F, the radius of gyration R_G and the hydrodynamic radius R_H. While R_F is useful to rapidly compare the different models of polymer conformation, R_G and R_H are experimentally accessible and are therefore more relevant in practice.

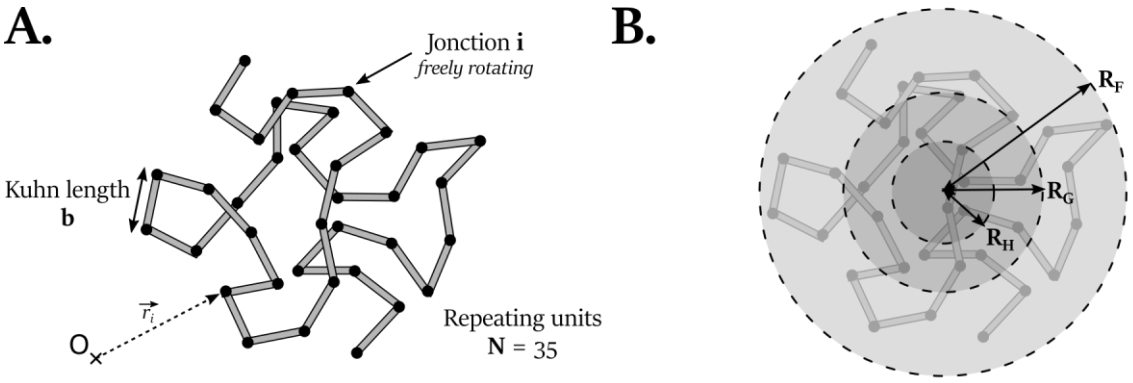

Figure 2.1. A. Schematic representation of a simplified polymer chain, useful for its modelling. **B.** Characteristic lengths of a polymer coil, with R_F the end-to-end distance, R_G the radius of gyration and R_H the hydrodynamic radius.

We consider a linear polymer containing *N* bonds of length *b* with each joint *i* characterized by its position $\vec{r_i}$ (*i* between 0 and *N*) (Figure 2.1.A). First, its **contour length L_C** corresponds to the maximum end-to-end distance when the chain is fully stretched and can therefore be written as:

$$L_C \overset{\text{def}}{=} b \times N \tag{2.1}$$

The root-mean-square end-to-end distance, or end-to-end distance, R_F is defined as:

$$R_F^2 \overset{\text{def}}{=} \langle (\vec{r_N} - \vec{r_o})^2 \rangle \tag{2.2}$$

The **end-to-end distance R_F** therefore characterizes the distance between the two chain ends. Several models have been developed to determine R_F. Ideal polymers in solution have the conformation of freely jointed chains following a random walk. Their monomers can point to any direction, independently of the orientation of its adjacent monomers. Moreover, it is assumed that monomers can cross and, hence, occupy the same position. In this model, it can be demonstrated that $R_{F,ideal}$ is:

$$R_{F,ideal} = b \times N^{1/2} \tag{2.3}$$

Ideal chains are also referred to as **Gaussian chains**, since the distribution of the end-to-end distances follows a normal distribution.

For real chains, the excluded volume of each monomer is considered. The macromolecule follows a self-avoiding random walk where subsequent monomers adopt independent orientations but cannot overlap. In that case, in a good solvent, we obtain:

$$R_{F,real} = b \times N^{3/5} \quad (2.4)$$

Thus, the relationship between the end-to-end distance and the number of monomers can be generalized to:

$$R_F = b \times N^{\nu} \quad (2.5)$$

with **ν the Flory coefficient**, characterizing the conformation of the polymer in solution; for instance, ν = 0.5 for ideal chains, ν = 0.6 for real chains in good solvents and ν ≈ 0.33 for real chains in poor solvents. In the freely-jointed-chain model, the bond length b is named the **Kuhn length**.

While the freely-jointed-chain model is suitable for flexible polymers, the worm-like-chain (WLC) model is more relevant for semi-flexible polymers. The polymer chain is considered as a continuous string where there is a correlation between the orientation of adjacent units, which decays exponentially with increasing distance and is characterized by the **persistence length L_P**. It can be shown that the end-to-end distance is then given by:

$$R_F^2 = 2 L_p L_C - 2 L_P^2 (1 - e^{-L_C/L_P}) \quad (2.6)$$

Two extreme situations can be deduced from this formula. First, in the case of flexible polymers where $L_C \gg L_P$, R_F^2 reduces to $2 L_P L_C$. By comparison, for an ideal chain, we wrote earlier that $R_{F,ideal}^2 = b^2 \times N = b \times L_c$, whence $2 L_P = b$. In other words, the Kuhn length corresponds to twice the persistence length for flexible polymers. For rigid rods, on the other hand, where $L_P \gg L_C$, we obtain $R_F = L_C$, as expected. Even though L_P is used in the framework of the WLC model for semi-flexible chains, it may still be relevant for flexible polymers, especially when they are short. Notably, L_P can be measured by small-angle neutron scattering (SANS), which we used in previous reports to determine the persistence length of poly(ethylene glycol) (PEG).[16]

Following the same formalism, the radius of gyration is determined compared to the center of gravity of the polymer chain at position $\overrightarrow{r_G}$, considering that all joints have the same mass and are connected by massless bonds. The root-mean-square radius of gyration, or **radius of gyration, R_G** is defined as:

$$R_G^2 \overset{\text{def}}{=} \frac{1}{N+1} \sum_{i=0}^{N} \langle (\overrightarrow{r_i} - \overrightarrow{r_G})^2 \rangle \quad (2.7)$$

The radius of gyration therefore characterizes the average length between the monomers and the center of mass of the polymer. Equation 2.7) can be rewritten by using the following identity:

$$\sum_{i,j=0}^{N} (\overrightarrow{r_i} - \overrightarrow{r_j})^2 = 2 (N+1) \sum_{i=0}^{N} (\overrightarrow{r_i} - \overrightarrow{r_G})^2 \quad (2.8)$$

hence

$$R_G^2 = \frac{1}{2 (N+1)^2} \sum_{i,j=0}^{N} \langle (\overrightarrow{r_i} - \overrightarrow{r_j})^2 \rangle \quad (2.9)$$

In this sense, R_G^2 can therefore also be seen as half of the average square distance between any monomers of the polymer chain. For ideal chains, it can be shown that:

$$R_{G,\,ideal} = \frac{R_{F,ideal}}{\sqrt{6}} \tag{2.10}$$

Importantly, R_G is experimentally accessible, for instance by SANS.

Finally, the hydrodynamic radius can be determined by considering first the Stokes-Einstein equation, which links the diffusion coefficient *D* of a hard sphere to its radius R_S:

$$D = \frac{k_B T}{6\pi\mu_S R_S} \tag{2.11}$$

with k_B the Boltzmann constant ($k_B = 1.38 \times 10^{-23}\,J.K^{-1}$), T the temperature and μ_S the dynamic viscosity of the solvent. R_S is sometimes called the Stokes radius.

The **hydrodynamic radius R_H** of a polymer corresponds to the radius of a hard sphere having the same diffusion behavior as the coil in solution, whence:

$$R_H = \frac{k_B T}{6\pi\mu_S D} \tag{2.12}$$

The inverse of R_H can also be expressed as the average of the inverse distance between any monomer of the chain:

$$\frac{1}{R_H} = \left\langle \frac{1}{\left\| \vec{r_i} - \vec{r_j} \right\|} \right\rangle \tag{2.13}$$

R_H is proportional to R_G but the exact factor depends on the solvent and the temperature. For instance, according to the Kirkwood-Risemann model, $R_H = 0.665\,R_G$ for ideal chains.[17] Since R_H depends on the diffusion behavior of polymer chains, it can be determined, for instance, by light scattering techniques.

Single polymer chains can therefore be described by several characteristic lengths in solution (Figure 2.1.B), which can be determined by different experimental techniques. In practice, however, they are surrounded by other macromolecules and different concentration regimes can be observed, which is not the case for solutions of small molecules.

2.1.2 Concentration regimes of polymer solutions

In the previous subsection, we discussed the characteristic lengths of single polymer chains in solution. A polymer chain is composed of N monomers of volume b^3 so the macromolecule itself occupies of volume $N \times b^3$. The overall coil, however, occupies a larger volume. For instance, considering the end-to-end distance of an ideal chain, the volume of the corresponding coil is $N^{3/2} \times b^3$. Consequently, the volume fraction of a swollen ideal chain inside its volume $\phi^*_{s,\,ideal}$ is:

$$\phi^*_{s,\,ideal} = \frac{N \times b^3}{N^{3/2} \times b^3} = N^{-1/2} \tag{2.14}$$

Therefore, the polymer chain itself represents only a small fraction of the total volume it occupies, and this fraction decreases with increasing molecular weights.

This behavior explains the existence of three concentration regimes for polymer solutions: the dilute regime, the semi-dilute regime, and the concentrated regime (Figure 2.2). In the dilute regime, polymer coils are far apart from each other, and they mostly do not interact. Above a concentration threshold, namely the overlap concentration c*, coils overlap, and intermolecular interactions appear; however, the volume fraction of polymers remains low, whence the term 'semi-dilute' regime. The concentrated regime is reached when the concentration is above a critical value c**. Coils strongly interpenetrate, intermolecular interactions are predominant, and the polymer volume fraction is high.

In the frame of this thesis, the overlap concentration c* is of prime interest. We determined in our previous studies that the best contraction performance was obtained with gels reticulated at that concentration because the coils just overlap, which ensures a proper reticulation of the polymer chains while minimizing the number of initial entanglements.[15,16] c* is proportional to ϕ_s^* described earlier (equation 2.14), since the polymer volume fraction at that concentration is identical to the one in a single coil. Therefore, we can write:

$$c^* = \rho \times \phi_s^* \propto N^{1-3\nu} \tag{2.15}$$

with ρ the density of the polymer and symbol '$\propto$' represents proportionality. For ideal and real chains, the exponent of N is negative and, hence, c* decreases with increasing degree of polymerization. In other words, the semi-dilute regime is reached at lower concentrations for polymer chains having higher molecular weights.

c* can be determined by viscometry, which is the method used in this thesis. First, we can define the overlap concentration as the concentration of polymer inside its volume:

$$c^* = \frac{M}{\mathcal{N}_A \times \frac{4}{3} \pi R_G^3} \tag{2.16}$$

with M the molecular weight of the polymer and $\mathcal{N}_A$ the Avogadro constant (6.022×10^{23} mol^{-1}).

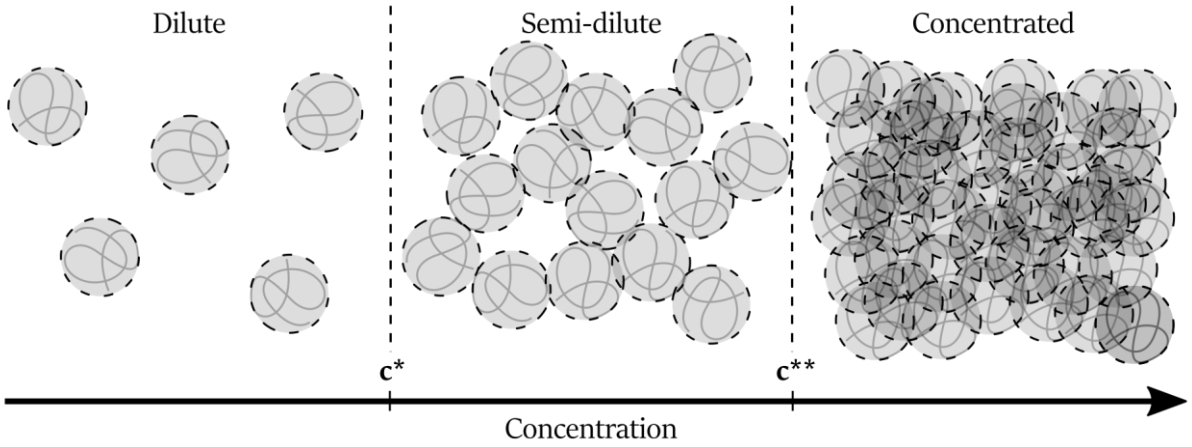

Figure 2.2. The different concentration regimes of polymer solutions. In the dilute regime, the coils mostly do not interact. In the semi-dilute regime, above the overlap concentration c*, coils interact but the volume fraction of polymer chains remains low. In the concentrated regime, above c**, the volume fraction of polymer chains is high, and the different macromolecules strongly interact.

As stated earlier, R_H and R_G are proportional:

$$R_H = \alpha R_G \tag{2.17}$$

and R_H is related to the intrinsic viscosity $[\eta]$ of the polymer, following the Flory-Fox equation:[18]

$$R_H^3 = \frac{[\eta] \times M}{\Phi_o} \tag{2.18}$$

with Φ_o a constant characteristic of the polymer-solvent system, equals to 3.67×10^{24} mol^{-1} for a real polymer in a good solvent. Equation 2.18 can therefore be rewritten as:

$$c^* = \frac{\Phi_o \times \alpha^3}{N_A \times \frac{4}{3} \pi [\eta]} \approx \frac{1.45 \times \alpha^3}{[\eta]} \tag{2.19}$$

Since the value of α is not known but usually slightly below 1, c^* is often approximated as:

$$c^* \approx \frac{1}{[\eta]} \tag{2.20}$$

The overlap concentration c^* corresponds to the inverse of the intrinsic viscosity $[\eta]$, which can be measured by viscometry. Several semi-empirical models have been used for the measurement of $[\eta]$[19] and we decided to follow the Huggins model, which is valid for neutral polymers at low concentrations:

$$\eta_{red} \approx [\eta] + k_H [\eta]^2 c \tag{2.21}$$

with η_{red} the reduced viscosity and k_H the Huggins parameter. Therefore, extrapolation of η_{red} to zero concentration gives $[\eta]$ at the intercept and, consequently, c^* can be calculated. By definition:

$$\eta_{red} \overset{def}{=} \frac{\eta_{sp}}{c} \tag{2.22}$$

with η_{sp} the specific viscosity of the polymer solution at concentration c, which is itself defined as:

$$\eta_{sp} \overset{def}{=} \frac{\eta}{\eta_o} - 1 \tag{2.23}$$

where η and η_o are the dynamic viscosities of the polymer solution and of the solvent, respectively. In the present work, Ostwald capillaries were used to determine kinematic viscosities μ of the solutions, which were then converted to the corresponding dynamic viscosities by multiplying by their densities. In other words, to be concise, we measured the viscosities of a series of polymer solutions to determine their overlap concentration c^*.

This first section was devoted to the understanding of the conformation of polymer chains in solutions. The most important parameter for the formation of our gels is the overlap concentration c^*, which can be determined by viscometry measurements. Therefore, materials presented in this thesis have been formed according to their own optimal conditions and the influence of other parameters could be systematically varied. The next section presents the theoretical background necessary for investigating the network properties.

2.2 Properties of polymer networks

Polymer networks fall into different categories. First, we should consider dry materials, which are classified depending on their operation temperature compared to their glass transition temperature T_g. When materials are used below their T_g, thermoplastics and thermosets are distinguished. Thermoplastics consist of non-crosslinked macromolecules and, hence, are not covalent networks. However, entanglements act as physical crosslinks that hinder free flowing of the material. Therefore, at their operating temperature, they behave as solids; when heated above their T_g, however, the material can be reprocessed. Thermosets, on the other hand, are chemically crosslinked networks and, in that case, they cannot be reprocessed even when they are heated above their T_g. When the operation temperature of a crosslinked network is above its T_g, it is called an elastomer. They are usually loosely crosslinked and flexible, but the presence of crosslinks limits the free flow of the polymer chains and, hence, mechanical deformations are reversible; the material is thus elastic.[20]

When polymer networks are swollen in a solvent, they are referred to as gels. Crosslinks can be chemical (covalent) or physical (non-covalent). When immersed in a fluid, the polymer chains tend to diffuse because of the osmotic pressure, but the presence of crosslinks restrains their position; therefore, the network swells but does not fully dissolve.[20,21]

Polymer networks can be prepared by different synthetic pathways. For instance, they may be prepared by the polymerization of monomers, either in the bulk or in solution. When the mixture contains monomers having more than two functional groups, polymerization may ultimately lead to the formation of a network. Another strategy consists in vulcanization, where preformed polymer chains are crosslinked by addition of another reactant that covalently binds functional groups present on the polymer backbone. Finally, networks can be prepared by end-linking of telechelic chains having functional groups at their chain ends.[20]

In this work, we focus on the integration of molecular motors in polymer gels and liquid-crystalline elastomers. The first section is therefore devoted to theoretical aspects of the properties we investigated for our swollen networks, while the second section presents some specificities of liquid-crystalline elastomers and discusses few examples of such stimuli-sensitive systems.

2.2.1 Swelling equilibrium and elasticity of polymers gels

As discussed previously (see Chapter 1), our team reported the integration of molecular motors as crosslinks in PEG-based gels. The braiding of polymer strands caused by the unidirectional rotation of the motors lead to a change in their swelling equilibrium, where the volume decreases over time under UV irradiation.[22,23] Therefore, this section provides the basis for understanding how the creation of new entanglements leads to a volume change.

The **swelling ratio Q** is defined as the ratio between the volume of the swollen network V_{sw} and the volume of the dry network V_{dry} and, hence, can also be expressed as the inverse of the volume fraction of the polymer in the gel ϕ_{sw}:

$$Q \overset{\text{def}}{=} \frac{V_{sw}}{V_{dry}} = \frac{1}{\phi_{sw}} \tag{2.24}$$

During the contraction of our gels under light irradiation, we observe the evolution of the relative volume over time $\%_V(t)$, which can be expressed as follows:

$$\%_V(t) = \frac{V_{sw}(t)}{V_{sw}(t=0)} = \frac{Q(t)}{Q(t=0)} = \frac{\phi_{sw}(t=0)}{\phi_{sw}(t)} \tag{2.25}$$

The volume fraction ϕ_{sw} and, hence, the swelling ratio Q are related to the average molecular weight between crosslinks $\overline{M_c}$ following the Flory-Rehner equation:[24,25]

$$\frac{1}{\overline{M_c}} = \frac{2}{\overline{M_n}} - \frac{\ln(1-\phi_{sw}) + \phi_{sw} + \chi\,\phi_{sw}^{\,2}}{V_1 \rho_{dry}\left(\phi_{sw}^{\,1/3} - \frac{\phi_{sw}}{2}\right)} \tag{2.26}$$

with $\overline{M_n}$ the average number molecular weight of the polymer before crosslinking, χ the polymer-solvent interaction parameter, V_1 the molar volume of the solvent and ρ_{dry} the dry density of the polymer network. This equation was determined by supposing that the swelling equilibrium is reached when the free energy of elasticity of the network —disfavouring swelling because it works against deformation— and the free energy from the osmotic pressure —favouring swelling because it leads to the diffusion of the polymer chains— are balanced.

From this equation, it appears that the swelling ratio decreases when the molecular weight between crosslinks decreases (Figure 2.3). When $\overline{M_c}$ tends to 0, Q tends to 1, as the polymer network cannot accommodate any solvent molecules. For our gels, the rotation of molecular motors creates new entanglements in the network, effectively creating new physical crosslinks. Therefore, the apparent $\overline{M_c}$ decreases and, consequently, Q decreases. Therefore, the relative volume $\%_V$ decreases over time under light irradiation. The Flory-Rehner equation was developed for vulcanized polymer networks and, hence, does not consider for instance, the initial state of the network when it is formed in solution, or the functionality of the crosslinks. Such corrections have been developed later and updated versions have been reported;[21,26] nevertheless, the general trend is the same, and the concept is valid for our swollen networks as well.

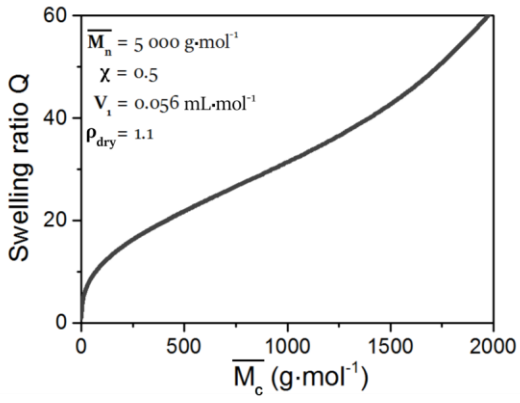

Figure 2.3. Evolution of the swelling ratio Q as a function of the molecular weight between crosslinks $\overline{M_c}$ as predicted by the Flory-Rehner equation. When $\overline{M_c}$ decreases, Q decreases as well.

Another property that we previously investigated is the evolution of the elastic modulus of our gels depending on their extended or contracted state.[16] There are several models to describe the elasticity of polymer gels, such as the affine model, the phantom model, or the percolate network model.[21] The

affine model, for instance, supposes that individual polymer strands are deformed the same way as the overall network. In that case, the **shear modulus G** is given by:

$$G = \nu k_B T \tag{2.27}$$

with ν the number density of elastically active polymer strands in the network, which is proportional to ϕ_{sw}. Therefore, when the gels contract under light irradiation, ν increases and, consequently, G increases; in other words, materials get stiffer when new entanglements are created by the rotation of molecular motors, which is the behaviour that we previously observed.[16] Different models give slightly different equations, but the overall trends remain the same.

The statistical behaviour of the conformation of polymer chains in solution explains the observed macroscopic properties of polymer gels. The consequences of braiding polymer chains with molecular motors, which create new entanglements, can be rationalized with different models, such as the Flory-Rehner equation. The first section of this chapter and the present subsection were devoted to the theory of polymer chains and networks. The following (sub)sections will discuss examples of polymer materials, starting with liquid-crystalline elastomers.

2.2.2 Liquid-crystalline elastomers as soft actuators

Liquid crystals are an intermediate state of matter between isotropic liquids and crystalline solids (Figure 2.4.A). As the name suggests, it combines the fluid-like properties of liquids while maintaining long-range orientational order of crystals. Consequently, liquid crystals are anisotropic. Molecules inducing liquid-crystalline phases are called **mesogens**, as they can generate intermediate (*meso*-) phases. They typically have anisotropic shapes; for instance, calamitic mesogens have an elongated, rod-like shape, while discotic ones have a disk-like shape.[27]

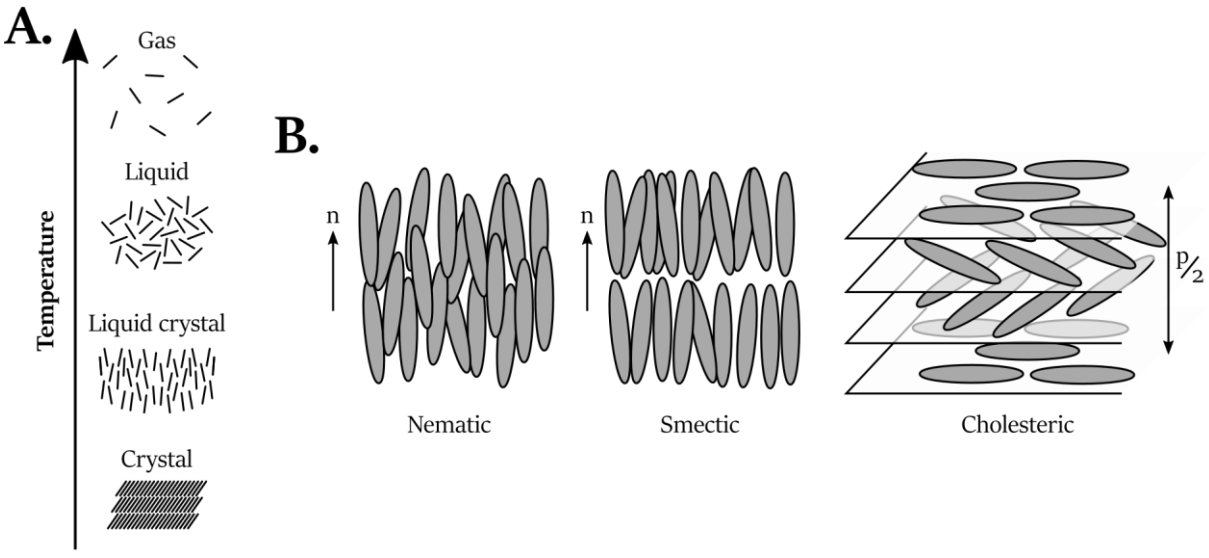

Figure 2.4. A. States of matter for liquid-crystalline materials. The liquid-crystalline phase exists between the liquid and the crystal phases, and it combines fluidity with long-range order. **B.** Examples of liquid-crystalline phases for calamitic mesogens. In the nematic phase, all directors of the mesogens follow the same direction. In the smectic phase, directors are also oriented in the same direction and centers of mass of the mesogens are organized in layers. In the cholesteric phase, layers of mesogens have the same orientation, but directors rotate from one layer to another, leading to a helical pitch p.

Moreover, different liquid-crystalline phases exist depending on the order of the mesogens (Figure 2.4.B). For instance, the orientation of calamitic mesogens is defined by their director vector $\vec{n}$, parallel to their long axis. In nematic phases, directors are oriented in the same direction but centers of mass of the molecules are isotropically distributed. In smectic phases, however, directors also follow the same direction, but centers of mass are organized in layers. In cholesteric phases, centers of mass of the mesogens are organized in layers but directors for each layer are oriented differently, and they rotate from one layer to another, resulting in a helicoidal organization characterized by a helical pitch p. Cholesteric phases may be obtained with chiral calamitic mesogens or by doping nematic phases with chiral molecules, for instance.[27]

Liquid-crystalline polymers (LCP) are polymers containing mesogenic units in their structure, conferring them liquid-crystalline properties. Mesogenic units can be attached as side groups or incorporated in the main chain (Figure 2.5). Liquid-crystalline elastomers (LCE) are slightly crosslinked networks of LCP and can, hence, be formed either by polymerization of mesogenic units with at least trifunctional crosslinkers, or by post-polymerization reticulation of LCP.[28] The vast majority of actuators based on LCE are prepared by copolymerization of mesogenic acrylates or methacrylates, for instance.[29,30]

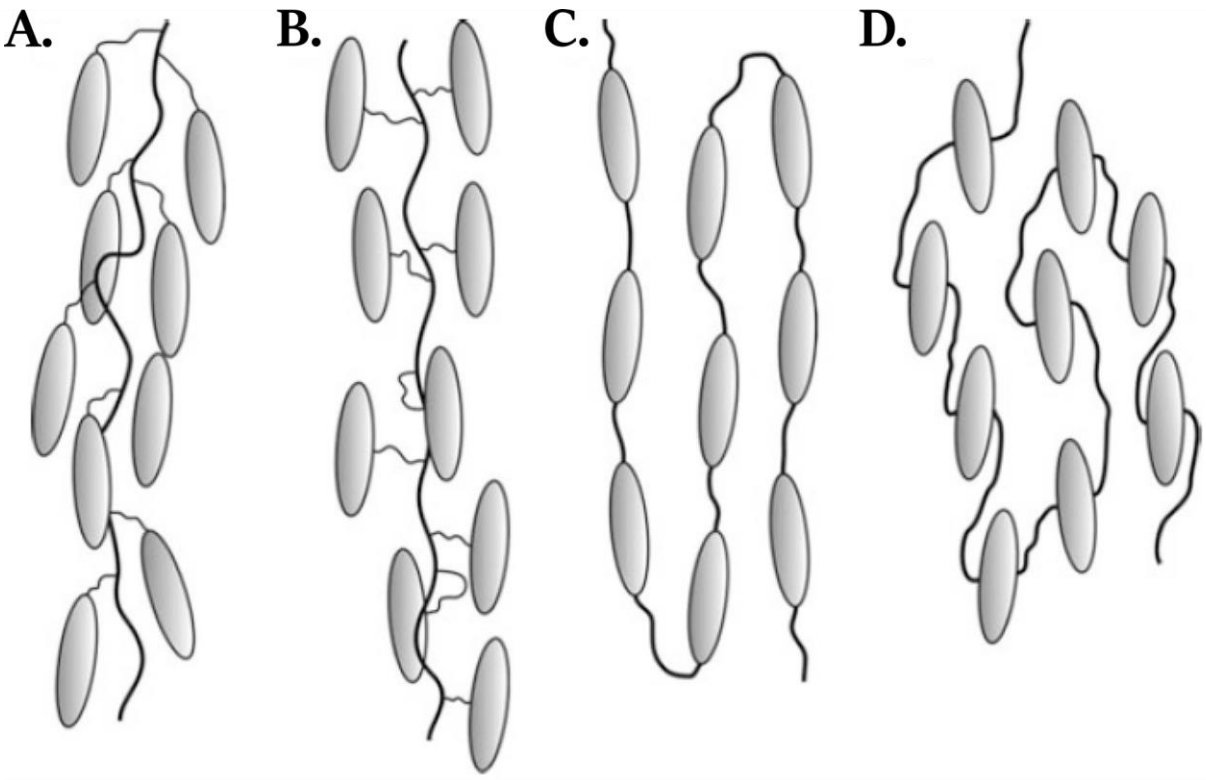

Figure 2.5. Liquid-crystalline polymers (LCP) with different modes of attachment of the mesogenic units. First, mesogens can be attached either as end-on **(A)** or as side-on **(B)** side chains. Alternatively, mesogens can be attached either as end-on **(C)** or as side-on **(D)** main chain. Adapted from reference [28]

An important feature for the preparation of actuating LCE is their macroscopic orientation. The concept behind the stimuli-sensitive shape change of these materials is the transition between the ordered, liquid-crystalline phase and the disordered, isotropic one. For instance, a nematic LCE consists, as explained earlier, of mesogens aligned in the same direction. Upon application of a

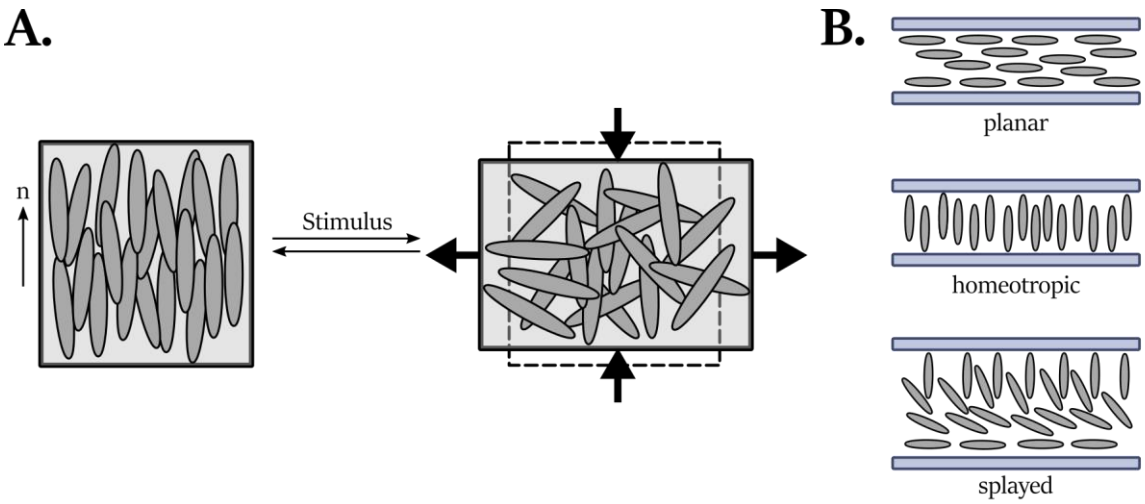

Figure 2.6. A. Mechanism for the deformation of LCE under stimulation. The loss of order occurring between the liquid-crystalline phase and the isotropic phase triggers a contraction along the initial director axis and an expansion in orthogonal directions. **B.** Surface anchoring orientation leads to different organizations of mesogens in LCE. With planar anchoring, directors are oriented parallel to the surface. With homeotropic anchoring, directors are perpendicular to the surface. When one surface favours planar orientation and the other favours homeotropic orientation, the LCE has a splayed conformation with a gradient in orientation of the directors along the thickness.

stimulus, such as heat, the material may reach its isotropic phase; mesogens will therefore deviate from their initial orientation and this change in order will lead to a contraction of the material along the initial director and an expansion in the other directions (Figure 2.6.A).[29] However, the long-range order of LCE only occurs in microdomains, similar to the behavior of crystals. Consequently, any deformation that may occur in these domains has little influence at the macroscopic scale because the material is overall isotropic. Therefore, it is necessary to macroscopically orient the system to induce a significant shape change. Different techniques have been used, such as the application of a magnetic field prior to reticulation or stretching the material during the crosslinking process.[31] For LCE films, surface anchoring is a common strategy to induce macroscopic orientation (Figure 2.6.B). Surfaces can be functionalized to favor either planar or homeotropic alignment of mesogens. Planar alignment is usually induced with polymer-coated substrates that have been unidirectionally rubbed, and directors of the mesogenic units are parallel to the surface. Homeotropic alignment, on the other hand, are usually induced with substrates that were functionalized with amphiphilic molecules, and mesogens have their directors perpendicular to the surface.[27] When the liquid-crystalline mixture is sandwiched between a substrate inducing planar alignment and another one inducing homeotropic alignment, it results in a splayed arrangement of the mesogens where their directors gradually rotate along the thickness of the material. This configuration is of particular interest for actuators because it leads to large deformations, since one face of the material extends while the other one contracts upon stimulation.

Light is commonly used to trigger the deformation of LCE, since it can be easily addressed both in time and space. As we discussed in the previous paragraph, LCE deform when they are heated to their isotropic phase; hence, photothermal agents are commonly used as dopants in these materials since they release heat when irradiated.[32] In this thesis, we are interested in the integration of molecular machines, such as photoswitches or molecular motors, in these polymer networks. Azobenzene is a common photoswitch used as dopant in liquid-crystalline systems because of its

elongated shape. Upon light irradiation, it isomerizes from its most stable *trans*- isomer to its *cis*-isomer (Figure 2.7.A). When incorporated into LCE, two mechanisms triggering shape change are at play: the photothermal and the photomechanical effects. In the former case, absorption of light energy by azobenzene leads to dissipation of heat, which increases the temperature of the material above its transition temperature to the isotropic phase and, hence, trigger actuation. For the photomechanical effect, however, the increased excluded volume of azobenzene after its isomerization locally disrupts the order of the liquid-crystalline phase. Therefore, it leads to the same transition as when the temperature is increased, from an ordered to a disordered network, and triggers actuation as well. In practice, both effects contribute to the shape change of LCE and the exact influence of each aspect is still subject to investigation.[33]

Soft actuators based on light sensitive LCE are regularly reported and comprehensive reviews of the field can be found elsewhere.[29,30,34] Among the most recent systems, Schenning and coworkers reported a reprogrammable LCE-based actuator. The photoactive liquid-crystalline film was deposited on a thermoplastic substrate of poly(ethylene terephthalate) (PET). Upon light irradiation, the composite material could reversibly actuate between two shapes. The initial shape of the substrate could be changed by heating above its T_g, applying a deformation, and cooling it down; light irradiation then led to a different shape change (Figure 2.7.B).[35] In another example, Schenning, den Toonder and coworkers reported a soft robotic device based on a platform having four LCE-based 'legs'. Sequential light irradiation of specific legs triggered their bending and unbending, which ultimately led to the directional displacement of the platform (Figure 2.7.C).[36] In the previous chapter

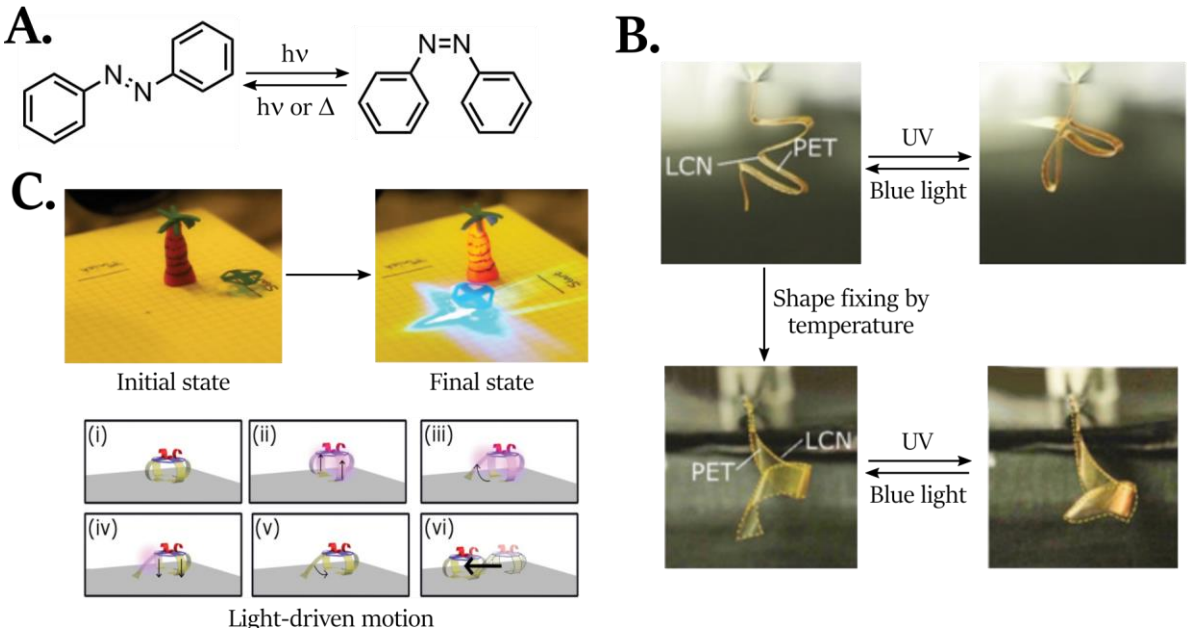

Figure 2.7. A. Chemical structure of *trans*- and *cis*-azobenzene. The *cis*-isomer is accessible by photoisomerization and recovery of the most stable *trans*-isomer can be triggered by light or heat. **B.** Reprogrammable LCE-based actuator. A LCE film is deposited on a thermoplastic PET substrate. Light irradiation leads to actuation. Since the initial shape can be programmed by heating the material above its T_g, different actuation modes are accessible. The length of the material is 2 cm. Adapted from reference [35]. **C.** Soft robotic device consisting of a platform having four LCE-based 'legs'. The mechanism is as follows: (i) the platform is at its initial position and (ii) irradiation of two opposite legs lifts it. (iii) Irradiation of a third leg unfolds it and (iv) the platform is lowered by removing light on the first opposite legs. (iv) Removal of light source on the third leg triggers its bending, which (vi) drags the platform in the corresponding direction. The corresponding snapshots of the initial and final positions are shown. Adapted from reference [36].

(section 1.3), we presented reports from Feringa, Broer and coworkers, and Yang and coworkers, where the incorporation of molecular motors inside LCE triggers actuation, and both photothermal and photomechanical effects were observed.[2,37]

In this work, our goal was to incorporate our tetra-functional molecular motors inside LCE. Our hypothesis was that the conformation of the oriented polymer chains in the dry network would be partially conserved when the material was swollen in a solvent. Therefore, the braiding of the chains by the motors may lead to an anisotropic shape change of the gels. Results regarding our investigations are detailed in Chapter 6. Apart from LCE, we also investigated and optimized the operation of isotropic polymer gels, and several chemical structures were considered. The next section presents an overview of the polymers we used and introduces their main properties and applications.

2.3 Polymers investigated in this work

As mentioned in the introduction, one goal of this thesis was to investigate how the chemical structure of our polymer networks changes the contractile behaviour of our materials. In our first reports,[22,23] PEG-based networks were prepared and are, hence, discussed first in this subsection. We then discuss the properties of poly(dimethylsiloxane) (PDMS), which is also commercially available as telechelic chains. We also investigated two vinyl polymers, namely poly(*N*-isopropylacrylamide) (PNIPAAm) and sodium poly(styrene sulfonate) (NaPSS), and prepared poly(3-hexylthiophene) (P3HT), a conjugated polymer, and their main characteristics are presented briefly. Finally, we collaborated with Prof. Lecommandoux's team in Bordeaux to form materials based on poly(γ-benzyl-L-glutamate) (PBLG) and poly(glutamic acid) (PGA), which properties are presented in the last section.

2.3.1 Poly(ethylene glycol) (PEG)

PEG is a biocompatible polyether (Scheme 2.1) soluble in aqueous solutions and most organic solvents.[38] As such, PEG-based systems are widely used in the biomedical field, for instance as scaffolds for wound healing or for drug-delivery platforms.[39,40] The polymer can be prepared by cationic, anionic or coordination polymerization of ethylene oxide and end-functionalized macromolecules are commercially available.[41] It is a flexible macromolecule and we previously determined that its persistence length was close to 1 nm.[15,16]

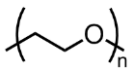

Scheme 2.1. Chemical structure of PEG.

The preparation of PEG-based hydrogels by end-linking polymers *via* 'click' coupling has been reported by several research groups. For instance, Hawker and coworkers prepared a series of networks with PEG having different molecular weights by crosslinking telechelic linear chains with tetrafunctional crosslinkers by copper(I)-catalyzed azide-alkyne cycloaddition (CuAAC).[42] More recently, Xu, Fu and colleagues also reported the preparation of networks from linear chains and multifunctional crosslinkers by CuAAC, where the reactive Cu(I) species were thermally generated.[43]

Sakai and coworkers widely explored gels formed with end-functional tetra-arm PEG,[44,45] where the unique topology led to negligible amounts of defects in the network.[46]

Considering the commercial availability of end-functionalized PEG and the literature on the study of the corresponding gels, this polymer was selected to form the initial networks that we reported.[22] In this thesis, we aimed to determine the influence of several parameters on the contractile behaviour of PEG-based hydrogels and our results are presented in Chapter 4.

2.3.2 Poly(dimethylsiloxane) (PDMS)

The peculiarity of PDMS (Scheme 2.2) among the other polymers discussed in this thesis is its low $T_g \approx -120°C$, and a low melting temperature $T_m \approx -40°C$.[47] Therefore, dry networks at room temperature behave as elastomers and such materials have been used, for instance, for flexible electronics or for biomedical applications.[48] Functional polymers are usually prepared by ring-opening polymerization (ROP) of octamethylcyclotetrasiloxane[47] and, similarly to PEG, telechelic linear polymers are commercially available. It is also a flexible polymer, since its persistence length is close to 0.5 nm.[49,50]

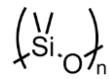

Scheme 2.2. Chemical structure of PDMS.

As for PEG, PDMS-based networks can be formed by end-linking processes. These 'ideal' networks were thoroughly studied to test theories about mechanical properties of elastomers and gels.[51,52] For instance, Urayama and coworkers investigated PDMS networks prepared by hydrosilylation between vinyl-terminated linear polymers and tetrafunctional crosslinkers.[53] The preparation of PDMS-based gels and elastomers crosslinked with molecular motors was investigated in the present thesis, and the results are presented in Chapter 5**,** section 5.4.

One of the main properties of elastomers is their elastic modulus. As will be presented in the relevant chapter, we therefore investigated the elasticity of our PDMS-based networks by dynamic mechanical analysis (DMA).[54] A periodic strain ε is applied to the material at a frequency f:

$$\varepsilon = \varepsilon_0 \sin(\omega t) \tag{2.28}$$

with ε_0 the maximum strain and ω the angular frequency, defined as $\omega = 2\pi f$. The stress response σ of the material have a phase lag δ because of the viscoelastic nature of the polymer network:

$$\sigma = \sigma_0 \sin(\omega t + \delta) \tag{2.29}$$

with σ_0 the maximum stress. In tensile tests, the **tensile storage modulus E'**, representing the elastic contribution of the material, is given by:

$$E' = \frac{\sigma_0}{\varepsilon_0} \cos \delta \tag{2.30}$$

while the **loss modulus E''**, characterizing the viscous contribution of the material, is given by:

$$E'' = \frac{\sigma_0}{\varepsilon_0} \sin \delta \tag{2.31}$$

Therefore, the **tangent of the phase angle tan δ** gives the ratio of the loss modulus over the storage modulus:

$$\tan \delta = \frac{E''}{E'} \tag{2.32}$$

Consequently, DMA of our PDMS-based networks may provide information on the formation of new entanglements since it would alter the elastic modulus of the material. These results are also presented in Chapter 5, section 5.4.2.

*2.3.3 Poly(*N*-isoproprylacrylamide) (PNIPAAm)*

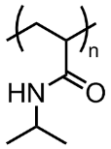

Scheme 2.3. Chemical structure of PNIPAAm.

PNIPAAm is a vinyl polymer bearing amide substituents (Scheme 2.3). We were interested in its thermoresponsiveness since it has a lower critical solution temperature (LCST) around 30°C in water;[55] in other words, it is soluble in aqueous solutions below this temperature and it precipitates at higher temperatures. Therefore, PNIPAM-based networks are often used as thermoresponsive actuators with potential applications in the biomedical field.[29,56] As for the two previous polymers, it is a flexible polymer with a persistence length close to 1 nm.[57,58]

The preparation of end-functional vinyl polymers can be achieved by reversible-deactivation radical polymerization (RDRP). The most popular techniques in this class of polymerization are nitroxide-mediated polymerization, reversible addition-fragmentation chain transfer, and atom-transfer radical polymerization (ATRP).[59] In our case, we chose ATRP because it leads to halogenated chain ends that can be substituted, and because of the commercial availability of the difunctional initiators necessary to synthesize linear telechelic polymers. Specifically, we used dimethyl 2,6-dibromoheptanedioate (DBHD) for the polymerization, in our case.[60]

As for any RDRP, ATRP relies on the equilibrium between dormant and active species during the polymerization. The active radical is in redox equilibrium with a dormant alkyl halide and the reaction is catalyzed by a metal complex. Therefore, propagation occurs only with the active species (Scheme 2.4). Deactivation ensures a low concentration of radicals, which limits the occurrence of termination reactions, and leads to a narrow dispersity. The expected molecular weight is determined by the ratio between the concentrations of monomer and initiator, while the amount of transition metal and ligand must be tightly controlled to ensure fast deactivation without impairing the polymerization process.[61]

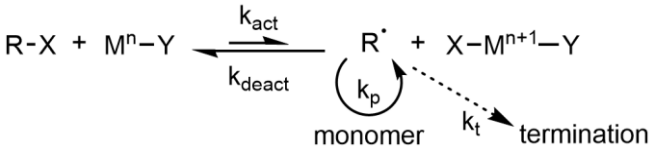

Scheme 2.4. General mechanism for ATRP. The dormant alkyl halide R-X is in redox equilibrium with the reactive radical species R˙. The atom transfer process is catalyzed by a transition metal M^n, which can bear another halogen atom or a ligand Y. The active species may undergo propagation with a rate k_p. Fast deactivation (k_{deact}) lowers the number of radicals in the medium and, hence, limits the occurrence of termination (k_t).

For our systems, we followed the procedure reported by Haddleton and coworkers,[62,63] who synthesized PNIPAAm in alcohol / water mixtures over a wide range of molecular weights with a high retention of end-group functionality. They used single-electron transfer ATRP (SET-ATRP)

where the Cu(I) catalyst undergoes complete disproportionation into Cu(0) and Cu(II) in water with tris[2-(dimethylamino)ethyl]amine (Me_6TREN) as ligand. In SET-ATRP, Cu(0) activates the dormant species, while Cu(II) deactivates the active radical. The mechanism of activation / deactivation of the propagating chains is then different than classical ATRP, but the general principle remains similar.[64] Our results are presented in Chapter 5**,** section 5.3.

2.3.4 Sodium poly(styrene sulfonate) (NaPSS)

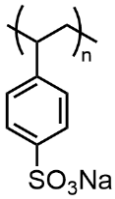

Scheme 2.5. Chemical structure of NaPSS.

NaPSS is a polyelectrolyte derived from polystyrene (Scheme 2.5). It is commonly mixed with poly(3,4-ethylenedioxythiophene) (PEDOT) to form PEDOT:PSS composites for applications in flexible electronics.[65] It is also used as a polymer matrix for ion exchange resins.[66] Importantly, the persistence length of NaPSS depends on the ionic strength of the solution, since screening effects between adjacent charges alters the flexibility of the polymer chain. It can range between 1 nm, at high ionic strengths, and 6 nm, at low ionic strengths.[67]

End-functional NaPSS can be synthesized by two main pathways. The first one is by sulfonation of telechelic polystyrene but it requires harsh conditions to achieve full functionalization, which may cleave the chain or induce the reaction with the end groups.[68] Alternatively, sodium styrene sulfonate may be directly polymerized. We preferred the latter option to achieve full sulfonation, as several reports present the ATRP of styrene sulfonate;[69–71] we followed these procedures with the same initiator as envisioned for PNIPAAm. Our results are presented in Chapter 5, section 5.2.

2.3.5 Poly(3-hexylthiophene) (P3HT)

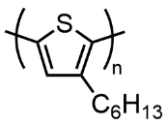

Scheme 2.6. Chemical structure of P3HT.

P3HT is a conjugated polymer (Scheme 2.6) and, as such, is investigated for its application in organic photovoltaics and flexible electronics.[72,73] Its persistence length is close to 3 nm[74,75] and we expected that the more rigid structure might lead to a different contractile behavior compared to the more flexible polymers presented in previously.

Several strategies can be envisioned for the synthesis of P3HT, such as electrochemical polymerization, or polymerization by oxidative coupling.[76] We followed the Grignard-initiated metathesis (GRIM) polymerization reported by McCullough and coworkers as it gives linear telechelic P3HT bearing bromide or hydrogen atoms at chain ends,[77] which can then be further functionalized for CuAAC.[78,79] The polymerization occurs following a chain-growth mechanism. First, the monomers are activated with an organometallic compound to form the corresponding metalated 3-hexylthiophene. Addition of dichloro(1,3-bis(diphenylphosphino)propane)nickel ($Ni(dppp)Cl_2$) initiates the polymerization by forming a complex with two activated monomers. After reductive elimination, a dimer of 3-hexylthiophene is formed. Importantly, the nickel initiator does not fully dissociate from the dimer and oxidative addition occurs at the chain end. Another monomer can therefore be added to the growing chain after substitution on the nickel complex and reductive

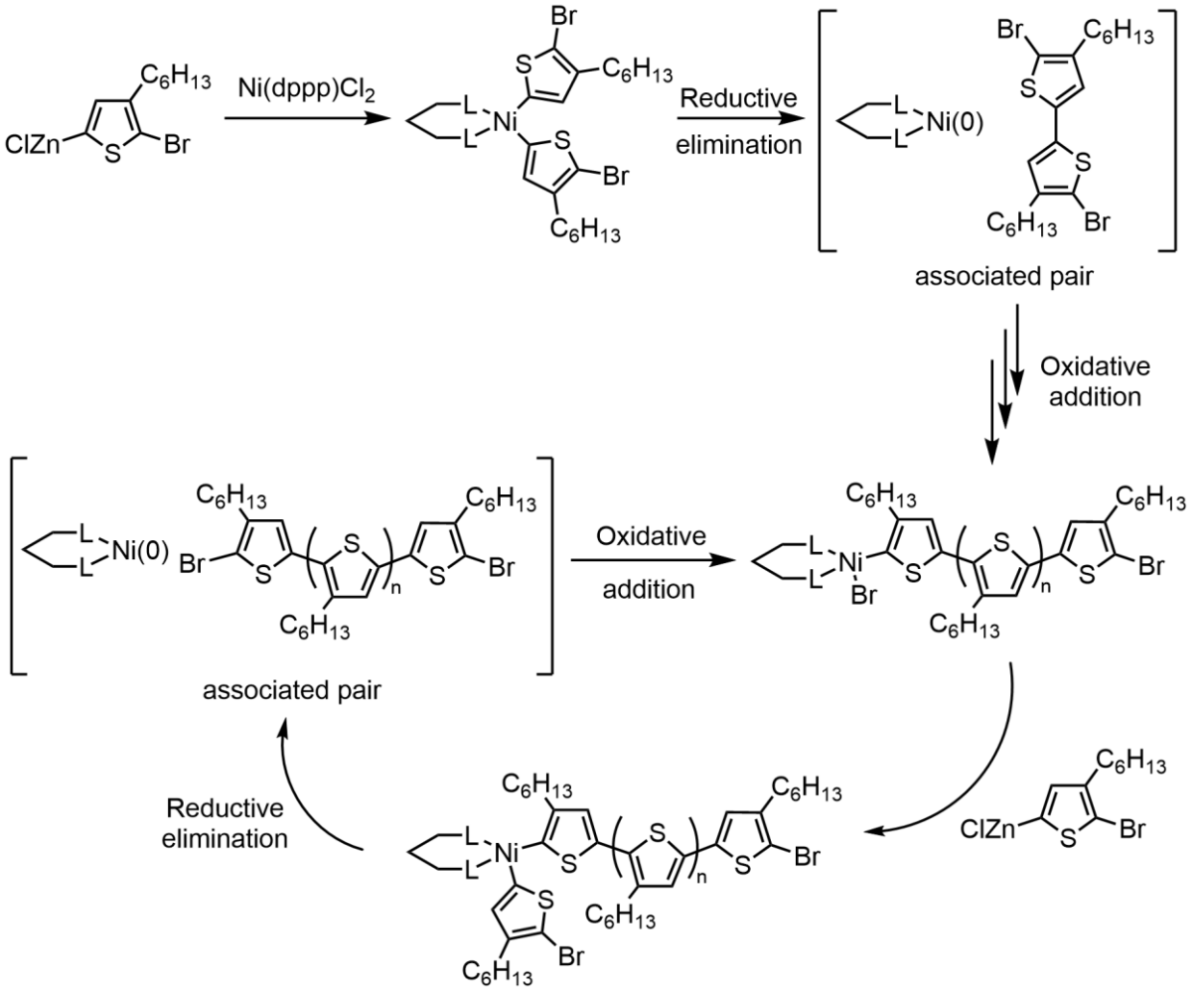

Scheme 2.7. Mechanism of GRIM polymerization. The polymerization follows a chain-growth mechanism where the nickel complex acts as the initiator. Subsequent oxidative additions and reductive eliminations of the metallic complex between monomers and the growing chains propagates the polymerization. Moreover, the metallic complex is not fully detached from the growing chain after reductive elimination and forms an associated pair, ensuring growth of the chain at its end.

elimination. Repetition of oxidative additions and reductive eliminations with associated pairs intermediate between the nickel initiator and the growing chain leads to the formation of stereoregular P3HT with narrow dispersity (Scheme 2.7).[80] Our results on the polymerization and functionalization of P3HT are presented in Chapter 5, section 5.1.

2.3.6 Poly(γ-benzyl-L-glutamate) (PBLG) and poly(L-glutamic acid) (PGA)

PBLG and PGA are polypeptides that can form helicoidal supramolecular structures in solution (Scheme 2.8).[81,82] The presence of these helices can induce the formation of physical gels at a suitable concentration in helicogenic solvents, such as toluene; PGA, which bears carboxylic acids, may also form networks *via* hydrogen bonding.[83,84] Therefore, we aimed to incorporate molecular motors in these physical networks to create reversible

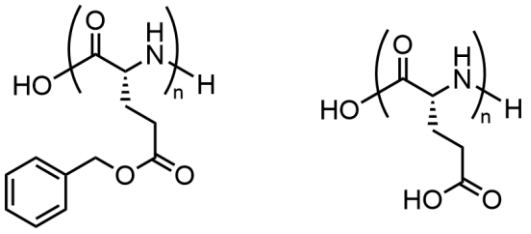

Scheme 2.8. Chemical structure of PBLG (left) and PGA (right).

contractile gels. Moreover, the presence of helices greatly increases the persistence length of the chain, which could also impact the contraction of the material. Finally, we hypothesized that the rotation of the motor may influence the conformation of the helices when the topology of the chains is 'locked' in a network. We investigated these systems in collaboration with the group of Prof. Lecommandoux, who prepared the polymers, and our results are presented in Chapter 5, section 5.5.

In conclusion, we presented in this chapter the concepts that are necessary to understand the evolution of volume of our photoactive networks. The conformation of individual polymer chains in solution explains the different concentration regimes of polymer solutions. The overlap concentration c* was proven to be essential to form our materials in optimal conditions, and we highlighted the theory behind its determination by viscometry. The conformation of polymer chains also explains the evolution of the volume of the gels when the molecular weight between crosslinks decreases over the course of irradiation, as well as the concomitant increase in elastic modulus. Finally, we gave an overview of the different polymer systems that were investigated in this work, and our results are reported in the following chapters.

References

1. A. S. Lubbe, J. C. M. Kistemaker, E. J. Smits, B. L. Feringa, *Phys. Chem. Chem. Phys.* **2016**, *18*, 26725–26735.
2. R. Lan, J. Sun, C. Shen, R. Huang, Z. Zhang, C. Ma, J. Bao, L. Zhang, L. Wang, D. Yang, et al., *Adv. Funct. Mater.* **2020**, 2000252.
3. I. Teraoka, *Polymer Solutions*, John Wiley & Sons, Inc., **2002**.
4. M. Rubinstein, R. H. Colby, *Polymer Physics*, Oxford University Press, **2003**.
5. P. G. de Gennes, *Scaling Concepts in Polymer Physics*, Cornell University Press, **1979**.
6. M. Doi, *Introduction to Polymer Physics*, Clarendon Press, **1995**.
7. H. Staudinger, *Berichte der Dtsch. Chem. Gesellschaft (A B Ser.* **1920**, *53*, 1073–1085.
8. H. Staudinger, J. Fritschi, *Helv. Chim. Acta* **1922**, *5*, 785–806.
9. H. Frey, T. Johann, *Polym. Chem.* **2020**, *11*, 8–14.
10. J. E. Winandy, R. M. Rowell, in *Chem. Solid Wood*, American Chemical Society, **1984**, pp. 211–255.
11. D. Crespy, M. Bozonnet, M. Meier, *Angew. Chem. Int. Ed.* **2008**, *47*, 3322–3328.
12. J. Zalasiewicz, C. N. Waters, J. A. Ivar do Sul, P. L. Corcoran, A. D. Barnosky, A. Cearreta, M. Edgeworth, A. Gałuszka, C. Jeandel, R. Leinfelder, et al., *Anthropocene* **2016**, *13*, 4–17.
13. A. L. Andrady, Ed. , *Plastics and the Environment*, John Wiley & Sons, Inc., Hoboken, NJ, USA, **2003**.
14. M. Chanda, Ed. , *Plastics Technology Handbook*, CRC Press, **2018**.
15. G. Mariani, J.-R. Colard-Itté, E. Moulin, N. Giuseppone, E. Buhler, *Soft Matter* **2020**, *16*, 4008–4023.
16. J.-R. Colard-Itté, Q. Li, D. Collin, G. Mariani, G. Fuks, E. Moulin, E. Buhler, N. Giuseppone, *Nanoscale* **2019**, *11*, 5197–5202.

17. J. G. Kirkwood, J. Riseman, *J. Chem. Phys.* **1948**, *16*, 565–573.

18. P. J. Flory, T. G. Fox, *J. Am. Chem. Soc.* **1951**, *73*, 1904–1908.

19. W.-M. Kulicke, C. Clasen, *Viscosimetry of Polymers and Polyelectrolytes*, Springer Berlin Heidelberg, Berlin, Heidelberg, **2004**.

20. Y. Gu, J. Zhao, J. A. Johnson, *Angew. Chem. Int. Ed.* **2020**, *59*, 5022–5049.

21. T. Sakai, *Physics of Polymer Gels*, Wiley-VCH Verlag GmbH, **2020**.

22. Q. Li, G. Fuks, E. Moulin, M. Maaloum, M. Rawiso, I. Kulic, J. T. Foy, N. Giuseppone, *Nat. Nanotechnol.* **2015**, *10*, 161–165.

23. J. T. Foy, Q. Li, A. Goujon, J.-R. Colard-Itté, G. Fuks, E. Moulin, O. Schiffmann, D. Dattler, D. P. Funeriu, N. Giuseppone, *Nat. Nanotechnol.* **2017**, *12*, 540–545.

24. P. J. Flory, J. Rehner, *J. Chem. Phys.* **1943**, *11*, 512–520.

25. P. J. Flory, J. Rehner, *J. Chem. Phys.* **1943**, *11*, 521–526.

26. N. R. Richbourg, N. A. Peppas, *Prog. Polym. Sci.* **2020**, *105*, 101243.

27. I. Dierking, *Textures of Liquid Crystals*, Wiley-VCH Verlag GmbH, **2003**.

28. W. H. de Jeu, *Liquid Crystal Elastomers: Materials and Applications*, Springer Berlin Heidelberg, **2012**.

29. D. Dattler, G. Fuks, J. Heiser, E. Moulin, A. Perrot, X. Yao, N. Giuseppone, *Chem. Rev.* **2020**, *120*, 310–433.

30. F. Lancia, A. Ryabchun, N. Katsonis, *Nat. Rev. Chem.* **2019**, *3*, 536–551.

31. R. S. Kularatne, H. Kim, J. M. Boothby, T. H. Ware, *J. Polym. Sci. B Polym. Phys.* **2017**, *55*, 395–411.

32. L. Dong, Y. Zhao, *Mater. Chem. Front.* **2018**, *2*, 1932–1943.

33. M. Pilz da Cunha, E. A. J. van Thoor, M. G. Debije, D. J. Broer, A. P. H. J. Schenning, *J. Mater. Chem. C* **2019**, *7*, 13502–13509.

34. H. K. Bisoyi, Q. Li, *Chem. Rev.* **2016**, *116*, 15089–15166.

35. R. C. P. Verpaalen, M. Pilz da Cunha, T. A. P. Engels, M. G. Debije, A. P. H. J. Schenning, *Angew. Chem. Int. Ed.* **2020**, *59*, 4532–4536.

36. M. Pilz da Cunha, S. Ambergen, M. G. Debije, E. F. G. A. Homburg, J. M. J. den Toonder, A. P. H. J. Schenning, *Adv. Sci.* **2020**, *7*, 1902842.

37. J. Hou, A. Mondal, G. Long, L. Haan, W. Zhao, G. Zhou, D. Liu, D. J. Broer, J. Chen, B. L. Feringa, *Angew. Chem. Int. Ed.* **2021**, anie.202016254.

38. Q. W. Yuan, in *Polymer Data Handbook* (Ed.: J.E. Mark), Oxford University Press, **1999**, pp. 542–552.

39. D. Hutanu, *Mod. Chem. Appl.* **2014**, *02*, DOI 10.4172/2329-6798.1000132.

40. T. T. Hoang Thi, E. H. Pilkington, D. H. Nguyen, J. S. Lee, K. D. Park, N. P. Truong, *Polymers* **2020**, *12*, 298.

41. J. Herzberger, K. Niederer, H. Pohlit, J. Seiwert, M. Worm, F. R. Wurm, H. Frey, *Chem. Rev.* **2016**, *116*, 2170–2243.

42. M. Malkoch, R. Vestberg, N. Gupta, L. Mespouille, P. Dubois, A. F. Mason, J. L. Hedrick, Q. Liao, C. W. Frank, K. Kingsbury, et al., *Chem. Commun.* **2006**, 2774.

43. K. W. Li, L. Cen, C. Zhou, A. K. Zhang, F. Yao, L. H. Tan, L. Q. Xu, G. D. Fu, *Macromol. Mater. Eng.* **2016**, *301*, 1374–1382.

44. T. Sakai, in *Physics of Polymer Gels* (Ed.: T. Sakai), Wiley-VCH Verlag GmbH, **2020**, pp. 153–159.

45. M. Shibayama, X. Li, T. Sakai, *Colloid Polym. Sci.* **2019**, *297*, 1–12.

46. Y. Akagi, T. Matsunaga, M. Shibayama, U. Chung, T. Sakai, *Macromolecules* **2010**, *43*, 488–

493.

47. A. C. M. Kuo, in *Polymer Data Handbook* (Ed.: J.E. Mark), Oxford University Press, **1999**, pp. 411–435.
48. M. P. Wolf, G. B. Salieb-Beugelaar, P. Hunziker, *Prog. Polym. Sci.* **2018**, *83*, 97–134.
49. T. J. Senden, J.-M. di Meglio, P. Auroy, *Eur. Phys. J. B* **1998**, *3*, 211–216.
50. A. V. Dobrynin, J.-M. Y. Carrillo, M. Rubinstein, *Macromolecules* **2010**, *43*, 9181–9190.
51. J. E. Mark, J. L. Sullivan, *J. Chem. Phys.* **1977**, *66*, 1006–1011.
52. G. Hild, *Prog. Polym. Sci.* **1998**, *23*, 1019–1149.
53. K. Urayama, *Polym. J.* **2008**, *40*, 669–678.
54. K. P. Menard, *Dynamic Mechanical Analysis*, CRC Press, **2008**.
55. N. A. Peppas, in *Polymer Data Handbook* (Ed.: J.E. Mark), Oxford University Press, **1999**, pp. 625–626.
56. X. Xu, Y. Liu, W. Fu, M. Yao, Z. Ding, J. Xuan, D. Li, S. Wang, Y. Xia, M. Cao, *Polymers* **2020**, *12*, 580.
57. Z. Ahmed, E. A. Gooding, K. V. Pimenov, L. Wang, S. A. Asher, *J. Phys. Chem. B* **2009**, *113*, 4248–4256.
58. P. Zhu, L. Chen, *Phys. Rev. E* **2019**, *99*, 022501.
59. K. Matyjaszewski, B. S. Sumerlin, N. V. Tsarevsky, J. Chiefari, *Controlled Radical Polymerization: Mechanisms*, Oxford University Press, **2015**.
60. K. A. Davis, B. Charleux, K. Matyjaszewski, *J. Polym. Sci. Pol. Chem.* **2000**, *38*, 2274–2283.
61. K. Matyjaszewski, J. Xia, *Chem. Rev.* **2001**, *101*, 2921–2990.
62. Q. Zhang, P. Wilson, Z. Li, R. McHale, J. Godfrey, A. Anastasaki, C. Waldron, D. M. Haddleton, *J. Am. Chem. Soc.* **2013**, *135*, 7355–7363.
63. A. Simula, V. Nikolaou, A. Anastasaki, F. Alsubaie, G. Nurumbetov, P. Wilson, K. Kempe, D. M. Haddleton, *Polym. Chem.* **2015**, *6*, 2226–2233.
64. C. Boyer, N. A. Corrigan, K. Jung, D. Nguyen, T.-K. Nguyen, N. N. M. Adnan, S. Oliver, S. Shanmugam, J. Yeow, *Chem. Rev.* **2016**, *116*, 1803–1949.
65. Y. Yang, H. Deng, Q. Fu, *Mater. Chem. Front.* **2020**, *4*, 3130–3152.
66. F. de Dardel, T. V. Arden, in *Ullmann's Encyclopedia of Industrial Chemistry*, Wiley-VCH Verlag GmbH, **2008**.
67. M. N. Spiteri, F. Boué, A. Lapp, J. P. Cotton, *Phys. Rev. Lett.* **1996**, *77*, 5218–5220.
68. J. E. Coughlin, A. Reisch, M. Z. Markarian, J. B. Schlenoff, *J. Polym. Sci. Pol. Chem.* **2013**, *51*, 2416–2424.
69. P. Balding, R. Cueto, P. S. Russo, W. R. Gutekunst, *J. Polym. Sci. Pol. Chem.* **2019**, *57*, 1527–1537.
70. P. D. Iddon, K. L. Robinson, S. P. Armes, *Polymer* **2004**, *45*, 759–768.
71. C.-K. Choi, Y.-B. Kim, *Polym. Bull.* **2003**, *49*, 433–439.
72. A. Marrocchi, D. Lanari, A. Facchetti, L. Vaccaro, *Energy Environ. Sci.* **2012**, *5*, 8457.
73. R. M. Pankow, B. C. Thompson, *Polymer* **2020**, *207*, 122874.
74. B. McCulloch, V. Ho, M. Hoarfrost, C. Stanley, C. Do, W. T. Heller, R. A. Segalman, *Macromolecules* **2013**, *46*, 1899–1907.
75. M. Nagai, J. Huang, T. Zhou, W. Huang, *J. Polym. Sci. B Polym. Phys.* **2017**, *55*, 1273–1277.
76. P. Sista, C. K. Luscombe, in *P3HT Revisited - From Molecular Scale to Solar Cell Devices* (Ed.: S. Ludwigs), **2014**, pp. 1–38.
77. R. S. Loewe, S. M. Khersonsky, R. D. McCullough, *Adv. Mater.* **1999**, *11*, 250–253.

78. C. Enders, S. Tanner, W. H. Binder, *Macromolecules* **2010**, *43*, 8436–8446.

79. R. A. Krüger, T. J. Gordon, T. Baumgartner, T. C. Sutherland, *ACS Appl. Mater. Interfaces* **2011**, *3*, 2031–2041.

80. E. E. Sheina, J. Liu, M. C. Iovu, D. W. Laird, R. D. McCullough, *Macromolecules* **2004**, *37*, 3526–3528.

81. P. Doty, A. Wada, J. T. Yang, E. R. Blout, *J. Polym. Sci.* **1957**, *23*, 851–861.

82. H. E. Huxley, M. F. Perutz, *Nature* **1951**, *167*, 1054–1054.

83. A. Niehoff, A. Mantion, R. McAloney, A. Huber, J. Falkenhagen, C. M. Goh, A. F. Thünemann, M. A. Winnik, H. Menzel, *Colloid Polym. Sci.* **2013**, *291*, 1353–1363.

84. S. Yan, T. Wang, X. Li, Y. Jian, K. Zhang, G. Li, J. Yin, *RSC Adv.* **2017**, *7*, 17005–17019.

Part II
Results and discussion

Chapter 3
Gram-scale synthesis of crosslinking rotary molecular motors based on overcrowded alkenes

Special thanks to Joakim Heiser for the gram-scale synthesis of the indanethione

Our strategy to amplify the controlled nanoscopic motion of artificial molecular motors relies on the integration of active crosslinking units inside polymer networks. In our design, as presented in Chapter 1**,** the work produced by each individual machine is 'stored' in the polymer chains of the network; since all polymer chains are connected to form a material, all these nanoscopic contributions are accumulated and cause changes in macroscopic properties.

The molecular motors that are used for the preparation of these systems must satisfy several requirements. First, using a molecular motor with a well-known operating cycle is crucial to properly determine the relationship between the nanoscopic motion and the resulting macroscopic actuation. Therefore, considering the large amount of literature produced by the group of Feringa to correlate the structure of molecular motors to their function (Chapter 1, section 1.2.3), we chose to design our active crosslinking agents based on the structure of overcrowded alkenes. Moreover, they offert the advantage of being powered by light, which is more easily addressed precisely, both spatially and temporally.

The second requirement is that our molecular motors should rotate fast at a reasonable temperature, preferentially room temperature. A slow rotation speed implies a long exposure to UV light to observe macroscopic changes, which may, in parallel, lead to dissolution of the materials over time by degrading either the motors or the polymer chains. Second-generation molecular motors offer the advantage having a symmetric 'stator', which means that the two thermal helix inversions of the operation cycle of the motors are identical and, hence, the rotation speed can be more easily optimized. Moreover, the relationship between the chemical structure of these motors and their rotation speed has already been explored (Chapter 1, section 1.2.3), which helps to choose the proper design of our crosslinking agents.

Since molecular motors are used as crosslinks, they must bear at least three functional groups. Tetrafunctional crosslinking agents, however, are usually used for the preparation of 'ideal' polymer networks.[1] Therefore, the 'rotor' and the 'stator' were designed to each bear two functional groups, which have to be orthogonal in order to address them separately, for instance to better control the topology of our gels or to graft motors to surfaces.

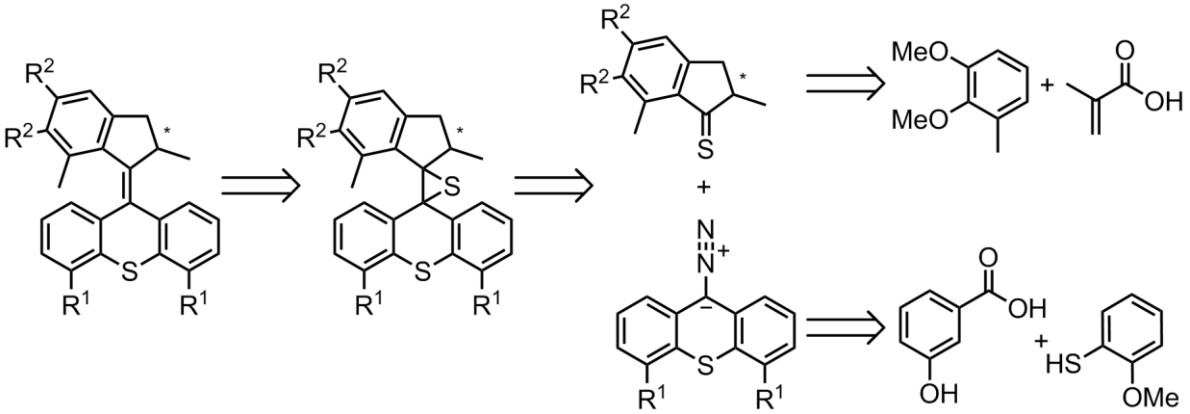

Scheme 3.1. Retrosynthetic scheme for the molecular motor used in this thesis. R^1 and R^2 represent two orthogonal functional groups, R^2 being chiral for an easier purification of the diastereoisomeric episulfides.

The last requirement is to obtain optically pure motors to know in which direction they are rotating, ensuring a proper determination of the structure-property relationship of our systems. Since the purification of enantiomers requires expensive techniques, such as chiral HPLC, we opted for the introduction of chiral moieties on the functional groups to obtain the corresponding diastereoisomers, which are more easily separated from each other with standard chromatography techniques.

Considering all these criteria, the synthesis of the motor was therefore envisioned by a convergent pathway where the overcrowded alkene was synthesized by a Barton-Kellogg coupling, consisting of the condensation between a diastereoisomeric indanethione and a diazo thioxanthone, to get the corresponding overcrowded alkene (Scheme 3.1).

The chapter is therefore divided in four parts. The first one will describe the synthesis of the thioxanthone, which we will refer to as the stator part, since it bears the asymmetric center. The rotor part, that is, the indanone, is the subject of the second subsection. The Barton-Kellogg coupling and a summary of the gram-scale synthesis are detailed in the third part. Finally, the various functionalizations of the motor, as they are all closely related, are the subject of the fourth section of this chapter.

The masses and the yield indicated in the following subsections are the typical ones obtained for one batch; some reactions were repeated several times to obtain large quantities of the expected product. The full characterization of all compounds presented in this section can be found in Appendix A.

3.1 Synthesis of the thioxanthone stator

Feringa and coworkers reported that the replacement of an oxygen atom by a sulfur one on the stator greatly improved the rotation speed of the resulting molecular motors (Chapter 1, section 1.2.3),[2] which is one of the requirements for our light-sensitive polymer gels. The synthesis of a similar difunctional stator based on a thioxanthone has already been reported by the same team.[3] The thioxanthone hydrazone of interest **7** is obtained in seven steps (Scheme 3.2).

On the one hand, 3-hydroxybenzoic acid was activated with thionyl chloride to form the corresponding acyl chloride. Subsequent nucleophilic attack by diethylamine afforded 59.4 g of *N,N*-diethyl-3-hydroxybenzamide **1** with an excellent yield. The phenol was then protected with methyl iodide to afford 83.3 g of *N,N*-diethyl-3-methoxybenzamide **2** in a quantitative yield. On the other hand, 2-methoxythiophenol was oxidized with diiodine to obtain 69.3 g of the corresponding symmetric disulfide **3** quantitatively.

Compounds **2** and **3** were then coupled by thiolarylation. First, compound **2** was deprotonated by directed ortho-metallation with *s*-butyllithium (*s*-BuLi). The subsequent aromatic electrophilic substitution with **3** led to 20.4 g of thioether **4** in reasonable yield. Interestingly, the derivative bearing the thioether at the *para* position of the methoxy group or the *para* position of the amide of **2** was not observed, indicating that both the amide and the methoxy are *ortho*-directing groups for the metalation.

Finally, thioxanthone **5** was obtained by intramolecular acylation. Lithium diisopropylamide was formed *in situ* by deprotonation of diisopropylamine with *n*-butyllithium (*n*-BuLi) and the subsequent addition of compound **4** led to its cyclization, affording 20.6 g of **5** in quantitative yield.

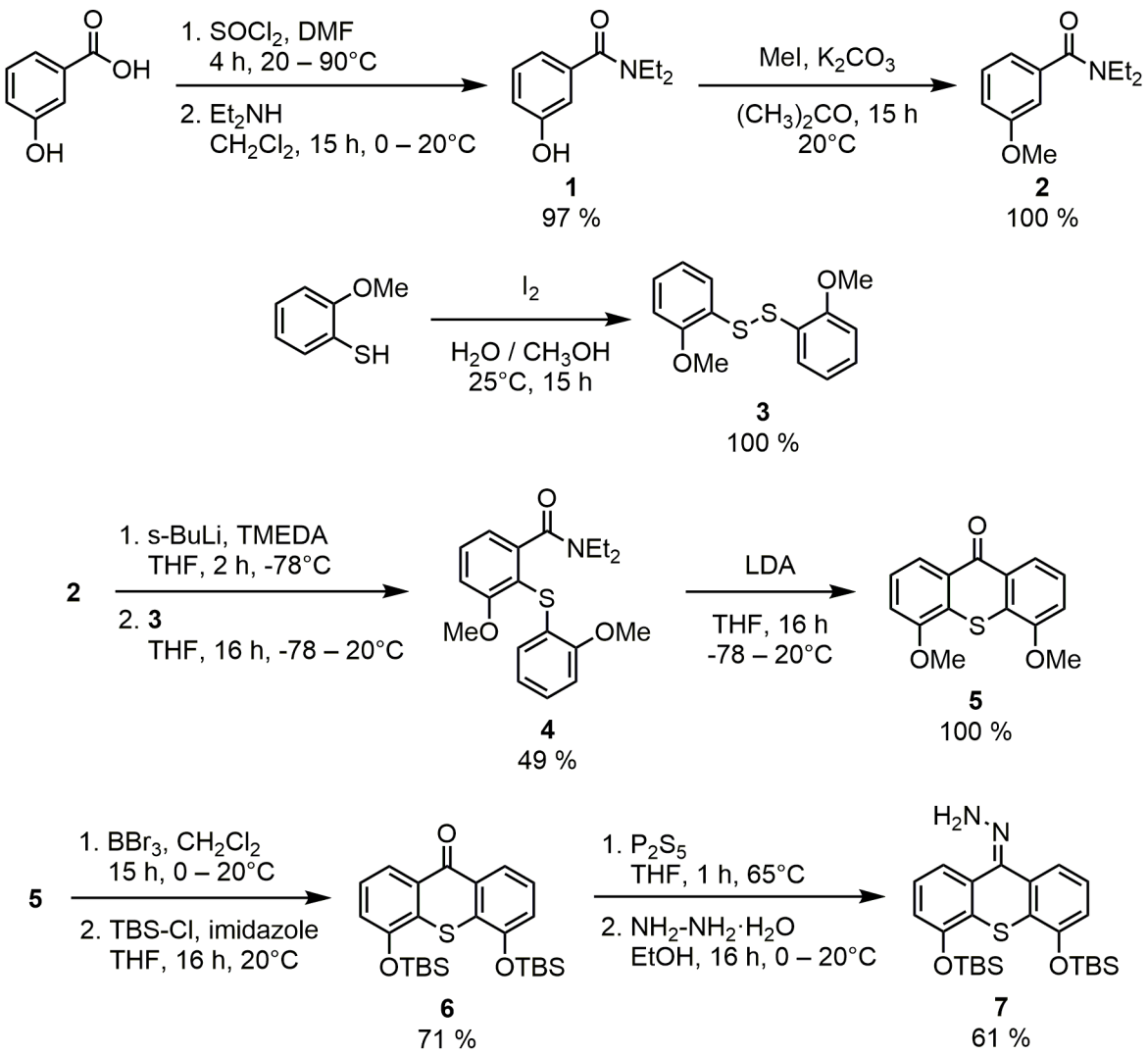

Scheme 3.2. Seven-step synthesis of the TBS-protected thioxanthone stator **7**.

As explained further later (section 3.4), *tert*-butyldimethylsilyl (TBS) protecting groups ensure a better orthogonality for the selective deprotection of the rotor. Thioxanthone **5** was therefore deprotected with boron tribromide and reprotected by nucleophilic substitution of the phenols with *tert*-butyldimethylsilyl chloride, affording 43.3 g of TBS-protected thioxanthone **6** in good yield.

For the Barton-Kellogg coupling, the thioxanthone must be converted to an hydrazone. The carbonyl group of thioxanthone **6** was therefore converted to the corresponding thioketone with phosphorus pentasulfide. Subsequent addition of hydrazine led to the formation of 13 g of thioxanthone hydrazone **7** in good yield.

The thioxanthone hydrazone was therefore obtained in seven steps with an overall 21 % yield, the key step of this synthesis being the directed thiolarylation to obtain thioether **4**. Although this yield might seem relatively low, it was however possible to obtain 13 g of final compound **7** in a single batch.

3.2 Synthesis of the rotor

The synthesis of a similar difunctional indanethione rotor has also been described by Feringa and coworkers.[4] The synthesis of the diastereoisomeric mixture of indanethione is performed in four steps (Scheme 3.3).

The indanone core is formed by a Friedel-Crafts-type reaction between 2,3-dimethoxytoluene and methacrylic acid in polyphosphoric acid, to form a racemic mixture of 102 g of **8** in good yield. Then, the methoxy groups of indanone **8** are removed using boron tribromide, affording 29.9 g of 5,6-dihydroxy-2,7-dimethylindanone **9** in an almost quantitative yield.

The corresponding aromatic ethers with *(S)*-ethyl lactate are synthesized by a Mitsunobu reaction involving diisopropylazodicarboxylate (DIAD) and triphenylphosphine as reagents. Since the Mitsunobu etherification inverts the absolute configuration of the alcohol group from the lactate, it leads to 20.4 g of a diastereoisomeric mixture of *(R,R,R)* and *(R,R,S)* of compound **10** in reasonable

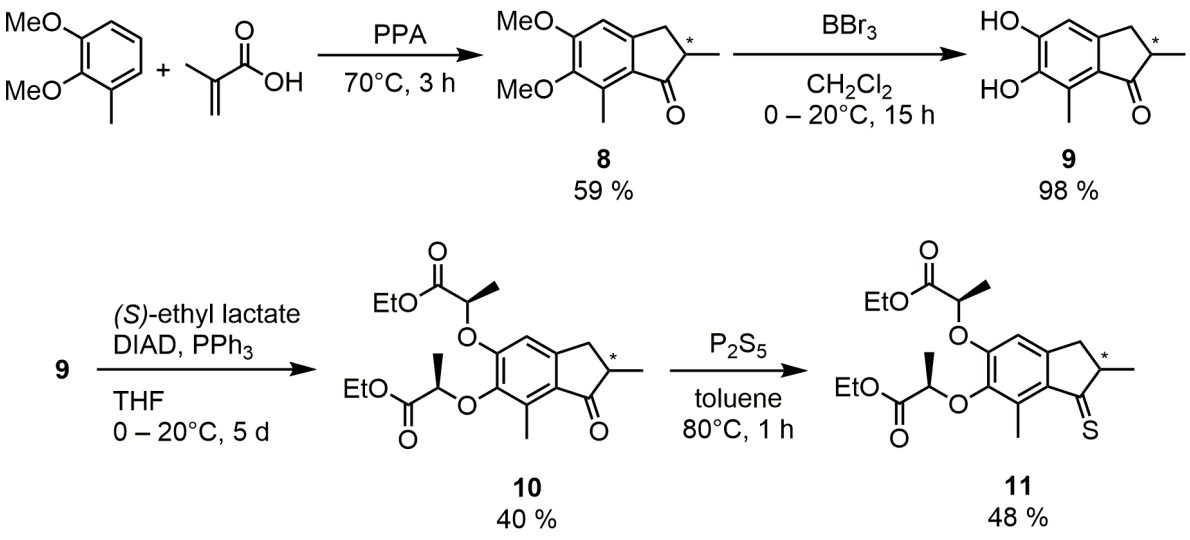

Scheme 3.3. Four-step synthesis of the diastereoisomeric indanethione rotor **11**.

yield. Thin layer chromatography does not show, at this stage, significant separation between the two diastereoisomers, which would still racemize considering the ceto-enolic equilibrium that may take place. The separation was therefore conducted later.

For the Barton-Kellogg coupling, the necessary thioketone derivative was obtained by reacting indanone **10** with phosphorus pentasulfide, affording 8 g of indanethione **11** in reasonable yield. Since the thioketone is sensitive to air, the sulfuration is performed just before the final coupling.

The functionalized indanethione was therefore obtained in four steps with an overall 11 % yield, which is explained by the low yields of both the initial cyclization and the Mitsunobu coupling. Nevertheless, the stator and rotor parts can be synthesized at the multigram scale to perform the Barton-Kellogg coupling.

3.3 Barton-Kellogg coupling and gram-scale synthesis of molecular motors

The Barton-Kellogg coupling is the most important step of the motor synthesis. It consists in two steps: the formation of an episulfide, and its subsequent reduction into the double bond, resulting in the formation of the molecular motors (Scheme 3.4). We chose this coupling rather than a McMurry condensation because it leads exclusively to the formation of asymmetric alkenes. Moreover, it is performed in moderate conditions, contrariwise to Wittig coupling. Moreover, the mechanism of the Barton-Kellogg coupling involves a gradual increase of the steric hindrance close to the double bond, which increases the selectivity of the reaction.

The thioxanthone hydrazone **7** was first converted to its diazo form by oxidation using manganese dioxide. The diazo compound is then filtered through a canula into a solution of thioketone **11** to form an unstable thiadiazoline ring that forms the episulfide bond after elimination of dinitrogen. This step must be performed in the dark under inert conditions to ensure the stability of the diazo compound.

Diastereoisomers can be separated at this step by simple column chromatography on silica gel, since the R_f is 0.7 for *(R,R,R)*-**12** and 0.65 for*(R,R,S)*-**12** in toluene : ethyl acetate, 6 : 1. It highlights

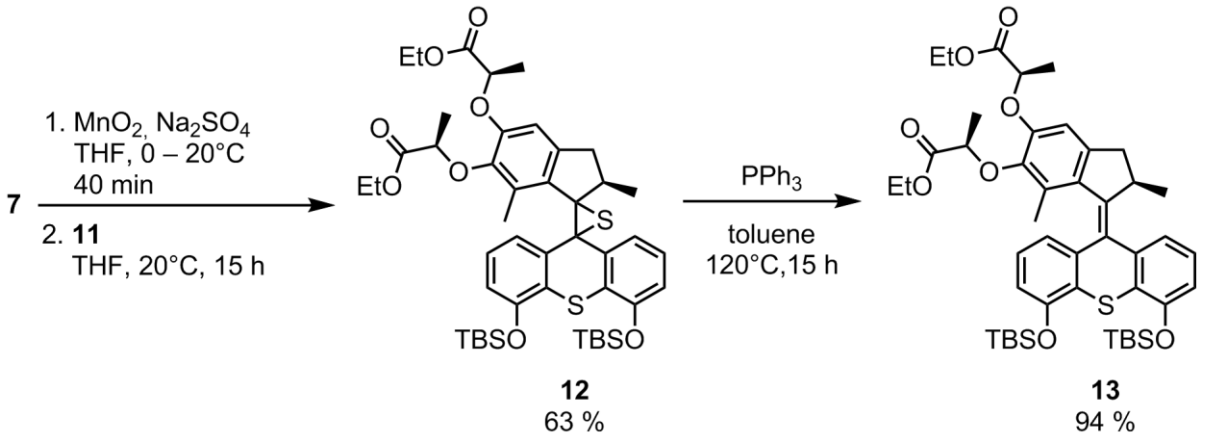

Scheme 3.4. Barton-Kellogg coupling between indanethione **11** and thioxanthone **7**. An intermediate episulfide **12** is obtained, which is then reduced to obtain molecular motor **13**. Diastereoisomers of compound **12** are separated by simple column chromatography on silica gel.

the advantage of having diastereoisomers over enantiomers; since optically pure motors are necessary to ensure that the crosslinks turn in only one direction, the separation of enantiomers would involve chiral column chromatography. In the case of diastereoisomers, however, standard column chromatography is sufficient for the separation, which is a cheaper technique and, hence, allows for multigram scale synthesis of motors without overly increasing the cost of this step. Two column chromatographies are performed; the first one allows to separate the diastereoisomers from other impurities while the second, with a slower gradient, results in the separation of the diastereoisomers. The separation affords 3.70 g of *(R,R,R)*-**12**, 4.02 g of *(R,R,S)*-**12** and 800 mg of mixture, in good yield. The *(R)* and *(S)* fractions were assigned by X-ray diffraction analysis of the corresponding crystals.[5]

Since episulfide derivatives are also used for control experiments, these derivatives are kept for storage. From our experience, they also proved to be more stable in this form than with the central double bond. The gram-scale synthesis was therefore performed until this step, and the reduction was performed at a lower scale. For instance, triphenylphosphine was added to compound *(S)*-**12** to afford 870 mg of *(S)*-motor **13** in very good yield.

Compared with our previously published work, the two halves were synthesized at a scale ten times higher and the episulfide three times larger than in our initial publication.[5] Compared to our report on the gram-scale synthesis of molecular motors, the stator was synthesized at a scale ten times larger and the rotor at one and a half time larger, while the episulfide was synthesized at a scale twice larger (Table 3.1).[6]

Table 3.1. Synthetic scale of some key-steps compounds used to synthesize molecular motors.

	Nat. Nanotechnol. **2015**	*Tetrahedron* **2017**	This thesis
Thioxanthone hydrazone **7**	1.17 g	1.37 g	13 g
Indanethione **11**	0.683 g	5.46 g	8 g
Episulfide **12**	1.26 g	1.82 g	3.70 g

Overall, the motor was obtained with an overall yield of 6.5 % over thirteen steps. They were then functionalized with different moieties depending on the structure of the targeted materials. The different derivatives obtained after functionalization are presented in the next section.

3.4 Functionalization of molecular motors for their integration in photoactive systems

The first step for the functionalization of the molecular motors concerns the deprotection of the stator. Several protecting groups were previously studied; in addition to TBS, methoxy and benzyl groups were investigated as protecting groups for the phenols. In the case of methoxy-protected stator, no deprotection was observed in conditions where the esters of the rotor were not cleaved. When benzyl groups were used, on the other hand, the separation of the diastereoisomers was more

complicated than when TBS groups were used. Consequently, it was concluded that protection of the phenols of the stator with TBS was the best choice for our molecular motors.[6]

When used as crosslinks in polymer networks, we chose to modify our original molecular motors by grafting four identical functional groups. In the first design of our first polymer gels, they were functionalized with two polymer chains with azide groups on the rotor, and two tri(ethylene glycol) (TEG) spacers with alkyne groups on the stator.[5] This architecture led to the formation of eight-shaped molecules in dilute conditions and polymer gels in concentrated conditions, both showing a reduction of their size when irradiated with UV light.[5] The main constraint of this synthetic pathway, however, is that it required the use of heterotelechelic polymer chains bearing two different end groups to functionalize the stator. Such structures are, first, usually expensive and, second, not commercially available for any polymer architecture. Moreover, the purification of the motor derivatives bearing the polymer chains involved column chromatography using reverse phase silica gel, and this method may not be as efficient for other polymer chains.

The advantage of using molecular motors with four identical functional groups is that they can be coupled with homotelechelic polymer chains, having two identical end groups. Such architectures are either already commercially available, or they can be readily synthesized, considering the amount of literature available on end-functionalized polymers (Chapter 2). The main challenge resides in the end-group functionalization of these polymers and will be one of the focus of this thesis.

The synthesis of homotetrafunctional motors involves first the synthesis of functional TEG spacers. Functionalization of the phenols of the stator necessitates that one of the TEG end group is easily substituted while functionalization of the rotor is done with an amine terminated TEG to obtain the corresponding amide bond, which is stronger than an ester one towards hydrolysis. Moreover, the spacers should bear either an azide or an alkyne group at the other end group for the crosslinking step by copper-catalyzed Huisgen 1,3-dipolar cycloaddition.

The TEG spacers functionalized with azide end groups were obtained in three steps (Scheme 3.5). The first step is the activation both alcohols by substitution with tosyl chloride, to afford 23.2 g of

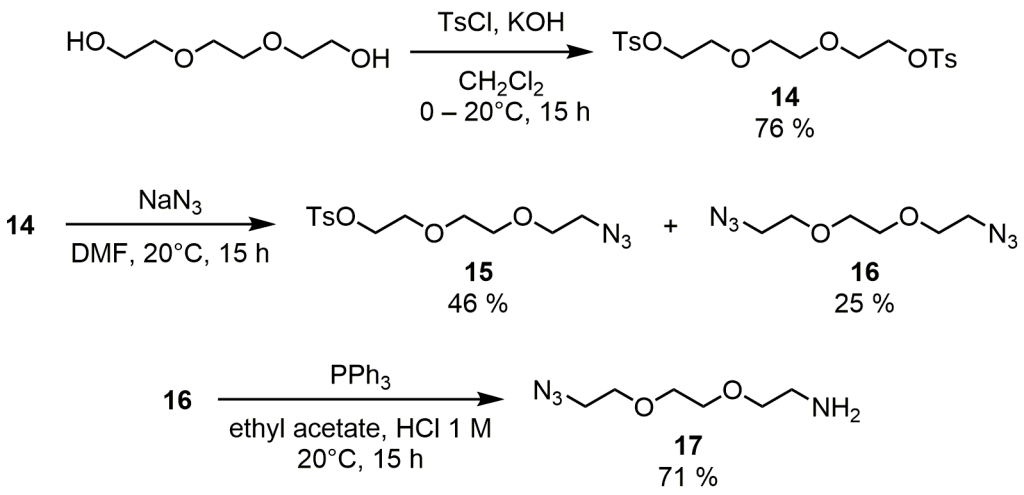

Scheme 3.5. Synthesis of TEG spacers bearing azide groups. The tosyl derivative **15** is used to functionalize the stator and the amine derivative **17** is used to functionalize the rotor.

α,ω-tosyl-TEG **14** in good yield. The subsequent substitution with sodium azide leads to the statistical functionalization of the terminal tosyl groups, to afford 4.9 g of α-tosyl-ω-azido-TEG **15** (46 % yield) and 1.66 g of α,ω-azido-TEG **16** (25 % yield). Derivative **15** can be used directly for the functionalization of the stator, and triphenylphosphine was added to coumpound **16** to reduce one of the azide by Staudinger reaction, leading to 1.24 g of α-azido-ω-amino-TEG **17**, in good yield, that can be used to functionalize the rotor.

Synthesis of the TEG spacers functionalized with alkyne end groups occurs according to a similar pathway (Scheme 3.6). First, one of the alcohols is functionalized by substitution with propargyl bromide to afford 4.6 g of α-hydroxy-ω-alkyne-TEG **18** (91 % yield with respect to propargyl bromide). The remaining alcohol is substituted with tosyl chloride to afford 5.0 g of α-tosyl-ω-alkyne-TEG **19** in an almost quantitative yield. This derivative can be directly used to functionalize the stator. For the functionalization of the rotor, however, it must be then substituted with sodium azide to afford 1.8 g of α-azido-ω-alkyne-TEG **20** with a quantitative yield. Finally, the azide is reduced by Staudinger reaction with triphenylphosphine to afford 0.72 g of α-amino-ω-alkyne-TEG **21** in good yield, which can be used to functionalize the rotor.

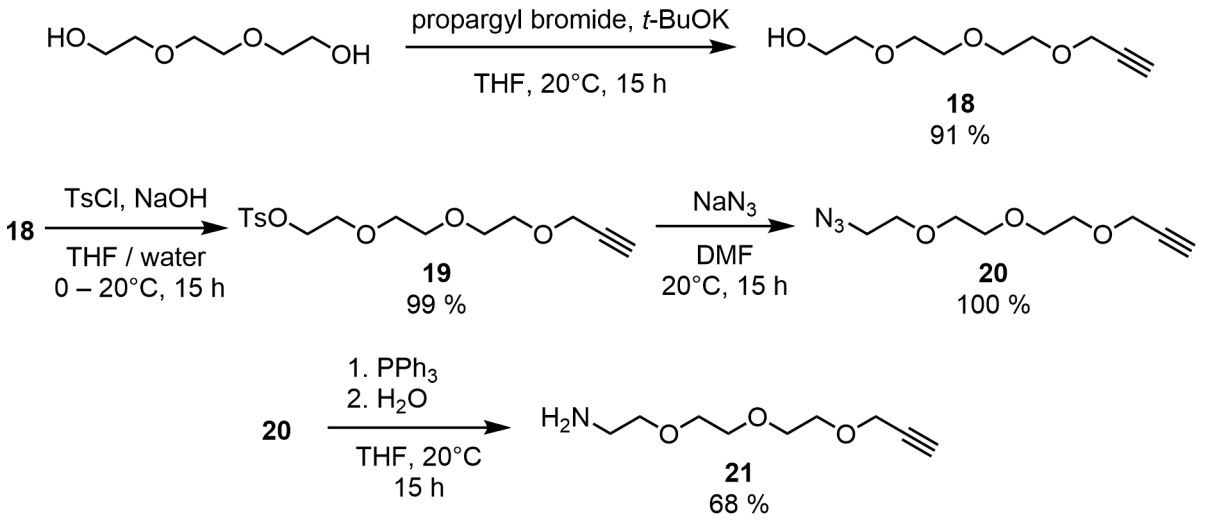

Scheme 3.6. Synthesis of TEG spacers bearing alkyne groups. The tosyl derivative **19** is used to functionalize the stator and the amine derivative **21** is used to functionalize the rotor.

The synthesis of the tetra-azido or tetra-alkyne molecular motors are similar, the only difference lies in the TEG spacers used for their functionalization. For both cases, the first step consists in the deprotection of the phenols on the stator with tetrabutylammonium fluoride (TBAF) to afford 1.42 g of ethyl-protected bisphenol motor *(S)*-**22** in excellent yield (Scheme 3.7).

For the tetra-azide derivative, the subsequent step concerns the functionalization of the stator by substitution with the α-tosyl-ω-azido-TEG **15**, affording 251.5 mg of ethyl-protected bis-azido motor *(S)*-**23** in very good yield (Scheme 3.7). Then, saponification of the ethyl esters leads to 189 mg of bis-acid bis-azide motor *(S)*-**24** in very good yield. Finally, the desired compound is obtained by grafting α-azido-ω-amino-TEG **17** to the carboxylic acids by amide coupling with 1-ethyl-3-(3-dimethylaminopropyl)carbodiimide hydrochloride (EDC·HCl) and hydroxybenzotriazole (HOBt), affording 220 mg of tetra-azide motor *(S)*-**25** in very good yield.

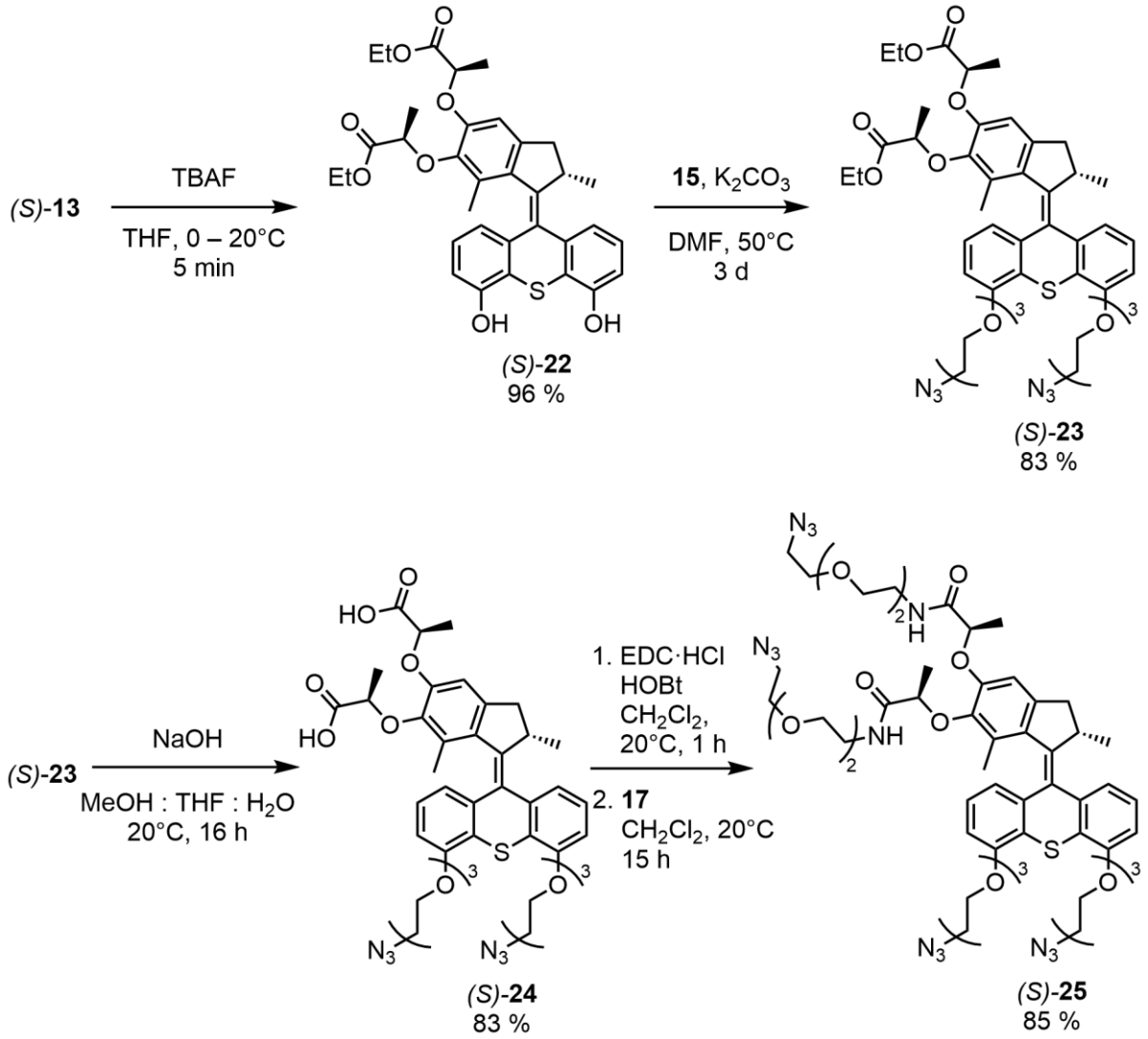

Scheme 3.7. Four-step synthesis of tetra-azide motor *(S)*-**25** from fully protected motor *(S)*-**13**.

For the tetra-alkyne derivative, on the other hand, functionalization of the stator of motor *(S)*-**22** with α-tosyl-ω-alkyne-TEG **19** affords 194 mg of ethyl-protected bis-alkyne motor *(S)*-**26** in very good yield (Scheme 3.8). Similarly to the tetra-azide motor, saponification of the esters afforded 435 mg of bis-acid bis-alkyne motor *(S)*-**27** in good yield. Finally, amide coupling with α-amino-ω-alkyne-TEG **21**, EDC·HCl and HOBt afforded 150 mg of tetra-alkyne motor *(S)*-**28** in good yield.

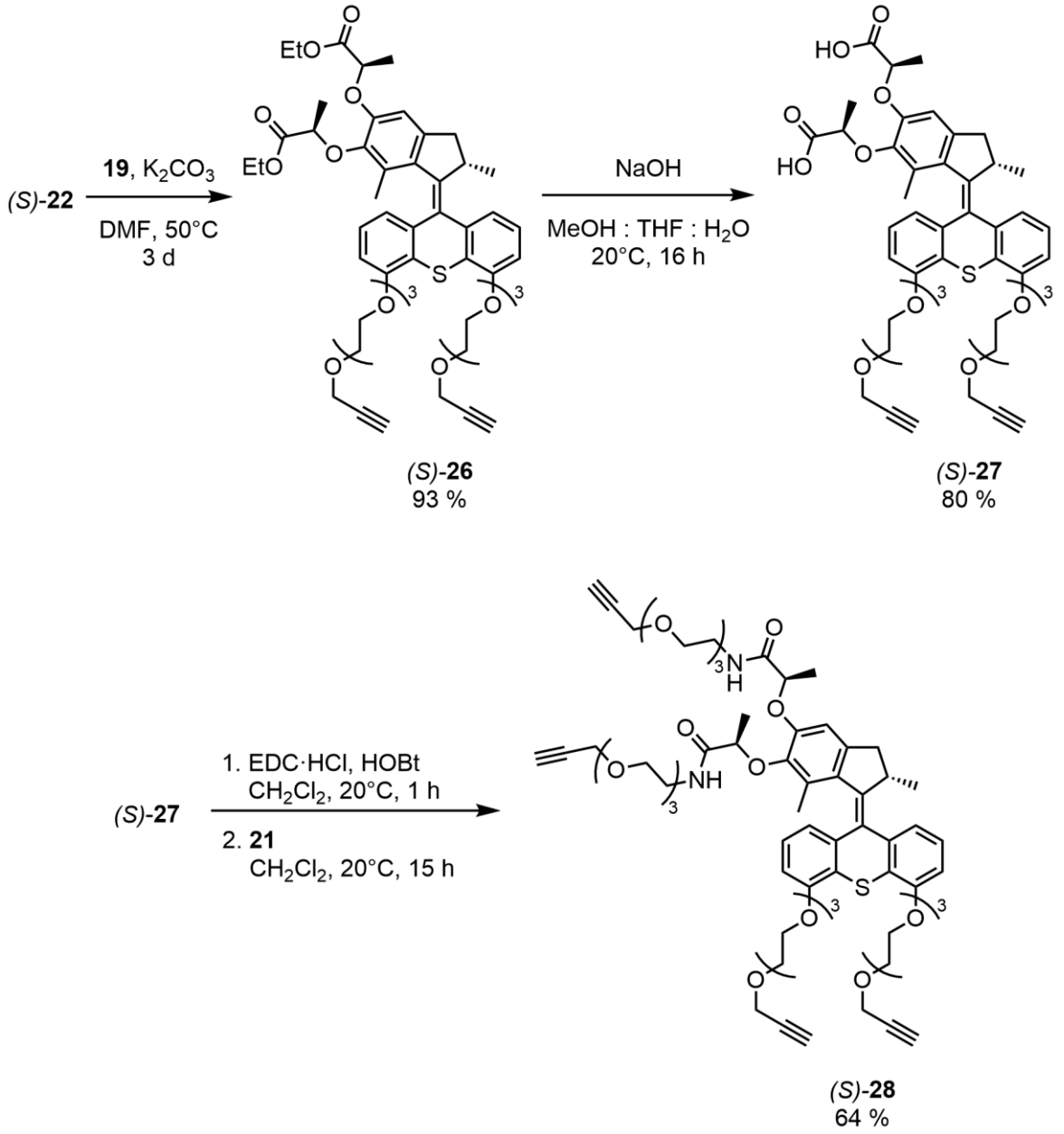

Scheme 3.8. Three-step synthesis of tetra-alkyne motor *(S)*-**28** from ethyl-protected bisphenol motor *(S)*-**22**.

Two other molecular motors derivatives were synthesized. The first one was a tetra-acrylate molecular motor to be used as a crosslinker in liquid crystalline elastomers (Chapter 6), and the second one was a tetra-amine one to be used as an initiator for the ring opening polymerization of γ-benzyl-L-glutamate N-carboxyanhydride (Chapter 5, section 5.5).

Synthesis of the tetra-acrylate molecular motor involved first the preparation of another spacer bearing an acrylate group. For simplicity, in that case, the same spacer is used for the four functionalizations. Consequently, 6-aminohexyl acrylate **30** was synthesized. Starting from 6-amino-1-hexanol, the first step consisted in protecting the terminal amine with a *tert*-butoxycarbonyl (Boc) group. The terminal alcohol was then directly functionalized by acylation with acryloyl chloride, affording 1.4 g of 6-((*tert*-butoxycarbonyl)amino)hexyl acrylate **29** in good yield. The protected amine was then deprotected with HCl in diethyl ether, affording 0.81 g of 6-aminohexyl acrylate hydrochloride **30** in good yield (Scheme 3.9).

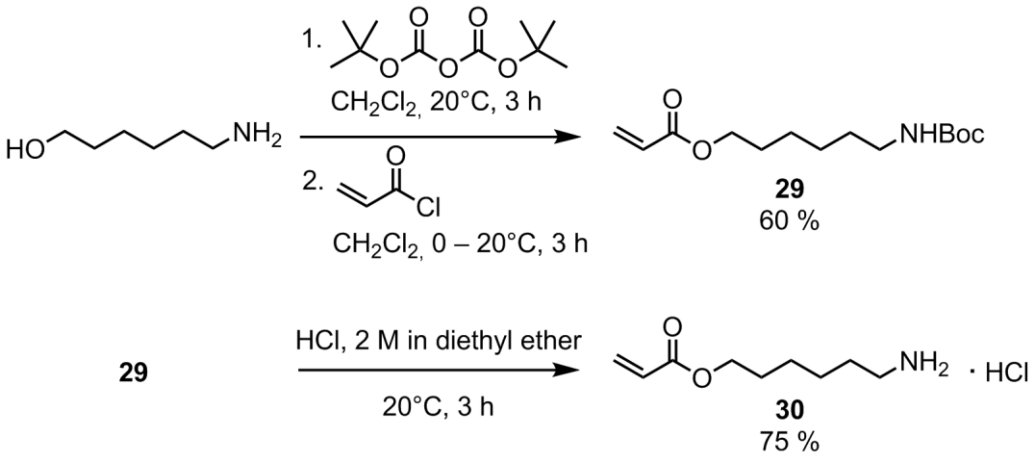

Scheme 3.9. Synthesis of 6-aminohexyl acrylate **30** as a spacer for the functionalization of molecular motors.

In order to obtain the tetra-acrylate derivative, a tetra-acid motor was prepared to simultaneously functionalize the four sites of the molecule. Substitution of the phenols of *(R)*-**22** with *tert*-butyl bromoacetate afforded the tetra-ester *(R)*-motor **31** in very good yield. Saponification of all four ethyl esters with sodium hydroxide provided tetra-acid *(R)*-motor **32** in quantitative yield. Tetra-acrylate motor **33** was then obtained in the 100 mg scale in reasonable yield after amide coupling with spacer **30** in the presence of EDC·HCl and HOBt (Scheme 3.10).

The tetra-amine motor was obtained from commercially available spacers from the bis-phenol bis-ester motor *(R)*-**22**. First, functionalization of the stator was performed by nucleophilic substitution with 3-(Boc-amino)propyl bromide to obtain bis-ester bis-*N*-Boc motor *(R)*-**34** in quantitative yield. The esters of the rotor were then saponified with sodium hydroxide to afford bis-acid bis-NHBoc motor *(R)*-**35** in quantitative yield as well. The rotor was then functionalized by amide coupling with *N*-Boc-ethylenediamine to obtain tetra-*N*-Boc motor *(R)*-**36** in good yield. Finally, all amine groups were deprotected with trifluoroacetic acid (TFA) to obtain the final tetra-amine motor *(R)*-**37**, in quantitative yield (Scheme 3.11).

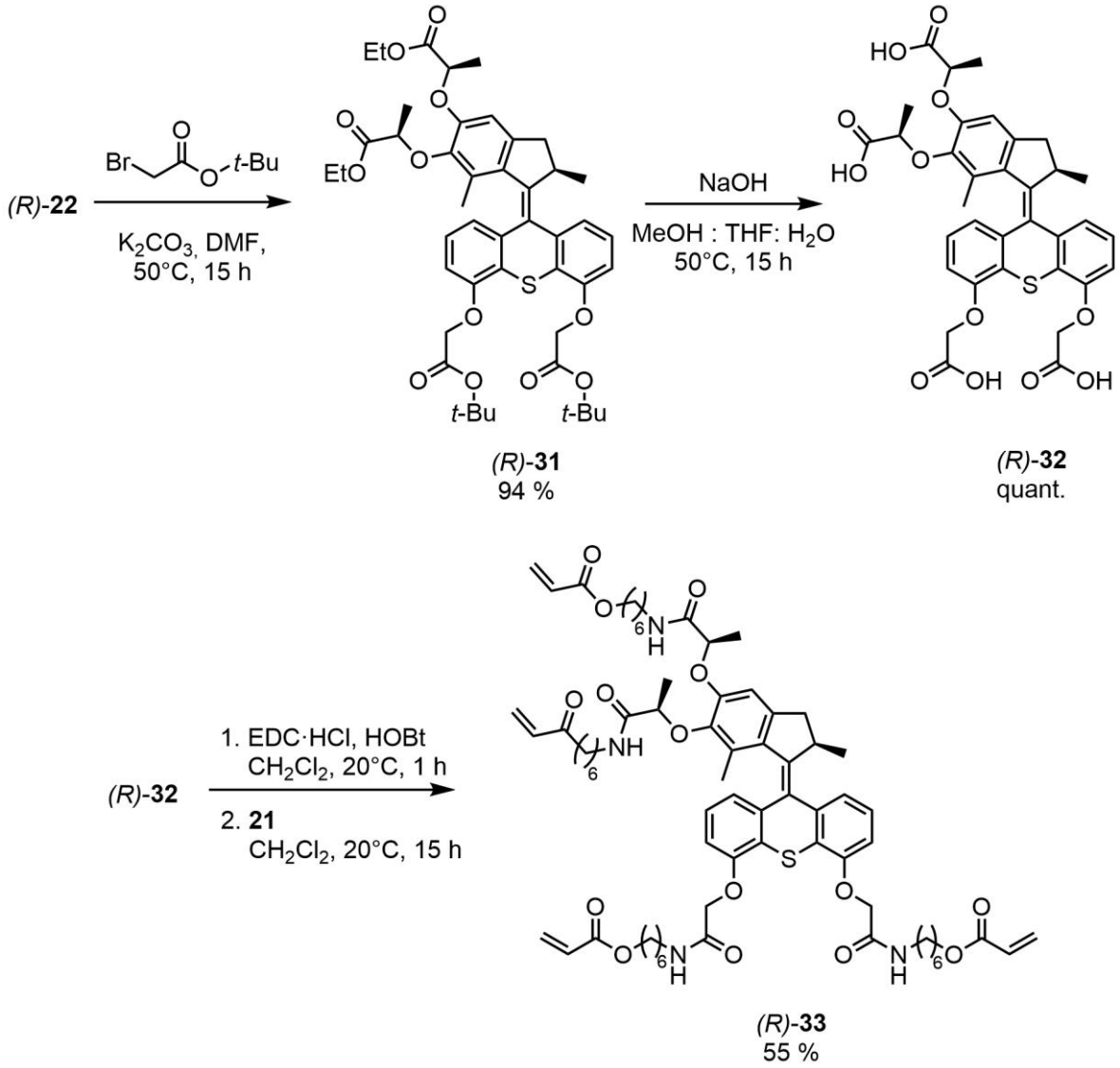

Scheme 3.10. Synthesis of tetra-acrylate motor *(R)*-**33** for its incorporation in liquid crystalline elastomers.

The synthesis of functional molecular motors for their integration in materials involves many steps and the preparation of several spacers. Nevertheless, the synthesis of the motor core was optimized to the point that it is efficient at the multigram scale. Even though the large-scale synthesis of the final derivatives was not explored here, the yields of the reactions involved are reasonably high and, hence, even these molecules could be prepared at the gram scale for the preparation of materials. In the scope of this thesis, the synthetic scale achieved, in the order of hundreds of milligrams, was still largely sufficient for a systematic study of our polymer networks that are discussed in the following chapters.

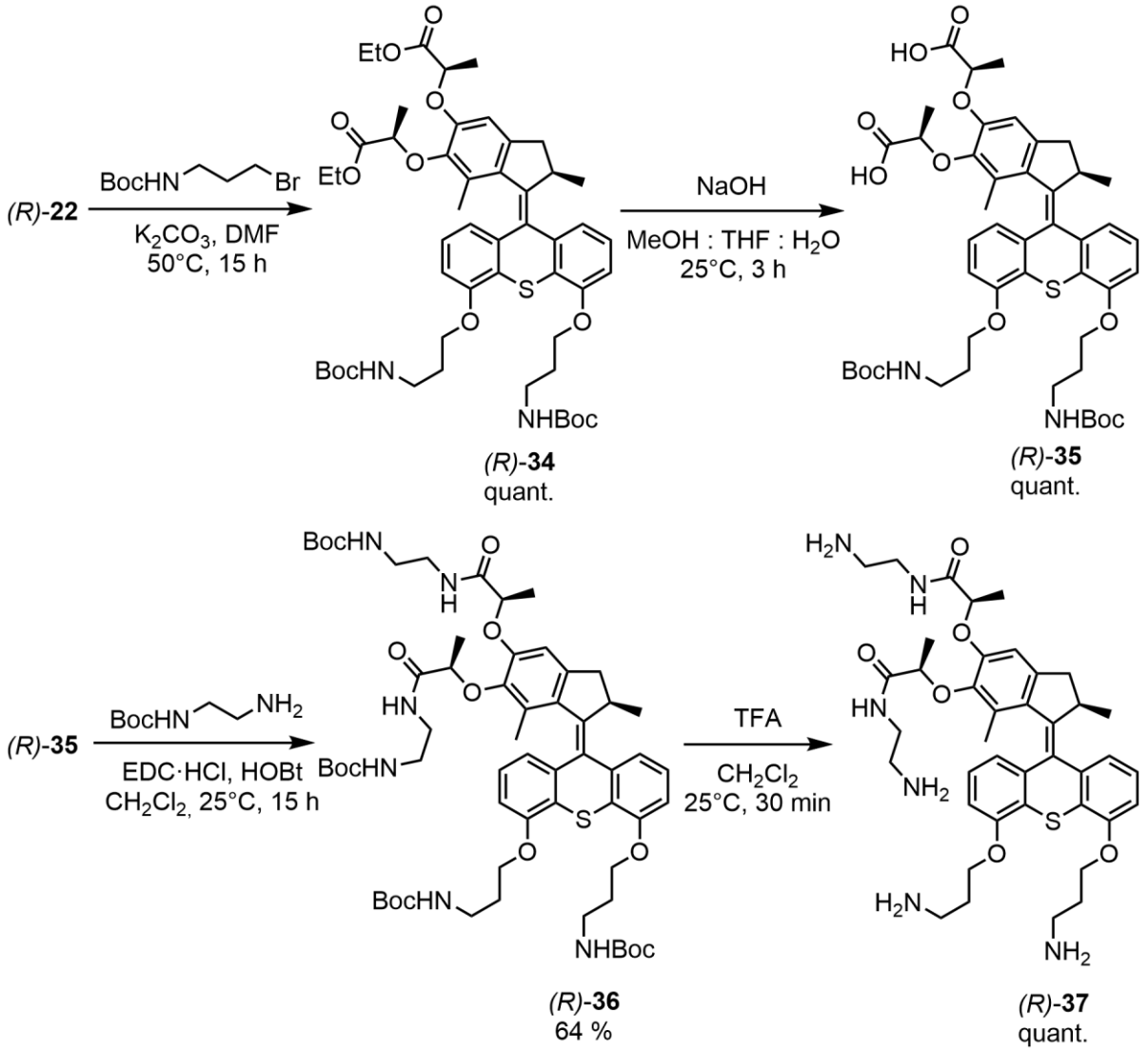

Scheme 3.11. Synthesis of tetra-amine motor *(R)*-**37**, which is used as an initiator for ring-opening polymerization.

References

1. M. Shibayama, X. Li, T. Sakai, *Colloid Polym. Sci.* **2019**, *297*, 1–12.
2. M. Klok, N. Boyle, M. T. Pryce, A. Meetsma, W. R. Browne, B. L. Feringa, *J. Am. Chem. Soc.* **2008**, *130*, 10484–10485.
3. M. M. Pollard, M. K. J. ter Wiel, R. A. van Delden, J. Vicario, N. Koumura, C. R. van den Brom, A. Meetsma, B. L. Feringa, *Chem. Eur. J.* **2008**, *14*, 11610–11622.
4. G. London, G. T. Carroll, T. Fernández Landaluce, M. M. Pollard, P. Rudolf, B. L. Feringa, *Chem. Commun.* **2009**, *13*, 1712–1714.
5. Q. Li, G. Fuks, E. Moulin, M. Maaloum, M. Rawiso, I. Kulic, J. T. Foy, N. Giuseppone, *Nat. Nanotechnol.* **2015**, *10*, 161–165.
6. Q. Li, J. T. Foy, J.-R. Colard-Itté, A. Goujon, D. Dattler, G. Fuks, E. Moulin, N. Giuseppone, *Tetrahedron* **2017**, *73*, 4874–4882.

Chapter 4
End-functionalization of poly(ethylene glycol) and optimization of the corresponding gels crosslinked with molecular motors

I thank Prof. Buhler for its valuable help on the structural characterization of the gels and on the interpretation of the data.

Our first reported gels were formed after crosslinking molecular motors functionalized with two poly(ethylene glycol) (PEG) chains (Chapter 1).[1] As already explained throughout the previous chapters, we desired to change this synthetic pathway by using tetrafunctional motors and homotelechelic polymer chains instead. Tetrafunctional motors can be used to form different materials with compatible functional polymers and their synthesis was described in the previous chapter. Moreover, homotelechelic polymers are usually more accessible, either commercially or synthetically. The present chapter describes first the synthesis of end-functionalized linear PEG chains will be described, along with their characterization. In the second section, determination of the overlap concentration of the chains and formation of the gels at this concentration will be presented. Finally, the third section will detail the influence of several parameters on the contractile behavior of the gels.

4.1 Synthesis and characterization of telechelic poly(ethylene glycol)

The formation of PEG-based gels crosslinked with molecular motors requires homotelechelic linear polymers. The reticulation is performed by copper(I)-catalyzed azide-alkyne cycloaddition (CuAAC); therefore, PEG chains must either have azide or alkyne end-groups to be crosslinked with the complementary tetrafunctional molecular motors. Both polymers can be found commercially for different molecular weights but are often expensive —for instance, 1 g of α,ω-diazido-PEG with an average molecular weight $\overline{M_n}$ = 20,000 g·mol^{-1} costs 249 € with Sigma-Aldrich.[2] Moreover, we had access to α,ω-dihydroxy-PEG from Clariant and, hence, performed the end-functionalization with on starting material.

4.1.1 End-functionalization of α,ω-dihydroxy-poly(ethylene glycol)

The synthesis of either alkyne-terminated or azide-terminated PEG requires two different strategies. An accessible reactant for the preparation of the former is propargyl bromide and, therefore, it was necessary to increase the nucleophilicity of the terminal alcohols by forming the corresponding alcoholates for the substitution. On the other hand, sodium azide is commonly used for the preparation of organic azides; in this case, it is necessary to activate the alcohols as leaving groups, which was achieved by either tosylation or mesylation (Scheme 4.1).

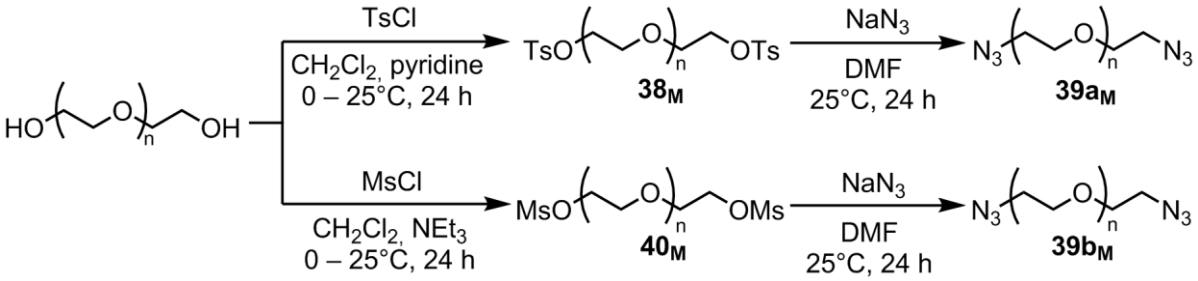

Scheme 4.1. Synthesis of α,ω-diazido-PEG **39**$_M$ of different molar masses M *via* either tosylation or mesylation.

We started by investigating the preparation of α,ω-diazido-PEG. The first envisioned synthetic pathway was the activation of the alcohol as leaving group with 4-toluenesulfonyl chloride (tosyl chloride, TsCl). When α,ω-dihydroxy-PEG was mixed with tosyl chloride in the presence of pyridine, formation of α,ω-ditosylate-PEG **38**$_M$ occurred (where M represents the molecular weight of the polymer). Subsequent substitution of the tosylates by sodium azide gave α,ω-diazido-PEG **39a**$_M$, where subscript '**a**' differentiates between the α,ω-diazido-PEG obtained *via* tosylation and the one obtained *via* mesylation (**39b**$_M$).

The efficiency of the functionalization was evaluated by calculating the degree of functionalization *f* of the polymers, which is the ratio between the end-groups bearing the function of interest and the total number of end-groups. NMR spectrometry was used to determine *f* by comparing the relative intensities of the methylenic protons in α-position of the end-group, as discussed further in the next section.

Table 4.1. Degrees of functionalization *f* of telechelic PEG for various molecular weights at different stages of their functionalization.

Molecular weight (g·mol^{-1})	f_{OTs} (%)	f_{N3} (%)	f_{OMs} (%)	f_{N3} (%)
1500	96	96	quant.	quant.
3000	96	96	quant.	quant.
4000	27	Ø	quant.	quant.
6000	Ø	Ø	quant.	quant.
10000	Ø	Ø	quant.	quant.
20000	Ø	Ø	quant.	quant.

Activation of the end-alcohols by tosylation did not work for all molecular weight. While it was almost complete for shorter chain lengths ($\mathbf{38}_{1500}$ and $\mathbf{38}_{3000}$), *f* drastically drops for $\mathbf{38}_{4000}$ and only reaches 27 %. The lower *f* obtained for $\mathbf{38}_{4000}$ might be explained by the decreased reactivity of the hydroxyl end-groups towards substitution with increasing molar mass. Therefore, azidation of the chain ends was only performed on $\mathbf{38}_{1500}$ and $\mathbf{38}_{3000}$ to observe if the substitution of the tosylates was quantitative. The functionalization was complete, and *f* had the same value between α,ω-diazido-PEG and their α,ω-ditosylate-PEG precursors (Table 4.1).

Considering that tosylation did not work for all molar masses, mesylation was considered instead. Since methanesulfonyl chloride (mesyl chloride, MsCl) is smaller than tosyl chloride, we considered that it could be able to access more easily the hydroxyl end-groups, even for chains of high masses. When α,ω-dihydroxy-PEG was mixed with mesyl chloride for the substitution of the end-groups, we indeed observed quantitative functionalization for all PEG tested, having molecular weights ranging from 1 500 g·mol^{-1} to 20 000 g·mol^{-1}. As for α,ω-ditosylate-PEG, substitution of the end-groups of α,ω-dimesylate-PEG $\mathbf{40}_{\mathbf{M}}$ with sodium azide was also quantitative to give fully functional α,ω-diazido-PEG $\mathbf{39b}_{\mathbf{M}}$ of varying molecular weights (Table 4.1).

The synthesis of α,ω-dipropargyl-PEG was conducted with an intermediate deprotonation of the terminal hydroxyl groups. The formation of alcoholates can be achieved in the presence of strong bases, such as diphenylmethylpotassium (DPMK) and sodium hydride (NaH).

First, it was necessary to prepare a solution of DPMK. Naphthalene and metallic potassium were initially mixed in dry THF to form the corresponding radical anion, and addition of diphenylmethane led to the formation of DPMK, which was obtained in very good yield, as determined by titration. Addition of this solution to α,ω-dihydroxy-PEG of various molar masses led to the formation of the alcoholates at the extremities of the chains and the reaction was followed by colorimetry. Substitution with propargyl bromide gave α,ω-dipropargyl-PEG $\mathbf{42a}_{\mathbf{M}}$ with *f* = 100 % for all molar masses M that

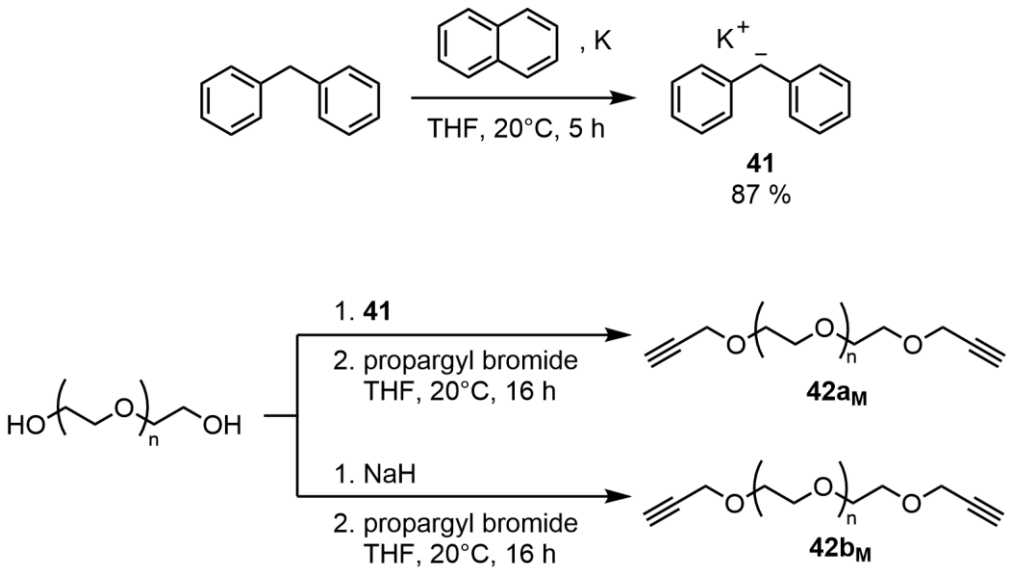

Scheme 4.2. Synthesis of α,ω-dipropargyl-PEG $\mathbf{42}_{\mathbf{M}}$ of different molar masses M *via* deprotonation of the terminal alcohols by either DPMK **41** or NaH.

were tested, according to ^{1}H NMR analysis (see section 4.1.2). The main advantage of this synthetic pathway is that the formation of the alcoholates can be followed by colorimetry, since DPMK has a deep red color. However, its synthesis involves the use of metallic potassium, which requires careful handling.

Sodium hydride is a safer alternative to DPMK for the formation of the alcoholates. Here, the deprotonation can be followed by the evolution of gas bubbles upon addition of the hydride to the solution of α,ω-dihydroxy-PEG. After completion of this step, substitution with propargyl bromide formed α,ω-dipropargyl-PEG **42b$_M$** with, again, full end-group functionalization for all molar masses, according to the ^{1}H NMR spectra.

The preparation of either azide- or alkyne-terminated PEG from commercially available precursors is straightforward. Considering the different pathways that were tested, we decided to preferentially synthesize α,ω-dipropargyl-PEG **42b$_M$** for further studies, as NaH is safer to use than DPMK and because the functionalization worked for a wide array of molar masses, from 1 500 to 20 000 g·mol^{-1}. All these polymers were carefully characterized and, specifically, ^{1}H NMR analysis was critical to determine the efficiency of the functionalization, as described in the next section.

4.1.2 Characterization of end-functionalized PEG

The formation of gels crosslinked with tetrafunctional molecular motors requires, in our design, fully functionalized homotelechelic linear PEG. It was therefore necessary to assess that, first, our synthetic pathway led to full conversion of the chain ends and, second, that the conditions did not degrade the polymer chains. The distribution was probed by gel permeation chromatography (GPC) and the end-groups functionalization was assessed by ^{1}H NMR spectrometry and MALDI-TOF analysis.

GPC analysis was conducted for the initial α,ω-dihydroxy-PEG and for the final end-functionalized polymers (Appendix B). Different molar masses were used: 1 500, 3 000, 4 000, 6 000, 10 000 and 20 000 g·mol^{-1}. Commercial PEG samples all had small dispersities, the maximum being 1.10 for PEG_{3000}; analysis of PEG_{20000} showed, however, the presence of a peak of high molecular weight, probably caused by the presence of small aggregates that are not fully dissolved, which alter the distribution of the peak of interest. After functionalization, the final polymers essentially had the same distribution, showing that the synthesis did not alter the chains. Interestingly, in the case of **42b$_M$**, many GPC chromatograms showed the presence of species with high molar masses. This may be explained by the presence of hydrophobic propargyl end groups, which favor the formation of aggregates.[3,4]

^{1}H NMR spectrometry was essential to determine the efficiency of the different functionalization steps. PEG with different end groups have distinct peaks when analyzed in toluene-*d8* (Figure 4.1). The NMR spectrum of α,ω-dihydroxy-PEG shows a triplet at 3.59 ppm corresponding to the methylenic protons in α-position of the hydroxyl end groups and integrates for four protons. This signal shifts to 3.92 ppm after tosylation (**38**), 3.97 ppm after mesylation (**40**) and 3.24 ppm after azidation (**39**). In the case of **42**, a characteristic doublet at 3.93 ppm was observed, corresponding to the four methylenic protons of the two propargyl end groups. Moreover, in the case of **38** and **40**,

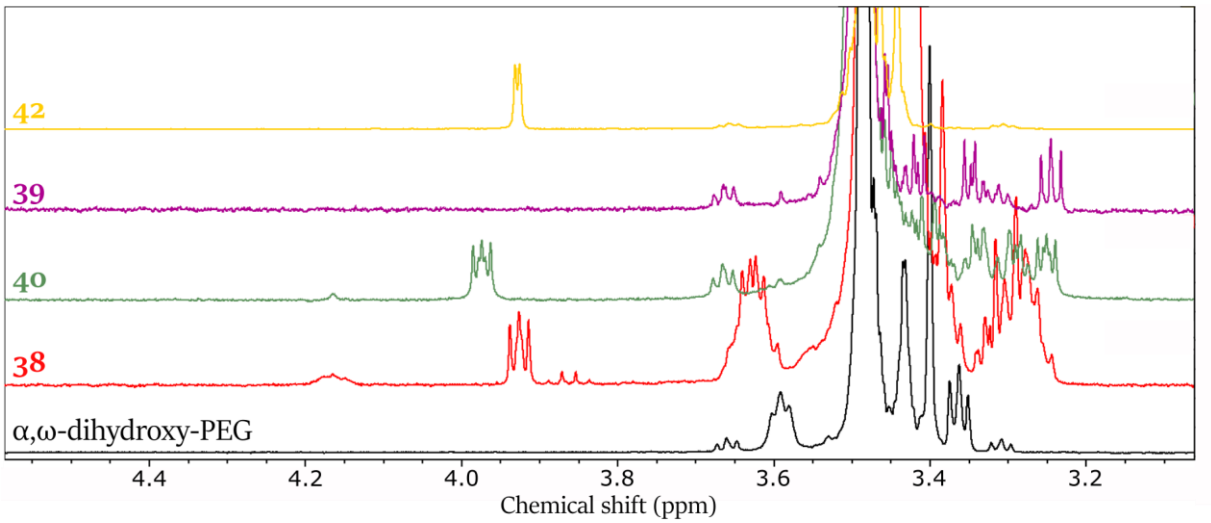

Figure 4.1. ^{1}H NMR spectra in toluene-*d8* in the range 4.5 – 3.1 ppm of different end-functionalized PEG. The relative integration of characteristic signals signals was used to determine *f*.

other peaks corresponding to either the tosyl or mesyl groups, respectively, were observed (see Appendix A for the full attribution of signals). The degree of functionalization *f* can be determined by measuring the ratio of the normalized integration I of one characteristic peak over the sum of the normalized integrations of the same characteristic peak and the peak of the protons in α-position of the hydroxyl end groups in α,ω-dihydroxy-PEG:

$$f = \frac{\text{I(characteristic peak)}}{\text{I(characteristic peak)} + \text{I(3.59 ppm)}} \times 100 \qquad (4.1)$$

This equation gave values reported in the previous section. When no significant peak was observed at 3.59 ppm, the functionalization was considered as quantitative.

MALDI-TOF analysis is also a powerful tool to determine the end-groups of polymers.[5] The mass of the peaks obtained by this technique corresponds to:

$$\frac{m([M+X]^{z+})}{z} = \frac{n \times m_{mono} + m_{end} + m_X}{z} \qquad (4.2)$$

with M is the polymer, X^{z+} is a cationic species with charge z, n the degree of polymerization, m_{mono} the exact mass of the monomer, m_{end} the exact mass of the end group and m_X the atomic mass of X. In our case, m_{mono} equals to 44.03 g·mol^{-1} and m_{end} equals to 18.01, 112.05 and 94.04 g·mol^{-1} for α,ω-dihydroxy-PEG, α,ω-diazido-PEG **39** and α,ω-dipropargyl-PEG **42**, respectively. Moreover, X^{z+} was either Na^+ (m_{Na} = 22.99 g·mol^{-1}), K^+ (m_K = 38.96 g·mol^{-1}) or Li^+ (m_{Li} = 7.02 g·mol^{-1}). Considering these values, the data obtained by MALDI-TOF analysis of the end-functionalized polymers are in good agreement with the theoretical values (Appendix B). The limitation of this technique, however, is that it did not give clear spectra for polymers of high molecular weights and, hence, may require optimization for the ionization process of large PEG molecules. Nevertheless, considering the data obtained from ^{1}H NMR experiments, we considered the functionalization as complete even if MALDI-TOF spectra did not provide additional proof for the polymers with high molecular weights.

Characterization of the end-functionalized PEG proved that the synthetic pathways that we designed gave polymers with fully substituted end groups, and without degradation of the polymer chain itself. As stated in the previous section, we decided to focus on propargyl-terminated polymers

because their synthesis works efficiently for a wide array of molar masses. Therefore, the following sections reports studies on a series of **42b$_M$** with different molar masses M, namely 3 000, 6 000, 10 000 and 20 000 g·mol^{-1}.

4.2 Determination of the overlap concentration c* and formation of the gels

The overlap concentration c* represents the critical concentration between the dilute and semi-dilute regimes of polymer solutions (Chapter 2, section 2.1.2). As stated in Chapter 1, previous studies in our group highlighted the importance to form gels at this concentration;[6,7] indeed, at this concentration, polymer coils just start to be in contact with each other, thereby ensuring a proper reticulation while limiting the formation of entanglements in the initial state.

Consequently, prior to the formation of our materials by CuAAC, it was necessary to determine c* for the end-functionalized PEG that were prepared, which was achieved by viscometry analysis of the polymer solutions. The polymer gels could then be formed in optimal conditions.

4.2.1 Measurement of c of end-functionalized PEG by viscometry*

As discussed in detail in Chapter 2, the intrinsic viscosity [η] of polymer solutions can be correlated to their c*. The determination of [η] was performed, in our case, by extrapolating the reduced viscosity η_{red} to zero concentration, following Huggins' model. The reduced viscosity was measured with an Oswald capillary, following the formula:

$$\eta_{red} = \frac{1}{c} \times \left(\frac{\rho t}{\rho_o t_o} - 1 \right) \quad (4.3)$$

with c the concentration of the solution (mg·mL^{-1}), ρ the density of the solution, t the flow time of the solution measured with the capillary, ρ_o the density of the solvent, and t_o the flow time of the solvent.

Since we perform the crosslinking step in DMF, viscometry measurements were performed in this same solvent for **42$_{3000}$**, **42$_{6000}$**, **42$_{10000}$** and **42$_{20000}$** (Figure 4.2). For all polymers, a linear fit of the reduced viscosities as a function of concentration corresponds well for low concentrations. However, for higher mass concentrations, η_{red} deviates from linearity and increases more; this evolution is a known limitation of the Huggins' model. Nevertheless, extrapolation to zero concentration provided [η] for the four polymers in DMF (Table 4.2).

Table 4.2. Determination of [η] for a series of **42** and the corresponding overlap concentrations c* in DMF.

Polymer	**42$_{3000}$**	**42$_{6000}$**	**42$_{10000}$**	**42$_{20000}$**
[η] (mL·mg^{-1})	0.0113	0.0148	0.0171	0.0306
c*(mg·mL^{-1})	77	59	51	28

The overlap concentration c* scales with [η]$^{-1}$ (Chapter 2, section 2.1.2) but the exact coefficient can vary depending on the polymer/solvent system. In our case, we previously measured the overlap

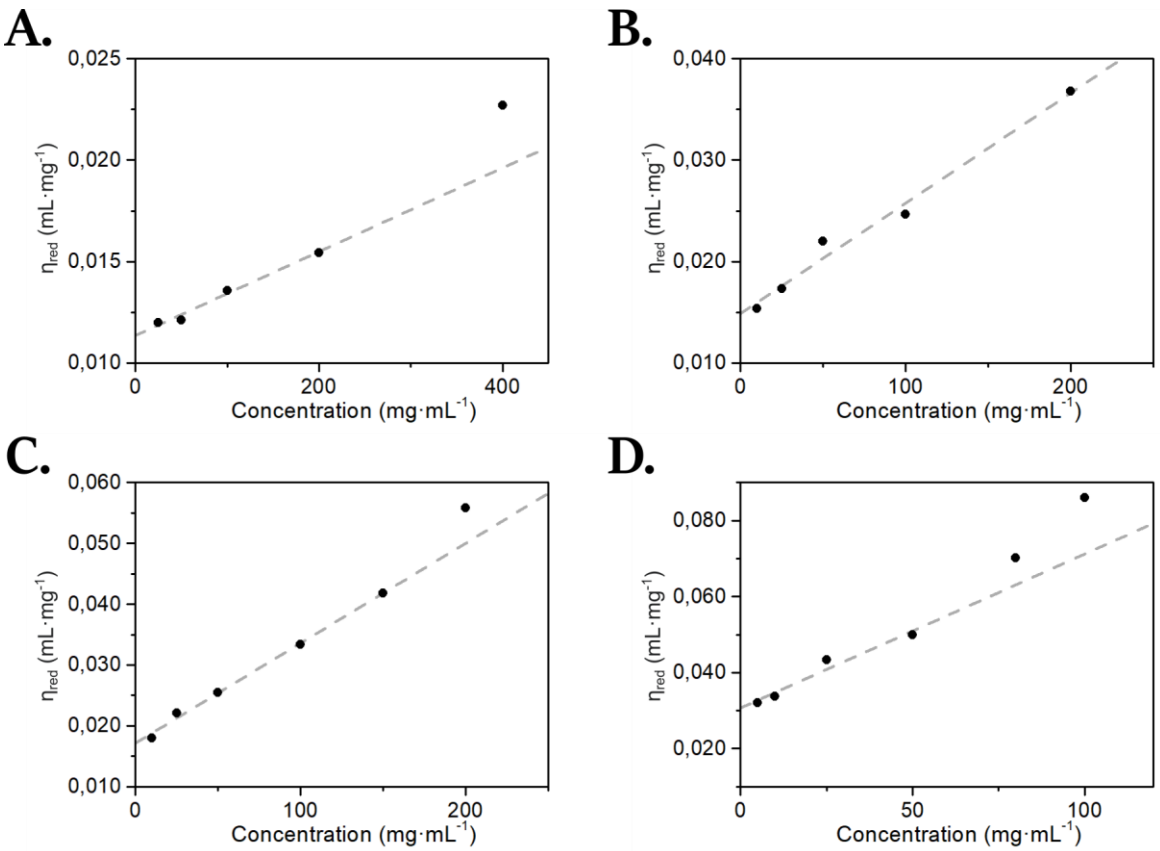

Figure 4.2. Evolution of the reduced viscosity η_{red} as a function of the polymer concentration in DMF for **A**: **42$_{3000}$**; **B**: **42$_{6000}$**; **C**: **42$_{10000}$**; **D**: **42$_{20000}$**. Errors bars are included in the size of the points.

concentration of PEG with a molecular weight of 6 000 g·mol^{-1} by neutron scattering,[6,7] which can be used as a reference point for the calculation of c* in the present case. We obtain:

$$c^* = \frac{0.87}{[\eta]} \tag{4.4}$$

The values of c* can therefore be calculated for the four polymers in DMF (Table 4.2). Consequently, gels made of PEG crosslinked with molecular motors can be formed under optimal concentration conditions.

4.2.2 *Reticulation of end-functionalized PEG with tetrafunctional molecular motors*

'Click' reactions are distinguished by the fact that they proceed with very high yields, are modular and can be applied to a wide set of reactants, lead to inoffensive byproducts, and are stereospecific.[8] They are increasingly used in the field of materials science for straightforward functionalization of polymer chains, grafting on surfaces or formation of networks.[9] Among these reactions, copper-catalyzed azide-alkyne cycloaddition (CuAAC) is one of the most used because of the availability of organic compounds possessing terminal azide or alkyne groups.[10,11] The cycloaddition between these two functional groups leads exclusively to the formation of 1,4-disubstituted triazoles without any byproducts and, hence, was ideal for the formation of our gels (Scheme 4.3).

The experimental setup for the formation of the materials was optimized compared to our first report,[1] where gels were formed in glass vials. Here, we formed gels in custom-made metal molds of 2 cm × 2 cm × x mm, where x is the thickness (Figure 4.3, left). This system minimizes the liquid-air interface and allows for a better control of the thickness of the final material.

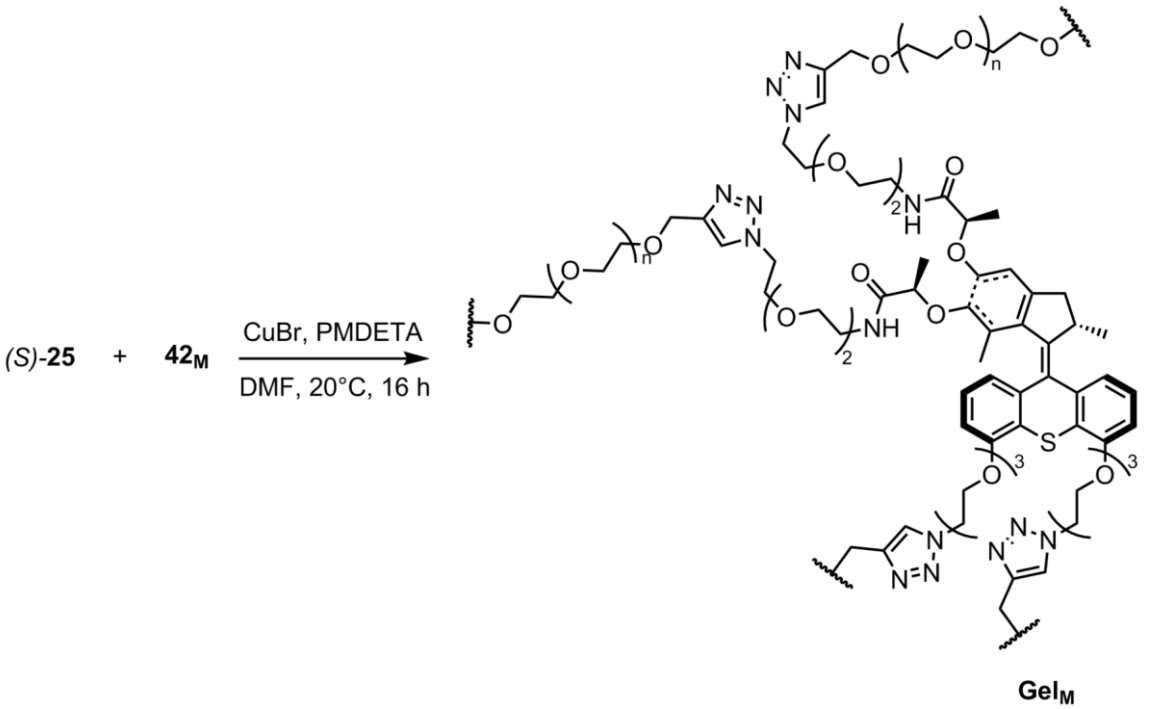

Scheme 4.3. Preparation of gels of PEG $\mathbf{Gel_M}$ crosslinked with molecular motors by CuAAC between molecular motor *(S)*-**25** and polymer $\mathbf{42_M}$.

$\mathbf{Gel_M}$	Thickness x (mm)	Volume of solvent (µL)	Mass of $\mathbf{42_M}$ (mg)	Mass of **25** (mg)
$\mathbf{Gel_{3000}}$	0.5	300	23.1	5.66
$\mathbf{Gel_{6000}}$**-0.5**	0.5	300	17.7	3.10
$\mathbf{Gel_{6000}}$**-0.75**	0.75	450	26.6	4.67
$\mathbf{Gel_{6000}}$**-1**	1	600	35.4	6.21
$\mathbf{Gel_{6000}}$**-2**	2	1200	70.8	12.4
$\mathbf{Gel_{10000}}$	0.5	300	15.3	1.05
$\mathbf{Gel_{20000}}$	0.5	300	8.4	0.496

Figure 4.3. Left, snapshot of the custom-made metal mold for the formation of gels. The two parts are screwed together, and the gel is formed in the cavity. The size of the cavity is 2 cm × 2 cm × x mm, with x the thickness. **Right,** list of gels formed; notably, they were all formed at the c* of the polymer chains. The amount of solvent used was more than what was needed to ensure complete filling of the cavity.

Hence, gels were formed by mixing appropriate amounts of tetrafunctional motor and homotelechelic PEG. More specifically, two solutions were prepared. The first one was the solution of motor *(S)*-**25** (1 eq.) in half the amount of needed solvent, along with copper bromide (CuBr) (5 eq.) and *N,N,N′,N″,N″*-pentamethyldiethylenetriamine (PMDETA) (5 eq.) as a ligand. The second one was the polymer $\mathbf{42_M}$ (2 eq.) solution in the remaining half of solvent. The concentration in polymer was twice c*, since mixing the two solutions dilutes the system, and the concentration in motor was calculated to match the number of equivalents relative to the concentration in polymers. Importantly, the solvent was degassed prior to the preparation of the solutions and copper(I) was

added first to the motor solution to avoid Glaser coupling. The series of gels **Gel$_M$**, with M the molecular weight of the polymer chain, that were prepared are summed up in Figure 4.3, right. Gels were formed for four different end-functionalized molecular weights; moreover, **Gel$_{6000}$** was prepared with different thicknesses ranging from 0.5 to 2 mm and are referred to as **Gel$_{6000}$-x**, with x the thickness in mm.

The formation of these gels at c* ensures that all materials are in similar initial conditions where the presence of entanglements is minimized while the efficiency of reticulation is still high, no matter the molecular weight of the polymer. This represent a main advance compared to our previous studies on the properties of the gels, where only gels with PEG of 6 000 g·mol^{-1} were in c* conditions while other systems deviated from this 'ideal' topology.[6,7] Therefore, the study of the impact of several parameters on the contractile behavior of the materials presented in the next section represents a main advance in our understanding of these systems.

4.3 Contractile behavior of gels crosslinked with molecular motors depending on external and internal parameters

Under UV irradiation, the rotation of the molecular motors intertwines together the polymer chains composing the network. The creation of new physical entanglements leads to the macroscopic contraction of the gel. The contractile behavior of the material should depend on the structure of the material. First, external parameters, such as solvent, temperature, or light power, are expected to play a role because they can alter the conformation of the polymer inside the network and the efficiency of the rotation of the motor. Second, internal parameters of the network itself, such as the molecular weight between crosslinks, should also have an impact since the rotation of the motor entangles the polymer chains together. These parameters have therefore been investigated to tune the contraction of the gels and results are discussed in the next subsections.

4.3.1 Setting up the irradiation system

Full details on the devices used for the irradiation of gels are presented in Appendix A. For the sake of clarity, however, few aspects related to the irradiation system are presented in the following paragraphs.

Gels formed from the molds, discussed in the previous section, were first cut into smaller pieces, and placed in a sample cell for irradiation. The sample cell is a cylindrical screwed quartz cell (Figure 4.4.B); the gel was sandwiched between two glass windows separated by a glass spacer, with a thickness adapted to the one of the materials and filled with the swelling solvent. The diameter of the opening of the cell was 1.6 cm.

The sample cell was placed at a distance where the light beam completely covered the surface of its opening (typically, 2 cm) and an USB camera was placed on the opposite side to capture the evolution of the surface of the material over time under UV irradiation (Figure 4.4.A). The light power of the

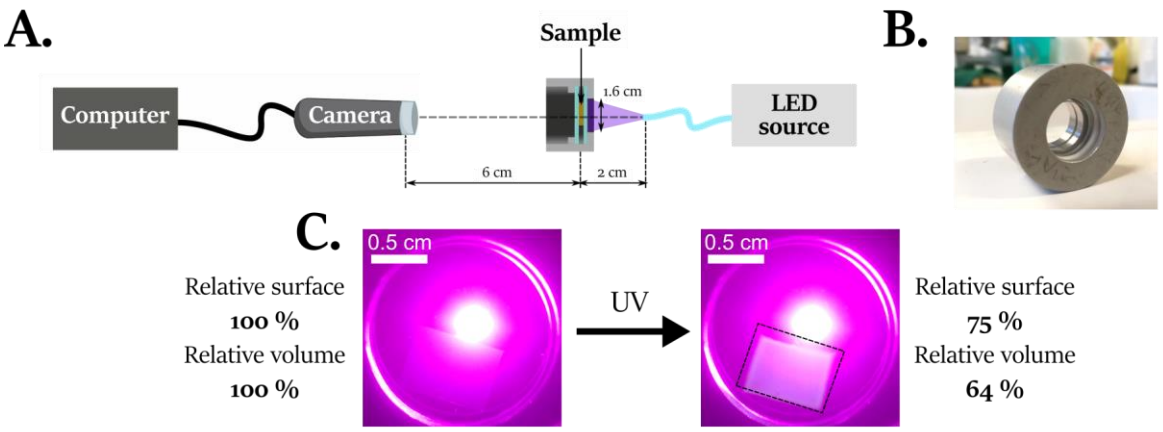

Figure 4.4. A. Schematic representation of the irradiation setup. The beam of the LED source (purple) is set to completely irradiate the surface of the sample cell. The camera is placed on the opposite side to capture the evolution of the material. **B.** Snapshot of the sample cell used. It is a cylindrical screwed quartz cell where the sample is sandwiched between two glass slides separated by a glass spacer. **C.** Representative example of snapshots taken over the course of the irradiation. The relative surface was converted to the relative volume. Dashed rectangle highlights the shape of the material before UV irradiation.

LED source was measured close to the beam source and normalized by the surface of the opening to obtain the surface light power density in $mW \cdot cm^{-2}$. Gels were irradiated with UV light at 365 nm.

Raw data treatment gives the evolution of the surface of the material as a function of irradiation time. As the contraction was considered isotropic, evolution of the volume of the gel as a function of time is given by the following formula:

$$\%_V(t) = \left(\frac{S(t)}{S(0)}\right)^{3/2} \quad (4.5)$$

with $\%_V(t)$ the relative volume at time t, S(t) the surface measured at time t and S(0) the initial surface of the gel (see Appendix A for the demonstration). Data plotted in the next subsections were obtained with this formula. However, it may not hold when the thickness of the gels increases, as discussed later (section 4.3.3).

This irradiation setup is also a major improvement compared to our first reports. The possibility to systematically change parameters, such as light power, thickness, or temperature, allows the precise investigation of the structure-property relationship of our systems. Moreover, all experiments were performed on four pieces of gel at least, from two different batches, to ensure reproducibility of the observed behavior.

4.3.2 *Changing the reticulation or swelling solvent of the gels*

Solvents influence the conformation of polymers in solution. During the reticulation step, the conformation is captured by the formation of crosslinks and can, hence, alter the contraction of the materials under UV light. For the same reasons, the swelling solvent can also influence the contractile behavior of the gels. Consequently, these two parameters were investigated to determine the optimal solvent conditions for our systems.

The reticulation solvent was first investigated. The previous section focused on the determination of c* for $\mathbf{42_M}$ in DMF; the same analysis was conducted for $\mathbf{42_{6000}}$ in dichloromethane and, in these conditions, c* = 45 $mg \cdot mL^{-1}$ (Appendix B). Under the same irradiation conditions, gels crosslinked

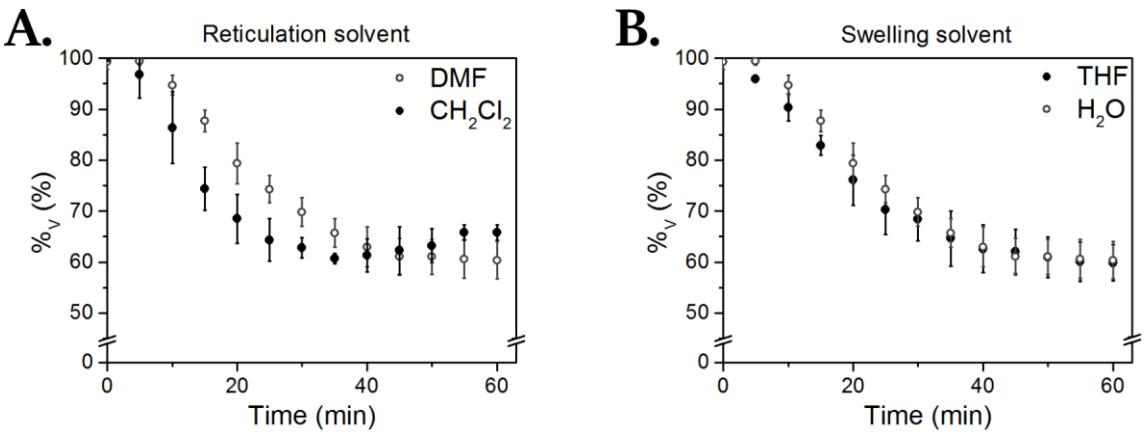

Figure 4.5. Evolution of the relative volume $\%_V$ of **Gel_{6000}-0.5** as a function of UV irradiation time. Light power: 80 mW.cm^{-2} **A**. Influence of the reticulation solvent. The gels were swollen in water. **B.** Influence of the swelling solvent. The gels were crosslinked in DMF. Other solvents were tested but only THF and water led to contraction of the material. Error bars represent the standard deviation.

in DMF contracted slower than the ones crosslinked in dichloromethane but both systems reached the same final relative volume (60 ± 4 %) (Figure 4.5.A). It indicates that the final conformation of the polymer in the swelling solvent is the same regardless of the reticulation solvent, as long as gels are formed at their respective c*; consequently, materials reach the same final relative volume. For gels formed in dichloromethane, however, a slight increase in volume is observed for long irradiation time, indicating degradation of the gel. Therefore, reticulation in DMF was preferentially chosen for the preparation of gels.

The difference in contraction kinetics may be explained by the concentration of active motors in the gels. For the gels formed in dichloromethane, there may be less aggregates than for the ones formed in DMF and, hence, more motors can rotate under UV light. This hypothesis may also explain the shorter activation time before reaching the linear contraction regime for gels formed in dichloromethane. Moreover, the presence of less heterogeneities can also explain the degradation of gels for longer irradiation time; when network strands are cleaved under UV irradiation, the presence of these physical crosslinking points may help maintaining the integrity of the network. Neutron scattering analysis (section 4.4) seem to corroborate the fact that the gels formed in dichloromethane have less heterogeneities than the ones formed in DMF.

Several swelling solvents were tested for our systems; however, only gels swollen in water or THF contracted over irradiation time (Figure 4.5.B). Halogenated solvent, such as dichloromethane or dichloroethane, led to a gradual increase in volume of the gel until its complete dissolution. Irradiation with UV light might lead to the formation of radicals in such solvents, which accelerate the degradation rate of the network. Other solvents, such as toluene, DMF or MeOH, did not always lead to contraction and sometimes led to full dissolution of the gel. In these solvents, the gels tend to strongly stick to the glass windows. In our first report, materials were contracted when swollen in toluene[1] but, in these systems, they were placed in a glass vial with limited contact with the glass itself. In the present system, however, even though similar results could be obtained occasionally, these results were not reproducible.

Contractions when **Gel$_{6000}$-0.5** were swollen in either THF or water are essentially identical. They both show the same kinetics and reach the same final relative volume of 60 ± 4 % (Figure 4.5.B). Therefore, it can be concluded that the contraction behavior does not depend on the swelling solvent of the gel, as long as it is a good solvent for the polymer. Considering the lower vapor pressure of THF, water was preferentially chosen as the swelling solvent for subsequent studies.

Determining the best solvent conditions was critical for the optimization of our systems. In order to ensure reproducibility of the data, DMF was chosen as the crosslinking solvent and water as the swelling solvent of the gels. Unless otherwise stated, results obtained in the following subsections were from **Gel$_M$** formed under these conditions.

4.3.3 Influence of the light power and the thickness of the gels

Light power and thickness are tightly related parameters. They both change the amount of photons available per motor in the gel and, hence, may alter the contractile behavior in the same manner.

First, the thickness x of **Gel$_{6000}$-x** was varied, and four different ones were tested: 0.5, 0.75, 1 and 2 mm. The evolution of their volume was measured under UV irradiation at 80 mW·cm^{-2} (Figure 4.6.A). The thinnest gels contracted faster. **Gel$_{6000}$-0.5** and **Gel$_{6000}$-0.75** reached the same final relative volume of 60 ± 5 %, indicating that the maximum extent of contraction is determined by the mesh size of the network, which is the same regardless of the thickness. For **Gel$_{6000}$-1**, however, the material does not reach this maximum value and do not contract beyond 73 ± 4 % of its initial volume; we hypothesize that it is caused by UV degradation of the gel. The rate of UV degradation does not change with the thickness, while the rate of contraction is lower with increasing thickness; for **Gel$_{6000}$-1**, we may reach a critical situation where too many network strands are cleaved to achieve complete contraction. Finally, **Gel$_{6000}$-2** hardly contracts and only reaches 94 ± 6 % of its initial volume, which may be due to the combination of a very slow rate of contraction and UV decomposition of the network.

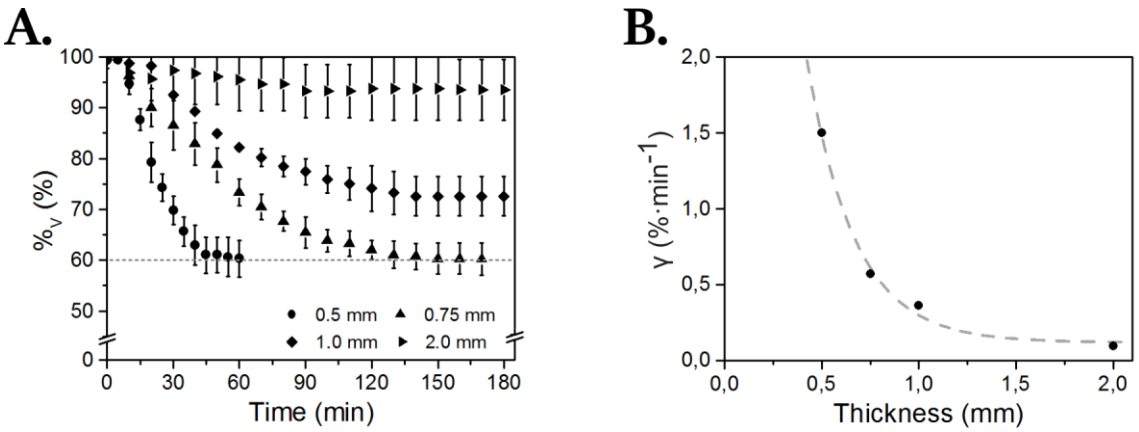

Figure 4.6. A. Evolution of the relative volume $\%_V$ of **Gel$_{6000}$-x** as a function of UV irradiation time for different thicknesses x. Light power: 80 mW.cm^{-2}. Error bars represent the standard deviation. **B.** Evolution of the maximum contraction rate as a function of the thickness of the gel. Exponential fit (grey dashed line) serves as a guideline for the eye.

We evaluated the maximum rate of contraction γ of our materials by measuring the maximum slope of the evolution of $\%_V$ over time (Figure 4.6.B). γ seems to decrease exponentially with the thickness of the gels. Lambert's law states that the intensity of light decreases exponentially with its penetration depth inside a medium. Consequently, with our gels, we expect that the rotation rate of the motors also decreases the further they are from the irradiated surface. It results in a contraction gradient along the thickness of the material; however, since the gel is sandwiched between two glass windows, we only observe the evolution of its surface over time. The equation converting the surface evolution into volume evolution may therefore not hold. It is worth noting that the light power, the rotation rate of the motor and the volume change of the material do not scale linearly to each other. Therefore, no straightforward relationship can be determined between the thickness and the maximum contraction rate γ without further modelling.

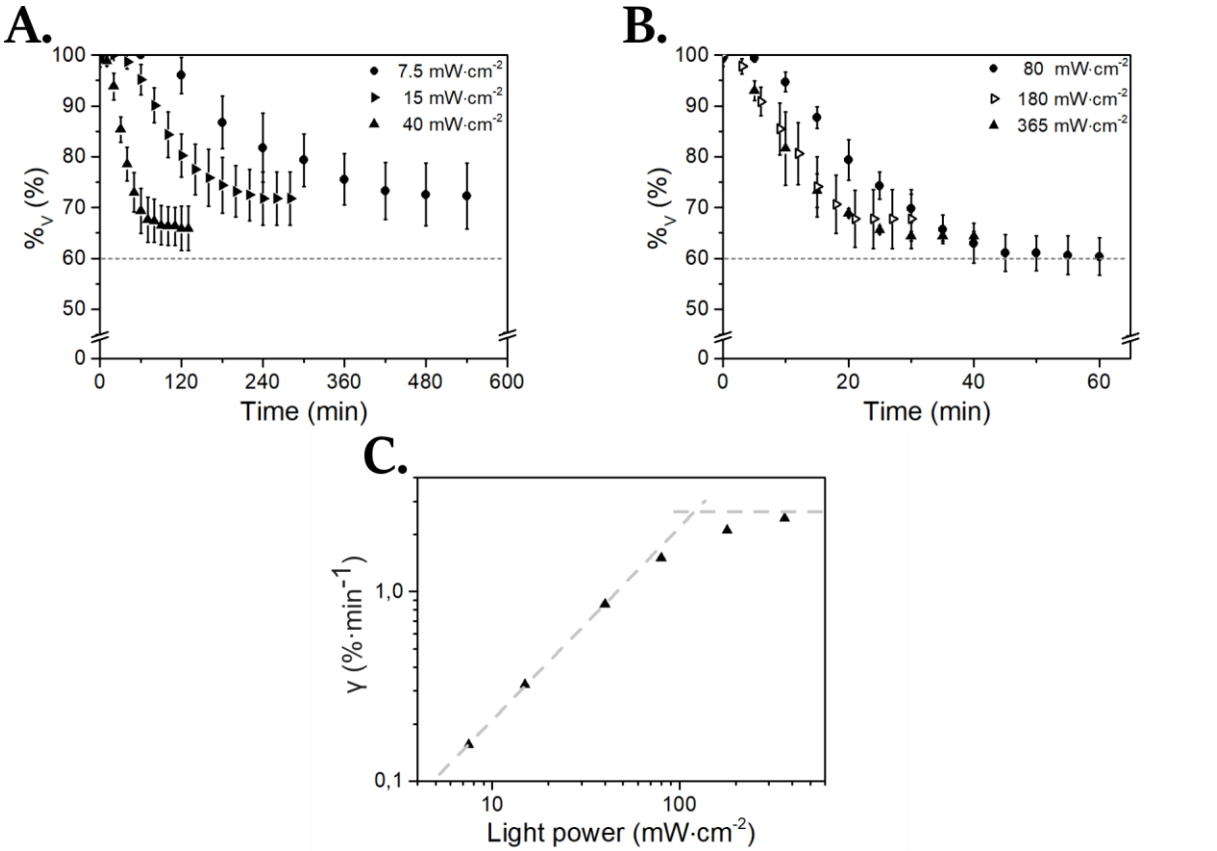

Figure 4.7. A and **B.** Evolution of the relative volume $\%_V$ of **Gel$_{6000}$-0.5** as a function of UV irradiation time for different light power densities. Error bars represent the standard deviation. **C.** Evolution of the maximum contraction rate as a function of the light power. Grey dashed lines are guides for the eye.

The influence of the light power on the contractile behavior of our systems was then investigated. **Gel$_{6000}$-0.5** was irradiated at different light power densities ranging from 7.5 to 365 mW·cm^{-2} (Figure 4.7.A and B). Gels contract faster when subjected to higher light intensities, but they all statistically reach the same final relative volume of 67 ± 10 %, which indicates again that the final relative volume only depends on the structure of the network.

The evolution of log γ as a function of the logarithm of the light power shows a linear increase for low powers before reaching a limiting value at higher powers (Figure 4.7.C). This result is expected, considering previous work on the kinetics of molecular motors by Feringa and coworkers.[12] The

authors showed that motors are 'photochemically rate limited' at low light intensities. In that case, the amount of photons per molecular motor is not high enough to populate the metastable state after photoisomerization faster than it is depopulated by thermal helix inversion. In other words, statistically, any motor that undergoes photoisomerization is instantly relaxed to its most stable state. For higher irradiation powers, however, the system becomes 'thermally rate limited'. The rate of thermal helix inversion cannot lead to the relaxation of all motors reaching the metastable state. Consequently, statistically, motors in their metastable conformation are more likely to be photoisomerized back to their initial state. Therefore, when motors are thermally rate-limited, the unidirectionality is increasingly lost at higher powers and the overall rotation rate do not vary above a threshold value.[12] In our case, the threshold power is close to 120 $mW \cdot cm^{-2}$ and a maximum rate of contraction γ of 2.7 $\%\cdot min^{-1}$ can be achieved. This threshold value is relatively low and indicates that the rate of thermal helix inversion of our motors in the gel may also be slow.

Thickness and light power both alter the contractile behavior of our gels. The maximum contraction rate of our materials decreases exponentially with increasing thickness and, hence, we pursued our studies with 0.5-mm-thick gels to ensure fast contraction while maintaining good mechanical properties to easily handle the material. Moreover, γ increases with light intensity until reaching a maximum value for powers higher than 120 $mW \cdot cm^{-2}$. Consequently, we performed our subsequent tests, presented in the next subsections, at 80 $mW \cdot cm^{-2}$ to be in the 'photochemically rate limited' regime where the rotation rate is close to its maximum and mostly unidirectional, unless otherwise stated.

4.3.4 Impact of the temperature on the contractile behavior

Temperature may also influence the volume change of our systems in two ways. First, it can alter the conformation of the polymer in the network and, hence, alter the braiding process of the strands. Second, the rotation process of the motors involves a thermal step. Therefore, temperature can influence their overall rotation rate and cause a change in the rate of contraction.

The first set of experiments consisted in heating the material stepwise to 70°C and perform the irradiation at this temperature (Figure 4.8.A). Increasing the temperature leads to the contraction of the material at 55 ± 5 % of its initial volume. This effect may be first explained by the change in the equilibrium of the gel caused by the temperature since it contributes to the free energy of mixing and the osmotic pressure (Chapter 2, section 2.2.1). Moreover, it may also be caused by the lower critical solution temperature (LCST) of PEG in water, which ranges from 100 to 150°C depending on the molecular weight of the polymer.[13,14] Subsequent irradiation with UV light leads to a final relative volume of 25 ± 5 % after 30 min.

In a second set of experiments, the gels were first irradiated before stepwise heating to 70°C (Figure 4.8.B). After 30 min of UV light, materials reached 67 ± 14 % of their initial volume. The standard deviation observed in these experiments is higher than those obtained in the previous subsection. The irradiation system was slightly different for controlling the temperature; gels were placed in a special cell connected to a temperature controller. We consider that the gels have not been in the best configuration because the spacing between the glass windows was not sufficient or because gels stick more to the glass windows in this setup. These effects are probably not as important when

temperature is increased first, and only the contraction under UV light remains highly sensitive to these experimental conditions. Nevertheless, subsequent heating of the material led to a final volume of 39 ± 6 % relative to the initial state, which is slightly higher than for the previous set of experiments when heating was performed first.

The normalized evolution of the relative volume under light irradiation at 20°C and 70°C shows no significant difference between these two temperatures (Figure 4.8.C). The contraction at 70°C seems to be faster than the one at 20°C but the standard deviation obtained for the latter indicates that there is no statistically significant change. As discussed in the previous subsection, motors are in a photochemically rate-limited regime at this light power (80 mW·cm^{-2}).[12] Therefore, we expected that temperature would only have a marginal effect on the contraction rate in these conditions.

When gels are irradiated at 20°C, they reach 67 ± 14 % of their initial volume, while irradiation at 70°C leads to contraction to 50 ± 6 % of their initial volume. Therefore, there is no significant differences in the contractile behavior of our gels in the range of temperature that was explored. It might seem counterintuitive since the gels have a lower volume at higher temperature. However, it indicates that the polymer strands behave the same way at these two temperatures and have a conformation of a chain swollen in a good solvent in both scenarios. Therefore, the LCST behavior

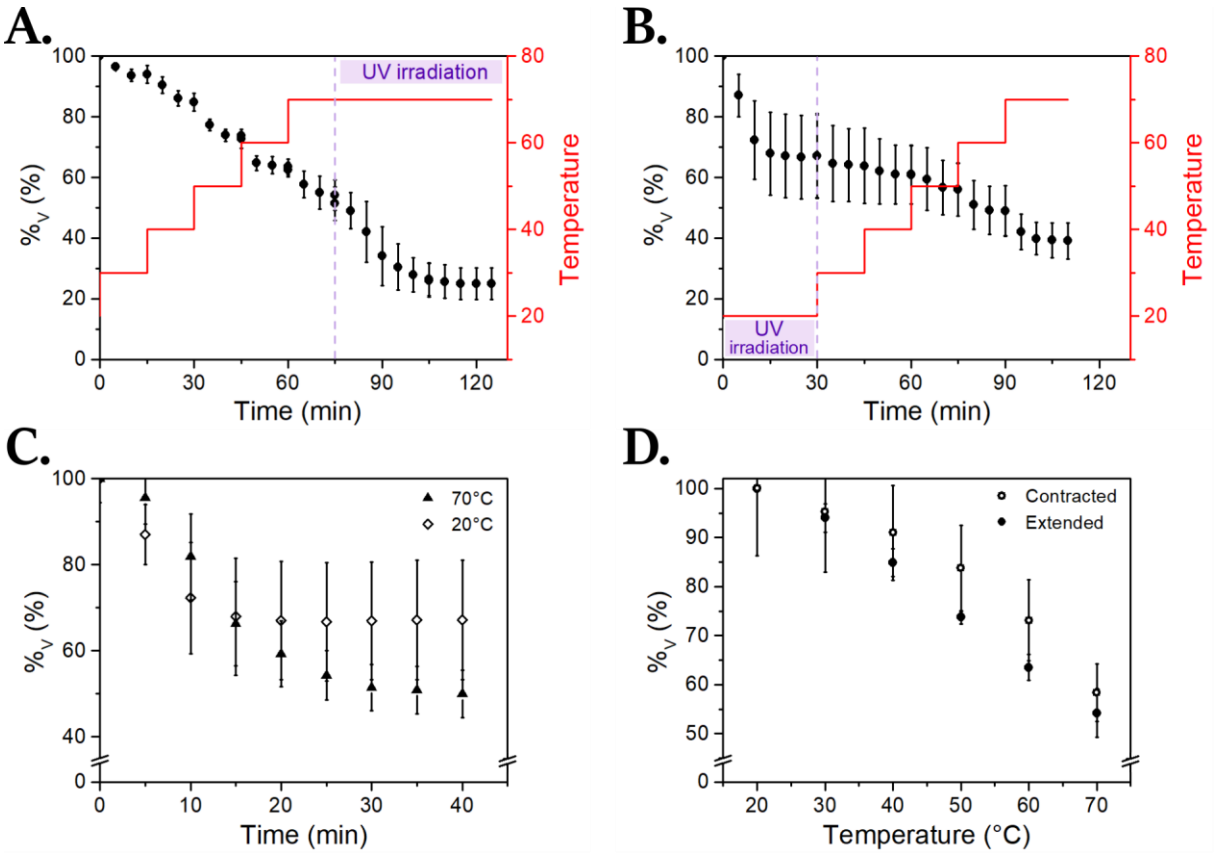

Figure 4.8. A to C. Evolution of the relative volume %$_V$ of **Gel$_{6000}$-0.5** depending on the irradiation time under UV irradiation at 80 mW·cm^{-2}. **A.** Gels were first subjected to heating before irradiation at 70°C. **B.** Gels were first irradiated at 20°C before heating to 70°C. **C.** Gels were irradiated at two different temperatures under UV light. **D.** Normalized evolution of %$_V$ with temperature depending on the extended or contracted state of the gel. Error bars represent the standard deviation.

only have a minimal effect on the volume change of the gels in this range of temperature, since the change in the balance between polymer—polymer and polymer—solvent interactions occurring during the LCST would change the conformation of the chains. However, no clear conclusion can be reached from these data because of the large standard deviation.

Similarly, the normalized evolution of $\%_V$ in the absence of UV irradiation as a function of the temperature do not significantly vary between the extended and contracted states of the materials (Figure 4.8.D). For all temperatures where the volume was measured, the relative volume is statistically identical regardless of the state of the gels: it reaches 54 ± 5 % of the initial volume at 70°C when the system is extended and 58 ± 6 % at the same temperature when the system is contracted. This experiment suggests that, in both states, polymers adopt the conformation of a chain swollen in a good solvent. Therefore, the formation of new entanglements does not alter the balance between polymer—polymer and polymer—solvent interactions, and temperature changes the swelling equilibrium in the same manner.

In the conditions explored, temperature does not affect the contractile behavior of our gels. These results confirm that all since the experiments are conducted in the photochemically rate-limited regime of our motors. These investigations could therefore be completed by gel irradiation at higher light power to be in the thermally rate-limited regime; however, in that case, UV irradiation may lead to a faster dissolution of the materials. Moreover, it seems that the formation of new entanglements does not alter the conformation of the polymer strands in the network, which is corroborated by Small-Angle Neutron Scattering (SANS) experiments (section 4.4).

4.3.5 Contractile behavior for different molecular weights

Changing the molecular weight of the polymeric precursor **42M** for the formation of the gels should influence the contractile behavior of our materials. The polymers have lower overlap concentrations c* for higher molecular weights (section 4.2.1) and, hence, the initial polymer strand density $\phi_{s,i}$ of the network decreases when the molecular weight increases, since:

$$\phi_{s,i} = c^* \times \nu \tag{4.6}$$

with ν the specific volume of the polymer, which is 0.89 $cm^3 \cdot g^{-1}$ for PEG (see section 4.4). Therefore, as the structure of the network changes, we expected different contraction curves for **Gel$_M$** made of different molecular weights.

First, it is necessary to highlight the importance of degassing the solvent before the experiments. As an example, **Gel$_{10000}$** was irradiated with and without degassing water by bubbling argon for 30 min (Figure 4.9.A). When the solvent was not degassed, the gel reaches a maximum relative volume $\%_{V,max}$ of 74 ± 3 % after 50 min; however, when the solvent was degassed, the material reaches $\%_{V,max}$ = 53 ± 2 % after 40 min. The maximum rate of contraction γ also changes, going from 1.1 $\%\cdot min^{-1}$ to 3.2 $\%\cdot min^{-1}$ without and with degassing, respectively. We assessed that this change was caused by the presence of oxygen by performing a control experiment with a gel crosslinked with a tetra-azide episulfide, which do not rotate under UV light. The data obtained for **Gel$_{10000}$** without degassing was then corrected by the volume increase observed for the control

experiment, and the resulting evolution in volume closely matches the results for **Gel$_{10000}$** in degassed conditions.

Similar experiments were conducted for **Gel$_{3000}$**, **Gel$_{6000}$** and **Gel$_{20000}$**. For **Gel$_{3000}$** and **Gel$_{6000}$**, degassing the solvent did not significantly change their contraction curves. The strand density of these materials is higher than for **Gel$_{10000}$** and, hence, cleavage of polymer chains may not alter the integrity of the network in the timescale of UV irradiation. For **Gel$_{20000}$**, however, we observed dissolution of the material even in degassed conditions. In that case, contrariwise to the others, the strand density of the network is low, and the contraction kinetics is probably not high enough to compensate the rate of chains cleavage. An increase in volume is even observed for **Gel$_{10000}$** for long irradiation times.

Therefore, contraction experiments were conducted for **Gel$_{3000}$**, **Gel$_{6000}$** and **Gel$_{10000}$** (Figure 4.9.B). Two trends can be extracted. First, the maximum relative volume $\%_{V,max}$ decreases with increasing molecular weight and, second, the maximum rate of contraction γ increases with increasing molecular weights (Figure 4.9.C). In other words, since the molecular weight of the polymer and the concentration of c_{motor} are inversely proportional, $\%_{V,max}$ increases and γ decreases with increasing concentration in motors c_{motor} (Figure 4.9.D).

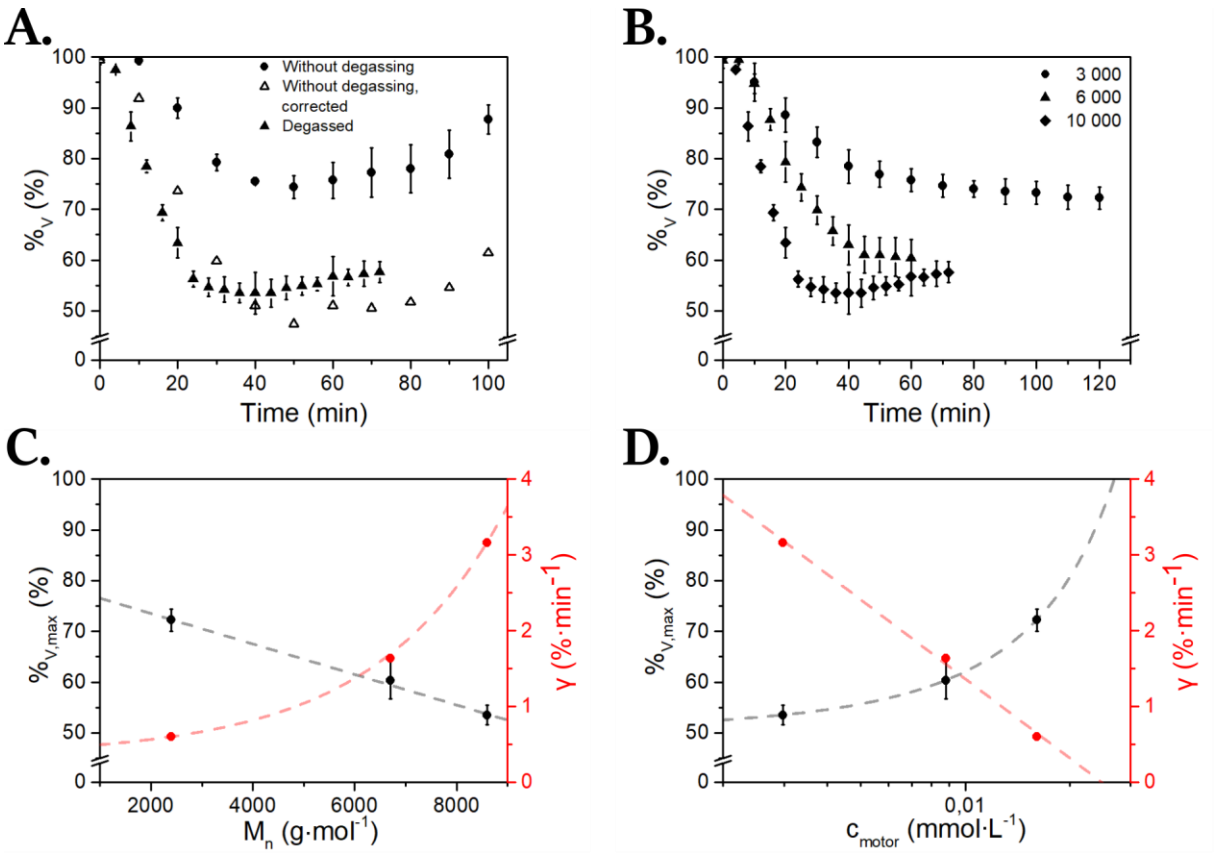

Figure 4.9. A. Evolution of the relative volume $\%_V$ of **Gel$_{10000}$** under UV irradiation at 80 mW·cm^{-2}, depending on whether the solvent was degassed or not. The corrected curve was obtained by subtracting the data 'without degassing' by the data obtained with a non-photoactive gel crosslinked with episulfides. **B.** Evolution of the relative volume $\%_V$ for **Gel$_M$** prepared from PEG having different molecular weights M under UV light. **C.** Maximum relative volume $\%_{V,max}$ and maximum contraction rate γ as a function of the molecular weight of the crosslinked PEG. Red and grey dashed lines are guidelines for the eye. **D.** Maximum relative volume $\%_{V,max}$ and maximum contraction rate γ as a function of the concentration of motors in the gels. Red and grey dashed lines are guidelines for the eye.

The maximum relative volume $\%_{V,max}$ is correlated to the molecular weight of the chains between crosslinks (Figure 4.9.C). We propose that such evolution is caused by the polymer strand density of the network. We suppose that motors can intertwine polymer strands until an apparent critical strand density $\phi_{s,crit}$ is achieved, where the volume becomes too low to allow for the braiding of the chains by motors. Therefore, when polymer chains are longer and, hence, the initial strand density $\phi_{s,i}$ is higher, motors can perform more rotations before reaching this minimum value. Consequently, increasing the molecular weight of the crosslinked polymer chains causes a decrease of $\%_{V,max}$ of the gel.

On the other hand, the maximum contraction rate γ is correlated to the concentration in motors c_{motor} in the material (Figure 4.9.D). This situation is similar to the one discussed in the section dealing with the light power (section 4.3.3). For a given light intensity, decreasing the concentration of motors increases the amount of photons received per motor. Therefore, their rotation rate increases and the gels contract faster. As for the light intensity, there should be a critical concentration c_{motor} below which the rotation rate, and, hence, γ, should not increase anymore. We do not, however, observe this evolution in the range of molecular weights that we tested. Moreover, γ may also be dependent on the initial strand density of the network $\phi_{s,i}$, which is proportional to c*. When the strand density decreases, polymers may move more freely and be easier to entangle, whence an increase in γ.

The last subsections aimed to understand and optimize the contractile behavior of gels of PEG crosslinked with molecular motors. Among all the parameters we investigated, we observed that the maximum relative volume $\%_{V,max}$ only depends on the molecular weight of the polymers used for the preparation of the material, because it is the only parameter that changes the structure of the network. The maximum contraction rate γ, however, was sensitive to almost all the parameters that were investigated. From these studies, it seems that **Gel$_{10000}$** with a thickness of 0.5 mm irradiated at 365 mW·cm^{-2} should be the fastest system (Figure 4.10). In that case, we obtain $\%_{V,max}$ = 67 ± 3 %, which is higher than what was obtained for the same material at lower light power and is probably caused by a faster rate of cleavage of the network strands. Nevertheless, and as expected, γ reaches 5.1 %·min^{-1} for this gel and is, indeed, the fastest rate that we obtained.

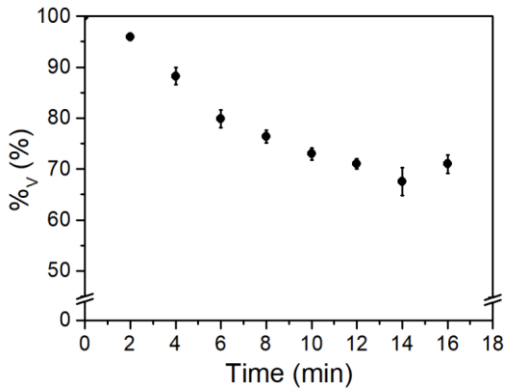

Figure 4.10. Evolution of the relative volume $\%_V$ of **Gel$_{10000}$** with a thickness of 0.5 mm as a function of UV irradiation time at 365 mW·cm^{-2}.

We proposed several mechanisms to explain the observed behavior depending on these parameters. Structural analysis of the network is, however, necessary to validate —or deny— our hypothesis. We thus performed neutron scattering on our gels for this purpose.

4.4 Structural analysis by neutron scattering

Small-Angle Neutron Scattering (SANS) is sensitive to the nuclei of the atoms composing the sample. Therefore, by exploiting the high difference in scattering between hydrogen and deuterium atoms, it is possible to detect the signal originating from hydrogenated polymers solubilized in deuterated solvents. This technique has been widely used in materials science, including polymers gels,[15,16] and we recently reported a thorough analysis of our initial systems by SANS to probe the presence of heterogeneities and the evolution of the network structure depending on the extended or contracted state of the gels.[7]

SANS analysis provides information for lengths ranging from few ångströms to tens of nanometers. For our systems, we can therefore probe the gels down to the conformation of individual polymers chains and up to the scale of large aggregates.

First, it is important to determine which part of the network is responsible for the majority of the signal observed in SANS. The intensity I(q) of the signal is proportional to the square of the difference in scattering length density between the polymer and the solvent $\Delta\rho^2$. This parameter was estimated for our systems (Table 4.3, see Appendix A for details on the calculation). It varies depending on the chemical nature of the polymer used for reticulation and is of the same order for the repeating unit of $\mathbf{Gel_M}$ and for $\mathbf{42_M}$. It indicates that the signal obtained by SANS mostly arises from the polymer chains of the network.

Table 4.3. $(\Delta\rho)^2$, characterizing the contrast, of the different elements composing $\mathbf{Gel_M}$ used for SANS.

	Repeating unit of $\mathbf{Gel_M}$	**$\mathbf{42_M}$**	**25**
$(\Delta\rho)^2$ in water ($\times 10^{-11}$ Å^{-4})	3.0 – 3.2	3.1 – 3.2	2.2
$(\Delta\rho)^2$ in toluene ($\times 10^{-11}$ Å^{-4})	2.3 – 2.4	2.3 – 2.4	1.5

SANS spectra were recorded for $\mathbf{Gel_M}$ in two different conditions (Figure 4.11). For one set of experiments, gels were crosslinked in DMF at their c* and swollen in water, as the ones presented in the previous sections (Figure 4.11.A, C and E); for the other set of experiments, gels were crosslinked in dichloromethane and swollen in toluene (Figure 4.11.B, D and F). In the latter case, measurements were initially performed to be compared with our first design of the gels, whence the use of toluene as swelling solvent, but they may also be discussed in comparison to the latest design presented in this thesis. Moreover, these gels were formed at 22 mg·mL^{-1}. Considering that c* scales with $M_n^{-4/5}$ in a good solvent[7] and knowing that c* for $\mathbf{42_{6000}}$ is 45 mg·mL^{-1} in dichloromethane (section 4.3.2),

c* equals 78 mg·mL^{-1} for **42$_{3000}$** and 30 mg·mL^{-1} for **42$_{10000}$**. Therefore, all the gels were formed below their c* in dichloromethane.

All gels present a similar evolution. In the low-q range, the upturn in scattering intensity with a slope -4 or -3 indicates the presence of large objects that may be aggregates. Comparing the scattering vector q_{onset} at which the transition occurs may provide information about the relative size of the heterogeneities between different systems. In the mid-q range, the spectra have a Lorentzian shape and fitting the data in this range gives the correlation length of the mesh of the network ξ (see Appendix A for details). At higher q, the decrease in the scattering intensity scales with $q^{-5/3}$, which is characteristic of a polymer chain swollen in a good solvent, and which is observed for the gels both before and after irradiation. This result corroborates our explanation when we studied the thermally

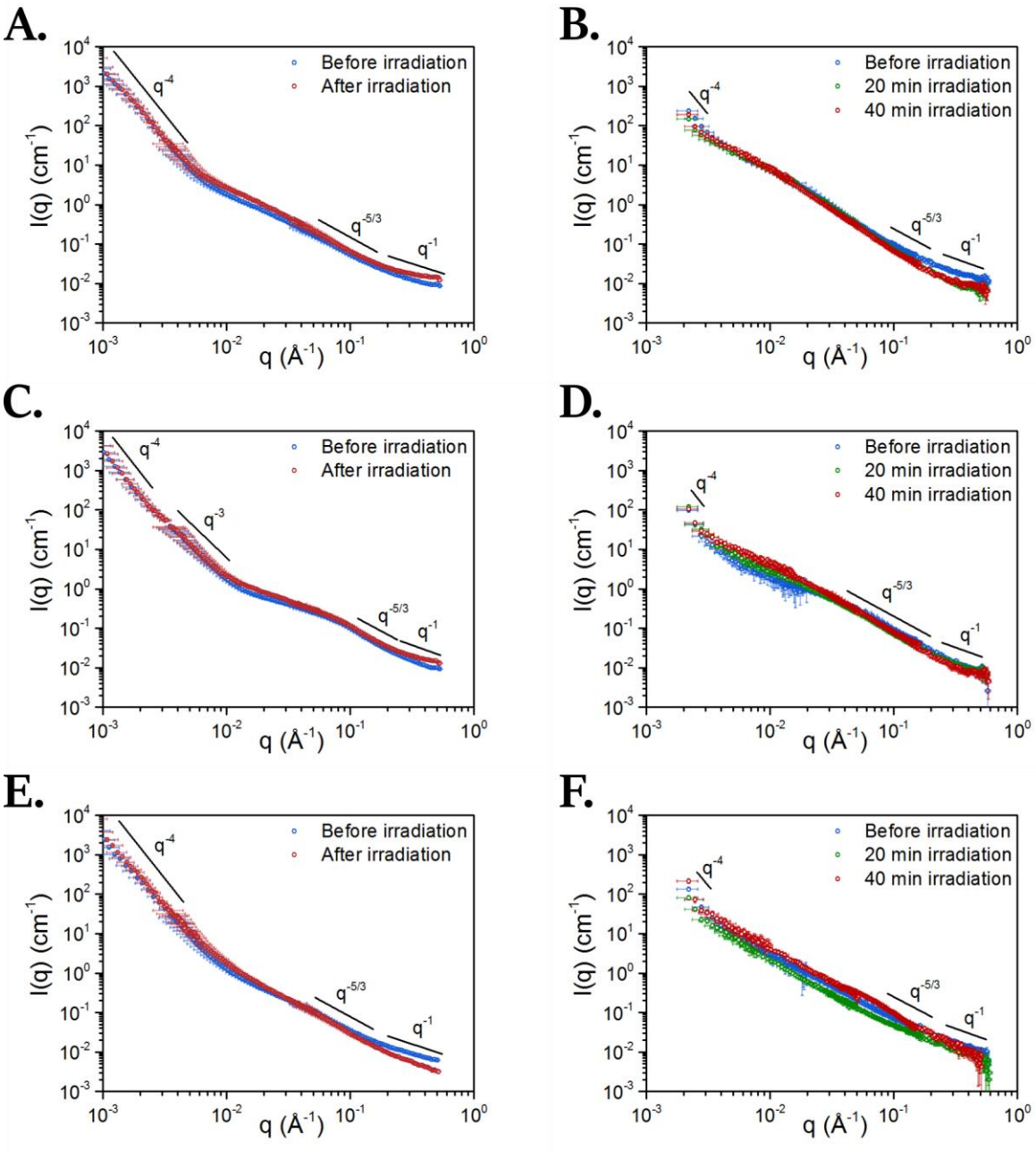

Figure 4.11. SANS spectra for **Gel$_{3000}$** (**A** and **B**), **Gel$_{6000}$** (**C** and **D**) and **Gel$_{10000}$** (**E** and **F**) at different irradiation times. Spectra **A**, **C** and **E** were obtained with gels crosslinked in DMF and swollen in water. Spectra **B**, **D** and **F** were obtained with gels crosslinked in dichloromethane and swollen in toluene.

Table 4.4. Structural parameters of **Gel$_M$** as determined by SANS. **Gel$_{3000}$** and **Gel$_{6000}$** were irradiated for 1 h, and **Gel$_{10000}$** was irradiated for 40 min at 365 nm at 80 mW·cm^{-2}.

	Gel$_{3000}$		**Gel$_{6000}$**		**Gel$_{10000}$**	
	Extended	*Contracted*	*Extended*	*Contracted*	*Extended*	*Contracted*
	Crosslinked in CH_2Cl_2, swollen in toluene, at c = 22 mg·mL^{-1}					
q_{onset} (× 10^{-3} Å^{-1})	3.1	3.1	3.4	3.8	3.1	3.1
l_p (nm)	0.7	0.7	0.7	0.7	1.4	1.4
ξ (nm)	20.3	32.7	4.8	9.9	6.7	10.0
	*Crosslinked in DMF, swollen in water at their respective c**					
q_{onset} (× 10^{-3} Å^{-1})	10.2	8.6	4.2	4.2	6.4	6.4
l_p (nm)	0.7	0.7	1.1	1.1	1.1	0.8
ξ (nm)	2.2	2.3	7.3	8.5	4.8	6.9

induced volume change of the gels between their extended and contracted states (section 4.3.4), where no significant differences were observed between them, indicating that polymer strands have the same conformation in both cases. Finally, we observe a decrease in scattering intensity scaling with q^{-1}, which is characteristic of the rigid-rod-like conformation of the polymer when probed below its persistence length l_p.

The scattering vector q* at which the $q^{-5/3}$ – q^{-1} transition occurs gives l_p, according to this formula:

$$l_p = \frac{1.91}{q^*} \tag{4.7}$$

Three parameters, q_{onset}, ξ and l_p, were measured for all gels in the two conditions at different irradiation times (Table 4.4). First, for the three molecular weights, q_{onset} is higher for gels formed in DMF than for the ones formed in dichloromethane. It indicates that there may be less heterogeneities for gels formed in dichloromethane, which seems to confirm our observations when we modified the reticulation solvent (section 4.3.2).

The persistence length l_p is also similar for most of the gels. We determineed values ranging from 0.7 to 1.1 nm, similar to what we previously reported for our systems.[7] The only exception is for **Gel$_{10000}$** swollen in toluene, where l_p = 1.4 nm. This slight deviation may be explained by the fact that, for this system, the $q^{-5/3}$ – q^{-1} transition was not sharp and the value for l_p is provided with a larger error.

The mesh size of the network is linked to the correlation length ξ. In all cases, ξ increases after UV irradiation, as observed in our recent report.[7] The intertwining of the polymer chains by molecular motors increases the distance between pairs of polymers and, hence, increases the mesh size of the network.

In the case of gels formed in dichloromethane, ξ is large for **Gel$_{3000}$**. Considering that the gel was formed at only 28 % of its c*, this value may indicate the high content of defects in the network, such as dangling chains. For **Gel$_{6000}$**, the reticulation concentration was closer to its c* and ξ is

smaller than for **Gel$_{3000}$**, indicating that the gels may contain less defects in that case. Finally, ξ is higher for **Gel$_{10000}$** than for **Gel$_{6000}$**, which is expected considering that c* and, hence, the strand density is lower. Before and after irradiation, ξ increases by a factor of 1.6 and 1.5 for **Gel$_{3000}$** and **Gel$_{10000}$**, respectively, while ξ is multiplied by 2 for **Gel$_{6000}$**. We expected ξ to increase more in the case of **Gel$_{10000}$** since the initial strand density $\phi_{s,i}$ is lower; however, we observed previously that this system was the most sensitive to UV degradation (sections 4.3.2 and 4.3.5), which may explain the deviation from the expected trend.

Considering gels formed in DMF at their respective c*, we expected ξ to increase with higher molecular weights because of the lower strand density of the gels. However, **Gel$_{10000}$** does not follow this evolution and its ξ before irradiation is lower than the one of **Gel$_{6000}$**. Moreover, ξ is multiplied by 1.05, 1.2 and 1.4 after irradiation for **Gel$_{3000}$**, **Gel$_{6000}$** and **Gel$_{10000}$**. Here, the increase in correlation length scales with the molecular weight, which was expected because of the lower polymer strand density when the molecular weight increases.

SANS provides valuable information on the structure of our systems depending on their extended or contracted state. The reticulation solvent has an impact on the presence of heterogeneities in the network. However, other trends cannot be clearly distinguished, and further experiments should be conducted to draw precise conclusions.

4.5 Conclusion and perspectives

The present thorough investigation on the contractile behavior on PEG-based gels crosslinked with molecular motors provides a better understanding of our materials for their optimization. The first achievement was the synthesis of homotelechelic polymer chains, which provided the modularity needed to easily vary the molecular weight between crosslinks of the network. The second achievement was the optimization of the solvent system, both for reticulation and swelling, which gave reproducible results. Finally, our exploration of this wide array of parameters led to the third achievement, which was to form a material that could contract at a maximum rate of 5 %·min^{-1}.

The present work lays the foundation for further investigation of materials crosslinked with molecular motors. Some developments are currently undergoing in our team, and some other systems are presented in the following chapters. Considering the vast field of polymer networks, there are many possibilities to explore the effect of molecular motors on soft matrices and vice-versa.

It is important to highlight, however, that our gels are still not optimal. We observed that materials are highly sensitive to oxygen for long polymer chains; hence, further investigations have to be performed under inert atmosphere in this direction. We may also reproduce this study with molecular motors powered by visible light, which would limit the degradation of the network. Another possibility is to investigate shorter polymer chains or molecular weights in between the ones that were tested, where degradation was less significant. These investigations are critical to draw clear conclusions on the trends observed. Moreover, we plan to develop models to correlate the

nanoscopic motion of the motors to its consequence at the macroscopic scale. It would provide a significant step towards the understanding of the structure-property relationship of our gels.

References

1. Q. Li, G. Fuks, E. Moulin, M. Maaloum, M. Rawiso, I. Kulic, J. T. Foy, N. Giuseppone, *Nat. Nanotechnol.* **2015**, *10*, 161–165.
2. Accessed on July 8th 2021, Sigma-Aldrich, "Poly(ethylene glycol) bisazide," can be found under https://www.sigmaaldrich.com/FR/fr/product/aldrich/756601?context=product, **2021**.
3. C. Chassenieux, T. Nicolai, D. Durand, *Macromolecules* **1997**, *30*, 4952–4958.
4. C. Chassenieux, T. Nicolai, D. Durand, J. François, *Macromolecules* **1998**, *31*, 4035–4037.
5. G. de los Santos-Villarreal, L. E. Elizalde, in *Handbook of Polymer Synthesis, Characterization, and Processing* (Eds.: E. Saldívar-Guerra, E. Vivaldo-Lima), John Wiley & Sons, Inc., **2013**, pp. 337–354.
6. J.-R. Colard-Itté, Q. Li, D. Collin, G. Mariani, G. Fuks, E. Moulin, E. Buhler, N. Giuseppone, *Nanoscale* **2019**, *11*, 5197–5202.
7. G. Mariani, J.-R. Colard-Itté, E. Moulin, N. Giuseppone, E. Buhler, *Soft Matter* **2020**, *16*, 4008–4023.
8. H. C. Kolb, M. G. Finn, K. B. Sharpless, *Angew. Chem. Int. Ed.* **2001**, *40*, 2004–2021.
9. W. H. Binder, R. Sachsenhofer, *Macromol. Rapid Commun.* **2007**, *28*, 15–54.
10. M. Meldal, C. W. Tornøe, *Chem. Rev.* **2008**, *108*, 2952–3015.
11. L. Liang, D. Astruc, *Coord. Chem. Rev.* **2011**, *255*, 2933–2945.
12. M. Klok, W. R. Browne, B. L. Feringa, *Phys. Chem. Chem. Phys.* **2009**, *11*, 9124.
13. S. Saeki, N. Kuwahara, M. Nakata, M. Kaneko, *Polymer* **1976**, *17*, 685–689.
14. Y. C. Bae, S. M. Lambert, D. S. Soane, J. M. Prausnitz, *Macromolecules* **1991**, *24*, 4403–4407.
15. T. Sakai, X. Li, in *Physics of Polymer Gels*, Wiley, **2020**, pp. 173–178.
16. M. Shibayama, *Polym. J.* **2011**, *43*, 18–34.
17. T. M. Alam, J. E. Jenkins, in *Advanced Aspects of Spectroscopy*, InTech, **2012**.

Chapter 5
Preparation of other telechelic polymers for their integration in networks crosslinked with molecular motors

I thank Andrei Golushko for his contribution to the synthesis and characterization of PNIPAAm. I thank Prof. Lecommandoux, Dr Bonduelle and Mr Badreldin for the synthesis of PBLG.

As demonstrated in the previous chapter, our understanding of gels made of poly(ethylene glycol) (PEG) crosslinked with molecular motors improved, which was in part possible because of the preparation of telechelic linear chains that allowed to easily modulate the structure of the network. Another main advantage of this synthetic pathway for the preparation of gels is that the nature of the polymer can also be easily modulated; any homotelechelic chain could, in principle, be crosslinked with the synthesized tetrafunctional motors. In this chapter, we present our investigations with several other polymers, which were described more precisely in Chapter 2. We discuss first the synthesis of poly(3-hexylthiophene) (P3HT), which we investigated because of its rigidity and electronic properties. Then, we present the synthesis of sodium poly(styrene sulfonate), a well-known polyelectrolyte. Our investigations then concern the synthesis and characterization of thermosensitive poly(*N*-isopropylacrylamide) (PNIPAAm). The synthesis and the formation of photoactive networks from poly(dimethylsiloxane) (PDMS) is then reported. We end the chapter by discussing our investigations on materials formed from poly(γ-benzyl-L-glutamate) (PBLG) and poly(L-glutamic acid) (PGA).

5.1 Synthesis of telechelic poly(3-hexylthiophene)

As explained in detail in Chapter 2, P3HT is a conjugated polymer and, therefore, we expected to alter the electronic properties of our materials depending on its extended or contracted state. Moreover, it has a longer persistence length than PEG. Grignard metathesis (GRIM) polymerization was used to prepare telechelic P3HT following the McCullough's method.[1] Few reports present the synthesis of end-functionalized P3HT[2,3] and we followed the procedure of Baumgartner, Sutherland and colleagues,[4] who showed an almost complete functionalization of their linear polymer chains.

GRIM polymerization takes place in two steps. The first one consists in the activation of the monomer 2,5-dibromo-3-hexylthiophene with methylmagnesium bromide. Addition of [1,3-

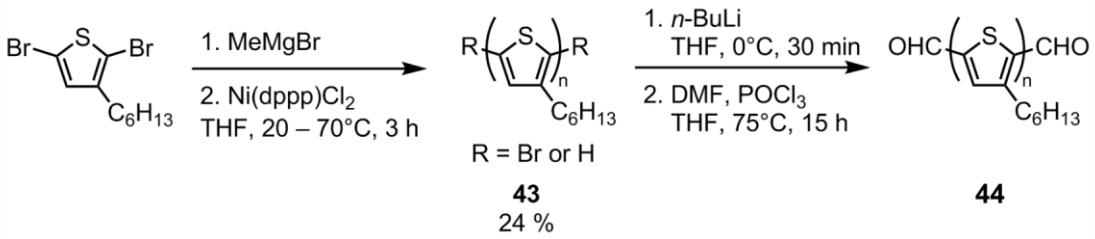

Scheme 5.1. Synthesis of telechelic P3HT by GRIM polymerization and further end-functionalization.

bis(diphenylphosphino)propane]dichloronickel(II) ($Ni(dppp)Cl_2$) starts the polymerization to afford poly(3-hexylthiophene) **43** with 24 % yield in mass (Scheme 5.1). We explained previously that GRIM polymerization of P3HT leads to polymer having either hydrogen or bromide end-groups (Chapter 2, section 2.3.5). The relative amount of these end-groups can be determined by ^{1}H NMR because they provide characteristic signals, where α-methylene protons of the alkyl chains of the final thiophene unit gives a triplet at 2.65 ppm and 2.57 ppm when either a hydrogen or a bromide are present, respectively (Figure 5.1).[5] In our case, we obtain an average number molecular weight $\overline{M_n}$ of 2 500 g·mol^{-1}, which is similar to what was obtained by MALDI-TOF (M_p = 3 300 g·mol^{-1}). GPC analysis, however, gave a much higher value ($\overline{M_n}$ = 24 000 g·mol^{-1}, see Appendix B), which may indicate the presence of aggregates. Moreover, **43** seems to have 70 % of bromine end-groups considering the relative integration of the aforementioned characteristic triplets.

Since all end groups are not identical, it was necessary to remove the terminal bromides before pursuing the functionalization. This can be achieved by lithiation followed by hydrolysis, thereby leading to polymers having terminal hydrogens. End-groups can then be converted to aldehydes group by the Vilsmeier-Haack reaction with dimethylformamide (DMF) and phosphorus oxychloride $POCl_3$ to afford α,ω-diformyl-P3HT **44** (Scheme 5.1). ^{1}H NMR characterization of this compound, however, did not show any peak around 10 ppm, characteristic of the presence of aldehydes. The characterization of the intermediate compound obtained after lithiation showed little debromination

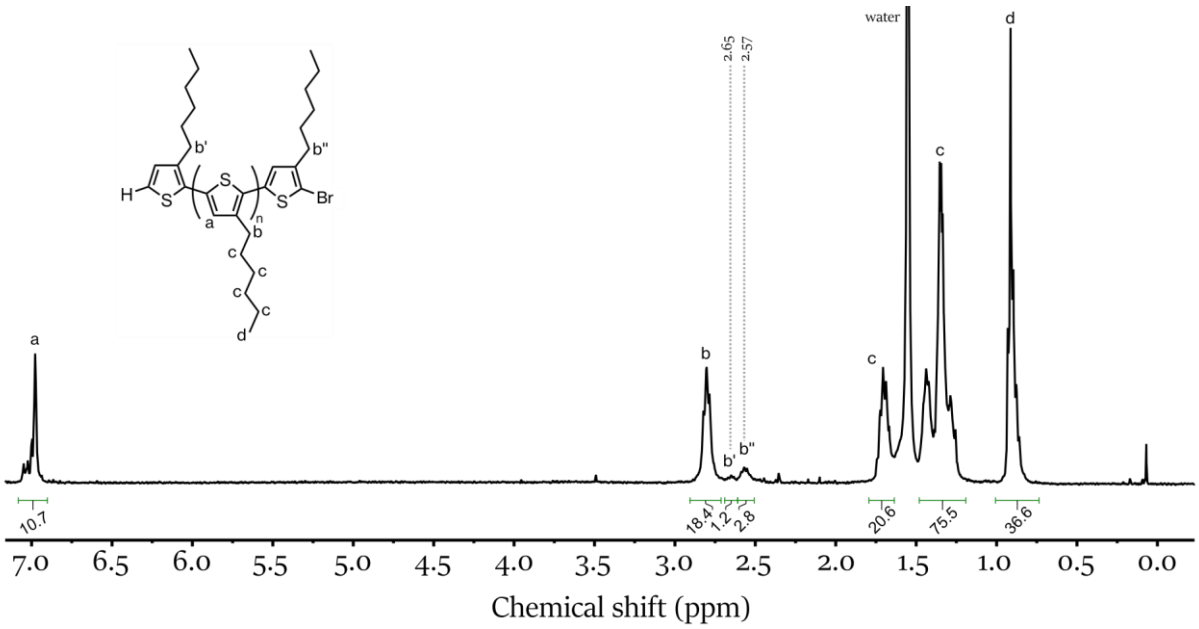

Figure 5.1. ^{1}H NMR spectrum of compound **43** in $CDCl_3$. The average molecular weight can be estimated by integrating the end-groups at 2.65 and 2.57 ppm.

(55 % of remaining terminal bromides) so this step requires some optimization. For instance, the reaction with *n*-BuLi could be run for longer times.

We have not yet further optimized the synthesis of telechelic P3HT. The reaction leading to the formation of terminal hydrogens did not work as efficiently as expected and optimization of the synthetic pathway has to be performed. In order to obtain 'clickable' telechelic P3HT, we envision to reduce the aldehydes to obtain the corresponding alcohols. Then, similarly to the synthetic pathway already used for PEG (Chapter 4, section 4.1), mesylation and substitution with sodium azide, or deprotonation and substitution with propargyl bromide, may lead to the functional polymers of interest.

5.2 Synthesis of sodium poly(styrene sulfonate)

NaPSS is a polyelectrolyte and, therefore, its persistence length depends on the ionic strength of the solution in which it is dissolved. Atom-transfer radical polymerization (ATRP), which detailed mechanism was discussed previously (Chapter 2, section 2.3.3), is commonly used for the synthesis of telechelic vinyl polymers. The preparation of end-functionalized NaPSS has already been described in the literature in protic media in the presence of copper chloride (CuCl) and 2,2'-bipyridyl (bpy).[6,7]

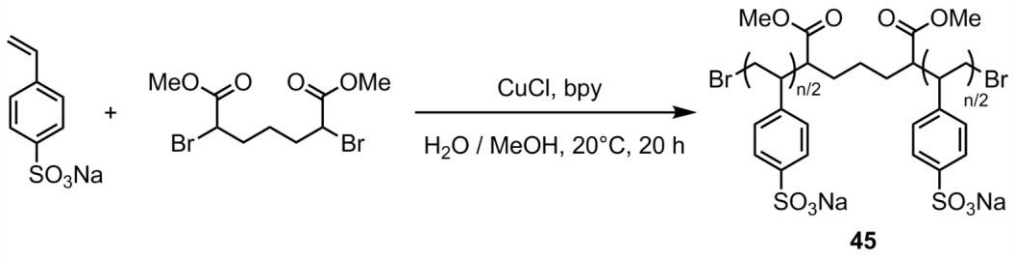

Scheme 5.2. Synthesis of telechelic NaPSS **45** by ATRP initiated with DBHD.

We conducted the polymerization in these conditions with dimethyl 2,6-dibromoheptanedioate (DBHD) as difunctional initiator (Scheme 5.2) to obtain α,ω-dibromo-PSS **45**. The conversion was followed by ^{1}H NMR by comparing the relative integration of the vinyl hydrogens of the monomer and the main-chain hydrogens of the polymer. We performed the synthesis several times and the conversion never exceeded 50 %, which is below reported values in the literature.[6] We expected low conversion because the solution turned from a dark red color to a light blue one after 30 min only, indicating conversion from the Cu(I) complex to Cu(II) and, hence, interruption of the polymerization.

We performed the same polymerization with a monofunctional initiator used in the literature, sodium 4-(bromomethyl)benzoate,[6,8] to assess if this issue was caused by DBHD. The same low conversion was observed. Therefore, the most probable explanation is that our system was not airtight and, consequently, oxidation of Cu(I) to Cu(II) occurred faster than the polymerization. This issue is purely technical, and optimization of the setup is currently undergoing to obtain the telechelic polymers.

Once a proper conversion is obtained for the polymerization of **45**, functionalization should be straightforward. Conversion of bromine end-groups to azide ones in the presence of Cu(I) was already reported for polymers formed by ATRP in a 'one pot' reaction,[9] and this strategy has been applied to NaPSS.[8] The current limitation, for now, is related to the yield of polymerization in our case.

5.3 Synthesis and characterization of poly(*N*-isopropylacrylamide)

The synthesis of PNIPAAm by ATRP has been widely investigated,[10,11] especially by Haddleton and coworkers.[12,13] We decided to follow their procedures described using the SET-ATRP of PNIPAAm in aqueous solutions.

The first step consisted in preparing a solution of catalyst. CuBr and tris[2-(dimethylamino)ethyl]amine (Me_6TREN) were dissolved in a 4 : 1 mixture in volume of deoxygenated water : methanol. The solution turned blue due to the disproportionation of Cu(I) into Cu(II) and we observed the formation of dark particles, which are certainly Cu(0) resulting from the same reaction. The mixture was further deoxygenated by bubbling argon to ensure that limited amount of oxygen was present. The ratio initiator : metal : ligand was always kept at 1 : 1.6 : 0.8 for all the reactions.

Separately, a solution of monomer and bifunctional initiator was prepared. *N*-isopropylacrylamide and DBHD were solubilized in the same deoxygenated solvent system as for the catalyst. The ratio monomer : initiator was varied to reach different polymerization degrees and, hence, molar masses, namely $\overline{M_{n,th}}$ = 5 500 (n = 50), 17 000 (n = 150) and 36 000 (n = 320) g·mol^{-1}. The mixture was thoroughly deoxygenated and transferred to the catalyst solution for polymerization (Scheme 5.3). The conversion was followed by ^{1}H NMR, where the relative integration of the signals from the vinyl protons of the monomer and from the protons of the polymer were compared. In all three cases, full conversion was reached before 1 hour of reaction. Importantly, it was necessary to cool the system to 0°C for n = 50 to avoid the formation of a gel; in this case, the higher concentration of propagating radicals may lead to more side reactions when the polymerization is performed at room temperature.

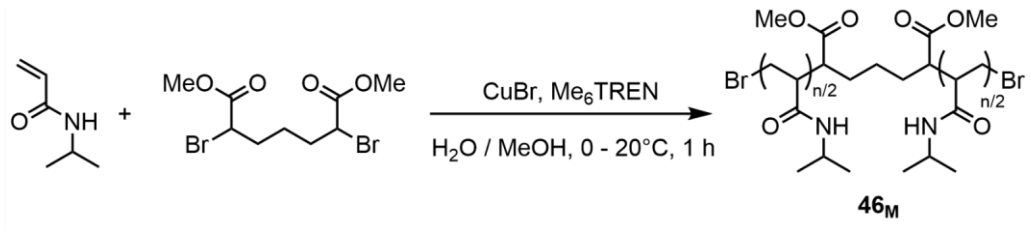

Scheme 5.3. Synthesis of telechelic PNIPAAm $\mathbf{46_M}$ by SET-ATRP.

The different polymers were further characterized by GPC and MALDI-TOF. GPC provided average number molecular weights $\overline{M_{n,GPC}}$ of 30 600, 29 900 and 54 600 g·mol^{-1} for $\mathbf{46_{5500}}$, $\mathbf{46_{17000}}$ and $\mathbf{46_{36000}}$ respectively (**see Appendix B)**. These three values are higher than the theoretical ones predicted from the ratio between the monomer and the initiator. One possible explanation is that not

all active sites initiated polymerization, which may be caused by low solubility of DBHD in the solvent. Concerning MALDI-TOF analysis, only **46$_{5500}$** provided an exploitable spectrum; for higher molecular weights, spectra were ill-defined, and a quantitative analysis was not possible. It may be caused by the fact that polymers with high molecular weights cannot be properly ionized and an optimization of the matrix or of the experimental conditions is necessary.

MALDI-TOF of **46$_{5500}$** was used for probing the nature of the end groups of the polymer (Figure 5.2). Two distributions are observed; the one at higher molecular weights corresponds to $[M]^+$ and the other one corresponds to $[M]^{2+}$ / 2. Moreover, each of these two distributions is constituted of two sets of peaks (Figure 5.2.B). The pairs of peaks are spaced by $\Delta(^{m}/_{z}) = 113$ g·mol^{-1}, corresponding to the molecular weight of the monomer. Following equation 4.2 (Chapter 4, section 4.1.2) for the determination of the end groups by MALDI-TOF, one set of peaks closely matches the molecular masses of polymer chains with fully hydrolyzed chain ends, where the bromine groups were replaced by alcohols. In that case, m_{mono} = 113.08 g·mol^{-1} and m_{end} = 220.09 g·mol^{-1}. For n = 48, we obtain $[M+Na]^+$ = 5 670.93 g·mol^{-1} and the experimental value is 5 672.55 g·mol^{-1}. On the other hand, the remaining set of peaks closely matches the theoretical values obtained for polymer chains with one hydrolyzed chain end. For this structure, we have m_{end} = 282.01 g·mol^{-1} and, for n = 48, we obtain $[M+Na]^+$ = 5 732.84 g·mol^{-1}, with an experimental value of 5 729.97 g·mol^{-1}. ATRP usually provides high-end group fidelity but, in our case, hydrolysis may have occurred because the polymers were left in solution for long times, especially during the purification by dialysis. Nevertheless, hydrolysis of PNIPAAm occurring after ATRP has previously been exploited to easily form hydroxy-terminated polymers.[13]

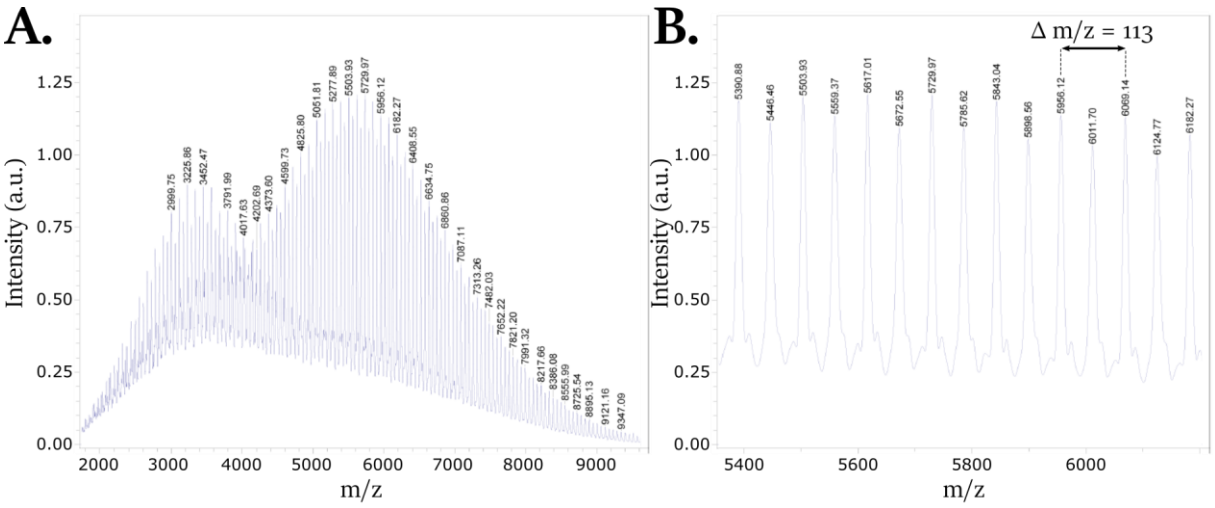

Figure 5.2. MALDI-TOF spectrum obtained for **46$_{5500}$** plotted in the range: **A**. 2000 – 10000 m/z; **B**. 5400 – 6200 m/z.

For our systems, we need fully homotelechelic polymers for the reticulation with tetrafunctional molecular motors. Therefore, our investigations are currently on-going to fully hydrolyze the synthesized PNIPAAm. The resulting α,ω-dihydroxy-PNIPAAm may consequently be functionalized following a similar synthetic pathway as previously used for PEG (Chapter 4, section 4.1.1). Another possibility is to perform a 'one-pot' azidation once polymerization reached full conversion, as we envisioned for NaPSS (section 5.2).[8]

5.4 End-functionalization and reticulation of poly(dimethylsiloxane)

Compared to all other polymers investigated for the formation of networks crosslinked with molecular motors, PDMS is the only one that has a glass transition below room temperature (see Chapter 2, section 2.3.2 for further details). Therefore, we expected that we could form a dry photoactive network. α,ω-dihydroxy-PDMS are commercially available, and the work presented here was performed on a polymer having a molecular weight of 8 000 g·mol^{-1}.

5.4.1 Synthesis and characterization of α,ω-diazido-PDMS

Since hydroxy-terminated PDMS is commercially available, the same synthetic pathway as for PEG (Chapter 4, section 4.1.1) was followed (Scheme 5.4). Terminal alcohols were first activated towards nucleophilic substitution by mesylation to afford α,ω-dimesylate-PDMS **47** in good yield. Subsequent substitution of the end groups with sodium azide led to the targeted α,ω-diazido-PDMS **48** in very good yield.

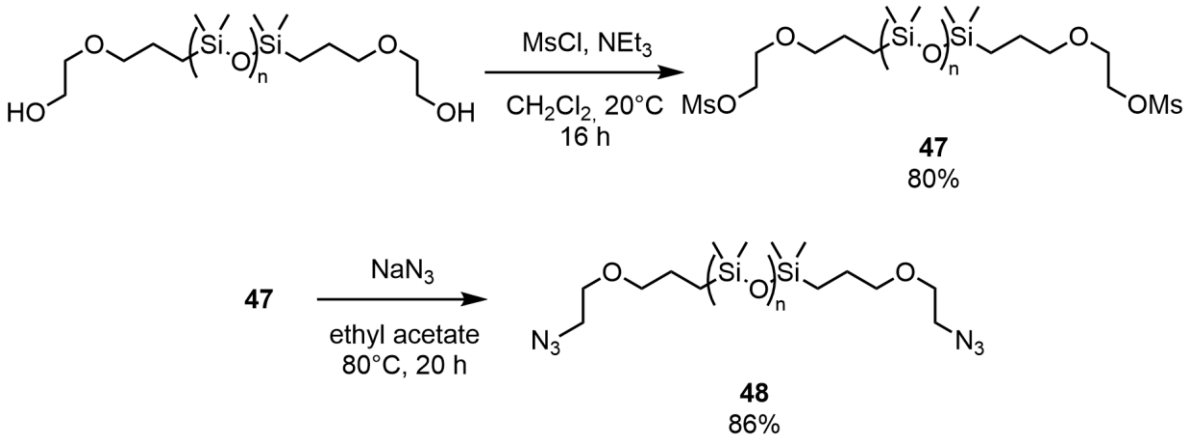

Scheme 5.4. End-functionalization of PDMS to obtain α,ω-diazido-PDMS **48** via intermediate mesylation of the terminal hydroxyl groups.

The functionalization was followed by ^{1}H NMR spectroscopy (Figure 5.3). Mesylation of the terminal alcohols led to a significant shift of the signals of the methylene protons close to the end groups and a new singlet at 3.60 ppm appeared, characteristic of the mesyl group. No residual signals

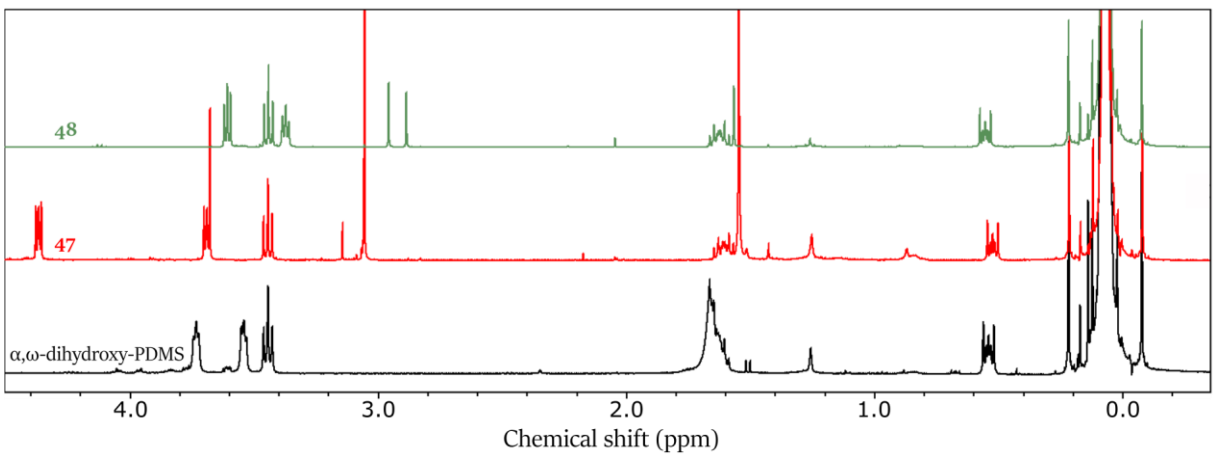

Figure 5.3. ^{1}H NMR spectra of α,ω-dihydroxy-PDMS, α,ω-dimesylate-PDMS **47** and α,ω-diazido-PDMS **48** in $CDCl_3$.

from the same protons of α,ω-dihydroxy-PDMS were observed, indicating full conversion. Azidation also shifted the signals of these protons and the peaks observed previously disappeared, meaning that full conversion of the end groups also occurred at this step. Normalized relative integration of the signals of the end groups compared to the signal of the main chain gave $\overline{M_{n,RMN}}$ = 8 500 g·mol^{-1}, which is close to the value obtained by GPC $\overline{M_{n,GPC}}$ = 7 700 g·mol^{-1} (see Appendix B).

We determined the overlap concentration c* of the polymer by viscometry (Figure 5.4). Following the procedure described for the determination of c* for different PEG (Chapter 4, section 4.2.1), we prepared a series of solution of **48** in dichloromethane to determine their reduced viscosities η_{red}. Extrapolation of η_{red} to zero concentration gives an intrinsic viscosity [η] = 0.01079 mL·mg^{-1} for the polymer. Finally, c* is taken as the inverse of [η], which gives c* = 93 mg·mL^{-1}. In practice, however, no gels were formed for concentrations below 110 mg·mL^{-1}. The discrepancy between these two values may be first explained by the need of a scaling factor between c* and [η], as observed for PEG (Chapter 4, section 4.2.1). The other possibility is related to the high dispersity of the polymer since higher molecular weights contribute more to the viscosity than lower ones; consequently, the value of [η] would correspond to a less disperse system of higher molecular weight.

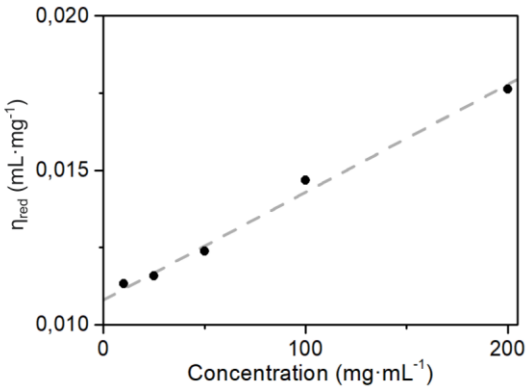

Figure 5.4. Evolution of the reduced viscosity η_{red} depending on the concentration of α,ω-diazido-PDMS **48** in CH_2Cl_2.

The end-functionalization of PDMS chains was achieved similarly to the one used for PEG and gave fully functionalized telechelic polymers that could be crosslinked with molecular motors. The optimal concentration determined by viscometry, however, did not lead to the formation of gels and a concentration of 110 mg·mL^{-1} was used instead.

5.4.2 Formation of photoactive networks of PDMS and their contraction behavior

The procedure for the formation of gels made of PDMS was almost identical to the one used for the formation of PEG-based gels (Chapter 4, section 4.2.2). The only difference was the use of motor *(S)*-**28** instead of *(S)*-**25** to match the terminal azides of the polymers for the 'click' reaction.

The gels **Gel$_{PDMS}$** were formed by copper-catalyzed azide-alkyne cycloaddition (CuAAC) between α,ω-diazido-PDMS **48** and tetra-alkyne motor *(S)*-**28** (Scheme 5.5). As for gels made of PEG, two solutions were separately prepared in dichloromethane: one containing the polymer and the copper catalyst, the other one containing the motor. Thus, contrariwise to what we described in the previous chapter, CuBr and its ligand were dissolved along with PDMS because, in this case, the motor bears

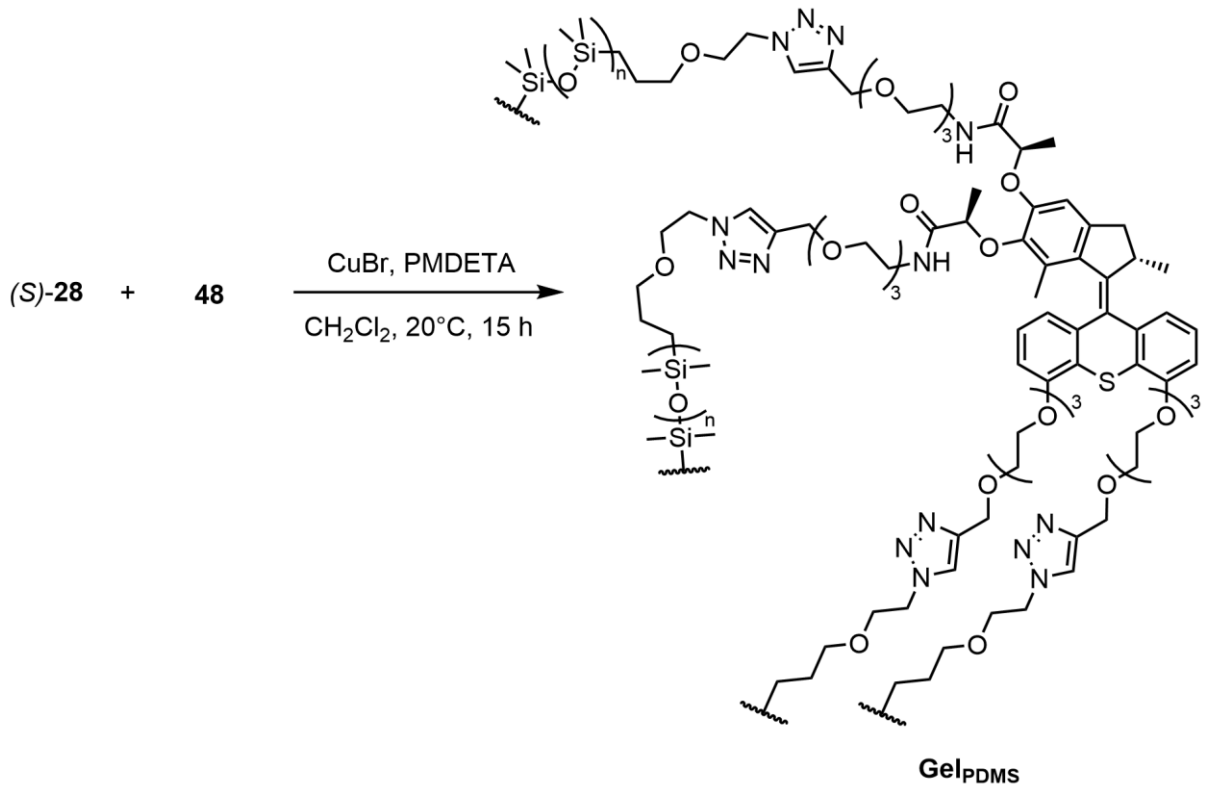

Scheme 5.5. Formation of **Gel$_{PDMS}$** from telechelic **48** and tetrafunctional *(S)*-**28** by CuAAC.

the alkyne groups where Glaser coupling must be avoided. Gels were prepared in molds of two different thicknesses. For irradiation experiments where networks are swollen, materials were formed with a thickness of 0.75 mm, as we determined previously that it led to faster contraction kinetics (Chapter 4, section 4.3.3). For experiments where the dry network is studied, however, we prepared gels with an initial thickness of 4 mm to accommodate the volume loss caused by the evaporation of dichloromethane. The dry films **Film$_{PDMS}$** were obtained after slow evaporation of the solvent at atmospheric pressure and further drying under vacuum.

Gel$_{PDMS}$ was irradiated with the same system as the one presented for the irradiation of PEG-based gels (Chapter 4, section 4.3.1). Gels were swollen in THF and transferred in a cylindrical quartz cell

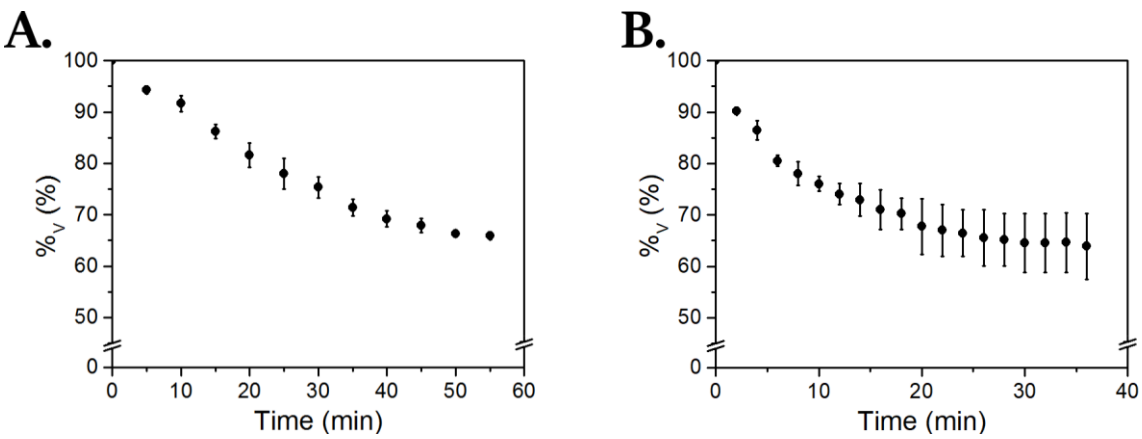

Figure 5.5. Evolution of the relative volume $\%_V$ as a function of irradiation time for **Gel$_{PDMS}$** at **A**. 80 mW·cm^{-2} and **B**. 365 mW.cm^{-2}.

placed in between a camera and the source of UV light. The relative surface of the material as seen by the camera was converted to the corresponding relative volume following equation 4.5 (Chapter 4), considering an isotropic contraction (Figure 5.5.A). **Gel$_{PDMS}$** was first irradiated at 80 mW·cm^{-2} because it was at that light power density that we measured the gels of PEG having different molecular weights (Chapter 4, section 4.3.5). The gel reaches a final volume $\%_{V,max}$ of 66 ±1 % with a maximum contraction rate of γ = 0.98 %·min^{-1}, which is in the same range of the values obtained for gels formed with PEG of 6 000 g·mol^{-1}.

Since the swelling equilibrium did not change between gels swollen in their reticulation solvent and gels swollen in their irradiation solvent, the polymer strand density ϕ_s can be calculated following equation 4.6 (Chapter 4, section 4.3.5). For PDMS, ν_{PDMS} = 1.03 mL·g^{-1}, and for PEG, ν_{PEG} = 0.89 mL·g^{-1} (see Appendix A). Therefore, **Gel$_{PDMS}$** has a strand density $\phi_{s,PDMS}$ of 0.113, while for PEG, we obtain $\phi_{s,3000}$ = 0.069 and $\phi_{s,3000}$ = 0.053 for **Gel$_{3000}$** and **Gel$_{6000}$**, respectively. Interestingly, such high strand density of the network lead to a surprisingly efficient contraction of **Gel$_{PDMS}$**. Considering our results for PEG-based gels (Chapter 4, section 4.3.5), we would have expected to have a detrimental impact on the contraction behavior, since the polymer chains have less available space to freely move during the braiding process. We believe that the higher flexibility of PDMS, with its shorter persistence length (*vide infra*), is responsible for this behavior by counterbalancing the higher strand density.

Considering this result, we investigated the contractile behavior at the highest available light power density (Figure 5.5.B). The gel contracts until $\%_{V,max}$ = 64 ± 7 % of its initial volume with a maximum contraction rate γ = 8.5 %·min^{-1} when irradiated with UV light at 365 mW·cm^{-2}. The final relative volume $\%_{V,max}$ is statistically identical to the one obtained with a lower light intensity, confirming our previous observations for gels based on PEG (Chapter 4, section 4.3.3). However, the value of γ is higher than the one obtained for the fastest PEG-based system, which was 5.1 %·min^{-1} for **Gel$_{10000}$**. Therefore, altering the flexibility of the polymer chains composing the network is another parameter to tune the contraction efficiency of our photoactive materials, where decreasing the persistence length of the strands increases the contraction rate.

Gel$_{PDMS}$ were also investigated by SANS (Figure 5.6). As for the gels based on PEG, we determined the persistence length l_p and the correlation length of the mesh ξ for this system (see Chapter 4,

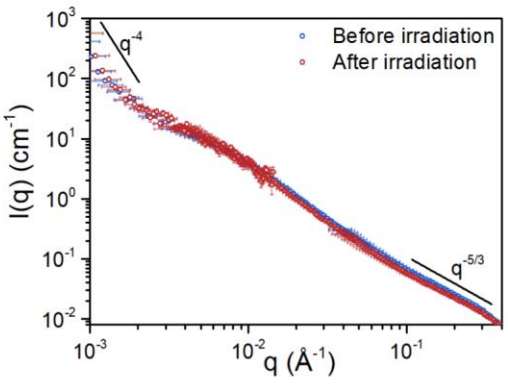

Figure 5.6. SANS spectra of **Gel$_{PDMS}$** in *d*-THF before and after 1 h of UV irradiation at 160 mW·cm^{-2}.

section 4.4 for details on the interpretation of SANS data). The scaling between I(q) and $q^{-5/3}$ in the high-q range indicates that PDMS behaves as a chain swollen in a good solvent. The $q^{-5/3}$ – q^{-1} transition is not seen in the spectra until $q^* = 0.4$ Å^{-1}, indicating that l_p is lower than 0.5 nm, which is in the range of previously reported value for PDMS.[14,15] This result corroborates the fact that PDMS is more flexible than PEG and may explain the difference in contractile behavior. A Lorentzian fit in the mid-q range gives ξ = 22 nm before irradiation and ξ = 29 nm after irradiation. The increase in ξ after irradiation is coherent with our previous studies on gels based on PEG (Chapter 4, section 4.4) where the braiding of polymer strands by molecular motors increases the distance between twisted pairs of chains and, hence, increases the mesh size.[16] For **Gel$_{PDMS}$**, ξ is multiplied by 1.3 after irradiation; this scaling factor is higher than the one obtained for **Gel$_{3000}$** prepared at its c*, for instance (Chapter 4, section 4.4). It corroborates the hypothesis that the higher polymer strand density is balanced by the increased flexibility of the chain, which leads to high contraction efficiency.

A dry **Film$_{PDMS}$** was also studied when irradiated with UV light (Figure 5.7). Films were formed by first drying **Gel$_{PDMS}$** at atmospheric pressure, followed by drying under vacuum until constant mass. The material laid flat on a surface and the films tend to stick; therefore, during the drying process, where the material contracts, the side in contact with the surface did not experience the same shear force as the one open to air, and this gradient led to bent films (Figure 5.7.A). The shape change of the films resembles bending, but quantification of the bending angle was not possible for all pieces that we investigated; consequently, we decided to observe the volume change of our films. The conversion from the relative surface to the relative volume over time was more difficult than for gels, but the calculations were performed by considering overlapped surfaces and averaging the evolution of the surface seen from the side and seen from the front at the same time. The films contracted to $\%_{V,max} = 83 \pm 10$ % of their initial volume. The standard deviation is relatively high because of limitations caused by the bent shape of the material. Nevertheless, the volume of **Film$_{PDMS}$** changed over time and this experiment shows for the first time the continuous unidirectional motion of molecular motors in dry amorphous polymer networks. Since the network is above its glass transition temperature, the surroundings of the photoactive motors are mobile enough to allow the rotation and, hence, the braiding of the network strands, which ultimately leads to a volume decrease

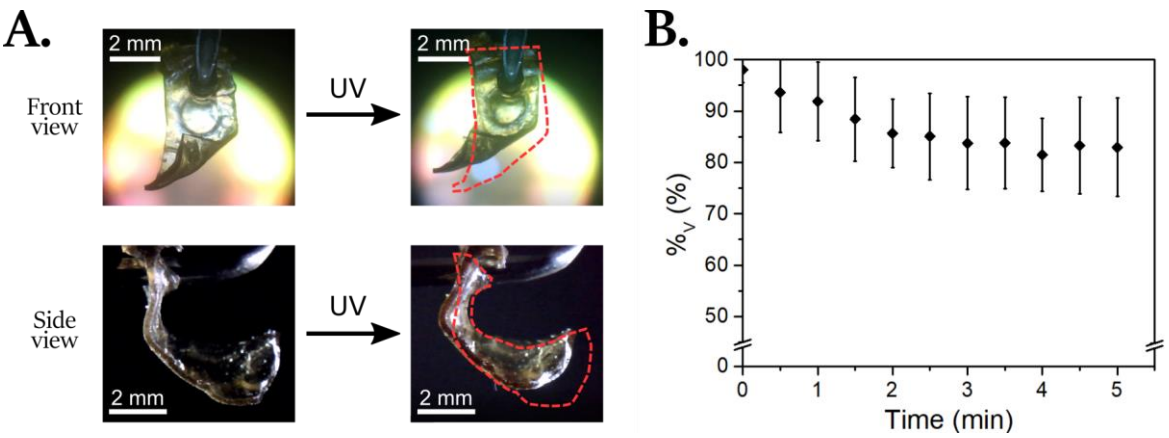

Figure 5.7. A. Snapshots of **Film$_{PDMS}$** from the front and from the side, before and after UV irradiation for 5 min at 365 mW·cm^{-2}. The dashed red lines highlight the shape of the film before irradiation. **B.** Relative volume $\%_V$ of **Film$_{PDMS}$** at different times under UV irradiation at 365 mW·cm^{-2}.

of the material. The higher $\%_{V,max}$, compared to the swollen **Gel$_{PDMS}$**, may be explained by the fact that, in the dry state, the polymer strands are already entangled because of their higher concentration. The maximum contraction rate of the system is γ = 6.4 %·min^{-1}, which is only 24 % lower than the value obtained for the swollen network irradiated at the same light intensity.

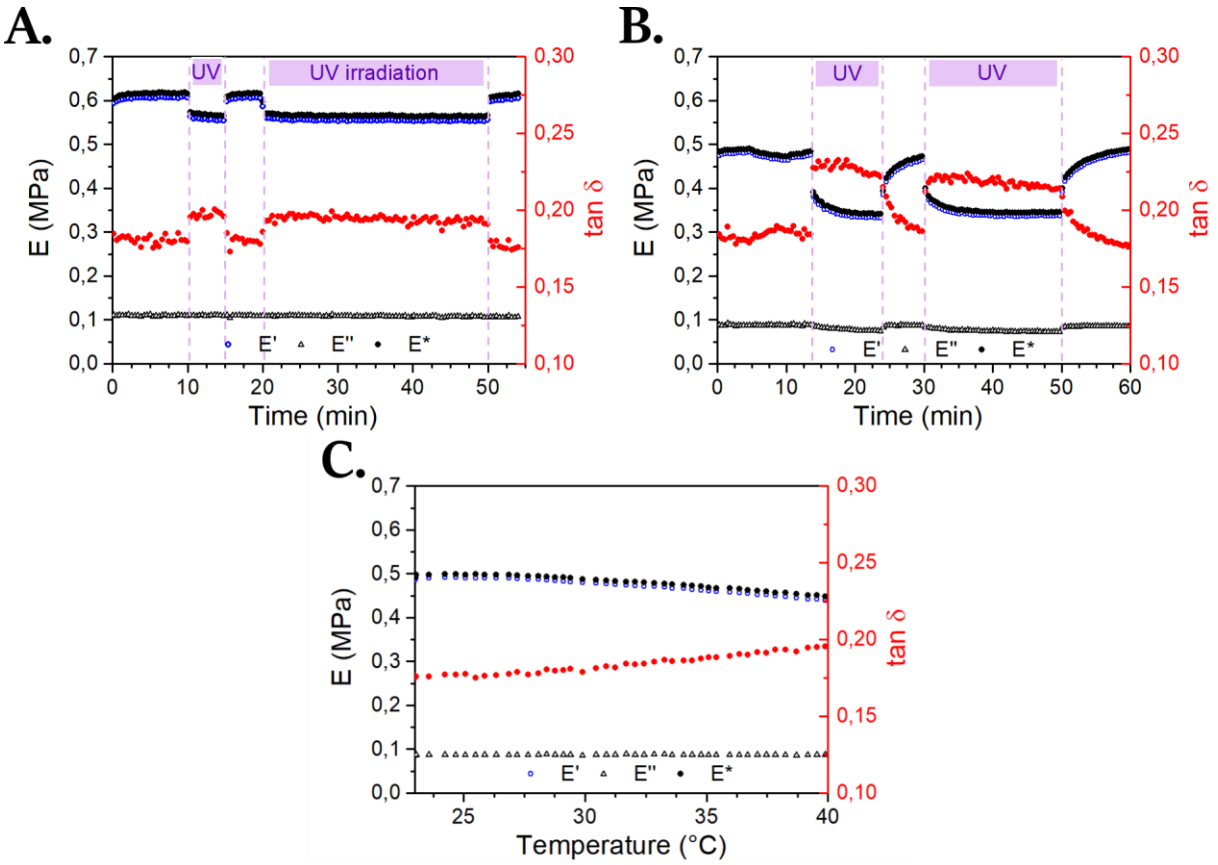

Figure 5.8. DMA of **Film$_{PDMS}$** in tensile mode with ε_o = 50 µm (2 %) at f = 1 Hz. **A.** The film was irradiated at different times (purple area) at 40 mW·cm^{-2}. **B.** The film was irradiated at different times (purple area) at 365 mW·cm^{-2}. **C.** The film was heated from room temperature to 40°C without UV light irradiation.

In order to further elucidate the mechanism leading to the contraction of **Film$_{PDMS}$**, the films were studied by dynamic mechanical analysis (DMA, Figure 5.8). Films were irradiated with two light power densities: 40 mW·cm^{-2} (Figure 5.8.A) and 365 mW·cm^{-2} (Figure 5.8.B). In both cases, UV irradiation leads to a decrease in storage modulus E' and, hence, an increase in tan δ. The loss modulus E'' does not significantly vary and only a slight decrease is observed when the material is irradiated with UV light at 365 mW·cm^{-2}. Moreover, E'' is comparatively low; consequently, E* ≈ E'. At 40 mW·cm^{-2}, irradiation of **Film$_{PDMS}$** leads to a decrease of E* of 8 % from 0.62 MPa to 0.58 MPa. At 365 mW·cm^{-2}, on the other hand, E* drops by 29 %, from 0.49 MPa to 0.35 MPa. Two different pieces of **Film$_{PDMS}$** were tested for the different light powers and the difference in initial E* may be explained by the inhomogeneities of the material. In both cases, turning off the light source restores E* to its initial value. We expected an increase in E* caused by a higher number of entanglements when the motors intertwine polymer chains, as observed for gels based on PEG.[17] Here, neither during irradiation nor after irradiation did we observe this behavior; only a decrease in E* was observed when the material was irradiated. This photo-softening effect is commonly observed for materials containing photoswitches and may be caused by two mechanisms: the photothermal one,

and the photomechanical one (see Chapter 2, section 2.2.2, for further details). For the former, heat is dissipated by the photoactive molecular motor and, hence, softens the matrix, as recently reported, for instance, for molecular motors incorporated in liquid crystalline elastomers.[18,19] The photomechanical effect, however, suggests that the motion of photoactive moieties increases their excluded volume and may locally increase the mobility of nearby polymer chains, hence softening the matrix as well. In practice, both mechanisms are involved.[20]

The contribution of the photomechanical effect can be investigated by heating **Film$_{PDMS}$** and observing the changes in mechanical properties (Figure 5.8.C). Heating the film from 23°C to 40°C decreased E* by 10 %, from 0.50 MPa to 0.45 MPa. If we consider a linear relationship between the decrease in E* and the temperature, it would be necessary to heat **Film$_{PDMS}$** to approximately 80°C to reach the same change in E* than when it is irradiated at365 mW·cm^{-2}. This temperature may be reached with photoswitches,[20] so the photothermal effect may be a significant factor to the behavior of **Film$_{PDMS}$** observed by DMA. However, the volume change observed for free-standing **Film$_{PDMS}$** (Figure 5.7) cannot be only explained with this mechanism, since the material did not recover its initial shape when UV light was turned off.

We hypothesized that only a photothermal effect was observed during DMA because of the load applied on **Film$_{PDMS}$** during the measurement. This force may oppose the torque generated by the rotation of the motors and, hence, decrease their rotation speed down to the point where they cannot operate. We tested this hypothesis by attaching a small load (10 mg) to free-standing **Film$_{PDMS}$** to observe if any change in the evolution of the relative volume $\%_V$ would occur. Irradiation of the loaded material with UV light at 365 mW·cm^{-2} did not lead to any significant change in volume (Figure 5.9). Considering the mass of the hook, the force on the film increased by approximately 0.1 mN, which is 100 times smaller than the force applied during DMA. Therefore, it seems that even small loads can alter the operation of molecular motors in our systems and, hence, the contractile properties of the films.

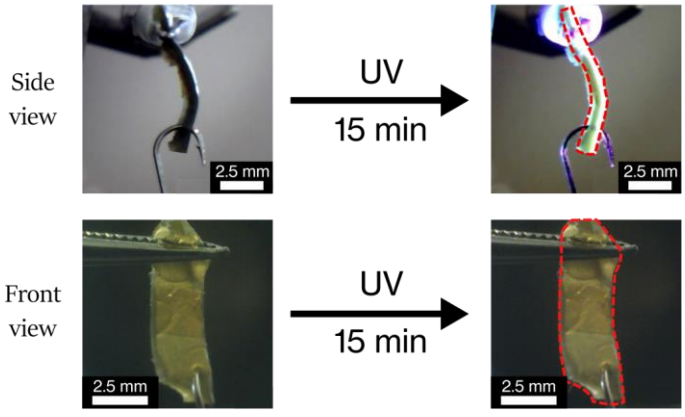

Figure 5.9. Snapshots of Film$_{PDMS}$ before and after UV light at 365 mW·cm^{-2} with a hook of 10 mg attached at the bottom, seen from the front and from the side. The shape does not change significantly under irradiation, as highlighted by the dotted red line.

Comparing the behavior of **Gel$_{PDMS}$** and gels based on PEG, it appears that the chemical nature of the polymer strands alters the photophysical properties of the materials. Proper modelling of the system must be conducted to better understand the structure-property relationship of our gels but,

nevertheless, this investigation provides insight on the effect of soft matrices on the operation of molecular motors. Our investigations on **Film$_{PDMS}$** provided the first example of actuation triggered by synthetic molecular motors in dry amorphous matrices. However, the contribution of the photothermal effect cannot be neglected for this material, and further investigation must be conducted to isolate the single effect of the rotation. Moreover, it seems that its operation is highly sensitive to external forces and exploring the impact of smaller loads might provide insight on this effect as well. Alternatively, studying the shape change for networks crosslinked with episulfides, which have a similar absorption spectrum but do not rotate, may also help determining the contribution of the photothermal effect alone.

5.5 Synthesis and gelation of four-arms poly(γ-benzyl-L-glutamate) and four-arms poly(L-glutamic acid) with cores based on molecular motors

PBLG and PGA are polypeptides that can adopt helicoidal secondary structures in solution (Chapter 2, section 2.3.6). PBLG can be synthesized by ring-opening polymerization (ROP) of γ-benzyl-L-glutamate *N*-carboxyanhydride (BLG-NGA) initiated with a primary amine. PGA may then be obtained by saponification of the esters (Scheme 5.6). This work was performed in collaboration with Prof. Lecommandoux's team (Bordeaux, France) for their expertise on the preparation and characterization of systems based on PBLG and PGA.

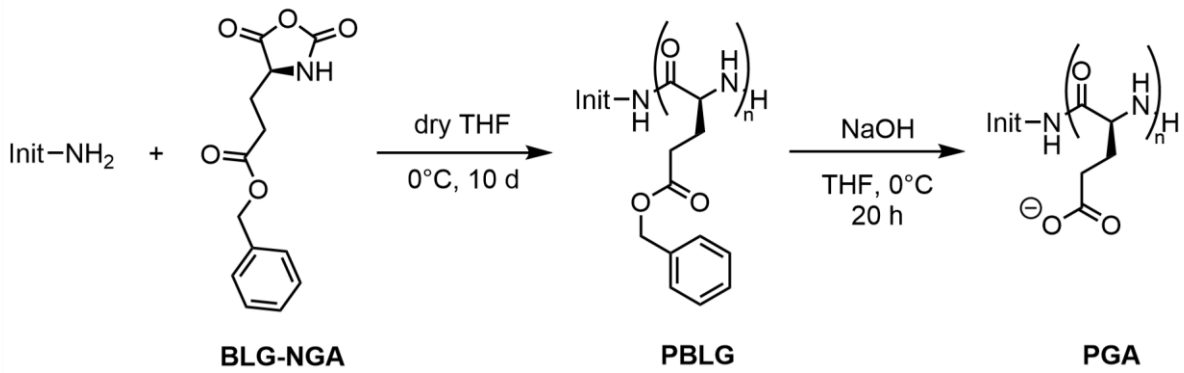

Scheme 5.6. General synthetic pathway for the synthesis of PBLG by ROP and subsequent deprotection of the benzyl groups to form PGA.

In a first attempt to prepare star-shaped polymers with PBLG and molecular motors, our collaborators prepared a linear PBLG bearing one azide at its C-extremity. All attempts to 'click' the polymers by CuAAC on tetra-alkyne motor *(S)*-**28** failed to form fully functionalized star-shaped molecules.

The strategy was then modified and tetra-amine motor *(R)*-**37** was considered as an initiator for the ROP of BLG-NGA. Our collaborators successfully synthesized **star-PBLG$_{400}$**, consisting of a motor core bearing four PBLG chains, each one containing 100 monomers on average. Moreover, saponification of this derivative successfully led to the formation of **star-PGA$_{400}$**, the deprotected analog of **star-PBLG$_{400}$**.

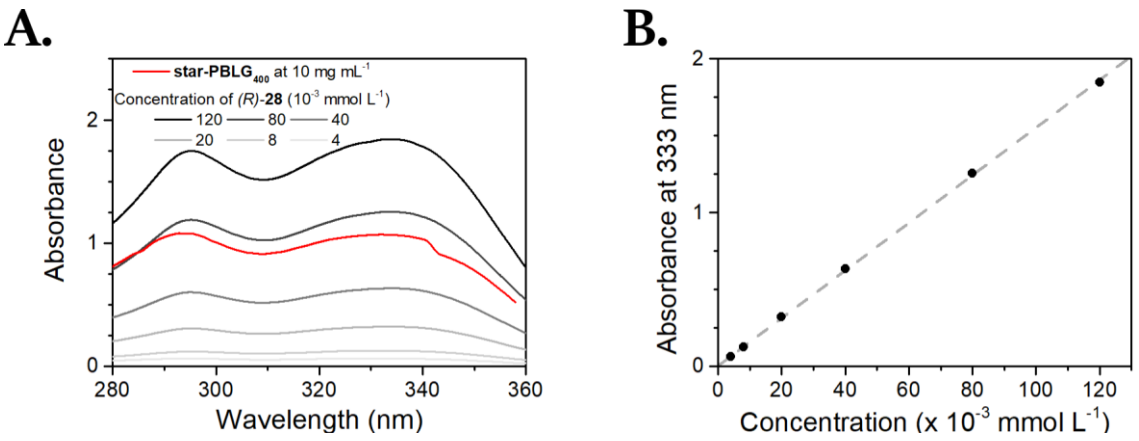

Figure 5.10. A. UV-Vis spectra of solutions of *(R)*-28 at different concentrations and star-PBLG$_{400}$ at 10 mg·mL^{-1} in DMF. **B.** Corresponding calibration curve for the determination of the concentration of motors in star-PBLG$_{400}$.

We then performed further analysis on **star-PBLG$_{400}$** and **star-PGA$_{400}$**. First, we assessed the presence of molecular motors in the star-like molecule by UV-Vis analysis (Figure 5.10). A series of solutions of *(R)*-**28** at different concentrations were prepared in DMF, as well as a solution of **star-PBLG$_{400}$** at 10 mg·mL^{-1}. Their UV-Vis spectra were recorded, and a calibration curve was established according to the Beer-Lambert law. We determined that the solution of **star-PBLG$_{400}$** at 10 mg·mL^{-1} contains a concentration of molecular motors of 69 × 10^{-3} mmol·L^{-1}, meaning that polymers have an average molecular weight of $\overline{M_n}$ = 1.5 × 10^5 g·mol^{-1}, which is in the same order of magnitude to the value obtained in Bordeaux by GPC.

As a preliminary experiment, we prepared a physical gel of **star-PBLG$_{400}$** in toluene (Figure 5.11). 20 mg of the polymer were dissolved in 1 mL of toluene upon heating at 80°C and with vigorous stirring. After cooling down to room temperature, a sol-to-gel transition occurred. The gel was irradiated with UV light at 365 mW·cm^{-2} and we observed syneresis. This phenomenon cannot be fully attributed to a photothermal effect from the motors, as observed for **Film$_{PDMS}$** (section 5.4.2), because when the UV light was turned off, the sol-to-gel transition did not occur. However, the system could return to its gel state by applying a new heating-cooling cycle. This newly formed gel was also irradiated again with UV light and syneresis was again observed. Therefore, this system represents the first example of a photoactive reversible physical gel based on our tetra-functional molecular motors.

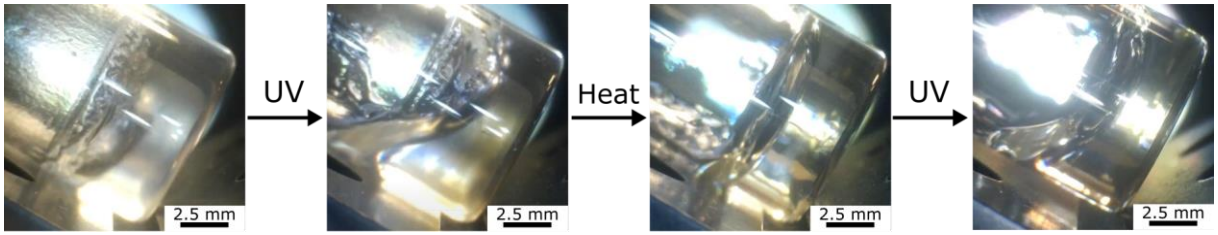

Figure 5.11. Physical gel of **star-PBLG$_{400}$** prepared in toluene at 20 mg·mL^{-1}. The gels were formed by heating the solution at 80°C while stirring it and letting it cool to room temperature. Under UV irradiation, syneresis occurred and the gel did not form back when the UV light was turned off. The gel state could be restored by re-heating and re-cooling the material, which would show syneresis again under UV light.

Although our collaboration with Prof. Lecommandoux's team is still at its infancy, these first experiments are promising. We have now designed a tetra-amine molecular motor that can be used as an initiator for ROP. The resulting polymers could form reversible physical gels where syneresis occurs under UV light. We are also currently investigating this system further since the effect that we observed do not seem to be cause only by a photothermal effect.

5.6 Conclusion and perspectives

The preparation of tetra-functional molecular motors allows the easy modulation of the nature of the telechelic polymer chains used for reticulation. The synthesis of end-functional macromolecules is well-described in the literature, but we still faced challenges to prepare azide- and alkyne-terminated chains. We believe, however, that we can succeed by optimizing the synthetic pathways that we followed.

Nevertheless, we managed to prepare photoactive networks of PDMS. From our studies, it appears that the higher flexibility of the chain enhances the kinetics of contraction of the gels, compared to the systems based on PEG. Moreover, and for the first time, we observed that molecular motors could operate their unidirectional motion in soft amorphous polymer matrices. Although there may be a significant contribution of the photothermal effect, the irreversibility of the shape change still suggests that the motors rotate in this system.

Finally, preliminary results of systems based on peptides are promising. We only tested the formation of physical gels containing our molecular motors, which were, for the first time as well, thermally reversible. Further investigations on these materials are currently ongoing.

The modularity of our design paves the way to a plethora of possibilities to prepare photoactive materials based on multifunctional molecular motors. A wide library of polymers with their own properties may therefore be integrated in these systems in order to study the influence of the work generated by molecular machines on their behavior. Similarly, this design allows for the study of the impact of different matrices on molecular motors, and we believe that it may provide valuable insight into the operation mechanism of molecular machines in soft matter.

References

1. R. S. Loewe, S. M. Khersonsky, R. D. McCullough, *Adv. Mater.* **1999**, *11*, 250–253.
2. M. Chevrier, G. Lopez, W. Zajaczkowski, J. Kesters, R. Lenaerts, M. Surin, J. De Winter, S. Richeter, W. Pisula, A. Mehdi, et al., *Synth. Met.* **2019**, *252*, 127–134.
3. C. Enders, S. Tanner, W. H. Binder, *Macromolecules* **2010**, *43*, 8436–8446.
4. R. A. Krüger, T. J. Gordon, T. Baumgartner, T. C. Sutherland, *ACS Appl. Mater. Interfaces* **2011**, *3*, 2031–2041.
5. D. S. Dissanayake, E. Sheina, M. C. Biewer, R. D. McCullough, M. C. Stefan, *J Polym Sci A Polym Chem* **2017**, *55*, 79–82.
6. P. D. Iddon, K. L. Robinson, S. P. Armes, *Polymer* **2004**, *45*, 759–768.
7. C.-K. Choi, Y.-B. Kim, *Polym. Bull.* **2003**, *49*, 433–439.

8. R. De, M. Jung, H. Lee, *Int. J. Mol. Sci.* **2019**, *20*, 5582.

9. A. J. de Graaf, E. Mastrobattista, C. F. van Nostrum, D. T. S. Rijkers, W. E. Hennink, T. Vermonden, *Chem. Commun.* **2011**, *47*, 6972.

10. Y. Xia, X. Yin, N. A. D. Burke, H. D. H. Stöver, *Macromolecules* **2005**, *38*, 5937–5943.

11. M. Teodorescu, K. Matyjaszewski, *Macromol. Rapid Commun.* **2000**, *21*, 190–194.

12. Q. Zhang, P. Wilson, Z. Li, R. McHale, J. Godfrey, A. Anastasaki, C. Waldron, D. M. Haddleton, *J. Am. Chem. Soc.* **2013**, *135*, 7355–7363.

13. A. Simula, V. Nikolaou, A. Anastasaki, F. Alsubaie, G. Nurumbetov, P. Wilson, K. Kempe, D. M. Haddleton, *Polym. Chem.* **2015**, *6*, 2226–2233.

14. A. V. Dobrynin, J.-M. Y. Carrillo, M. Rubinstein, *Macromolecules* **2010**, *43*, 9181–9190.

15. T. J. Senden, J.-M. di Meglio, P. Auroy, *Eur. Phys. J. B* **1998**, *3*, 211–216.

16. G. Mariani, J.-R. Colard-Itté, E. Moulin, N. Giuseppone, E. Buhler, *Soft Matter* **2020**, *16*, 4008–4023.

17. J.-R. Colard-Itté, Q. Li, D. Collin, G. Mariani, G. Fuks, E. Moulin, E. Buhler, N. Giuseppone, *Nanoscale* **2019**, *11*, 5197–5202.

18. J. Hou, A. Mondal, G. Long, L. Haan, W. Zhao, G. Zhou, D. Liu, D. J. Broer, J. Chen, B. L. Feringa, *Angew. Chem. Int. Ed.* **2021**, anie.202016254.

19. R. Lan, J. Sun, C. Shen, R. Huang, Z. Zhang, C. Ma, J. Bao, L. Zhang, L. Wang, D. Yang, et al., *Adv. Funct. Mater.* **2020**, 2000252.

20. M. Pilz da Cunha, E. A. J. van Thoor, M. G. Debije, D. J. Broer, A. P. H. J. Schenning, *J. Mater. Chem. C* **2019**, *7*, 13502–13509.

Chapter 6
Preparation of liquid-crystalline elastomers crosslinked with molecular motors

Liquid-crystalline elastomers (LCE) are a class of materials that have been widely investigated for their use as stimuli-responsive actuators. The combination of their mechanical properties and their long-range mechanical order makes them ideal candidate as soft systems capable of large deformations (see Chapter 2, section 2.2.2, for further details). There is a substantial amount of literature on light-sensitive LCEs based on photoswitches[1] but only few reports have focused on the use of molecular motors as crosslinks inside liquid-crystalline networks. We investigated two designs for the preparation of LCE based on our tetrafunctional molecular motors. For the first one, presented in the first section, we aimed to synthesize a main-chain LCE by thiol-ene and thiol-yne 'click' reaction.[2] For the second one, we investigated a more common synthetic pathway by preparing side-chain LCE based on the photopolymerization of acrylates, and our results are presented in the second section.

6.1 Main-chain liquid-crystalline elastomers crosslinked with molecular motors

The initial design that we envisioned consisted in the preparation of main-chain LCE. In this system, we hypothesized that the braiding of the polymer strands induced by the rotation of molecular motors in the swollen state would be more impactful if the mesogenic units were incorporated in the main chain. Thiol-ene and thiol-yne photo-'click' couplings appeared to be a convenient synthetic pathway to prepare our LCE, since it has already been reported for the preparation of liquid crystalline materials[3,4] and can be easily adapted to our tetra-alkyne motor *(S)*-**28**.

Therefore, the formulation required *(S)*–**28** motor, a mesogen, a spacer and a photoinitiator (Scheme 6.2). We used 2,2-dimethoxy-2-phenylacetophenone (DMPA) as photoinitiator, which can generate radicals when irradiated at 312 nm. Commercial dithiols being available, we decided to use 1,4-butanediol bis(thioglycolate) (BTG) for its high boiling point (> 350°C) that allows for the processing of the mixture at high temperatures. Consequently, we had to prepare a mesogenic unit bearing two alkene groups.

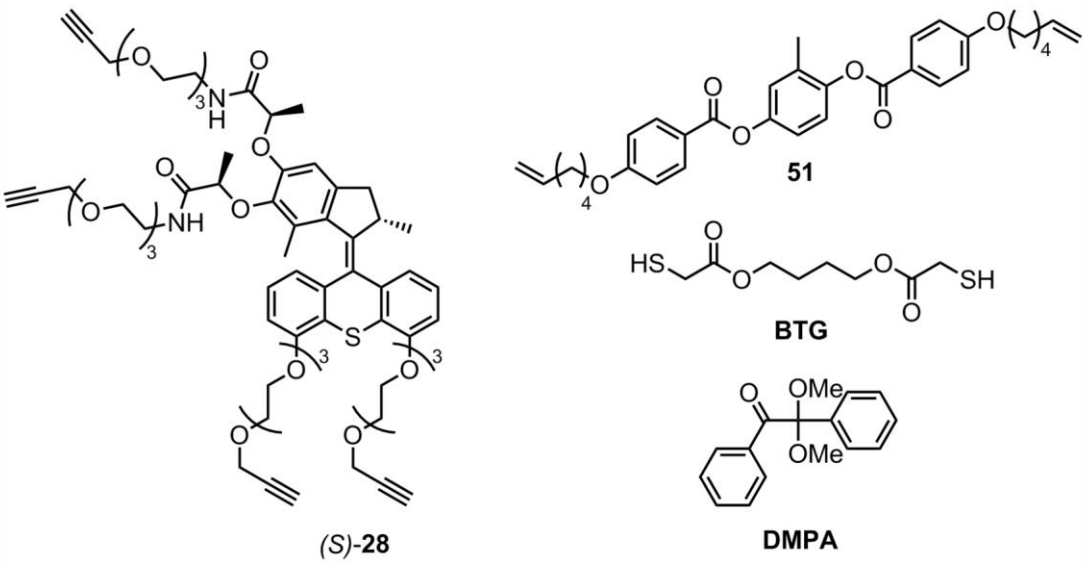

Scheme 6.2. Formulation of the main-chain LCE, consisting of tetra-alkyne motor *(S)*-**28**, dialkene mesogenic unit **51**, dithiol spacer **BTG**, and **DMPA** as photoinitiator.

The mesogen was synthesized in three steps (Scheme 6.1).[5] Mitsunobu reaction between methyl 4-hydroxybenzoate and hex-5-en-1-ol in the presence of triphenylphosphine and diisopropyl azodicarboxylate (DIAD) afforded methyl 4-(hex-5-en-1-yloxy)benzoate **49** in very good yield. Saponification of the methyl ester led to 4-(hex-5-en-1-yloxy)benzoic acid **50** in very good yield. Finally, Steglich esterification between **50** and methylhydroquinone using dicyclohexylcarbodiimide (DCC) and dimethylaminopyridine (DMAP) afforded the compound of interest, 2-methyl-1,4-phenylene bis(4-(hex-5-en-1-yloxy)benzoate) **51**, in good yield.

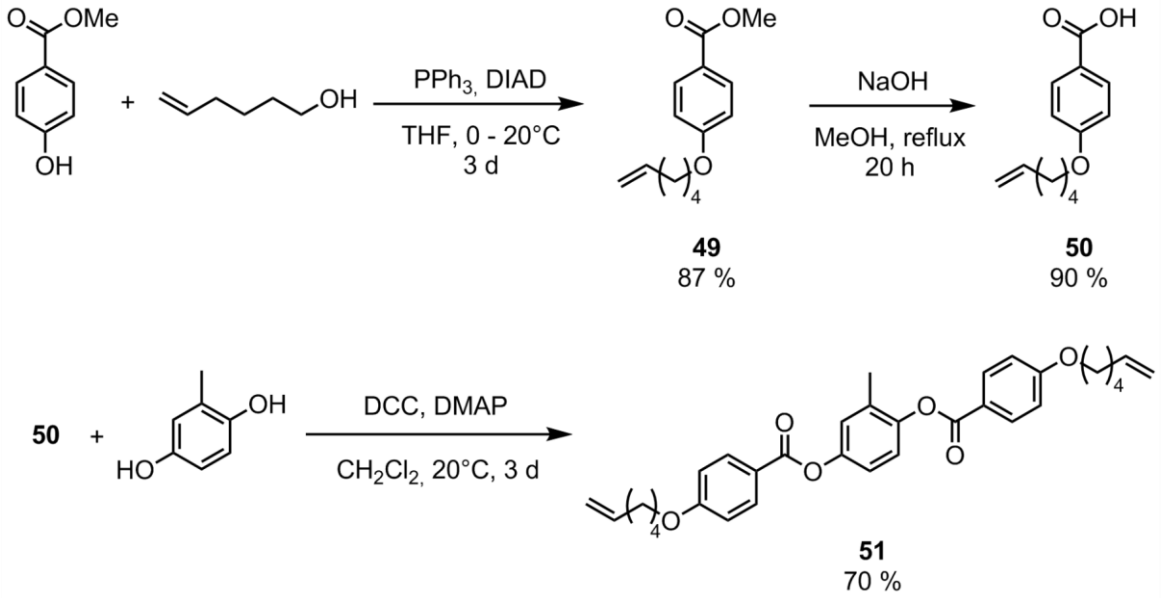

Scheme 6.1. Synthesis of mesogen **51** bearing two alkene groups for the preparation of main-chain LCE**.**

The thermal properties of **51** were investigated by differential scanning calorimetry (DSC) (Figure 6.1). Upon heating, three transitions were observed. The first two, between the solid state and the liquid crystalline state, occur at 64°C and 70°C and suggest that the material is composed of two distinct crystalline phases. The transition at 64°C is barely observed on the second heating cycle. The

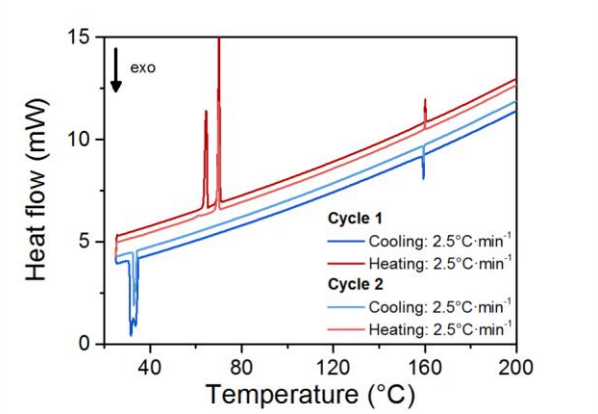

Figure 6.1. DSC thermogram of mesogen **51**.

third transition, between the liquid crystalline state and the isotropic state, takes place at 160°C. Therefore, the LCE should be formed between 80°C and 160°C.

Unfortunately, this formulation did not lead to the formation of materials that could be investigated. We prepared mixtures containing molecular motor *(S)*-**28** containing either 10 eq of **51** and 10 eq of bis-thiol (BTG), or 20 eq of **51** and 20 eq of bis-thiol (BTG), along with 10 %wt of DMPA;[3] therefore, the average number of repeating units between crosslinks was varied between 5 and 10, respectively. Mixtures were heated at 180°C and transferred between oriented glass slides by capillary suction (see Appendix A for details on the preparation of the slides). The liquid crystals were then cooled at 120°C and crosslinking was performed with UV light at 312 nm. In both cases, however, no free-standing films were formed. The materials were brittle and could not be handled easily. Some pieces were swollen in THF for further experiments but no significant shape change occurred under UV irradiation (λ = 365 nm, 80 mW·cm^{-2}).

Even though recent reports presented the synthesis of LCE by thiol-ene and thiol-yne photo-'click' reactions, we did not manage to obtain materials with our molecular motors following this synthetic pathway. We suppose that it may be caused by the high functionality of the motors. Considering that it bears four alkyne groups, eight polymer chains can possibly connect in a single point. This high functionality may tend to form more brittle materials and, hence, not elastomers. Another possibility is that the 'click' coupling is not quantitative in the conditions that we tested. Therefore, we investigated the formation of LCE by acrylate polymerization, which is more common in the literature.

6.2 Side-chain liquid-crystalline elastomers crosslinked with molecular motors

The formation of LCE from molecular motors has been recently reported independently by Chen, Feringa and coworkers, and Yang and coworkers.[6,7] They both use photo-initiated polymerization of acrylates to obtain light-responsive LCE based on molecular motors. Therefore, we investigated if this synthetic pathway could lead to materials starting from our tetra-functional molecular motors.

In their respective initial reports, Chen, Feringa and Yang used the motors as a crosslinking dopant along with another mesogenic crosslinking agent. In our formulation, however, we decided to only use our motors as crosslinkers since we ultimately wanted to study the braiding of the liquid-crystalline strands in the swollen state. Therefore, our system consisted in tetra-acrylate motor *(R)*-**33** (see Chapter 3, section 3.4 for its synthesis), 4-cyanophenyl 4'-(6-(acryloyloxy)hexyloxy)benzoate (RM23), 4-methoxyphenyl 4'-(6-(acryloyloxy)hexyloxy)benzoate (RM105), and bis(2,6-difluoro-3-(1-hydropyrrol-1-yl)phenyl)titanocene (Irg 784) as a photoinitiator (Scheme 6.3).

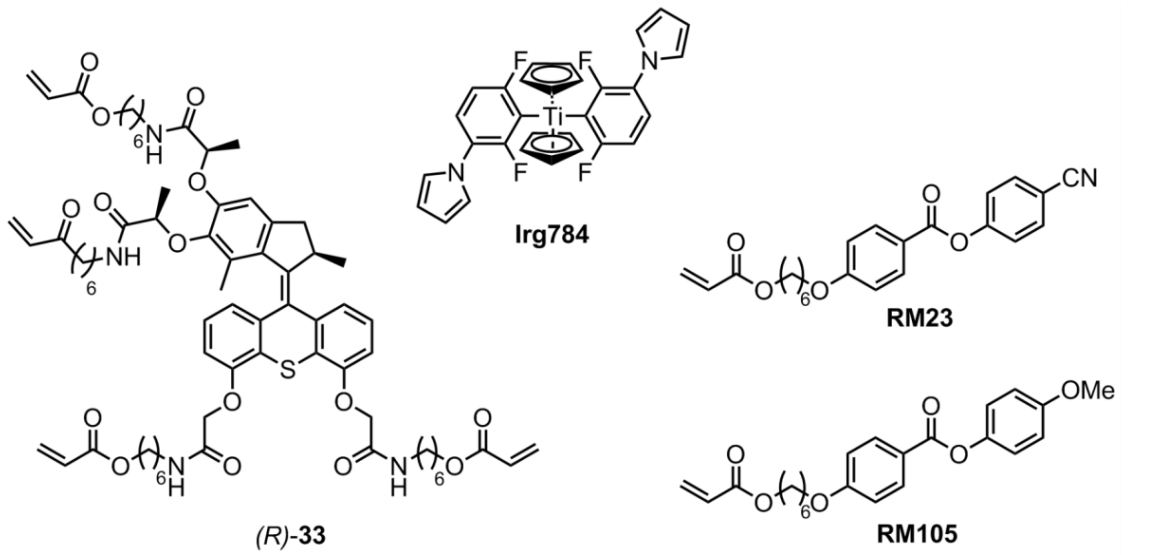

Scheme 6.3. Composition of main-chain LCE formulation based on molecular motor *(R)*-**33**, containing a mixture of **RM105** and **RM23**, and **Irg784** as a photoinitiator.

The liquid-crystalline mixtures were prepared with the same molar ratio **RM23** : **RM105** previously reported[6] and by replacing all the crosslinking agents by *(R)*-**33**. Therefore, we mixed *(R)*-**33** : RM23 : RM105 in a molar ratio 1 : 6 : 9, corresponding to a mass ratio of 4 : 7 : 11, and we added 4%wt of photoinitiator Irg 784. The mixture was melted at 80°C and transferred to the liquid-crystalline cell by capillary suction (see Appendix A for the preparation of the cells) and the system was cooled to 40°C before crosslinking with blue light at 535 nm at 100 mW·cm^{-2}. The processing temperatures were chosen according to the same report.[6] However, in our case, we did not obtain a free-standing film and the material was brittle, as observed for the systems described in the previous section.

Once again, despite previous reports, we did not obtain materials by photopolymerization of acrylates of molecular motors *(R)*-**33**. The system is currently under further investigations, since the transition temperatures of the liquid crystalline mixture may change significantly considering the high percentage of molecular motors and the absence of a second crosslinker. Moreover, for the same reasons stated in the previous section, the high functionality of the motor may lead to brittle materials. By comparison, LCE reported by other groups were prepared with molecular motors bearing at most three acrylate groups.[7] Nevertheless, we believe that this synthetic strategy can be applied for our molecules once the formulation and the processing conditions are optimized.

6.3 Conclusion and perspectives

Our investigations on LCE based on molecular motors were limited because of the inability to form materials from our tetra-functional motors. Between the two strategies that we tested, namely thiol-ene/thiol-yne photo-'click' coupling and photopolymerization of acrylates, we believe that the latter is the most promising since it has been reported previously with other molecular motors.

The challenge of our formulation rises from the fact that we aim for materials having only tetra-functional molecular motors as crosslinks, since we ultimately want to investigate the behavior of LCE in a swollen state to compare these systems to our previously reported gels.[8] However, the high content in molecular motors probably alter significantly the thermal behavior of the liquid-crystalline mixtures, and the high functionality of these crosslinkers may lead to more brittle materials. Further investigations must be performed to optimize the conditions of formation of LCE based on our molecules.

References

1. D. Dattler, G. Fuks, J. Heiser, E. Moulin, A. Perrot, X. Yao, N. Giuseppone, *Chem. Rev.* **2020**, *120*, 310–433.
2. A. B. Lowe, *Polym. Chem.* **2010**, *1*, 17–36.
3. Y. Li, Y. Zhang, M. Goswami, D. Vincent, L. Wang, T. Liu, K. Li, J. K. Keum, Z. Gao, S. Ozcan, et al., *Soft Matter* **2020**, *16*, 1760–1770.
4. D. Martella, C. Parmeggiani, D. S. Wiersma, M. Piñol, L. Oriol, *J. Mater. Chem. C* **2015**, *3*, 9003–9010.
5. M. Bispo, D. Guillon, B. Donnio, H. Finkelmann, *Macromolecules* **2008**, *41*, 3098–3108.
6. J. Hou, A. Mondal, G. Long, L. de Haan, W. Zhao, G. Zhou, D. Liu, D. Broer, J. Chen, B. L. Feringa, *Angew. Chem. Int. Ed.* **2021**, anie.202016254.
7. R. Lan, J. Sun, C. Shen, R. Huang, Z. Zhang, C. Ma, J. Bao, L. Zhang, L. Wang, D. Yang, et al., *Adv. Funct. Mater.* **2020**, 2000252.
8. Q. Li, G. Fuks, E. Moulin, M. Maaloum, M. Rawiso, I. Kulic, J. T. Foy, N. Giuseppone, *Nat. Nanotechnol.* **2015**, *10*, 161–165.

General conclusion and perspectives

Polymer gels that we designed uniquely exploit the unidirectional motion of synthetic molecular motors to trigger a macroscopic volume change of the material. Our first reports focused on the effect that the collective nanoscopic rotations have on the structure of the networks and how it led to its contraction. This thesis, on the other hand, aimed to understand how the matrix can affect the performance of molecular motors used as crosslinks, and the corresponding consequences on its own actuation.

The multigram-scale synthesis of our photoactive crosslinkers was essential to our study. We further optimized the synthetic protocols to enhance the gram-scale synthesis of tetra-functional motors that our group previously reported. The subsequent functionalization was modular, and we used different spacers to efficiently access molecular motors that could be used for several applications, such as 'click' couplings or as initiators for polymerization. A few selected systems were investigated in this thesis, but we believe that our design is versatile enough to be applied in many fields other than materials science. One main limitation, however, is that our motors are operated under UV light, which may preclude their application in biological systems, for instance; nevertheless, considering that molecular motors powered by visible light have been reported, it may be possible to design such multifunctional photoactive crosslinkers that are more suitable for these fields.

The first objective of this thesis was to improve our understanding of poly(ethylene glycol)-based gels crosslinked with molecular motors by varying different parameters while keeping an identical topology, which was achieved by forming the materials at their respective overlap concentrations. We observed that good swelling solvents had to be selected for an efficient contraction, and that the reticulation solvent may change the amount of heterogeneities in the materials, which have an important impact on the contraction behavior. The thickness of the gels and the light power density used for the contraction alter the kinetics of volume change since they both change the number of photons available per crosslinks; the thicker the gel, or the lower the light intensity, then the lower the contraction rate. The temperature, however, had no significant impact on the contractile behavior of the gels, which we attributed to the fact that the materials operate in a photochemically rate-limited regime. On that aspect, further investigations should be conducted to see if the temperature does have an effect when the gels are in a thermally rate-limited regime with higher light powers. Finally, changing the molecular weight of the precursors changed both the polymer strands density and the concentration of motors in the network, which altered the contractile properties of the gels. While the exact contribution of each aspect is not clear yet, decreasing the strand density and

increasing the concentration of motors improved both the kinetics and extent of contraction. This work represents a significant contribution to the optimization of the actuation of soft matrices containing molecular motors and should be further confirmed by studying the same parameters for different networks.

The second goal of this work was to investigate the influence of the chemical nature of the polymer strands. So far, we managed to form networks, crosslinked with molecular motors, based on poly(dimethylsiloxane) and poly(γ-benzyl-L-glutamate). Concerning the swollen networks of poly(dimethylsiloxane), we observed a surprisingly high contraction efficiency considering the polymer strand density of the network. We obtained higher contraction rates for this system at high light power than for any system based on poly(ethylene glycol), which we attributed to the higher flexibility, or lower persistence length, of the chain. Therefore, these gels are ideal candidate to conduct the same variation of parameters as we performed on gels based on poly(ethylene glycol), both to confirm the trends that we determined previously, and to isolate the effect of the persistence length. Moreover, we observed that the dry network also actuates under UV light with a significant contribution of the photothermal effect. Further investigations must be conducted on this material to understand the mechanism of actuation, for instance by probing the rotation of the molecular motors when the film is irradiated. The synthesis of star-like poly(γ-benzyl-L-glutamate) with a molecular motor as central core, on the other hand, led to the formation of thermally reversible physical gels exhibiting syneresis under irradiation. We are currently investigating this promising system further, for instance by altering the conditions of gel formation. Nevertheless, significant work remains to fully achieve our initial goal. For instance, the synthesis by atom-transfer radical polymerization of several polymers and their subsequent functionalization must be optimized to have more chemical structures available for the formation of the networks.

One last aim was the formation of anisotropic networks based on liquid-crystalline systems crosslinked with molecular motors. We investigated two synthetic pathways, one by thiol-ene/thiol-yne ‘click’ chemistry, and the other one by polymerization of acrylates. Unfortunately, neither of them led to the formation of robust films that could be further analyzed. Since a few reports present the design of such materials with molecular motors, we believe that this goal may be achieved after optimization of the formulations of the liquid-crystalline mixtures.

Deep investigations on the use of the unidirectional motion of synthetic molecular motors inside soft matter are still scarce. The present thesis represents a step towards the optimization of soft actuating materials based on molecular motors. By varying systematically several structural parameters of the networks, we determined some trends highlighting the interplay between the nature of the matrix and the operation of the photoactive crosslinkers. While we focused here on synthetic systems, we believe that our work may also improve our understanding of the operation of biological machines in living soft matter.

Appendix A

Experimental section

General experimental methods

All solvents and all commercially available reagents were purchased at the highest quality and used as received unless otherwise noted. Dry solvents were obtained by passing them through a double column SolvTech purification system. PEG samples were received from Clariant and reprecipitated in diethyl ether from THF before use. *N*-isopropylacrylamide was recrystallized from *n*-hexane before use.

Thin-layer chromatographies (TLCs) were performed using silica gel on TLC aluminium foils with fluorescent indicator at 254 nm (thickness of 500 µm, Sigma-Aldrich) and revealed under UV light (254 nm) or using staining solutions (phosphomolybdic acid in ethanol, $KMnO_4$/NaOH in water).

Ultra-performance liquid chromatography with mass spectrometry (UPLC-MS) analyses were conducted on a Waters Acquity UPLC-SQD apparatus equipped with a SQD mass spectrometer, a PDA detector (190 – 500 nm, 80 Hz), using a reverse phase column (Waters, BEH C18 1.7 µm, 2.1 × 50 mm), the MassLynx 4.1 – XP software and a gradient of water/acetonitrile + 0.1 % TFA as eluent.

Column chromatography was performed using silica gel (40 – 63 nm, VWR Chemicals) or aluminium oxide (Neutral 90, Macherey-Nagel; Active basic 90, Merck).

Dialysis was performed using SnakeSkin™ Dialysis Tubing with MWCO 3.5 kDa from Thermo Fisher Scientific.

Nuclear magnetic resonance (NMR) spectra were recorded on a Bruker Avance 400 at 25°C unless otherwise noted. ^{1}H NMR spectra were recorded at 400 MHz and ^{13}C NMR spectra were recorded at 100 MHz. The observed signals are reported as follows: chemical shift in ppm from the signal of TMS, with the residual solvent signal as internal standard (^{1}H NMR: $CDCl_3$ δ 7.26 ppm, CD_3OD-d_4 δ 3.31 ppm, $(CD_3)_2CO$-d_6 δ 2.05 ppm, toluene-*d8* δ 2.08 ppm; ^{13}C NMR: $CDCl_3$ δ 77.16 ppm, CD_3OD-d_4 δ 49.00 ppm, $(CD_3)_2CO$-d_6 δ 206.26 ppm and 29.84 ppm); multiplicity (singlet (s), doublet (d), triplet (t), quartet (q), quintuplet (qt), septuplet (sept), multiplet (m), broad (br)); integration. Coupling constants *J* are given in Hz.

Electrospray ionization mass spectrometry (ESI-MS) spectra were recorded with an SQD apparatus from Waters. **Matrix-assisted laser desorption-ionization – Time of flight (MALDI-TOF)** mass spectra were recorded on a Bruker Daltonics AutoflexII TOF spectrometer.

Gel permeation chromatography (GPC) chromatograms in water were measured using a DIONEX system, Ultimate 3000 series, with 4 Shodex columns OH-pak 30 cm and a pre-column, allowing a separation domain from 500 to 100 000 000 g·mol^{-1}. The system was equipped with a differential refractometer OPTILAB rEX (Wyatt Techn.) and a MALS detector DAWN HELEOS II (Wyatt Techn.). The flow rate was set to 0.5 mL·min^{-1} with Millipore water + 0.1 M $NaNO_3$ + NaN_3 (200 ppm) as eluent. GPC spectra in THF were recorded using a Shimadzu system, with 4 monoporosity columns (granulometry = 5 mm) PLGel 30 cm (internal diameter = 7.5 mm): 50 Å, 100 Å, 500 Å, 1 000 Å, allowing a separation range from 100 to 20 000 g·mol^{-1}. The PS calibration

curve was established with 10 Polymer Lab. standards with molar masses ranging between 162 and 20 650 g·mol^{-1}. The eluent was THF, HPLC quality, with a flow rate of 1 mL·min^{-1} and toluene was used as a flow rate marker.

Reported yields refer to purified, spectroscopically homogeneous (^{1}H NMR) materials.

Dynamic viscosities η were measured using an Oswald capillary with k = 0.01098 mm^2.s^{-2} placed in a thermostated bath Schott CT 52, and the flow time Δt was measured with a Schott AVS 360. The time Δt measured for a solution of density ρ is linked to its dynamic viscosity by the Poiseuille law:

$$\eta = \frac{\rho \, \Delta t}{k} \tag{A.1}$$

Densities were determined by measuring the mass of 1.000 ± 0.008 mL with a Mettler Toledo microbalance with an error Δm = 0.01 mg. For one sample, Δt is measured at least four times, until at least three values are within a range of ± 0.2 %. The values for η are therefore provided with an uncertainty of ± 0.9 %.

UV-Vis spectra were measured with a Lambda 25 spectrophotometer from PerkinElmer. The samples were placed in quartz cuvettes with a light path of 1 cm.

Small-angle neutron scattering (SANS) spectra were performed on the PAXY spectrometer at the Laboratoire Léon Brillouin (CEA Saclay, France) and on the D11 spectrometer at the Laue-Langevin Institute (Grenoble, France). For PAXY, four sets of sample-to-detector distances D and wavelengths λ were chosen (D = 6.7 m and λ = 15 Å; D = 5 m and λ = 8.5 Å; D = 3 m and λ = 5 Å; D = 1 m and λ = 4 Å) allowing a total *q*-range from 0.003 Å^{-1} to 0.3 Å^{-1}. For D11, three sets of D and λ were chosen (D = 30 m and λ = 12 Å; D = 16.5 m and λ = 6 Å; D = 2.5 m and λ = 6 Å) allowing a total *q*-range from 0.0007 Å^{-1} to 0.5 Å^{-1}. Data were corrected for empty cell scattering, electronic background and detector uniformity, and then converted into absolute scale (cm^{-1}) using normalization by the attenuated direct beam classical method. The solvent was carefully subtracted, as well as the incoherent background using the infinite projection of the flat points methods. The scattering vector *q* is defined as:

$$q = \frac{4\pi}{\lambda} \sin\left(\frac{\theta}{2}\right) \tag{A.2}$$

where θ is the scattering angle. The absolute neutron scattering intensity *I,* in cm^{-1}, combines the form factor of the scattered objects *P*(*q*) and the interparticles scattering factor $S_2(q)$:

$$I(q) = \frac{1}{V}\frac{d\sigma}{d\Omega} = (\Delta\rho)^2 (V_{\text{scattered objects}} \, \phi_{\text{Vol}} \, P(q) + S_2(q)) \tag{A.3}$$

where Δρ is the contrast difference per unit volume between the scattered objects and the solvent, $V_{scattered\ objects} = N \times v \times m \times 1.66 \times 10^{-24}$ is the volume of the *N* monomers or unimers with mass *m* in an object, *v* their specific volume, and ϕ_{Vol} their volume fraction. Δρ is defined as:

$$\Delta\rho = (\rho_{\text{monomer}} - \rho_{\text{solvent}}) \tag{A.4}$$

with $\rho_{monomer}$ and $\rho_{solvent}$ the scattering length densities of the monomer and the solvent, respectively, which can be calculated with their chemical compositions:

$$\rho = \sum \frac{n_i\, b_i}{N_A\, m\, v} \tag{A.5}$$

with b_i the scattering length of the n_i atom of the compound, m the molar mass of the molecule and v its specific volume, and N_A is Avogadro's number. The specific volume is 0.89 $cm^3 \cdot g^{-1}$ for PEG, 1.03 $cm^3 \cdot g^{-1}$ for PDMS, 0.93 $cm^3 \cdot g^{-1}$ for the molecular motor, 1.06 $cm^3 \cdot g^{-1}$ for deuterated toluene, 0.903 $cm^3 \cdot g^{-1}$ for deuterated water and 1.02 $cm^3 \cdot g^{-1}$ for deuterated THF. A Lorentzian fit of the data in the mid-q range is used to determine the correlation length ξ of the mesh of the network:

$$I(q) = \frac{I_0}{1 + q^2\, \xi^2} \tag{A.6}$$

Irradiation of the gels were performed by placing the gels in screwed cylindrical quartz cells and irradiating with UV light (365 nm) from one side *via* an LED source from ThorLabs (Figure A.1). One source was an M365FP1 LED coupled with an optical fiber, and the other one was an M365LP1 LED coupled with a set of condenser and lenses. The LED were powered with LED drivers LEDD1B (ThorLabs). The light power density was measured with a PM100D with a S415C detector from ThorLabs. For experiments in temperature, samples were placed in thermostated cells SM1L10H controlled with a temperature controller TC200 from ThorLabs. The contraction process was captured with an USB camera placed on the other side of the cells. The VideoVelocity software was used to capture the contraction movie at different speeds. Frames were analyzed with ImageJ software to measure the area of the surface of the gel S(t) as a function of time.

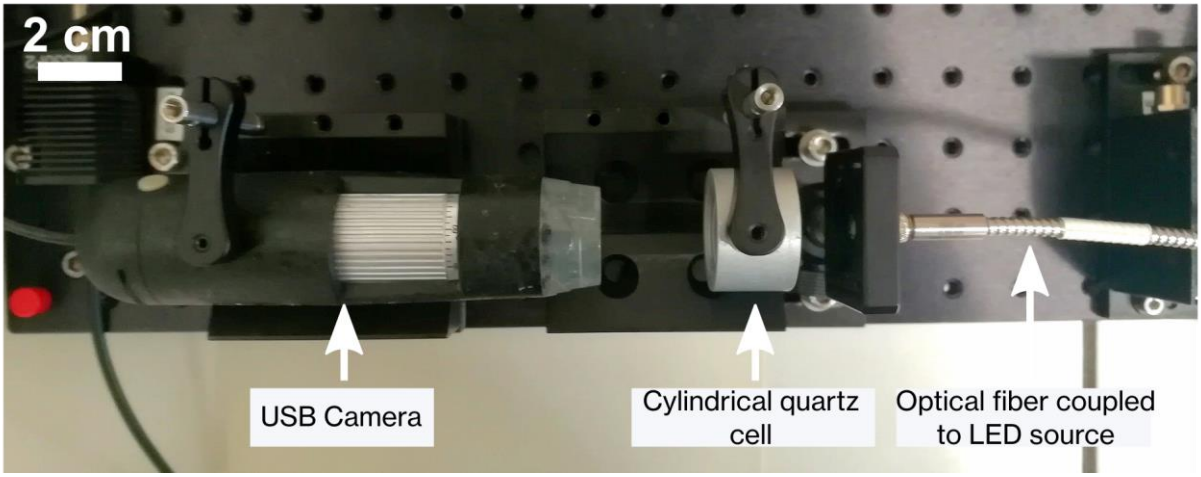

Figure A.1. Snapshot of the setup for the irradiation of gels.

Considering a contractile material shaped as a rectangular parallelepiped of length x(t), width y(t) and thickness z(t) at time t., its aspect ratio r(t) is defined as follows:

$$r(t) = \frac{x(t)}{y(t)} \tag{A.7}$$

The surface S(t) of the material observed with the camera is:

$$S(t) = x(t) \times y(t) \tag{A.8}$$

and the volume V(t) of the material is:

$$V(t) = x(t) \times y(t) \times z(t) = S(t) \times z(t) \tag{A.9}$$

The evolution of the relative volume $\%_V(t)$ as a function of time can therefore be expressed as:

$$\%_V(t) = \frac{V(t)}{V(0)} = \frac{S(t)\times z(t)}{S(0)\times z(0)} \quad (A.10)$$

First, we consider an anisotropic material with its director macroscopically aligned along the length. The contractile behavior will therefore be identical along the width and along the thickness:

$$\frac{y(t)}{y(0)} = \frac{z(t)}{z(0)} \quad (A.11)$$

Combining equations (A.7), (A.8) and (A.11), we can express the ratio of widths to the ratio of surfaces between t = 0 and t:

$$\frac{S(t)}{S(0)} = \frac{x(t)\times y(t)}{x(0)\times y(0)} = \frac{r(t)\times y^2(t)}{r(0)\times y^2(0)} = \frac{r(t)\times z^2(t)}{r(0)\times z^2(0)} \quad (A.12)$$

The ratio of widths can therefore be written as follows:

$$\frac{z(t)}{z(0)} = \left(\frac{S(t)}{S(0)}\frac{r(0)}{r(t)}\right)^{1/2} \quad (A.13)$$

Replacing it in equation (A.10), we obtain:

$$\%_V(t) = \left(\frac{S(t)}{S(0)}\right)^{3/2}\left(\frac{r(0)}{r(t)}\right)^{1/2} \quad (A.14)$$

In the case of isotropic materials with an isotropic contraction over time, the aspect ratio is constant so the equation can be simplified to:

$$\%_V(t) = \left(\frac{S(t)}{S(0)}\right)^{3/2} \quad (A.15)$$

Cells for the formation of LCE were composed of two glass slides glued to each other, which were separated with Teflon spacers with a thickness of 1 mm. The glass slides were cleaned with soapy water, ethanol and placed in a plasma chamber. They were then coated with either a polyimide solution (Sunever®, Nissan Chemical) or a poly(vinyl alcohol solution) (13 000 – 23 000 g·mol^{-1}, Aldrich) by spin-coating (5 s at 1 200 rpm, 1 000 rpm·s^{-1}; 40 s at 6 100 rpm, 1 200 rpm·s^{-1}). Coatings were dried for 10 min at 110°C and cured at 180°C for 1 h. Finally, surfaces were rubbed with a piece of textile to induce planar alignment, and they were glued in an antiparallel fashion.

Synthetic procedures

N,N-*diethyl-3-hydroxybenzamide 1*

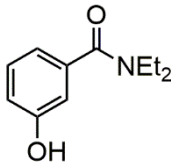

Under argon, 3-hydroxybenzoic acid (43.6 g, 0.315 mol) was dissolved in thionyl chloride (190 mL, 2.6 mmol) along with dimethylformamide (1.64 mL, 21.2 mmol). The mixture was heated under reflux for 4 h before allowing it to cool to room temperature. The excess of thionyl chloride was evaporated under vacuum, and further removed by azeotropic distillation with toluene (100 mL) twice. The residue was dissolved in dichloromethane (175 mL) and the mixture was cooled to 0°C before slow addition of diethylamine (117 mL, 1.14 mol). The solution was stirred overnight while allowing to warm to room temperature. The solvent was removed under vacuum and the oily residue

was dispersed in water (250 mL). The pH was then adjusted to 2 – 3 with hydrochloric acid. The product was extracted by washing three times with ethyl acetate (150 mL). The combined organic layers were dried over sodium sulfate and the solvent evaporated under vacuum, to afford *N,N*-diethyl-3-hydroxybenzamide (59.4 g, 0.307 mol, 97 %) as brown crystals. $\mathbf{R_f}$ = 0.13 (CH_2Cl_2 : Et_2O, 5 : 1). **^{1}H NMR** (400 MHz, $CDCl_3$) δ 7.15 (dd, *J* = 7.8, 7.8 Hz, 1H), 6.92 – 6.87 (m, 1H), 6.82 – 6.74 (m, 2H), 3.54 (q, *J* = 7.1 Hz, 2H), 3.27 (q, *J* = 7.1 Hz, 2H), 1.24 (t, *J* = 7.1 Hz, 3H), 1.10 (t, *J* = 7.1 Hz, 3H). **^{13}C NMR** (100 MHz, $CDCl_3$) δ 172.1, 157.0, 137.0, 129.4, 117.1, 116.9, 114.0, 43.5, 39.5, 14.0, 12.7. **MS** (ESI): calculated for $C_{11}H_{16}NO_2$ $[M+H]^+$ m/z = 194.12, found: 193.98.

N,N-*diethyl-3-methoxybenzamide 2*

Compound **1** (77.5 g, 0.40 mol) was dissolved in acetone (650 mL). Potassium carbonate (168 g, 1.22 mol) was added, followed by dropwise addition of methyl iodide (75 mL, 1.19 mol). The mixture was stirred overnight at room temperature. The solvent was evaporated under vacuum and the residue was partitioned with water (50 mL) and ethyl acetate (50 mL). The aqueous phase was further extracted with ethyl acetate (50 mL) twice. The combined organic phase was dried over sodium sulfate and the solvent evaporated under vacuum to afford *N,N*-diethyl-3-methoxybenzamide (83.3 g, 0.40 mol, 100 %) as a brown liquid. $\mathbf{R_f}$ = 0.3 (cyclohexane : Et_2O, 2 : 1). **^{1}H NMR** (400 MHz, $CDCl_3$) δ 7.28 (dd, *J* = 7.8, 7.8 Hz, 1H), 6.95 – 6.86 (m, 3H), 3.81 (s, 3H), 3.53 (br q, 2H), 3.25 (br q, 2H), 1.23 (s, 3H), 1.10 (s, 3H). **^{13}C NMR** (100 MHz, $CDCl_3$,) δ 170.8, 159.4, 138.4, 129.3, 118.2, 114.8, 111.5, 55.1, 43.1, 39.0, 14.1, 12.7. **MS** (ESI): calculated for $C_{12}H_{18}NO_2$ $[M+H]^+$ m/z = 208.13, found: 208.19.

1,2-bis(2-methoxyphenyl)disulfane 3

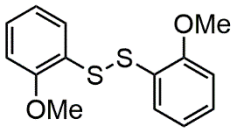

2-methoxythiophenol (30.8 mL, 0.50 mol) was dispersed in water (150 mL). A solution of diiodine (64.4 g) in methanol (500 mL) was prepared and added dropwise to the stirred solution of thiophenol until the brown color persisted. The mixture was then stirred at room temperature overnight. The product was collected by filtration and dried to afford 1,2-bis(2-methoxyphenyl)disulfane (69.3 g, 0.25 mmol, 100 %) as a white powder. $\mathbf{R_f}$ = 0.3 (cyclohexane : Et_2O, 6 : 1). **^{1}H NMR** (400 MHz, $CDCl_3$) δ 7.53 (dd, *J* = 7.8, 1.6 Hz, 2H), 7.19 (ddd, *J* = 8.1, 7.4, 1.6 Hz, 2H), 6.91 (ddd, *J* = 7.8, 7.8, 1.2 Hz, 2H), 6.85 (dd, *J* = 8.1, 1.2 Hz, 2H), 3.90 (s, 6H). **^{13}C NMR** (100 MHz, $CDCl_3$) δ 156.5, 127.7, 127.5, 124.5, 121.3, 110.4, 55.8. **MS** (ESI): calculated for $C_{14}H_{15}O_2S_2$ $[M+H]^+$ m/z = 279.05, found: 279.15.

N,N-*diethyl-3-methoxy-2-((2-methoxyphenyl)thio)benzamide 4*

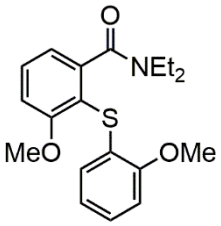

Under argon, *s*-BuLi at 1.4 mol.L^{-1} in cyclohexane (172 mL, 0.24 mol) were slowly added to a solution of tetramethylethylenediamine (18.2 mL, 0.12 mol) in dry THF (150 mL) cooled at -78°C and the mixture was stirred for 1 h at this temperature. A solution of compound **2** (25 g, 0.12 mol) in dry THF (100 mL) was then slowly added and the reaction was left under stirring for 1 h at -78°C. Finally, a solution of compound **3** (60.4 g, 0.22 mol) in dry THF (350 mL) was added to the medium. The reaction mixture was stirred overnight while allowing to warm to room temperature. Diethyl ether (600 mL) was then added to the solution and the organic phase was washed twice with an aqueous solution of sodium hydroxide at 1 mol.L^{-1} (350 mL). The crude product was dissolved in dichloromethane (200 mL) and poured in cold methanol (600 mL). The solid was filtered out. The filtrate was recovered, dried under vacuum and further purified by column chromatography (ethyl acetate : toluene, 0 : 1 → 1 : 2) to afford *N,N*-diethyl-3-methoxy-2-((2-methoxyphenyl)thio)benzamide (20.4 g, 0.059 mol, 49 %) as a white solid. $\mathbf{R_f}$ = 0.2 (ethyl acetate : toluene, 1 : 2). **^{1}H NMR** (400 MHz, $CDCl_3$) δ 7.43 (dd, *J* = 8.2, 8.2 Hz, 1H), 7.04 (ddd, *J* = 8.2, 7.0, 1.9 Hz, 1H), 6.98 – 6.86 (m, 2H), 6.80 (dd, *J* = 8.2, 1.1 Hz, 1H), 6.73 (ddd, *J* = 7.8, 7.8, 1.1 Hz, 1H), 6.69 (dd, *J* = 7.8, 1.9 Hz, 1H), 3.87 (s, 3H), 3.75 (s, 3H), 3.72 – 3.64 (m, 1H), 3.39 – 3.31 (m, 1H), 3.15 – 3.08 (m, 1H), 3.04 – 2.96 (m, 1H), 1.19 (t, *J* = 7.1 Hz, 3H), 0.98 (t, *J* = 7.1 Hz, 3H). **^{13}C NMR** (100 MHz, $CDCl_3$) δ 168.6, 160.5, 155.6, 145.2, 131.1, 127.0, 125.8, 125.4, 120.9, 118.7, 116.1, 111.2, 110.2, 56.1, 55.7, 42.6, 38.5, 13.8, 12.4. Analyses were in agreement with reference 1.

4,5-dimethoxythioxanthone 5

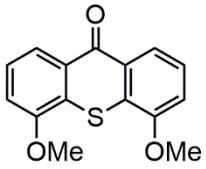

Under argon, *n*-BuLi at 1.6 mol.L^{-1} in cyclohexane (236 mL, 0.38 mol) was added to a solution of diisopropylamine (53.4 mL, 0.38 mol) in dry THF (530 mL) at -78°C. The mixture was stirred for 30 min at this temperature, then allowed to warm to 0°C. A solution of 33.7 g of **4** (0.076 mol) in 350 mL of dry THF was added dropwise over the course of 1 h. The reaction medium is stirred overnight while allowing to warm to room temperature. At the end of the reaction, a saturated solution of ammonium chloride (200 mL) was added. The aqueous layer was extracted three times with ethyl acetate (250 mL). The combined organic phase was dried over sodium sulfate and concentrated under vacuum to afford 4,5-dimethoxythioxanthone (20.6 g, 0.076 mol, 100 %) as an orange solid. $\mathbf{R_f}$ = 0.47 (toluene). **^{1}H NMR** (400 MHz, $CDCl_3$) δ 8.25 (dd, *J* = 8.1, 1.2 Hz, 2H), 7.45 (dd, *J* = 8.0, 8.0 Hz, 2H), 7.15 (dd, *J* = 8.0, 1.2 Hz, 2H), 4.06 (s, 6H). **^{13}C NMR** (100 MHz, $CDCl_3$) δ 180.2, 154.9, 130.0, 127.7, 126.0, 121.5, 112.1, 56.4. Analyses were in agreement with reference 1.

*4,5-bis((*tert*-butyldimethylsilyl)oxy)-thioxanthone 6*

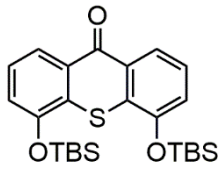

Under argon, boron tribromide (47.6 mL,.50 mol) were added to a solution of compound **5** (35.2 g, 0.13 mol) dissolved in dry dichloromethane (750 mL). The mixture was stirred overnight at room temperature. The solvent was evaporated under vacuum. The residue was dissolved in methanol (250 mL) and the solvent evaporated five times. The crude material is dissolved in dry THF (1.3 L) under argon. Imidazole (26.4 g, 0.39 mol) and *tert*-butyldimethylsilyl chloride (58.4 g, 0.39 mol) are added to the reaction medium. The solution is stirred overnight at room temperature and filtered. The filtrate is collected, dried and further purified by column chromatography (silica gel, toluene) to afford 4,5-bis((*tert*-butyldimethylsilyl)oxy)-thioxanthone (43.3 g, 0.092 mol, 71 %) as an orange solid. $\mathbf{R_f}$ = 0.7 (ethyl acetate : toluene, 1 : 6). **^{1}H NMR** (400 MHz, $CDCl_3$) δ 8.25 (dd, *J* = 8.0, 1.2 Hz, 2H), 7.35 (dd, *J* = 8.0, 8.0 Hz, 2H), 7.10 (dd, *J* = 8.0, 1.2 Hz, 2H), 1.11 (s, 18H), 0.35 (s, 12H). **^{13}C NMR** (100 MHz, $CDCl_3$) δ 180.6, 151.3, 130.6, 130.4, 125.7, 122.0, 119.7, 25.9, 18.5, -4.1. Analyses were in agreement with reference 1.

*4,5-bis((*tert*-butyldimethylsilyl)oxy)-thioxanthone hydrazone 7*

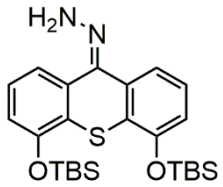

Under argon, diphosphorus pentasulfide (30.7 g, 0.14 mol) was added to a solution of compound **6** (22.2 g, 0.044 mol) in dry THF (300 mL). The mixture was stirred for 1 h at 65°C and filtered. The residue was washed thoroughly with dichlromethane (500 mL) and the filtrate was collected and dried. The crude solid was dissolved in ethanol (600 mL) under argon and hydrazine monohydrate (228 mL, 0.24 mol) was added dropwise at 0°C. The mixture was stirred overnight while allowing to warm to room temperature. The solvent is removed under vacuum and the product is purified by column chromatography (alumina gel, ethyl acetate : toluene, 1 : 2) to afford 4,5-bis((*tert*-butyldimethylsilyl)oxy)-thioxanthone hydrazine (13 g, 0.027 mol, 61 %) as an orange solid. **^{1}H NMR** (400 MHz, $CDCl_3$) δ 7.63 (dd, *J* = 7.9, 1.2 Hz, 1H), 7.43 (dd, *J* = 7.9, 1.2 Hz, 1H), 7.20 (dd, *J* = 7.9, 7.9 Hz, 1H), 7.16 (dd, *J* = 7.9, 7.9 Hz, 1H), 6.84 (dd, *J* = 8.0, 1.2 Hz, 1H), 6.78 (dd, *J* = 8.0, 1.2 Hz, 1H), 1.09 (s, 9H), 1.07 (s, 9H), 0.31 (s, 6H), 0.28 (s, 6H). **^{13}C NMR** (100 MHz, $CDCl_3$) δ 152.5, 150.7, 142.0, 135.1, 127.6, 126.6, 126.6, 125.2, 124.1, 120.5, 118.6, 117.6, 116.6, 25.9, 25.8, 18.4, 18.3, 14.3, 14.0. **MS** (ESI): calculated for $C_{25}H_{39}N_2O_2SSi_2$ $[M+H]^+$ m/z = 487.23, found: 487.31.

5,6-dimethoxy-2,7-dimethylindanone 8

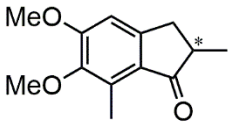

Methacrylic acid (127 mL, 1.5 mol) and 2,3-dimethoxytoluene (117 mL, 0.79 mol) were added in mechanically stirred polyphosphoric acid (371 mL) heated at 70°C. The mixture is stirred for 3 h at this temperature, poured onto ice and stirred overnight at 0°C. The aqueous layer is intensively extracted with ethyl acetate (200 mL) and the combined organic layers were washed with a saturated aqueous solution of sodium hydrogen carbonate (100 mL), water (100 mL) and brine (100 mL). The organic phase was dried over sodium sulfate and concentrated to a damp solid under vacuum. The product was recrystallized from *n*-heptane to afford 5,6-dimethoxy-2,7-dimethylindanone (102 g, 0.46 mol, 59 %) as brown crystals. $\mathbf{R_f}$ = 0.74 (ethyl acetate : cyclohexane, 1 : 1). **^{1}H NMR** (400 MHz, $CDCl_3$) δ 6.75 (s, 1H), 3.93 (s, 3H), 3.77 (s, 3H), 3.33 – 3.17 (m, 1H), 2.76 – 2.57 (m, 2H), 2.57 (s, 3H), 1.27 (d, *J* = 7.3 Hz, 3H). **^{13}C NMR** (100 MHz, $CDCl_3$) δ 208.9, 158.1, 151.8, 146.9, 132.1, 127.3, 105.9, 60.4, 55.8, 42.6, 34.5, 16.6, 10.6. Analyses were in agreement with reference 1.

5,6-dihydroxy-2,7-dimethylindanone **9**

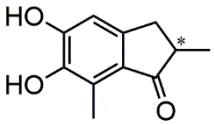

Under argon, boron tribromide (30.9 mL, 0.33 mol) was added dropwise to a solution of compound **9** (35 g, 0.16 mol) dissolved in dichloromethane (240 mL) cooled at 0°C. After complete addition, the mixture was stirred overnight while allowing to warm to room temperature. The mixture was quenched by dropwise addition of methanol. The solvent was evaporated under vacuum and the crude solid was dissolved in methanol. These two last steps were repeated three times, affording 5,6-dihydroxy-2,7-dimethylindanone (29.9 g, 0.16 mol, 98 %) as a dark blue solid. $\mathbf{R_f}$ = 0.5 (ethyl acetate : cyclohexane, 1 : 1). **^{1}H NMR** (400 MHz, CD_3OD) δ 6.68 (s, 1H), 3.25 – 3.14 (m, 1H), 2.65 – 2.46 (m, 2H), 2.46 (s, 3H), 1.21 (d, *J* = 7.3 Hz, 3H). **^{13}C NMR** (100 MHz, CD_3OD) δ 212.1, 153.7, 150.1, 144.2, 126.9, 125.3, 109.7, 43.9, 34.9, 17.1, 10.6. Analyses were in agreement with reference 1.

5,6-bis[(2R)-(1-ethoxy-1-oxopropan-2-yl)oxy]-2,7-dimethylindanone **10**

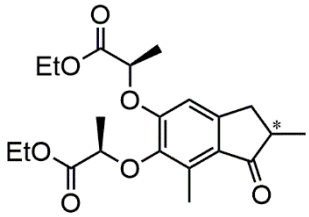

Under argon, a solution of compound **9** (25 g, 0.13 mol), *(S)*-(–)-ethyl lactate (40.8 mL, 0.36 mol) and triphenylphosphine (93.3 g, 0.36 mol) in dry THF (750 mL) was prepared and cooled to 0°C. Diisopropyl azodicarboxylate (75.6 mL, 0.36 mol) was added dropwise. The mixture was stirred for 5 d while warming to room temperature. The solvent was removed under vacuum. The crude product was dissolved in a mixture of diethyl ether : hexane (1 : 3), filtered and the filtrate was collected and dried. These last steps were repeated three times. The crude product was further purified by column chromatography (silica gel, cyclohexane : ethyl acetate, 1 : 0 → 5 : 1) to afford 5,6-bis[(*2R*)-(1-ethoxy-1-oxopropan-2-yl)oxy]-2,7-dimethylindanone (20.4 g, 0.052 mol, 40 %) as a slightly yellow oil. $\mathbf{R_f}$ = 0.4 (ethyl acetate : cyclohexane, 1 : 3). **^{1}H NMR** (400 MHz, $CDCl_3$) δ 6.55 (s, 1H), 4.86 (q, *J* = 6.8 Hz, 1H), 4.85 (q, *J* = 6.8 Hz, 1H), 4.34 – 4.08 (m, 4H), 3.35 – 3.08 (m, 1H), 2.69 – 2.56 (m, 1H), 2.61 (s, 3H), 2.58 – 2.49 (m, 1H), 1.67 (d, *J* = 6.8 Hz, 3H), 1.61 (d, *J* = 6.8 Hz, 3H),

1.30 – 1.21 (m, 9H). **^{13}C NMR** [100 MHz, $(CD_3)_2CO$] δ 208.5, 172.8, 171.8, 156.0, 152.0, 146.0, 132.9, 128.5, 108.3, 77.6, 73.3, 62.1, 61.4, 43.4, 35.0, 22.4, 19.3, 18.7, 16.8, 14.6, 11.7. Analyses were in agreement with reference 1.

5,6-bis[(2R)-(1-ethoxy-1-oxopropan-2-yl)oxy]-2,7-dimethylindanethione 11

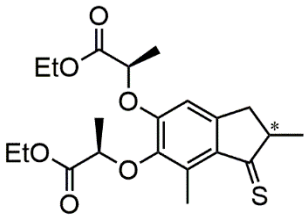

Under argon, diphosphorus pentasulfide (28.4 g, 0.13 mol) was added to a solution of compound **10** (16 g, 0.041 mol) in toluene (112 mL) heated at 80°C. The mixture was stirred for 1 h at this temperature. The solution was then filtered and intensively washed with ethyl acetate. The filtrate was collected, dried and further purified by column chromatography (silica gel, ethyl acetate : cyclohexane, 1 : 13) to afford 5,6-bis[(*2R*)-(1-ethoxy-1-oxopropan-2-yl)oxy]-2,7-dimethylindanethione (8 g, 0.020 mol, 48 %) as a purple oil. As it is sensitive to air, the product was directly used in the next step. **^{1}H NMR** (400 MHz, $CDCl_3$) δ 6.61 (s, 1H), 4.88 (q, *J* = 6.8 Hz, 1H), 4.82 (q, *J* = 6.8 Hz, 1H), 4.26 - 4.18 (m, 4H), 3.33 - 3.26 (m, 1H), 3.00 - 2.96 (m, 1H), 2.77 (s, 3H), 2.71 - 2.66 (m, 1H), 1.69 (d, *J* = 6.8 Hz, 3H), 1.62 (d, *J* = 6.8 Hz, 3H), 1.39 (d, *J* = 7.2 Hz, 3H), 1.25 (t, *J* = 6.8 Hz, 6H). **^{13}C NMR** (100 MHz, $CDCl_3$) δ 248.7, 172.1, 171.0, 154.6, 152.8, 145.2, 138.1, 135.1, 106.1, 77.2, 72.6, 60.9, 55.5, 43.4, 38.9, 21.6, 21.5, 18.6, 18.2, 14.0, 13.8. **MS** (ESI): calculated for $C_{21}H_{29}O_6S$ $[M+H]^+$ m/z = 409.17, found: 409.28.

2',3'-dihydrodispiro([5,6-bis[(2R)-(1-ethoxy-1-oxopropan-2-yl)oxy]-2,7-dimethylindene]-1,2'-thiirane-3',9"-[4",5"-bis[(tert-butyldimethylsilyl)oxy]-thioxanthene]) 12

Ethyl- and TBS-protected episulfide

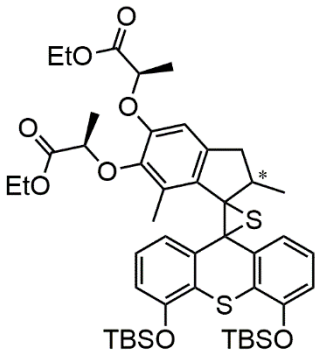

Under argon, compound **7** (7.21 g, 14.8 mmol) and sodium sulfate (19.2 g, 135 mmol) were dissolved in dry THF (60 mL) in an oven-dried flask protected from light. The mixture was cooled at 0°C and manganese dioxide (11.8 g, 135 mmol) was added. The reaction medium was stirred for 40 min while allowed to reach room temperature. The solution was then slowly filtered through a cannula into a solution of compound **11** (5.5 g, 13.5 mmol) in dry THF (60 mL) under argon cooled at 0°C. The resulting mixture was stirred overnight while allowed to reach room temperature. The solvent was then removed under vacuum and the crude residue was purified by column chromatography (silica gel, toluene : ethyl acetate, 1 : 0 → 50 : 1) resulting in a decent separation of

the diastereoisomers (*R,R,R* : *R,R,S* : mixture, 4 : 5 : 1, total 8.53 mmol, 7.38 g, 63 %) as yellow solids. **For *(R,R,R)*-isomer: R_f** = 0.7 (toluene : ethyl acetate, 6 : 1). **^{1}H NMR** (400 MHz, $CDCl_3$) δ 7.39 (dd, *J* = 7.9, 1.2 Hz, 1H), 7.24 (dd, *J* = 7.9, 1.2 Hz, 1H), 7.10 (dd, *J* = 7.9, 7.9 Hz, 1H), 7.01 (dd, *J* = 7.9, 7.9 Hz, 1H), 6.73 (dd, *J* = 7.9, 1.2 Hz, 1H), 6.61 (dd, *J* = 7.9, 1.2 Hz, 1H), 6.35 (s, 1H), 4.61 (q, *J* = 6.7 Hz, 1H), 4.31 – 4.12 (m, 5H), 3.19 (dd, *J* = 14.8, 6.3 Hz, 1H), 2.15 (s, 3H), 2.07 (d, *J* = 14.8 Hz, 1H), 1.53 (d, *J* = 6.7 Hz, 3H), 1.42 (d, *J* = 6.8 Hz, 3H), 1.37 – 1.30 (m, 1H), 1.31 (t, *J* = 7.1 Hz, 3H), 1.23 (t, *J* = 7.1 Hz, 3H), 1.05 (s, 9H), 0.97 (s, 9H), 0.92 (d, *J* = 6.9 Hz, 3H), 0.26 (s, 3H), 0.24 (s, 3H), 0.09 (s, 3H), -0.07 (s, 3H). **^{13}C NMR** (100 MHz, $CDCl_3$) δ 172.5, 171.9, 151.6, 151.5, 149.7, 144.7, 140.3, 139.9, 136.1, 131.6, 128.9, 127.9, 127.8, 126.2, 125.5, 123.5, 121.7, 117.5, 116.9, 108.9, 77.5, 77.2, 73.2, 71.6, 61.9, 60.9, 60.6, 41.1, 37.7, 25.9, 25.8, 21.1, 18.9, 18.4, 18.3, 18.2, 14.2, 14.1, 12.4, -3.9, -4.2, -4.3, -4.7. **MS** (ESI): calculated for $C_{46}H_{65}O_8S_2Si_2$ $[M+H]^+$ 865.37, found: 865.46. **For *(R,R,S)*-isomer: R_f** = 0.65 (toluene : ethyl acetate, 6 : 1). **^{1}H NMR** (400 MHz, $CDCl_3$) δ 7.38 (dd, *J* = 7.9, 1.2 Hz, 1H), 7.24 (dd, *J* = 7.9, 1.2 Hz, 1H), 7.10 (dd, *J* = 7.9, 7.9 Hz, 1H), 7.00 (t, *J* = 7.9, 7.9 Hz, 1H), 6.73 (dd, *J* = 7.9, 1.2 Hz, 1H), 6.59 (dd, *J* = 7.9, 1.2 Hz, 1H), 6.26 (s, 1H), 4.60 (q, *J* = 6.7 Hz, 1H), 4.57 (q, *J* = 6.8 Hz, 1H), 4.26 – 4.08 (m, 1H), 4.17 (q, *J* = 7.1 Hz, 2H), 4.16 (q, *J* = 7.1 Hz, 2H), 3.20 (dd, *J* = 14.9, 6.4 Hz, 1H), 2.12 (s, 3H), 2.05 (d, *J* = 14.9 Hz, 1H), 1.52 (d, *J* = 6.7 Hz, 3H), 1.28 (d, *J* = 6.8 Hz, 3H), 1.24 (t, *J* = 7.1 Hz, 3H), 1.18 (t, *J* = 7.1 Hz, 3H), 1.06 (s, 9H), 0.95 (s, 9H), 0.93 (d, *J* = 6.9 Hz, 3H), 0.26 (s, 3H), 0.24 (s, 3H), 0.07 (s, 3H), -0.10 (s, 3H). **^{13}C NMR** (100 MHz, $CDCl_3$) δ 172.7, 171.9, 151.5, 151.4, 149.1, 148.6, 143.8, 140.0, 139.7, 136.1, 131.5, 128.8, 127.9, 126.2, 125.5, 123.6, 121.7, 117.5, 116.9, 107.8, 77.2, 76.5, 72.5, 71.4, 61.7, 61.1, 60.6, 40.9, 37.6, 25.9, 25.8, 21.1, 18.6, 18.4, 18.3, 18.2, 14.1, 14.0, 12.4, -4.0, -4.2, -4.3, -4.8. Analyses were in agreement with reference 1.

*4,5-bis[(*tert*-butyldimethylsilyl)oxy]-thioxanthen-9-ylidene-[5',6'-bis[(2R)-(1-ethoxy-1-oxopropan-2-yl)oxy]-2',7'-dimethylindane] **13***

Ethyl- and TBS-protected motor

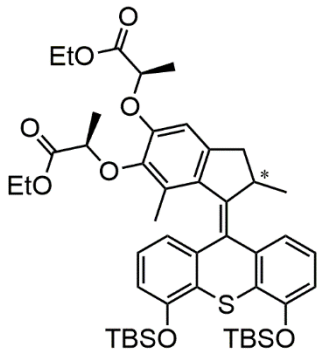

The same procedure can be applied for *(R,R,R)* and *(R,R,S)* isomers. Typically, compound *(S)*-**12** (957 mg, 1.11 mmol) was dissolved in toluene (35 mL) and triphenylphosphine (4.36 g, 16.6 mmol) was added. The mixture was stirred under reflux for 15 h. After evaporation of the solvent under vacuum, the crude material was purified by column chromatography (silica gel, toluene : ethyl acetate, 80 : 1 → 0 : 1) to afford compound *(S)*-**13** (870 mg, 1.04 mmol, 94 %) as a yellow solid. **For *(R,R,S)*-isomer: R_f** = 0.63 (toluene : ethyl acetate, 6 : 1). **^{1}H NMR** (400 MHz, $CDCl_3$) δ 7.29 (d, *J* = 7.9 Hz, 1H), 7.12 (dd, *J* = 7.9, 7.9 Hz, 1H), 6.86 (dd, *J* = 7.9, 7.9 Hz, 1H), 6.69 (dd, *J* = 7.9, 1.2 Hz, 1H), 6.63 (dd, *J* = 7.9, 1.2 Hz, 1H), 6.62 (dd, *J* = 7.9, 1.2 Hz, 1H), 6.53 (s, 1H), 4.75 (q, *J* = 6.8 Hz, 1H), 4.74 (q, *J* = 6.8 Hz, 1H), 4.30 – 4.07 (m, 5H), 3.33 (dd, *J* = 14.9, 6.3 Hz, 1H), 2.31 (d, *J* = 14.9 Hz, 1H), 1.61 (d, *J* = 6.8 Hz, 3H), 1.44 (d, *J* = 6.8 Hz, 3H), 1.22 (t, *J* = 7.1 Hz, 3H), 1.21 (t, *J* = 7.1 Hz, 3H), 1.20

(s, 3H), 1.09 (s, 9H), 1.08 (s, 9H), 0.62 (d, *J* = 6.7 Hz, 3H), 0.29 (s, 3H), 0.27 (s, 3H), 0.27 (s, 3H), 0.25 (s, 3H). **^{13}C NMR** (100 MHz, $CDCl_3$) δ 172.4, 171.9, 152.7, 152.2, 149.6, 145.5, 144.4, 141.9, 141.8, 138.3, 133.4, 130.8, 128.1, 127.7, 127.1, 126.4, 126.1, 120.9, 120.2, 116.3, 115.5, 108.1, 76.9, 72.9, 61.2, 60.6, 39.4, 37.9, 25.9, 18.9, 18.5, 18.4, 14.4, 14.1, 14.0, -3.9, -4.0, -4.3, -4.4. **MS** (ESI): calculated for $C_{46}H_{65}O_8SSi_2$ $[M+H]^+$ 833.39, found: 833.58. **For *(R,R,R)*-isomer: R_f** = 0.68 (toluene : ethyl acetate, 6 : 1). **^{1}H NMR** (400 MHz, $CDCl_3$) 7.29 (d, *J* = 8.2 Hz, 1H), 7.12 (dd, *J* = 7.9, 7.9 Hz, 1H), 6.89 (dd, *J* = 7.9, 7.9 Hz, 1H), 6.69 (dd, *J* = 8.2, 1.2 Hz, 1H), 6.66 (dd, *J* = 9.2, 1.2 Hz, 1H), 6.64 (dd, *J* = 9.2, 1.2 Hz, 1H), 6.56 (s, 1H), 4.77 (q, *J* = 6.7 Hz, 1H), 4.44 (q, *J* = 6.7 Hz, 1H), 4.32 – 4.04 (m, 5H), 3.32 (dd, *J* = 14.9, 6.2 Hz, 1H), 2.33 (d, *J* = 14.9 Hz, 1H), 1.62 (d, *J* = 6.8 Hz, 3H), 1.52 (d, *J* = 6.8 Hz, 3H), 1.29 (t, *J* = 7.1 Hz, 3H), 1.27 (t, *J* = 7.1 Hz, 3H), 1.19 (s, 3H), 1.09 (s, 9H), 1.08 (s, 9H), 0.61 (d, *J* = 6.7 Hz, 3H), 0.29 (s, 3H), 0.27 (s, 3H), 0.27 (s, 3H), 0.25 (s, 3H). **^{13}C NMR** (100 MHz, $CDCl_3$) δ 172.6, 172.3, 152.8, 152.3, 150.3, 145.6, 145.0, 142.5, 141.9, 138.5, 133.6, 131.0, 128.3, 127.7, 127.3, 126.6, 126.2, 121.1, 120.4, 116.5, 115.7, 108.3, 77.4, 73.0, 61.3, 60.8, 39.7, 38.1, 26.1, 25.7, 19.1, 18.9, 18.7, 18.5, 18.5, 14.6, 14.4, 14.3, -3.8, -3.9, -4.2, -4.3. NMR spectra can be found in Appendix C. **MS** (ESI): calculated for $C_{46}H_{65}O_8SSi_2$ $[M+H]^+$ m/z = 833.39, found: 833.58.

*1,2-bis[2-(4-methylbenzenesulfonyloxy)ethoxy]ethane **14***

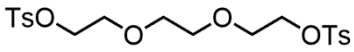

Tri(ethylene glycol) (8.93 mL, 66.6 mmol) and tosyl chloride (38.1 g, 199 mmol) were dissolved in dichloromethane (150 mL). The mixture was cooled at 0°C and potassium hydroxide (11.2 g, 199 mmol) was added in five portions. The reaction medium was stirred overnight while allowed to reach room temperature. The mixture was washed with cold water (60 mL) twice, cold brine (20 mL) and the organic layer was dried over sodium sulfate before evaporating the solvent under vacuum. The crude solid was purified by recrystallization in dichloromethane : *n*-hexane (1 : 1) to afford 1,2-bis[2-(4-methylbenzenesulfonyloxy)ethoxy]ethane (23.2 g, 50.6 mmol, 76 %) as white crystals. **^{1}H NMR** (400 MHz, $CDCl_3$) δ 7.80 – 7.72 (m, 4H), 7.33 – 7.27 (m, 4H), 4.17 – 4.12 (m, 4H), 3.68 – 3.62 (m, 4H), 2.44 (s, 6H), 1.56 (s, 4H). **^{13}C NMR** (100 MHz, $CDCl_3$) δ 144.5, 133.0, 129.9, 128.1, 70.5, 69.3, 68.5, 21.7. **MS** (ESI): calculated for $C_{20}H_{27}O_8S_2$ $[M+H]^+$ m/z = 459.11, found: 459.47.

*2-(2-(2-azidoethoxy)ethoxy)ethyl 4-methylbenzenesulfonate **15***

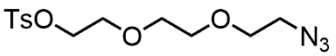

Under argon, compound **14** (15 g, 32.7 mmol) was dissolved in dry DMF (240 mL). Sodium azide (2.15 g, 32.7 mmol) was then added by portions. The mixture was stirred at room temperature overnight. The mixture was then concentrated under vacuum and the residue was purified by column chromatography (silica gel, ethyl acetate : cyclohexane, 0 : 1 → 1 : 1) to afford 2-(2-(2-azidoethoxy)ethoxy)ethyl 4-methylbenzenesulfonate (4.92 g, 14.9 mmol, 46 %) as a yellow liquid. **R_f** = 0.4 (ethyl acetate : cyclohexane, 1 : 6). **^{1}H NMR** (400 MHz, $CDCl_3$) δ 7.80 (d, *J* = 8.2 Hz, 2H), 7.42 – 7.31 (m, 2H), 4.16 (t, *J* = 4.8 Hz, 2H), 3.70 (t, *J* = 4.8 Hz, 2H), 3.64 (t, *J* = 5.2 Hz, 2H), 3.60 (s, 4H), 3.36 (t, *J* = 5.2 Hz, 2H), 2.45 (s, 3H). **^{13}C NMR** (100 MHz, $CDCl_3$) δ 144.8, 132.7, 130.1, 128.1, 71.2, 70.5, 70.0, 69.4, 68.9, 50.8, 21.5. **MS** (ESI): calculated for $C_{13}H_{20}N_3O_5S$ $[M+H]^+$ m/z = 330.10, found: 330.05.

1,2-bis(2-azidoethoxy)ethane 16

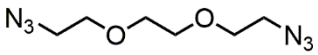

Under argon, compound **14** (15 g, 32.7 mmol) was dissolved in dry DMF (240 mL). Sodium azide (2.15 g, 32.7 mmol) was then added by portions. The mixture was stirred at room temperature overnight. The mixture was then concentrated under vacuum and the residue was purified by column chromatography (silica gel, ethyl acetate : cyclohexane, 0 : 1 → 1 : 1) to afford 1,2-bis[2-azidoethoxy]ethane (1.66 g, 8.29 mmol, 25 %) as a yellow liquid. $\mathbf{R_f}$ = 0.3 (ethyl acetate : cyclohexane, 1 : 6). **^{1}H NMR** (400 MHz, $CDCl_3$) δ 3.69 (t, *J* = 5.0 Hz, 4H), 3.68 (s, 4H), 3.39 (t, *J* = 5.0 Hz, 4H). **^{13}C NMR** (100 MHz, $CDCl_3$) δ 70.9, 70.2, 50.8. **MS** (ESI): calculated for $C_6H_{13}N_6O_2$ $[M+H]^+$ m/z = 201.10, found: 201.62.

2-(2-(2-azidoethoxy)ethoxy)ethylamine 17

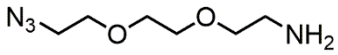

Compound **16** (2 g, 9.99 mmol) was dissolved in a mixture of ethyl acetate (30 mL) and aqueous hydrochloric acid at 1 mol.L^{-1} (15 mL). A solution of triphenylphosphine (2.62 g, 9.99 mmol) in ethyl acetate (30 mL) was prepared and added dropwise to the reaction medium. The mixture was vigorously stirred overnight at room temperature. At the end of the reaction, the organic layer was removed under vacuum, and the aqueous layer was washed with ethyl acetate (10 mL) twice. The pH of the aqueous solution was adjusted to 14 with sodium hydroxide pellets, and it was extracted with dichloromethane (30 mL) three more times. The combined organic phase was dried over sodium sulfate and the solvent was removed under vacuum to afford 2-(2-(2-azidoethoxy)ethoxy)ethylamine (1.24 g, 7.12 mmol, 71 %) as a yellow oil. **^{1}H NMR** (400 MHz, $CDCl_3$) δ 3.71 – 3.59 (m, 6H), 3.51 (t, *J* = 5.2 Hz, 2H), 3.39 (t, *J* = 5.0 Hz, 2H), 2.86 (t, *J* = 5.2 Hz, 2H). **^{13}C NMR** (100 MHz, $CDCl_3$) δ 73.2, 71.1, 70.5, 70.3, 50.8, 42.0. **MS** (ESI): calculated for $C_6H_{15}N_4O_2$ $[M+H]^+$ m/z = 175.11, found: 175.26.

2-(2-(2-(prop-2-yn-1-yloxy)ethoxy)ethoxy)ethanol 18

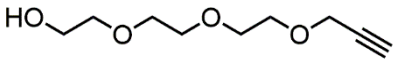

Under argon, a solution of tri(ethylene glycol (8.12 g, 54 mmol) in THF (190 mL) was prepared and potassium *tert*-butoxide (3.14 mg, 27 mmol) was added. The mixture was stirred for 30 min at room temperature and a solution of propargyl bromide (80 % in toluene, 2.9 mL, 27 mmol) diluted in THF (100 mL) was added dropwise. The reaction medium was stirred for 15 h at room temperature. The mixture was filtered through Celite® and washed with dichloromethane (100 mL). The crude residue was further purified by column chromatography (silica gel, ethyl acetate) to afford 2-(2-(2-(prop-2-yn-1-yloxy)ethoxy)ethoxy)ethanol (4.62 g, 25 mmol, 91 % with respect to propargyl bromide) as a slight yellow oil. $\mathbf{R_f}$ = 0.3 (ethyl acetate). **^{1}H NMR** (400 MHz, $CDCl_3$) δ 4.03 - 4.02 (m, 2H), 3.52 - 3.47 (m, 10H), 3.42 - 3.40 (m, 2H), 3.18 (br s, 1H), 2.37 - 2.36 (m, 1H). **^{13}C NMR** (100 MHz, $CDCl_3$) δ 79.2, 74.4, 72.5, 72.1, 70.5, 70.1, 69.8, 61.0, 58.5. **MS** (ESI): calculated for $C_9H_{17}O_4$ $[M+H]^+$ m/z = 189.11, found: 189.33.

2-(2-(2-(prop-2-yn-1-yloxy)ethoxy)ethoxy)ethyl 4-methylbenzene sulfonate 19

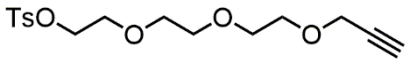

Sodium hydroxide (1.87 g, 47 mmol) was added to a solution of compound **18** (2.8 g, 15 mmol) dissolved in water (19 mL) cooled at 0°C. A solution of tosyl chloride (3.66 g, 19 mmol) dissolved in THF (19 mL) was added dropwise at 0°C. The mixture was stirred overnight while allowed to reach room temperature. The solution was diluted with of water (50 mL) and extracted with diethyl ether (50 mL) three times. The combined organic layers were washed with brine (50 mL), dried over sodium sulfate and the solvent was evaporated under vacuum to yield 2-(2-(2-(prop-2-yn-1-yloxy)ethoxy)ethoxy)ethyl 4-methylbenzene sulfonate (5.0 g, 15 mmol, 99 %) as a colorless oil. $\mathbf{R_f}$ = 0.45 (*n*-hexane : ethyl acetate, 1 : 1). **^{1}H NMR** (400 Mhz, $CDCl_3$) δ 7.80 (d, *J* = 8.4 Hz, 2H), 7.34 (d, *J* = 8.0 Hz, 2H), 4.19 (d, *J* = 2.4 Hz, 2H), 4.16 (t, *J* = 4.8 Hz, 2H), 3.70 - 3.67 (m, 4H), 3.65 - 3.63 (m, 2H), 3.60 (s, 4H), 2.45 (s, 3H), 2.42 (t, *J* = 2.4 Hz, 1H). **^{13}C NMR** (100 MHz, $CDCl_3$) δ 144.7, 133.0, 129.7, 127.9, 79.6, 74.5, 70.6, 70.5, 70.4, 69.2, 69.0, 68.6, 58.3, 21.6. **MS** (ESI): calculated for $C_{16}H_{22}O_6S$ $[M+H]^+$ m/z = 343.13, found: 343.01.

1-azido-2-{2-[2-(prop-2-yn-1-yloxy)ethoxy]ethoxy}ethane 20

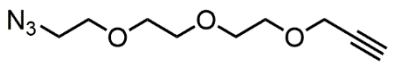

Under argon, sodium azide (1.14 g, 17.5 mmol) was added to a solution of compound **19** (3 g, 8.8 mmol) dissolved in DMF (50 mL). The temperature was then slowly raised to 65°C and the mixture was stirred overnight. The solution was removed under vacuum and the crude residue was purified by column chromatography (silica gel, cyclohexane : ethyl acetate, 7 : 3) to afford 1-azido-2-{2-[2-(prop-2-yn-1-yloxy)ethoxy]ethoxy}ethane (1.8 g, 8.44 mmol, 96 %). $\mathbf{R_f}$ = 0.4 (*n*-hexane : ethyl acetate, 7 : 3). **^{1}H NMR** (400 MHz, $CDCl_3$) δ 4.21 (d, *J* = 2.4 Hz, 2H), 3.73 – 3.62 (m, 6H), 3.67 (s, 4H), 3.39 (t, *J* = 5.1 Hz, 2H), 2.42 (t, *J* = 2.4 Hz, 1H). **^{13}C NMR** (100 Mhz, $CDCl_3$) δ 78.7, 76.4, 70.4, 70.1, 70.0, 69.5, 69.2, 60.3, 51.0. **MS** (ESI): calculated for $C_9H_{15}N_3O_3$ $[M+H]^+$ m/z = 214.11, found 214.12.

2-{2-[2-(prop-2-yn-1-yloxy)ethoxy]ethoxy}ethylamine 21

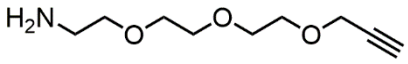

Under argon, compound **20** (1.2 g, 5.6 mmol) was dissolved in THF (62.5 mL), along with triphenylphosphine (3.0 g, 11.3 mmol). The mixture was stirred for 4 h at room temperature. Water (3.0 mL, 166 mmol) was then added and the reaction medium was stirred overnight. The solvent was evaporated under vacuum and the crude residue was purified by column chromatography (silica gel, dichloromethane : methanol : triethylamine$_3$, 50 : 1 : 0 → 10 : 1 : 0.1) to afford 2-{2-[2-(prop-2-yn-1-yloxy)ethoxy]ethoxy}ethylamine (0.72 g, 3.9 mmol, 68 %) as a yellow oil. $\mathbf{R_f}$ = 0.16 (dichloromethane : methanol : triethylamine, 10 : 1 : 0.1). **^{1}H NMR** (400 MHz, $CDCl_3$) δ 4.20 (t, *J* = 2.1 Hz, 2H), 3.72 - 3.61 (m, 8H), 3.51 (t, *J* = 5.3 Hz, 2H), 2.85 (t, *J* = 5.3 Hz, 2H), 2.24 (t, *J* = 2.1 Hz, 1H). **^{13}C NMR** (100 MHz, $CDCl_3$) δ 78.7, 76.4, 72.9, 70.4, 70.1, 69.5, 69.2, 60.3, 41.6. **MS** (ESI): calculated for $C_9H_{17}NO_3$ $[M+H]^+$ m/z = 189.12, found 189.13.

4,5-dihydroxythioxanthen-9-ylidene-[5',6'-bis[(2R)-(1-ethoxy-1-oxopropan-2-yl)oxy]-2',7'-dimethylindane] 22

Ethyl-protected bisphenol motor

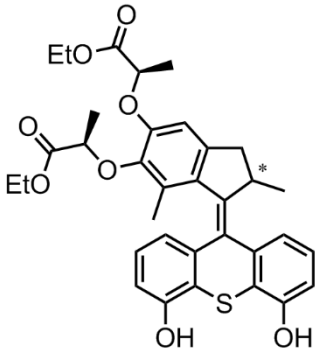

The same procedure is applied for *(R)*-**22** and *(S)*-**22**, starting from *(R)*-**13** and *(S)*-**13**, respectively. In a typical experiment, compound *(S)*-**13** (2.08 g, 2.45 mmol) was dissolved in THF (70 mL) and *tert*-butylammonium fluoride (1 M in THF, 8.5 mL, 8.5 mmol) was added at 0°C. The mixture was stirred at this temperature for 5 min. A saturated solution of ammonium chloride (120 mL) was added and the aqueous layer was extracted with dichloromethane (100 mL) three times. The combined organic layer was dried over sodium sulfate and concentrated under vacuum. The crude residue was purified by column chromatography (silica gel, dichloromethane : methanol, 1 : 0 → 10 : 1) to afford compound *(S)*-**22** (1.42 g, 2.35 mmol, 96 %) as a yellow solid. **For *(R,R,S)*-isomer:** R_f = 0.2 (CH_2Cl_2 : MeOH, 20 : 1). **^{1}H NMR** (400 MHz, $CDCl_3$) δ 7.31 (d, *J* = 7.6 Hz, 1H), 7.22 (dd, *J* = 8.0, 8.0 Hz, 1H), 6.95 (dd, *J* = 7.6, 7.6 Hz, 1H), 6.82 (dd, *J* = 8.0, 1.2 Hz, 1H), 6.74 (dd, *J* = 8.0, 1.2 Hz, 1H), 6.65 (dd, *J* = 7.6, 1.2 Hz, 1H), 6.56 (s, 1H), 4.81 (q, *J* = 6.8 Hz, 1H), 4.77 (q, *J* = 6.8 Hz, 1H), 4.30 – 4.08 (m, 5H), 3.37 (dd, *J* = 15.0, 6.1 Hz, 1H), 2.37 (d, *J* = 15.0 Hz, 1H), 1.62 (d, *J* = 6.8 Hz, 3H), 1.46 (d, *J* = 6.8 Hz, 3H), 1.32 (s, 3H), 1.23 (t, *J* = 7.1 Hz, 3H), 1.20 (t, *J* = 7.1 Hz, 3H), 0.71 (d, *J* = 6.7 Hz, 3H). **^{13}C NMR** (100 MHz, CD_3OD) δ 174.2, 173.5, 155.7, 155.2, 151.1, 146.5, 145.5, 143.8, 143.5, 140.2, 134.7, 131.9, 130.2, 127.9, 127.8, 124.0, 123.3, 120.5, 120.0, 113.2, 113.1, 109.4, 77.9, 74.1, 62.4, 62.0, 40.4, 39.3, 19.3, 18.9, 18.7, 15.0, 14.5, 14.4. **HRMS**: calculated for $C_{34}H_{36}LiO_8S$ $[M+Li]^+$ 611.2286, found: 611.2284. **For *(R,R,R)*-isomer:** R_f = 0.2 (CH_2Cl_2 : MeOH, 20 : 1). **^{1}H NMR** (400 MHz, $CDCl_3$) δ 7.31 (d, *J* = 7.6 Hz, 1H), 7.22 (dd, *J* = 7.9, 7.9 Hz, 1H), 6.99 (t, *J* = 7.9, 7.9 Hz, 1H), 6.82 (dd, *J* = 8.0, 1.2 Hz, 1H), 6.76 (dd, *J* = 8.0, 1.2 Hz, 1H), 6.68 (dd, *J* = 7.6, 1.2 Hz, 1H), 6.59 (s, 1H), 4.79 (q, *J* = 6.8 Hz, 1H), 4.54 (q, *J* = 6.8 Hz, 1H), 4.33 – 4.06 (m, 5H), 3.35 (dd, *J* = 14.8, 6.2 Hz, 1H), 2.38 (d, *J* = 14.8 Hz, 1H), 1.63 (d, *J* = 6.8 Hz, 3H), 1.53 (d, *J* = 6.8 Hz, 3H), 1.30 (s, 3H), 1.31 (t, *J* = 7.3 Hz, 3H), 1.25 (t, *J* = 7.3 Hz, 3H), 0.70 (d, *J* = 6.8 Hz, 3H).**^{13}C NMR** (100 MHz, CD_3OD) *δ* = 174.2, 173.5, 155.7, 155.2, 151.1, 146.5, 145.5, 143.8, 143.5, 140.2, 134.7, 131.9, 130.2, 127.9, 127.8, 124.0, 123.3, 120.5, 120.0, 113.2, 113.1, 109.4, 77.9, 74.1, 62.4, 62.0, 40.4, 39.3, 19.3, 18.9, 18.7, 15.0, 14.5, 14.4. **MS** (ESI): calculated for $C_{34}H_{36}O_8S$ $[M+H]^+$ m/z = 605.23, found: 605.22.

4,5-bis[2-(2-(2-azidoethoxy)ethoxy)ethoxy]-thioxanthen-9-ylidene-[(2'S)-5',6'-bis[(2R)-(1-ethoxy-1-oxopropan-2-yl)oxy]-2',7'-dimethylindane] 23

Ethyl-protected diazido-(S)-motor

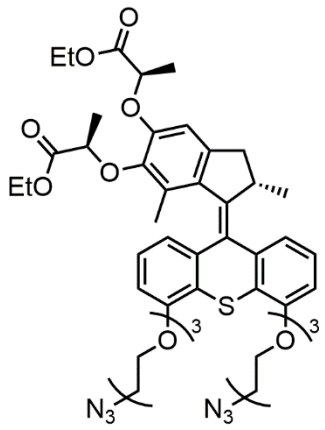

Compound *(S)*-**22** (200 mg, 0.33 mmol) was dissolved in DMF (20 mL) and compound **15** (408.5 mg, 1.24 mmol) was added along with potassium carbonate (171.4 mg, 1.24 mmol). The mixture was stirred for 2 d at 50°C and was then diluted with water (40 mL). The aqueous phase was extracted with dichloromethane (100 mL) three times. The combined organic layer was dried over sodium sulfate and the solvent was evaporated under vacuum. The crude product was further purified by column chromatography (silica gel, hexane : ethyl acetate, 3 : 1 → 1 : 1) to afford of compound *(S)*-**23** (251.5 mg, 0.27 mmol, 83 %) as an orange liquid. $\mathbf{R_f}$ = 0.6 (hexane : ethyl acetate, 6 : 1). **^{1}H NMR** (400 MHz, $CDCl_3$) δ 7.33 (d, *J* = 7.7 Hz, 1H), 7.21 (dd, *J* = 7.7, 7.7 Hz, 1H), 6.94 (dd, *J* = 7.7, 7.7 Hz, 1H), 6.77 (dd, *J* = 8.1, 1.1 Hz, 1H), 6.69 (dd, *J* = 8.1, 1.1 Hz, 1H), 6.64 (dd, *J* = 7.7, 1.1 Hz, 1H), 6.53 (s, 1H), 4.79 (q, *J* = 6.8 Hz, 1H), 4.76 (q, *J* = 6.8 Hz, 1H), 4.35 – 4.05 (m, 9H), 4.03 – 3.92 (m, 4H), 3.89 – 3.81 (m, 4H), 3.78 – 3.65 (m, 8H), 3.38 (t, *J* = 5.0 Hz, 4H), 3.34 (dd, *J* = 14.6, 5.9 Hz, 1H), 2.33 (d, *J* = 14.6 Hz, 1H), 1.62 (d, *J* = 6.8 Hz, 3H), 1.46 (d, *J* = 6.8 Hz, 3H), 1.22 (t, *J* = 7.1 Hz, 3H), 1.20 (s, 3H), 1.19 (t, *J* = 7.1 Hz, 3H), 0.62 (d, *J* = 6.7 Hz, 3H). **^{13}C NMR** (100 MHz, $CDCl_3$) δ 172.6, 172.1, 155.9, 155.4, 149.7, 146.0, 144.5, 142.0, 141.9, 138.4, 135.4, 131.1, 127.7, 126.9, 126.5, 125.0, 124.7, 121.0, 120.4, 109.6, 109.1, 108.1, 73.0, 71.3, 70.9, 70.2, 69.8, 68.9, 61.3, 60.8, 50.8, 39.6, 38.2, 27.0, 19.1, 18.7, 18.5, 14.6, 14.2. **MS** (ESI): calculated for $C_{46}H_{59}N_6O_{12}S$ $[M+H]^+$ 919.38, found: 919.45.

4,5-bis[2-(2-(2-azidoethoxy)ethoxy)ethoxy]-thioxanthen-9-ylidene-[(2'S)-5',6'-bis[(2R)-(2-methylethanoic acid)oxy]-2',7'-dimethylindane] 24

Diacid-, diazido-(S)-motor

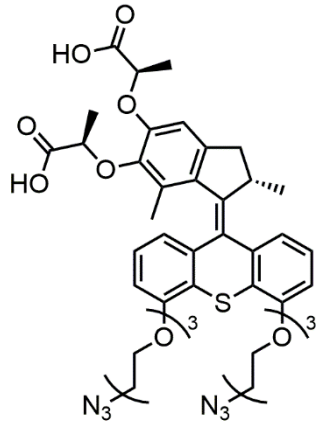

Compound *(S)*-**23** (243.2 mg, 0.26 mmol) was dissolved in a mixture of methanol (2 mL) and THF (2 mL). A solution of sodium hydroxide (1 M in water, 2 mL, 1.5 mmol) was then added and the mixture was stirred overnight at room temperature. The solution was neutralized by dropwise addition of aqueous hydrochloric acid at 1 M (2 mL). The aqueous layer was extracted with dichloromethane (20 mL) three times and the organic layer was consequently washed with brine (25 mL) twice. The organic phase was dried over sodium sulfate and the solvent was removed under vacuum to afford compound *(S)*-**24** (189 mg, 0.22 mmol, 83 %) as a green solid. **^{1}H NMR** (400 MHz, $CDCl_3$) δ 7.34 (d, *J* = 7.8 Hz, 1H), 7.24 (dd, *J* = 8.1, 8.1 Hz, 1H), 6.98 (dd, *J* = 7.8, 7.8 Hz, 1H), 6.79 (d, *J* = 8.1 Hz, 1H), 6.74 (d, *J* = 8.1 Hz, 1H), 6.69 (s, 1H), 6.65 (d, *J* = 7.8 Hz, 1H), 4.84 (q, *J* = 6.7 Hz, 1H), 4.36 – 4.10 (m, 6H), 4.00 – 3.95 (m, 4H), 3.87 – 3.83 (m, 4H), 3.74 – 3.65 (m, 8H), 3.38 (t, *J* = 5.1 Hz, 4H), 3.36 (d, *J* = 7.2 Hz, 1H), 2.40 (d, *J* = 15.1 Hz, 1H), 1.69 (d, *J* = 6.7 Hz, 3H), 1.46 (d, *J* = 6.9 Hz, 3H), 1.14 (s, 3H), 0.65 (d, *J* = 6.7 Hz, 3H). **^{13}C NMR** (100 MHz, $CDCl_3$) δ 172.5, 172.3, 156.4, 153.5, 145.6, 145.2, 142.6, 141.5, 138.3, 137.9, 131.1, 130.9, 128.7, 123.8, 126.7, 124.8, 124.5, 120.9, 120.3, 110.5, 109.8, 108.8, 71.3, 71.0, 70.9, 70.2, 69.9, 69.1, 68.9, 50.9, 39.7, 38.2, 32.1, 29.8, 22.8, 19.0, 18.5, 18.2, 15.2, 14.3. **MS** (ESI): calculated for $C_{42}H_{50}N_6O_{12}S$ $[M+H]^+$ m/z = 863.31, found: 863.45.

4,5-bis[2-(2-(2-azidoethoxy)ethoxy)ethoxy]-thioxanthen-9-ylidene-[(2'S)-5',6'-bis[(2R)-(N-(2-(2-(2-azidoethoxy)ethoxy)ethyl)propan-2-amide)oxy]-2',7'-dimethylindane] 25

Tetraazido*-(S)-*motor

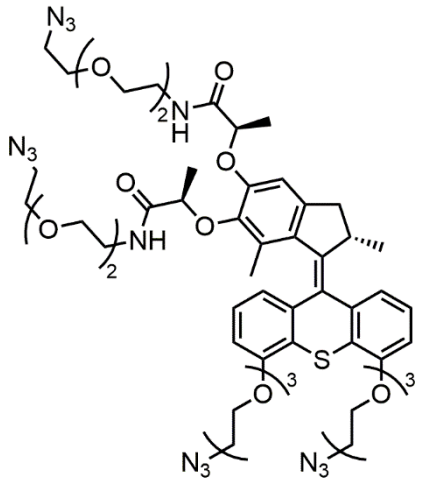

Compound *(S)*-**24** (189 mg, 0.22 mmol) was dissolved in dichloromethane (15 mL) and 1-ethyl-3-(3-dimethylaminopropyl)carbodiimide hydrochloride (252 mg, 1.31 mmol) was added along with hydroxybenzotriazole (67.6 mg, 0.50 mmol). The mixture was stirred 40 min at room temperature and compound **17** (87.8 mg, 0.50 mmol) was added. The solution was stirred overnight at room temperature. The solvent was removed under vacuum and the residue was purified by column chromatography (silica gel, dichloromethane : methanol, 100 : 1 ⟶ 10 : 1) to afford compound *(S)*-**25** (220 mg, 0.19 mmol, 86 %) as a green oil. $\mathbf{R}_f$ = 0.4 (dichloromethane : methanol, 10 : 1). **^{1}H NMR** (400 MHz, $CDCl_3$) δ 7.46 (t, *J* = 5.3 Hz, 1H), 7.33 (d, *J* = 7.9 Hz, 1H), 7.22 (dd, *J* = 7.9, 7.9 Hz, 1H), 6.98 (t, *J* = 5.3 Hz, 1H), 6.94 (dd, 1H), 6.77 (d, *J* = 8.1 Hz, 1H), 6.71 (d, *J* = 8.1 Hz, 1H), 6.66 (d, *J* = 7.9 Hz, 1H), 6.65 (s, 1H), 4.66 (q, *J* = 6.7 Hz, 1H), 4.46 (q, *J* = 6.7 Hz, 1H), 4.34 – 4.07 (m, 5H), 4.02 – 3.89 (m, 4H), 3.86 – 3.80 (m, 4H), 3.74 – 3.64 (m, 8H), 3.64 – 3.40 (m, 22H), 3.36 (t, *J* = 5.1 Hz, 4H), 3.31 – 3.24 (m, 4H), 2.36 (d, *J* = 15.2 Hz, 1H), 1.57 (d, *J* = 6.7 Hz, 3H), 1.28 (d, *J* = 6.7

Hz, 3H), 1.12 (s, 3H), 0.61 (d, *J* = 6.7 Hz, 3H). **^{13}C NMR** (100 MHz, $CDCl_3$) δ 172.4, 172.0, 156.0, 155.3, 149.7, 145.4, 143.5, 142.9, 141.5, 137.8, 134.2, 130.9, 128.3, 126.7, 126.6, 124.8, 124.2, 120.9, 120.1, 109.5, 109.1, 78.9, 77.3, 76.1, 71.2, 70.8, 70.8, 70.5, 70.5, 70.3, 70.2, 70.1, 70.0, 70.0, 69.8, 69.8, 69.7, 68.9, 68.7, 50.7, 50.6, 39.6, 38.8, 38.8, 38.0, 19.1, 18.9, 18.2, 15.2. NMR spectra can be found in Appendix C. **MS** (ESI): calculated for $C_{54}H_{75}N_{14}O_{14}S$ $[M+H]^+$ m/z = 1175.52, found 1175.23.

*4,5-bis[2-(2-(2-(prop-2-yn-1-yloxy)ethoxy)ethoxy)ethoxy]-thioxanthen-9-ylidene-[(2'S)-5',6'-bis[(2R)-(1-ethoxy-1-oxopropan-2-yl)oxy]-2',7'-dimethylindane] **26***
Ethyl-protected bis-alkyne (S)-motor

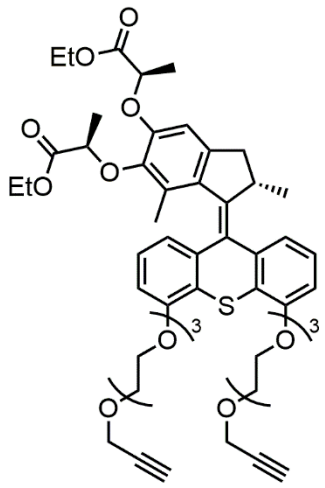

Compound *(S)*-**22** (134.6 mg, 0.22 mmol) was dissolved in DMF (15 mL) and the mixture was cooled at 0°C. Compound **19** (227.9 mg, 0.67 mmol) was then added and the reaction medium was stirred for 3 d while allowed to reach room temperature. A saturated solution of ammonium chloride (10 mL) was then added and the aqueous layer was extracted with dichloromethane (20 mL) three times. The combined organic layer was dried over sodium sulfate and the solvent was evaporated under vacuum. The crude residue was purified by column chromatography (silica gel, dichloromethane : methanol, 1 : 0 → 10 : 1) to afford compound *(S)*-**26** (194 mg, 0.21 mmol, 93 %) as a green solid. R_f = 0.2 (ethyl acetate : cyclohexane, 1 : 1). **^{1}H NMR** (400 MHz, $CDCl_3$) δ 7.33 (dd, *J* = 8.1, 8.1 Hz, 1H), 7.21 (dd, *J* = 7.9, 7.9 Hz, 1H), 6.93 (d, *J* = 7.9, 7.9 Hz, 1H), 6.76 (d, *J* = 8.1 Hz, 1H), 6.69 (d, *J* = 8.1 Hz, 1H), 6.64 (dd, *J* = 7.9, 1.1 Hz, 1H), 6.53 (s, 1H), 4.79 (q, *J* = 6.8 Hz, 1H), 4.76 (q, *J* = 6.8 Hz, 1H), 4.35 – 4.08 (m, 13H), 4.03 – 3.91 (m, 4H), 3.88 – 3.80 (m, 4H), 3.78 – 3.61 (m, 12H), 3.34 (dd, *J* = 14.9, 6.1 Hz, 1H), 2.45 – 2.39 (m, 2H), 2.32 (d, *J* = 14.9 Hz, 1H), 1.61 (d, *J* = 6.8 Hz, 3H), 1.46 (d, *J* = 6.8 Hz, 3H), 1.22 (t, *J* = 7.1 Hz, 3H), 1.19 (s, 3H), 1.19 (t, *J* = 7.1 Hz, 3H), 0.62 (d, *J* = 6.7 Hz, 3H). **^{13}C NMR** (100 MHz, $CDCl_3$) δ 172.5, 172.0, 155.8, 155.3, 149.6, 145.9, 144.4, 141.9, 141.7, 138.2, 133.4, 131.0, 127.6, 126.7, 126.4, 124.9, 124.6, 120.9, 120.3, 109.5, 109.0, 108.0, 79.7, 77.2, 76.8, 74.5, 72.9, 71.1, 70.8, 70.4, 69.7, 69.6, 69.1, 68.8, 61.2, 60.7, 58.4, 39.5, 38.1, 18.9, 18.6, 18.4, 14.5, 14.1, 14.0. **MS** (ESI): calculated for $C_{52}H_{65}O_{14}S$ $[M+H]^+$ m/z = 945.41, found: 945.51.

4,5-bis[2-(2-(2-(prop-2-yn-1-yloxy)ethoxy)ethoxy)ethoxy]-thioxanthen-9-ylidene-[(2'S)-5',6'-bis[(2R)-(2-methylethanoic acid)oxy]-2',7'-dimethylindane] 27

Diacid, bis-alkyne-(S)-motor

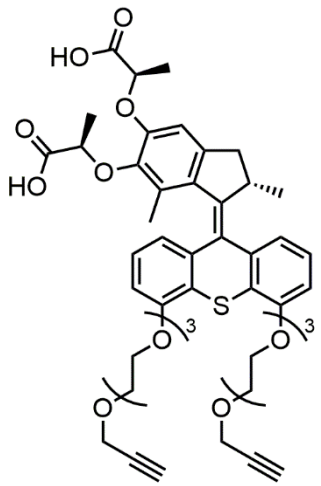

A solution of *(S)*-**26** (480 mg, 0.51 mmol) in a mixture of THF : MeOH (1 : 1, 3 mL) was prepared and a solution of sodium hydroxide (102 mg, 2.55 mmol) in water (1.5 mL) was added. The mixture was stirred at room temperature for 30 min and the solution was neutralized with aqueous hydrochloric acid at 1 M (1 mL). The aqueous phase was extracted with dichloromethane (10 mL) three times. The combined organic phase was dried over sodium sulfate and concentrated in vacuum. The residue was purified by column chromatography (silica gel, dichloromethane : methanol, 1 : 0 → 20 : 1) to afford compound *(S)*-**27** (435 mg, 0.49 mmol, 96 %) as a slightly green solid. $\mathbf{R}_f$ = 0.1 (dichloromethane : methanol, 100 : 1). **^{1}H NMR** (400 MHz, CD_3OD) δ 7.37 (d, *J* = 7.6 Hz, 1H), 7.27 (dd, *J* = 8.0, 8.0 Hz, 1H), 6.98 (dd, *J* = 8.0, 8.0 Hz, 1H), 6.87 (d, *J* = 7.6 Hz, 1H), 6.81 (d, *J* = 7.6 Hz, 1H), 6.67 (s, 1H), 6.60 (dd, *J* = 8.0, 1.2 Hz, 1H), 4.81 (q, *J* = 7.2 Hz, 1H), 4.62 (q, *J* = 6.8 Hz, 1H), 4.30 - 4.10 (m, 9H), 3.92 - 3.89 (m, 4H), 3.78 - 3.77 (m, 4H), 3.66 - 3.60 (m, 12H), 3.40 - 3.35 (m, 1H), 2.80 (t, *J* = 2.4 Hz, 1H), 2.79 (t, *J* = 2.4 Hz, 1H), 2.36 (d, *J* = 15.2 Hz, 1H), 1.60 (d, *J* = 6.8 Hz, 3H), 1.38 (d, *J* = 6.8 Hz, 3H), 1.17 (s, 3H), 0.60 (d, *J* = 6.8 Hz, 3H). **^{13}C NMR** (100 MHz, CD_3OD) δ 172.1, 175.2, 157.4, 156.8, 151.5, 147.2, 145.5, 143.8, 143.2, 139.5, 138.1, 134.5, 131.9, 129.3, 128.0, 126.4, 125.6, 122.0, 121.3, 110.8, 110.6, 109.5, 80.7, 78.4, 76.0, 74.3, 73.7, 72.1, 71.7, 71.6, 71.4, 70.9, 70.8, 70.2, 70.1, 62.3, 59.1, 40.4, 39.3, 19.3, 19.1, 18.8, 15.2. **MS** (ESI): calculated for $C_{48}H_{56}O_{14}S$ $[M+H]^+$ m/z = 889.35, found: 889.18.

*4,5-bis[2-(2-(2-(prop-2-yn-1-yloxy)ethoxy)ethoxy)ethoxy]-thioxanthen-9-ylidene-[(2'S)-5',6'-bis[(2R)-(N-(2-(2-(2-(prop-2-yn-1-yloxy)ethoxy)ethoxy)ethyl)propan-2-amide)oxy]-2',7'-dimethylindane] **28***

Tetra-alkyne* (S)-*motor

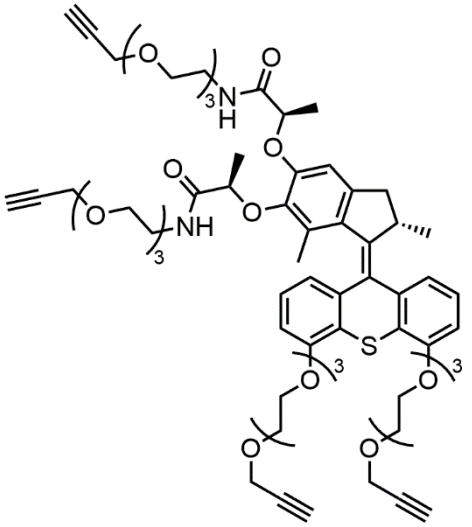

Under argon, compound *(S)*-**27** (130 mg, 0.15 mmol) was dissolved in dichloromethane (8 mL) and 1-ethyl-3-(3-dimethylaminopropyl)carbodiimide hydrochloride (210 mg, 0.89 mmol) was added along with hydroxybenzotriazole (51.4 mg, 0.33 mmol). The mixture was stirred for 40 min at room temperature and a solution of compound **21** (164 mg, 0.89 mmol) in dichloromethane (3 mL) was added. The solution was stirred overnight at room temperature. The mixture was diluted with dichloromethane (30 mL) and washed with water (10 mL) three times. The aqueous phase was extracted with dichloromethane (30 mL) three times. The combined organic layer was dried over sodium sulfate and the solvent was evaporated under vacuum. The residue was purified by column chromatography (silica gel, dichloromethane : methanol, 1 : 0 → 40 : 1) to afford compound *(S)*-**28** (150 mg, 0.12 mmol, 84 %) as a slightly yellow oil. $\mathbf{R_f}$ = 0.4 (dichloromethane : methanol, 100 : 1). **^{1}H NMR** (100 MHz, $CDCl_3$) δ 7.51 (t, *J* = 5.2 Hz, 1H), 7.34 (d, *J* = 7.9 Hz, 1H), 7.23 (dd, *J* = 7.9, 7.9 Hz, 1H), 7.04 (t, *J* = 5.2 Hz, 1H), 6.96 (dd, *J* = 7.9, 7.9 Hz, 1H), 6.78 (d, *J* = 7.9 Hz, 1H), 6.72 (d, *J* = 7.9 Hz, 1H), 6.68 (d, *J* = 6.5 Hz, 1H), 6.66 (s, 1H), 4.67 (q, *J* = 6.5 Hz, 1H), 4.44 (q, *J* = 6.5 Hz, 1H), 4.35 – 4.25 (m, 2H), 4.26 – 4.09 (m, 10H), 4.02 – 3.90 (m, 5H), 3.87 – 3.80 (m, 4H), 3.78 – 3.31 (m, 39H), 2.46 – 2.33 (m, 4H), 1.59 (d, *J* = 6.5 Hz, 3H), 1.30 (d, *J* = 6.5 Hz, 3H), 1.14 (s, 3H), 0.63 (d, *J* = 6.5 Hz, 3H).. **^{13}C NMR** (100 MHz, $CDCl_3$) δ 172.6, 172.1, 156.2, 155.5, 149.9, 145.5, 143.8, 143.0, 141.6, 137.9, 134.3, 131.1, 128.5, 126.8, 126.7, 125.1, 124.5, 121.0, 120.3, 109.7, 109.3, 109.2, 79.8, 79.7, 79.1, 77.4, 76.3, 74.8, 74.7, 74.7, 71.2, 70.9, 70.9, 70.6, 70.6, 70.5, 70.4, 70.4, 70.3, 69.9, 69.9, 69.8, 69.3, 69.2, 69.2, 69.0, 68.9, 58.5, 58.5, 39.8, 39.0, 39.0, 38.2, 19.3, 19.1, 18.4, 15.4. NMR spectra can be found in Appendix C. **MS** (ESI): calculated for $C_{66}H_{87}N_2O_{18}S$ $[M+H]^+$ m/z = 1227.56, found: 1227.95.

*6-((tert-butoxycarbonyl)amino)hexyl acrylate **29***

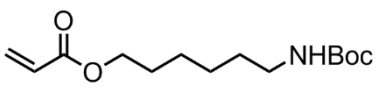

Under argon, 6-amino-hexan-1-ol (1 g, 8.5 mmol) was dissolved in dichloromethane (8 mL). Di-*tert*-butyl dicarbonate (2.05 g, 9.4 mmol) was slowly added and the solution was stirred for 3 h at room temperature. The mixture was then cooled to 0°C before adding triethylamine (1.4 mL,

10 mmol), followed by dropwise addition of acryloyl chloride (0.8 mL, 9.9 mmol). The solution was stirred for 3 h while allowed to reach room temperature. The resulting mixture was washed with aqueous hydrochloric acid at 1 M (10 mL) and aqueous sodium hydroxide at 1 M (10 mL). The organic layer was then dried over sodium sulfate and the solvent was evaporated to afford 6-((*tert*-butoxycarbonyl)amino)hexyl acrylate (1.4 g, 5.16 mmol, 60 %) as a colorless oil. **^{1}H NMR**. (400 MHz, $CDCl_3$) δ 6.39 (dd, *J* = 17.3, 1.5 Hz, 1H), 6.11 (dd, *J* =17.3, 10.4 Hz, 1H), 5.81 (dd, *J* = 10.4, 1.5 Hz, 1H), 4.14 (t, *J* = 6.7 Hz, 2H), 3.15 - 3.08 (m, 2H), 1.72 – 1.62 (m, 2H), 1.52 – 1.29 (m, 6H), 1.42 (s, 9H). **^{13}C NMR**. (100 MHz, $CDCl_3$) δ 166.1, 156.2, 130.4, 128.5, 78.9, 64.4, 40.4, 29.8, 28.4, 28.2, 26.2, 25.7. **MS** (ESI): calculated for $C_{14}H_{25}NO_4$ $[M+H]^+$ m/z = 272.18, found: 272.54.

6-aminohexyl acrylate hydrochloride **30**

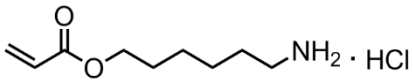

Compound **29** (1.4 g, 8.5 mmol) were dissolved in 10 mL of hydrochloric acid at 2 M in diethyl ether. The mixture was stirred for 3 h at room temperature. The precipitate was filtered, washed with diethyl ether and dried under vacuum to afford 6-aminohexylacrylate hydrochloride (0.81 g, 3.9 mmol, 75 %) as a white solid.**^{1}H NMR**. (400 MHz, CD_3OD) δ 6.29 (dd, *J* = 17.3, 1.6 Hz, 1H), 6.07 (dd, *J* = 17.3, 10.4 Hz, 1H), 5.80 (dd, *J* = 10.4, 1.6 Hz, 1H), 4.17 (t, *J* = 6.6 Hz, 2H), 3.70 (t, *J* = 6.3 Hz, 2H), 1.71 – 1.53 (m, 8H). **^{13}C NMR**. (100 MHz, $CDCl_3$) δ 166.2, 130.9, 128.5, 64.5, 41.9, 32.9, 28.4, 26.2, 25.7. **MS** (ESI): calculated for $C_9H_{19}NO_2$ $[M+H]^+$ m/z = 172.13, found: 171.89.

*4,5-bis[2-(*tert*-butoxy)-2-oxoethoxy]-thioxanthen-9-ylidene-[(2'R)-5',6'-bis[(2R)-(1-ethoxy-1-oxopropan-2-yl)oxy]-2',7'-dimethylindane]* **31**

Tetra-ester (R)-motor

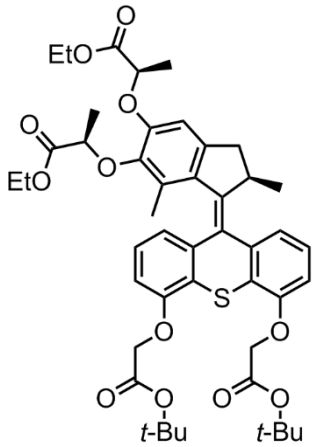

Compound *(R)*-**22** (100 mg, 0.17 mmol) was dissolved in DMF (12.5 mL). Potassium carbonate (114 mg, 0.82 mmol) and *tert*-butylbromoacetate (0.1 mL, 0.68 mmol) were added. The mixture was stirred overnight at 50°C. The solution was then diluted with water (10 mL) and thoroughly extracted with dichloromethane (100 mL). The organic phase was dried over sodium sulfate and the solvent was evaporated under vacuum. The crude residue was further purified by column chromatography (silica gel, ethyl acetate : toluene, 0 : 1 ⟶ 1 : 10) to afford compound *(R)*-**31** (129.3 mg, 0.16 mmol, 94 %) as a yellow solid. R_f = 0.6 (ethyl acetate : toluene, 1 : 10).**^{1}H NMR**. (400 MHz, $CDCl_3$) δ 7.35 (d, *J* = 7.7 Hz, 1H), 7.20 (dd, *J* = 8.1, 8.1 Hz, 1H), 6.93 (dd, *J* = 7.9, 7.9 Hz, 1H), 6.67 (dd, *J* = 7.7, 1.1 Hz, 1H), 6.65 (d, *J* = 7.7 Hz, 1H), 6.57 (dd, *J* = 8.1, 1.1 Hz, 1H), 6.54 (s, 1H),

4.77 (q, *J* = 6.6 Hz, 1H), 4.76 (q, *J* = 6.6 Hz, 1H), 4.68 – 4.59 (m, 4H), 4.29 – 4.08 (m, 5H), 3.34 (dd, *J* = 14.9, 6.3 Hz, 1H), 2.33 (d, *J* = 14.9 Hz, 1H), 1.61 (d, *J* = 6.8 Hz, 3H), 1.48 (s, 9H), 1.47 (s, 9H), 1.44 (d, *J* = 6.8 Hz, 3H), 1.25 – 1.15 (m, 9H), 0.63 (d, *J* = 6.7 Hz, 3H). **^{13}C NMR**. (100 MHz, $CDCl_3$) δ 174.5, 173.6, 169.9, 169.4, 155.2, 149.7, 151.2, 146.5, 145.6, 143.5, 143.4, 140.2, 134.7, 132.0, 130.2, 127.4, 127.0, 124.0, 123.3, 120.5, 120.0, 113.4, 113.1, 111.2, 82.1, 81.9, 77.9, 74.0, 66.4, 65.9, 62.1, 62.0, 40.5, 39.1, 27.6, 27.4, 19.4, 18.8, 18.7, 14.8, 14.5, 14.4. **MS** (ESI): calculated for $C_{46}H_{56}O_{12}S$ $[M+H]^+$ 833.35, found: 833.14.

4,5-bis(carboxymethoxy)-thioxanthen-9-ylidene-[(2'R)-5',6'-bis[(2R)-(2-methylethanoic acid)oxy]-,7'-dimethylindane] **32**

Tetra-acid (R)-motor

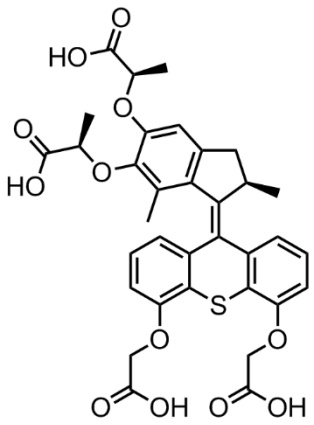

Compound *(R)*-**31** (129 mg, 0.15 mmol) was dissolved in a mixture methanol : water : THF (1 : 1 : 1, 10 mL). Sodium hydroxide at 1 M in water (0.93 mL) was then added. The mixture was stirred at 50°C for 2 h. The solution was neutralized with hydrochloric acid at 1 M in water (1 mL) and further extracted with dichloromethane (20 mL). The organic phase is finally washed with brine (10 mL) before being dried over sodium sulfate to afford compound *(R)*-**32** (102.9 mg, 0.15 mmol, quant.) as a green solid. **^{1}H NMR**. (400 MHz, CD_3OD) δ 7.42 (d, *J* = 7.8 Hz, 1H), 7.29 (dd, *J* = 8.0, 8.0 Hz, 1H), 7.01 (dd, *J* = 7.8, 7.8 Hz, 1H), 6.81 (dd, *J* = 8.1, 0.7 Hz, 1H), 6.76 (dd, *J* = 8.1, 1.1 Hz, 1H), 6.69 (s, 1H), 6.64 (dd, *J* = 7.7, 1.1 Hz, 1H), 4.82 – 4.77 (m, 5H), 4.60 (q, *J* = 7.1 Hz, 1H), 4.16 (t, *J* = 6.8 Hz, 1H), 3.41 (dd, *J* = 15.0, 6.2 Hz, 1H), 2.40 (d, *J* = 15.0 Hz, 1H), 1.60 (d, *J* = 6.8 Hz, 3H), 1.38 (d, *J* = 6.8 Hz, 3H), 1.19 (s, 3H), 0.63 (d, *J* = 6.7 Hz, 3H). **MS** (ESI): calculated for $C_{34}H_{32}O_{12}S$ $[M+H]^+$ m/z = 665.16, found: 664.95.

*4,5-bis[2-((6-(acryloyloxy)hexyl)amino)-2-oxoethoxy]-thioxanthen-9-ylidene-[(2'R)-5',6'-bis[(2R)-(N-((6-(acryloyloxy)hexyl)amino)propan-2-amide)oxy]-2',7'-dimethylindane] **33***

Tetra-acrylate (R)-motor

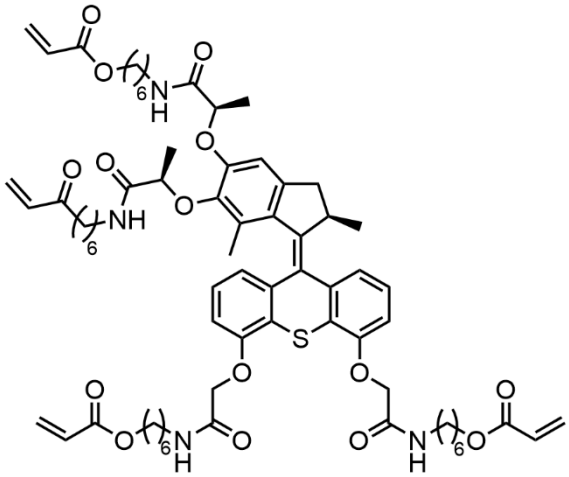

Compound *(R)*-**32** (102 mg, 0.15 mmol) was dissolved in dichloromethane (50 mL) alongside with 1-ethyl-3-(3-dimethylaminopropyl)carbodiimide hydrochloride (294.18 mg, 1.53 mmol) and hydroxybenzotriazole (20.74 mg, 0.15 mmol), and the mixture was stirred for 1 h at room temperature. Compound **30** (318.7 mg, 1.53 mmol) was then added and the solution was stirred overnight at room temperature. The solution was diluted with water (30 mL) and thoroughly extracted with dichloromethane (100 mL). The combined organic phase is washed with brine (20 mL) and the solvent is evaporated under vacuum. The crude residue was further purified by column chromatography (silica gel, dichloromethane : methanol, 1 : 0 → 50 : 1) to afford of compound *(R)*-**33** (108.4 mg, 0.085 mmol, 55 %) as a brown oil. R_f = 0.8 (dichloromethane : methanol, 10 : 1). **^{1}H NMR**. (400 MHz, $CDCl_3$) δ 7.45 (d, *J* = 7.7 Hz, 1H), 7.32 (dd, *J* = 8.1, 8.1 Hz, 1H), 7.06 (dd, *J* = 7.7, 7.7 Hz, 1H), 6.80 (d, *J* = 7.1 Hz, 1H), 6.76 (d, *J* = 8.4 Hz, 1H), 6.72 (s, 1H), 6.72 – 6.65 (m, 1H), 6.44 – 6.31 (m, 4H), 6.18 – 6.02 (m, 4H), 5.90 – 5.75 (m, 4H), 4.71 (q, *J* = 6.6 Hz, 1H), 4.68 – 4.54 (m, 4H), 4.40 (q, *J* = 6.9 Hz, 1H), 4.18 – 4.03 (m, 9H), 3.46 – 3.10 (m, 9H), 2.41 (d, *J* = 15.3 Hz, 1H), 1.72 – 1.18 (m, 32H), 1.62 (d, *J* = 6.8 Hz, 3H), 1.34 (d, *J* = 6.8 Hz, 3H), 1.17 (s, 3H), 0.66 (d, *J* = 6.8 Hz, 3H). **^{13}C NMR**. (100 MHz, $CDCl_3$) 172.4, 171.8, 170.5, 167.9, 167.8, 166.42, 166.40, 154.6, 154.1, 150.1, 147.0, 143.4, 143.0, 142.6, 139.0, 133.6, 130.80, 130.75, 130.69, 130.5, 128.6, 127.8, 127.7, 124.4, 123.7, 122.1, 121.8, 110.3, 109.9, 109.0, 77.7, 77.4, 76.1, 68.7, 68.6, 64.9, 64.5, 39.6, 39.24, 39.15, 39.12 38.3, 37.7, 29.8, 29.58, 29.57, 29.54, 28.68, 28.66, 28.61, 28.58, 26.7, 26.54, 26.52, 26.48, 25.74, 25.69, 25.66, 25.64, 19.3, 19.1, 18.4, 15.0. NMR spectra can be found in Appendix C. **MS** (ESI): calculated for $C_{70}H_{92}N_4O_{16}S$ $[M+H]^+$ m/z = 1277.62, found: 1278.02.

*4,5-bis[3-((tert-butoxycarbonyl)amino)propoxy]-thioxanthen-9-ylidene-[(2'R)-5',6'-bis[(2R)-(1-ethoxy-1-oxopropan-2-yl)oxy]-2',7'-dimethylindane] **34***

Bis-ester, bis-Boc-amine (R)-motor

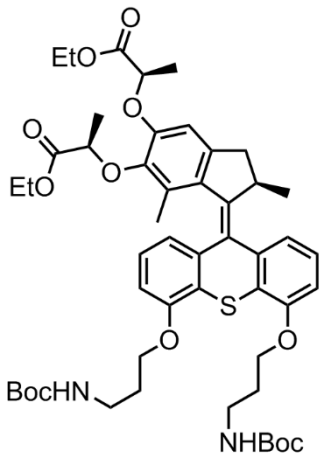

Compound *(R)*-**32** (30 mg, 0.05 mmol) was dissolved in dichloromethane (15 mL) and *tert*-butyl *N*-(3-bromopropyl)carbamate (50 mg, 0.21 mmol) was added alongside of potassium carbonate (30 mg, 0.22 mmol). The mixture was stirred overnight at 50°C. The solution was then diluted with dichloromethane (10 mL) and extensively washed with water (30 mL). The organic phase was dried over sodium sulfate and the solvent was evaporated under vacuum. The crude oil was further purified by column chromatography (silica gel, dichloromethane : methanol, 100 : 1) to afford of compound *(R)*-**34** (48 mg, 0.052 mmol, quant.) as a yellow oil. R_f = 0.5 (dichloromethane : methanol, 100 : 1). **^{1}H NMR**. (400 MHz, $CDCl_3$) δ 7.29 (d, *J* = 7.7 Hz, 1H), 7.19 (dd, *J* = 7.9, 7.9 Hz, 1H), 6.94 (dd, *J* = 7.9, 7.9 Hz, 1H), 6.72 (dd, *J* = 8.1, 1.1 Hz, 1H), 6.67 (dd, *J* = 8.2, 1.1 Hz, 1H), 6.64 (dd, *J* = 7.1, 1.1 Hz, 1H), 6.54 (s, 1H), 4.74 (q, *J* = 6.7 Hz, 1H), 4.48 (q, *J* = 6.8 Hz, 1H), 4.29 – 3.92 (m, 9H), 3.40 (t, *J* = 5.5 Hz, 4H), 3.30 (dd, *J* = 14.9, 6.2 Hz, 1H), 2.90 (s, 9H), 2.83 (s, 9H), 2.31 (d, *J* = 15.0 Hz, 1H), 2.02 (t, *J* = 6.0 Hz, 4H), 1.58 (d, *J* = 6.7 Hz, 3H), 1.47 (d, *J* = 6.8 Hz, 3H), 1.39 (s, 3H), 1.30 (t, *J* = 7.1 Hz, 3H), 1.22 (t, *J* = 7.1 Hz, 3H), 0.59 (d, *J* = 6.7 Hz, 3H).**^{13}C NMR**. (100 MHz, $CDCl_3$) δ 171.4, 171.1, 159.3, 159.1, 155.2, 154.9, 145.5, 144.5, 142.5, 138.2, 138.0, 132.6, 131.1, 130.0, 129.8, 128.9, 127.1, 126.8, 118.7, 118.6, 118.5, 111.1, 110.9, 108.1, 78.6, 78.3, 76.3, 76.0, 72.3, 61.8, 61.4, 43.5, 38.3, 38.1, 29.1, 29.0, 28.8, 28.4, 28.3, 22.0, 21.4, 21.2, 18.9, 18.5, 14.3, 14.1. **MS** (ESI): calculated for $C_{50}H_{66}N_2O_{12}S$ $[M+H]^+$ m/z = 919.43, found: 919.27.

4,5-bis[3-((tert-butoxycarbonyl)amino)propoxy]-thioxanthen-9-ylidene-[(2'R)-5',6'-bis[(2R)-(2-methylethanoic acid)oxy]-2',7'-dimethylindane] 35

Bis-acid, bis-Boc-amine (R)-motor

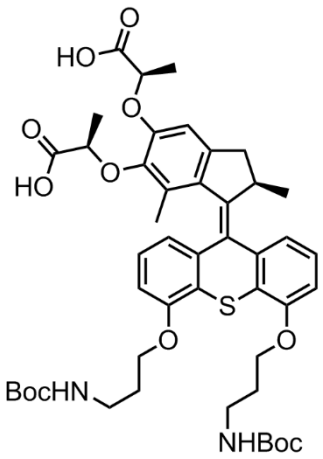

Compound *(R)*-**34** (47.8 mg, 0.052 mmol) was dissolved in a mixture of methanol : THF : water (1 : 1 : 1, 6 mL). Sodium hydroxide at 1 M in water (0.16 mL, 0.16 mmol) was added. The mixture was stirred overnight at room temperature. The solution was then neutralized with aqueous hydrochloric acid at 1 M (0.5 mL) and extracted with dichloromethane (10 mL). The organic layer was washed with brine (10 mL), dried over sodium sulfate and the solvent was evaporated under vacuum to afford of compound *(R)*-**35** (45.3 mg, 0.052 mmol, quant.) as a yellow oil. **^{1}H NMR**. (400 MHz, $CDCl_3$) δ 7.31 (d, *J* = 7.7 Hz, 1H), 7.20 (dd, *J* = 7.7, 7.7 Hz, 1H), 6.94 (dd, *J* = 7.1, 7.1 Hz, 1H), 6.74 (d, *J* = 8.1 Hz, 1H), 6.69 (d, *J* = 7.7 Hz, 1H), 6.66 (s, 1H), 6.64 (d, *J* = 6.5 Hz, 1H), 4.85 – 4.74 (m, 1H), 4.68 – 4.58 (m, 1H), 4.27 – 3.89 (m, 8H), 3.46 – 3.37 (m, 4H), 3.36 – 3.23 (m, 1H), 2.95 (s, 1H), 2.88 (s, 9H), 2.38 – 2.30 (m, 9H), 2.10 – 1.99 (m, 4H), 1.66 (d, *J* = 6.6 Hz, 3H), 1.43 (s, 3H), 0.63 (d, *J* = 6.5 Hz, 3H).**^{13}C NMR**. (100 MHz, $CDCl_3$) δ 171.5, 171.4, 158.2, 157.7, 155.9, 155.8, 145.8, 144.5, 143.8, 138.1, 138.0, 137.8, 137.7, 132.6, 129.4, 127.9, 127.6, 124.8, 122.0, 118.6, 118.4, 111.3, 111.1, 108.7, 79.9, 75.5, 75.2, 72.5, 72.4, 43.1, 38.0, 37.7, 29.5, 29.1, 29.0, 28.8, 28.6, 21.5, 21.3, 18.0, 17.5, 14.1. **MS** (ESI): calculated for $C_{46}H_{58}N_2O_{12}S$ $[M+H]^+$ m/z = 863.32, found: 863.34.

4,5-bis[3-((tert-butoxycarbonyl)amino)propoxy]-thioxanthen-9-ylidene-[(2'R)-5',6'-bis[((2R)-1-((2-((tert-butoxycarbonyl)amino)ethyl)amino)-1-oxopropan-2-yl)oxy)]-2',7'-dimethylindane] 36

Tetra-Boc-amine (R)-motor

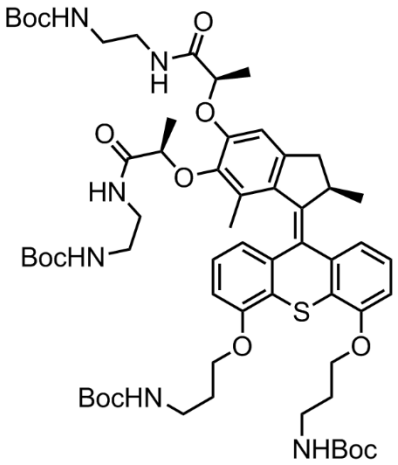

Compound *(R)*-**35** (45.3 mg, 0.040 mmol) was dissolved in dichloromethane (5 mL). 1-ethyl-3-(3-dimethylaminopropyl)carbodiimide hydrochloride (60.4 mg, 0.16 mmol) and hydroxybenzotriazole (24.11 mg, 0.16 mmol) were added to the mixture. The solution was stirred for 40 min and *N*-Boc-ethylenediamine were added (25.2 mg, 0.16 mmol). The solution was stirred overnight at room temperature. The mixture was then extracted with brine (10 mL) and water (10 mL). The combined organic layer was dried over sodium sulfate and the solvent was evaporated under vacuum. The crude oil was further purified by column chromatography (silica gel, dichloromethane : methanol, 100 : 1 ⟶ 10 : 1) to afford compound *(R)*-**36** (38.3 mg, 0.033 mmol, 64 %) as a brown oil. R_f = 0.3 (dichloromethane : methanol, 10 : 1). **^{1}H NMR**. (400 MHz, $CDCl_3$) δ 7.31 (d, *J* = 7.7 Hz, 1H), 7.22 (dd, *J* = 7.9, 7.9 Hz, 1H), 6.97 (dd, *J* = 7.9, 7.9 Hz, 1H), 6.75 (d, *J* = 7.9 Hz, 1H), 6.71 (d, *J* = 8.2 Hz, 1H), 6.65 (s, 1H), 6.64 (d, *J* = 3.9 Hz, 1H), 4.62 (q, *J* = 6.2 Hz, 1H), 4.43 (q, *J* = 6.2 Hz, 1H), 4.26 – 3.95 (m, 5H), 3.51 – 3.15 (m, 13H), 2.35 (d, *J* = 15.1 Hz, 1H), 2.10 – 2.02 (m, 4H), 1.55 (d, *J* = 6.8 Hz, 3H), 1.46 – 1.35 (m, 36H), 1.33 (d, *J* = 6.8 Hz, 3H), 1.17 (s, 3H), 0.63 (d, *J* = 6.7 Hz, 3H). **MS** (ESI): calculated for $C_{60}H_{86}N_6O_{14}S$ $[M+H]^+$ m/z = 1146.59, found: 1146.94.

4,5-bis[3-aminopropoxy]-thioxanthen-9-ylidene-[(2'R)-5',6'-bis[((2R)-1-((2-(aminoethyl)amino)-1-oxopropan-2-yl)oxy)]-2',7'-dimethylindane] 37

Tetra-amine (R)-motor

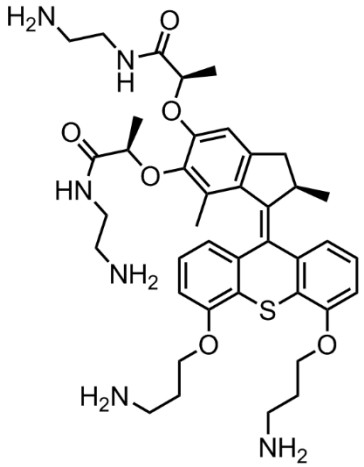

Compound *(R)*-**36** (38.3 mg, 0.033 mmol) was dissolved in dichloromethane (5 mL) and trifluoroacetic acid (0.5 mL, 6.7 mmol) was added. The mixture was stirred for 30 min at room temperature. The mixture was extracted with sodium hydroxide at 1 M in water (20 mL). The organic layer was dried over sodium sulfate and the solvent was evaporated under vacuum to afford compound *(R)*-**37f** (24.9 mg, 0.033 mmol, quant.). **^{1}H NMR**. (400 MHz, $CDCl_3$) δ 7.49 (t, *J* = 5.9 Hz, 1H), 7.32 (d, *J* = 7.9 Hz, 1H), 7.23 (dd, *J* = 7.9, 7.9 Hz, 1H), 7.02 (t, *J* = 5.9 Hz, 1H), 6.95 (dd, *J* = 7.9, 7.9 Hz, 1H), 6.76 (d, *J* = 7.9 Hz, 1H), 6.70 (br t, *J* = 4.2 Hz, 2H), 6.61 (dd, *J* = 7.9, 1.1 Hz, 1H), 4.69 (q, *J* = 6.8 Hz, 1H), 4.53 (q, *J* = 6.8 Hz, 1H), 4.29 – 4.00 (m, 4H), 3.61 – 3.46 (m, 1H), 3.47 – 3.28 (m, 4H), 3.25 – 3.15 (m, 1H), 3.02 (br q, *J* = 6.2 Hz, 4H), 2.86 (t, *J* = 6.2 Hz, 2H), 2.83 – 2.69 (m, 2H), 2.37 (d, *J* = 15.1 Hz, 1H), 2.12 – 1.92 (m, 4H), 1.58 (d, *J* = 6.8 Hz, 3H), 1.33 (d, *J* = 6.8 Hz, 3H), 1.16 (s, 3H), 0.64 (d, *J* = 6.8 Hz, 3H). NMR spectrum can be found in Appendix C. **MS** (ESI): calculated for $C_{40}H_{54}N_6O_6S$ $[M+H]^+$ m/z = 747.38, found: 747.46.

α,ω-ditosylate-poly(ethylene glycol) 38$_M$

M denotes the average number molecular weight of the polymer

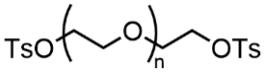

In a typical experiment, α,ω-dihydroxy-poly(ethylene glycol) (1 g of) of average number molecular weight M was dissolved in a mixture of dichloromethane : pyridine (2 : 8, v : v, 1 mL) and the solution is cooled to 0°C. In a separate flask, tosyl chloride (10 eq) were dissolved in pyridine (10 mL). This solution was then slowly added over the course of 24 h in the polymer solution at 0°C. At the end of the reaction, the mixture was poured in iced hydrochloric acid at 6 M (100 mL) and thoroughly extracted with dichloromethane (100 mL). The organic layer was further washed with cold aqueous hydrochloric acid at 2 M (50 mL) and dried over sodium sulfate. After the evaporation of the solvent, α,ω-ditosylate-poly(ethylene glycol) was obtained as a white solid. **^{1}H NMR** (400 MHz, toluene-d_8) δ 7.71 (d, J = 8.1 Hz, 4H), 6.77 (d, J = 8.1 Hz, 4H), 3.92 (t, J = 4.9 Hz, 4H), 3.69 – 3.22 (m, n × 4H), 1.93 (s, 6H).

38$_{1500}$ (n = 34): yield: 77 %; degree of functionalization: 96 %

38$_{3000}$ (n = 68): yield: 58 %; degree of functionalization: 96 %

38$_{4000}$ (n = 91): yield: 37 %; degree of functionalization: 27 %

α,ω-diazido-poly(ethylene glycol) 39a$_M$

M denotes the average number molecular weight of the polymer; obtained from 38$_M$

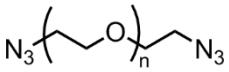

In a typical experiment, compound **38$_M$** (500 mg) was dissolved in DMF (2 mL). Sodium azide (10 eq) was then added and the mixture was stirred for two days at room temperature. The solvent was partially evaporated under reduced pressure and the solution was diluted with dichloromethane (3 mL). The mixture was dropped in cold diethyl ether (50 mL) and the solid was collected by filtration to afford α,ω-diazido-poly(ethylene glycol) as a white solid. **^{1}H NMR** (400 MHz, toluene-d_8) δ 3.69 – 3.28 (m, n × 4H), 3.24 (t, J = 5.0 Hz, 4H).

39a$_{1500}$ (n = 34): yield: 44 %; degree of functionalization: 96 %.

39b$_{3000}$ (n = 68): yield: 56 %; degree of functionalization: 96 %

α,ω-diazido-poly(ethylene glycol) 39b$_M$

M denotes the average number molecular weight of the polymer; obtained from 40$_M$

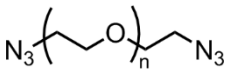

In a typical experiment, compound **40$_M$** (500 mg) was dissolved in DMF (10 mL). Sodium azide (10 eq) was then added and the mixture was stirred for two days at room temperature. The solvent was partially evaporated under reduced pressure and the solution was diluted with dichloromethane (10 mL). The mixture was dropped in cold diethyl ether (150 mL) and the solid was collected by filtration to afford α,ω-diazido-poly(ethylene glycol) as a white solid. **^{1}H NMR** (400 MHz, toluene-d_8) δ 3.69 – 3.28 (m, n × 4H), 3.24 (t, J = 5.0 Hz, 4H). **MALDI** and **GPC** results can be found in Appendix B.

39b$_{1500}$ (n = 34): yield: 14 %; degree of functionalization: quant.;

MALDI: M_p = 1580.89 (m/z), Δ(m/z) = 44; **GPC**: $\overline{M_n}$ = 5600 g·mol^{-1}, D = 1.04.

39b$_{3000}$ (n = 68): yield: 27 %; degree of functionalization: quant.

MALDI: M_p = 3174.33 (m/z), Δ(m/z) = 44; **GPC**: $\overline{M_n}$ = 3040 g·mol^{-1}, D = 1.02.

39b$_{4000}$ (n = 91): yield: 12 %; degree of functionalization: quant.

GPC: $\overline{M_n}$ = 3870 g·mol^{-1}, D = 1.06.

39b$_{10000}$ (n = 227): yield: 90 %; degree of functionalization: quant.

39b$_{20000}$ (n = 455): yield: 84 %; degree of functionalization: quant.

α,ω-dimesylate-poly(ethylene glycol) 40$_M$

M denotes the average number molecular weight of the polymer

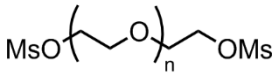

In a typical experiment, α,ω-dihydroxy-poly(ethylene glycol) (1 g) with an average number molecular weight M was placed in a flask and triethylamine (10 eq) was added. The flask was cooled to 0°C and a solution of mesyl chloride (10 eq) dissolved in dichloromethane (8 mL) was added dropwise over the course of one hour. After complete addition, the solution was allowed to warm to room temperature and stirring was pursued overnight. The mixture was then concentrated under vacuum and the solid was reprecipitated twice in cold isopropanol (100 mL) from dichloromethane (10 mL) to afford α,ω-dimesylate-poly(ethylene glycol) as a white powder. **^{1}H NMR** (400 MHz, toluene-d_8) δ 3.97 (t, J = 4.6 Hz, 4H), 3.71 – 3.21 (m, n × 4H), 2.59 (s, 6H).

40$_{1500}$ (n = 34): yield: quant.; degree of functionalization: quant.

40$_{3000}$ (n = 68): yield: 58 %; degree of functionalization: quant.

40$_{4000}$ (n = 91): yield: 87 %; degree of functionalization: quant.

40$_{6000}$ (n = 136): yield: 95 %; degree of functionalization: quant.

40$_{10000}$ (n = 227): yield: 89 %; degree of functionalization: quant.

40$_{20000}$ (n = 455): yield: 59 %; degree of functionalization: quant.

Diphenylmethyl potassium 41

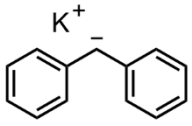

Metallic potassium (3.9 g, 99.7 mmol) and naphthalene (6.4 g, 49.9 mmol) were placed in a three-neck round-bottomed flask adapted with an argon entry, a 200-mL burette of dry THF under argon and a glass stopper. Three evacuate-refill cycles with argon were applied to the flask to ensure dry conditions. Then, THF (150 mL) was added to the flask and the burette was quickly replaced by a tubing with fritted glass under argon, which will be used to transfer the solution when needed. The mixture was stirred for 1 h; the solution turned green due to the conversion of naphthalene to its

radical anion. Diphenylmethane (17 mL, 102 mmol) was added next through an argon-purged syringe. The mixture was stirred for three days and turned dark red due to the formation of diphenylmethyl potassium. The solution was titrated with acetanilide and a concentration of 0.58 mol·L^{-1} (87 %) was obtained.

*α,ω-dipropargyl-poly(ethylene glycol) **42a**$_M$*

M denotes the average number molecular weight of the polymer; obtained with 41

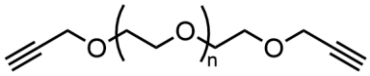

In a typical experiment, α,ω-dihydroxy-poly(ethylene glycol) (2 g) of average number molecular weight M were added in a flask adapted with an argon entry, a burette of dry THF and the tubing connected to the solution of compound **41** through fritted glass. The flask was purged with three evacuate-refill cycles with argon. Dry THF (50 mL) was then added and the solution was heated at 40°C until complete dissolution of the polymer. Then, the solution of compound **41** was added dropwise to the polymer solution until a slight red coloration persists. Finally, propargyl bromide was added dropwise to the mixture in an equimolar amount of the one of compound **41**. The mixture was stirred overnight at room temperature. At the end of the reaction, the solvent was removed under reduced pressure and the solid was dissolved in dichloromethane (10 mL). The polymer was then reprecipitated twice in cold diethyl ether (100 mL) from dichloromethane (10 mL) to obtain α,ω-dipropargyl-poly(ethylene glycol) as a white powder. **^{1}H NMR** (400 MHz, toluene-d_8) δ 3.93 (d, *J* = 2.7 Hz, 4H) 3.69 – 3.27 (m, (n + 1) × 4H). **MALDI** and **GPC** results can be found in Appendix B.

42a$_{1500}$ (n = 34): yield: 86 %; degree of functionalization: quant.

GPC: $\overline{M_n}$ = 2300 g·mol^{-1}, D = 1.03.

42b$_{3000}$ (n = 68): yield: 92 %; degree of functionalization: quant.

MALDI: M_p = 3302.68 (m/z), Δ(m/z) = 44; **GPC**: $\overline{M_n}$ = 2400 g·mol^{-1}, D = 1.02.

*α,ω-dipropargyl-poly(ethylene glycol) **42b**$_M$*

M denotes the average number molecular weight of the polymer; obtained with NaH

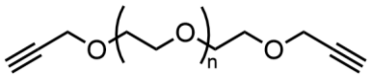

In a typical experiment, α,ω-dihydroxy-poly(ethylene glycol) (1 g) of average number molecular weight M were dissolved in dry THF (10 mL) at 40°C until complete dissolution. The solution was then allowed to reach room temperature and sodium hydride was added by portion until the formation of bubbles was not observed anymore. After 1 h of stirring, propargyl bromide was added dropwise to the mixture, in an equimolar amount to the one of sodium hydride added. The solution was then stirred overnight at room temperature. At the end of the reaction, the mixture was diluted with brine (10 mL) and thoroughly extracted with dichloromethane (50 mL). The combined organic layer was dried over sodium sulfate and the solution was concentrated under vacuum. The solid was reprecipitated twice in cold diethyl ether (100 mL) from dichloromethane (10 mL) to afford α,ω-dipropargyl-poly(ethylene glycol) as a white powder. **^{1}H NMR** (400 MHz, toluene-d_8) δ 3.93 (d, *J* = 2.7 Hz, 4H) 3.69 – 3.27 (m, n × 4H). **MALDI** and **GPC** results can be found in Appendix B.

42b$_{6000}$ (n = 136): yield: 90 %; degree of functionalization: quant.

MALDI: M_p = 6396.41 (m/z), Δ(m/z) = 44; **GPC**: $\overline{M_n}$ = 6700 g·mol^{-1}, D = 1.15.

42b$_{10000}$ (n = 227): yield: 85 %; degree of functionalization: quant.

MALDI: M_p = 11704.37 (m/z), Δ(m/z) = 44; **GPC**: $\overline{M_n}$ = 8700 g·mol^{-1}, D = 1.07.

42b$_{20000}$ (n = 455): yield: 78 %; degree of functionalization: quant.

MALDI: M_p = 22832.88 (m/z); **GPC**: $\overline{M_n}$ = 19900 g·mol^{-1}, D = 1.007.

Gel of PEG crosslinked with molecular motors Gel_M

M denotes the average number molecular weight of the polymeric precursor

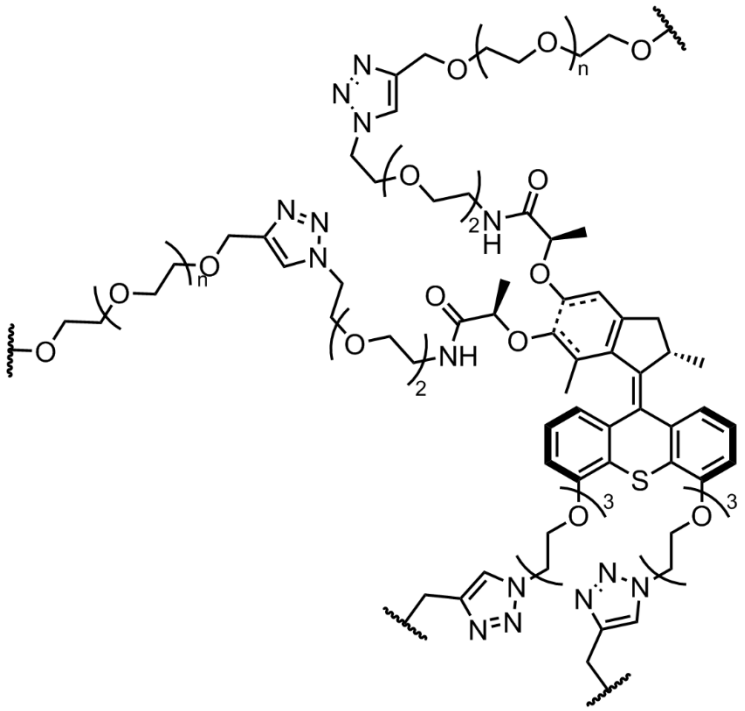

The reticulation solvent was degassed by bubbling argon for 30 min prior to the preparation of the solutions. In one vial, compound **42$_M$** was dissolved in half the amount of solvent needed to fill the mold (see Figure 4.3) at a concentration 2c*. In another vial, compound *(S)*-**25** was dissolved in the remaining amount of solvent at a concentration corresponding to half the molar concentration of polymer, and copper bromide and pentamethyldiethylenetriamine were added (5 eq. to the motor). After separate mixing to ensure complete dissolution, the two solutions were thoroughly mixed together and transferred to the metal mold. The mold was placed in a sealed container with a small amount of reticulation solvent to limit evaporation. The system was placed on a shaking plate for 16 h at room temperature. At the end of the reticulation, the mold was opened, and the gel was transferred in a solution of ethylenediaminetetraacetic acid (50 g·L^{-1}, pH 9) to remove most of the copper ions. The gel was further washed by placing it in a water bath, which was regularly changed until complete discoloration of the material. Finally, the gel was cut in nine identical pieces for further investigations.

Poly(3-hexylthiophene) 43

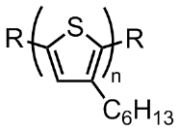

In an oven-dried flask, 2,5-dibromo-3-hexylthiophene (4 g, 12.3 mmol) was dissolved in dry THF (80 mL). Methylmagnesium bromide at 3 M in diethyl ether (4.09 mL, 12.3 mmol) was then slowly added, and the mixture was refluxed for 50 min under stirring. The solution was allowed to reach room temperature before adding dichloro(1,3-bis(diphenylphosphino)propane)nickel(II) (66 mg, 0.12 mmol). The polymerization was conducted for 2 h at 70°C. The crude polymer was recovered after precipitation in cold methanol (200 mL) and further purified by Sohxlet extraction (methanol then cyclohexane to remove impurities and oligomers, chloroform to recover the polymer). Final precipitation in cold methanol and filtration of the solid afforded poly(3-hexylthiophene) (480 mg, 24 %m) as a purple solid. **^{1}H NMR** (400 MHz, $CDCl_3$) δ 7.07 – 6.92 (m, n × 1H), 2.90 – 2.70 (m, n × 2H), 1.76 – 1.64 (m, n × 2H), 1.49 – 1.22 (m, n × 6H), 0.97 – 0.79 (m, n × 3H). **MALDI** and **GPC** results can be found in Appendix B. **MALDI**: M_p = 3556.03 (m/z), Δ(m/z) = 164; **GPC**: $\overline{M_n}$ = 24000 g·mol^{-1}, D = 1.28.

α,ω-diformyl-poly(3-hexylthiophene) 44

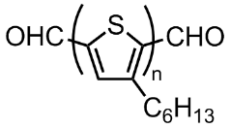

The following procedure was used for the preparation of compound **44**. Compound **43** (800 mg) was dissolved in dry THF (250 mL). The mixture was cooled to 0°C and a solution of *n*-BuLi at 5 M in cyclohexane (5 mL, 200 eq) was added. The mixture was stirred for 30 min at 0°C. The reaction was quenched by adding water. After evaporation of the solvent, the solid was dissolved in chloroform and the solution was thoroughly washed with water (100 mL). The organic layer was dried over sodium sulfate and evaporated to dryness. The residue was dissolved in dry toluene (150 mL), and dimethylformamide (1.5 mL, 480 eq) and phosphorus oxychloride (1.5 mL, 400 eq) were added. The mixture was stirred overnight at 75°C. The reaction was quenched with a saturated aqueous solution of sodium acetate (50 mL) and the crude polymer was recovered after precipitation in cold methanol (500 mL). The solid was further purified by Sohxlet extraction in methanol overnight and collected with chloroform. Evaporation of the solvent afforded a purple solid (630 mg) showing the characteristic peaks of P3HT by ^{1}H NMR analysis (see compound **43**). However, there was no signals that could be attributed to terminal aldehyde groups.

α,ω-dibromo-poly(styrene sulfonate), sodium salt 45

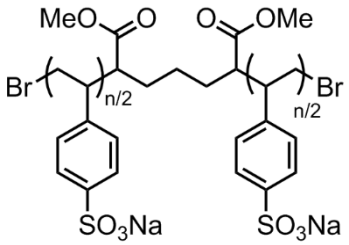

In one flask, sodium 4-styrenesulfonate (1 g, 4.85 mmol) and dimethyl 2,6-dibromoheptanedioate (5.3 µL, 0.024 mmol) were dissolved in a mixture of deoxygenated methanol (2 mL) and deoxygenated water (7 mL). The solution was further degassed by bubbling argon for 1 h. In another flask, copper chloride (3.8 mg, 0.039 mmol) and 2,2'-bipyridyl (3 mg, 0.019 mmol) were dissolved in deoxygenated water (3 mL) and the solution was also further degassed by bubbling argon for 1 h. The monomer solution was transferred to the catalyst solution with an argon-purged syringe. The polymerization proceeded at room temperature for 20 h. The solution was dialyzed against water (MWCO: 3 500 Da) and recovered after evaporation of the solvent. **^{1}H NMR** (400 MHz, D_2O) δ 7.90 – 6.18 (m, n × 2H), 6.89 – 6.12 (m, n × 2H), 1.88 – 0.91 (m, n × 3H).

*α,ω-dibromo-poly(*N*-isopropylacrylamide) 46$_M$*

M denotes the average number molecular weight of the polymer

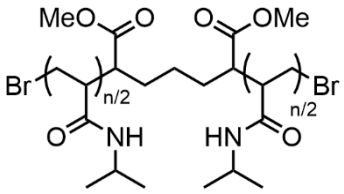

In a typical experiment, *N*-isopropylacrylamide (1 g, 8.84 mmol, n eq.) and dimethyl 2,6-dibromoheptanedioate (1 eq) were dissolved in a mixture of deoxygenated water (3 mL) and deoxygenated methanol (1 mL). The mixture was further degassed by bubbling argon for 1 h. In a separate flask, copper bromide (1.6 eq.) and tris[2-(dimethylamino)ethyl]amine (0.8 eq) were dissolved in a mixture of deoxygenated water (1 mL) and deoxygenated methanol (1 mL), and this solution was further degassed by bubbling argon as well. The monomer solution was then added to the catalyst solution with an argon-purged syringe. In the case of low molecular weights (high content in initiator), the solutions were cooled to 0°C prior to mixing the two solutions. Polymerization was conducted at room temperature and was complete within one hour. The polymers were purified by dialysis (MWCO: 3 500 Da) and evaporation of the solvent gave α,ω-dibromo-poly(*N*-isopropylacrylamide) as a white solid. **^{1}H NMR** (400 MHz, $CDCl_3$) δ 7.88 – 6.09 (br m, n × 1H), 4.21 – 3.82 (m, n × 1H), 2.59 – 1.87 (m, n × 1H), 1.94 – 1.34 (m, n × 2H), 1.34 – 0.59 (m, n × 6H). **GPC** results can be found in Appendix B.

46$_{5500}$: 82 % yield.

MALDI: M_p = 5729.97 (m/z), Δ(m/z) = 113; **GPC**: $\overline{M_n}$ = 30600 g·mol^{-1}, D = 1.26.

46$_{17000}$: 85 % yield.

GPC: $\overline{M_n}$ = 29900 g·mol^{-1}, D = 1.15.

46$_{36000}$: 74 % yield.

GPC: $\overline{M_n}$ = 54600 g·mol^{-1}, D = 1.14.

α,ω-dimesylate-poly(dimethylsiloxane) 47

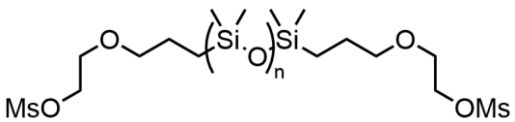

α,ω-dihydroxy-poly(dimethylsiloxane) (2 g, 0.25 mmol) was dissolved in dichloromethane (20 mL). Triethylamine (0.28 mL, 2 mmol) and mesyl chloride (0.15 mL, 2 mmol) were then added. The reaction was stirred overnight at room temperature. The mixture was washed with water (10 mL) and brine (20 mL). The combined organic layer was dried over sodium sulfate and the solvent was evaporated under vacuum to afford α,ω-dimesyl-poly(dimethylsiloxane) (1.6 g, 0.2 mmol, 80 %) as a colorless oil. **^{1}H NMR** (400 MHz, $CDCl_3$) δ 4.41 – 3.35 (m, 4H), 3.75 – 3.66 (m, 4H), 3.44 (t, *J* = 6.9 Hz, 4H), 3.60 (s, 6H), 1.67 – 1.56 (m, 4H), 0.53 (m, 4H), 0.23 – -0.09 (m, (n + 1) × 6H).

*α,ω-diazido-poly(dimethylsiloxane) **48***

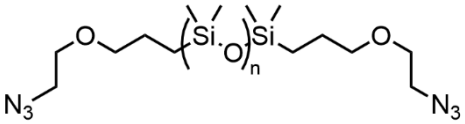

Compound **47** (5 g, 0.63 mmol) was dissolved in ethyl acetate (75 mL) and sodium azide (330 mg, 5 mmol) was added. The mixture was stirred under reflux overnight. The solution was then washed with sodium bicarbonate (50 mL), water (30 mL) and brine (50 mL). The organic phase was dried over sodium sulfate and evaporated under vacuum to afford α,ω-diazido-poly(dimethylsiloxane) (4.3 g, 0.54 mmol, 86 %) as a colorless oil. **^{1}H NMR** (400 MHz, $CDCl_3$) δ 3.61 (t, *J* = 5.1 Hz, 4H), 3.44 (t, *J* = 6.9 Hz, 4H), 3.37 (t, *J* = 5.1 Hz, 4H), 1.68 – 1.58 (m, 4H), 0.55 (m, 4H), 0.24 – -0.11 (m, (n + 1) × 6H). **GPC** results can be found in Appendix B, $\overline{M_n}$ = 7700 g·mol^{-1}, D = 2.48.

*Gel of PDMS crosslinked with molecular motors **Gel$_{PDMS}$***

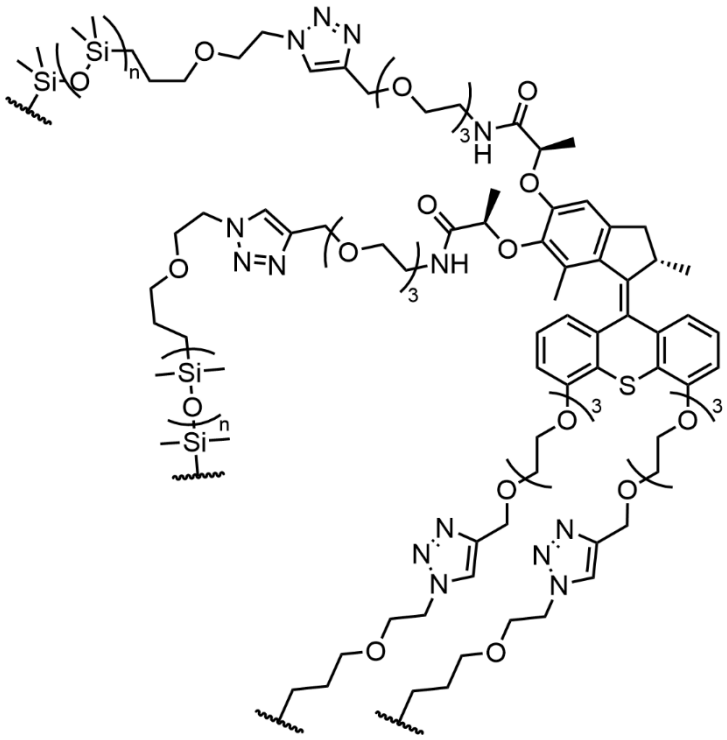

Gel formed in the mold of 4-mm thickness: compound **48** (220 mg, 0.028 mmol) was dissolved in dichloromethane (1 mL) and copper bromide (18 mg, 0.14 mmol) and pentamethyldiethylenetriamine (30 µL, 0.14 mmol) were added. Separately, compound *(S)*-**28** (16.8 mg, 0.014 mmol) was dissolved in dichloromethane (1 mL). The two solutions were then

thoroughly mixed and transferred to the mold. The mold was placed in a sealed container with a small amount of solvent to avoid evaporation. The system was placed on a shaking plate at room temperature overnight. At the end of the reticulation, **Gel$_{PDMS}$** was removed from the mold and placed in a fresh bath of dichloromethane, which was replaced regularly until complete discoloration of the material.

Gel formed in the mold of 0.5-mm thickness: all quantities were divided by 8.

Dry film of PDMS crosslinked with molecular motors ***Film$_{PDMS}$***

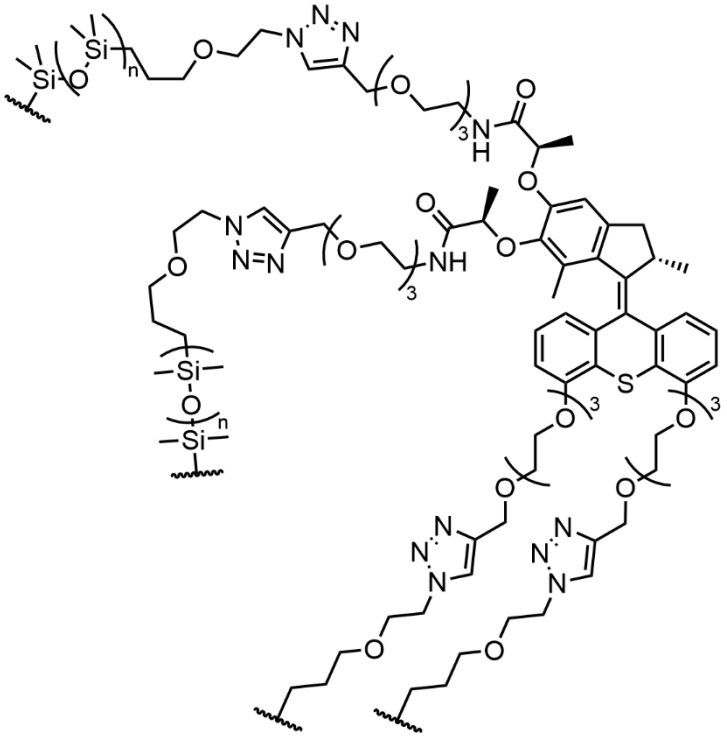

Gel$_{PDMS}$ with a thickness of 4 mm was left to dry at atmospheric pressure overnight until most of the solvent was removed. The film was then further dried under vacuum for 3 h to afford **Film$_{PDMS}$**.

Methyl 4-(hex-5-en-1-yloxy)benzoate ***49***

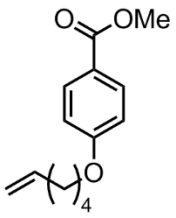

5-hexen-1-ol (3 mL, 26.3 mmol), methyl 4-hydroxybenzoate (4 g, 26.3 mmol) and triphenylphosphine (7.6 g, 28.9 mmol) were dissolved in THF (40 mL). The solution was cooled to 0°C and diisopropyl azodicarboxylate (5.8 g, 28.9 mmol) was slowly added. The mixture was allowed to reach room temperature and was stirred for three days. The solvent was evaporated under vacuum and the crude solid was purified by column chromatography (silica gel, cyclohexane : dichloromethane, 3 : 1) to afford methyl 4-(hex-5-en-1-yloxy)benzoate (5.4 g, 22.9 mmol, 87%) as a white solid. $\mathbf{R_f}$ = 0.65 (cyclohexane : dichloromethane$_2$, 5 : 1). **^{1}H NMR** (400 MHz, $CDCl_3$) δ 7.99 (d, *J* = 9.0 Hz, 2H), 6.92 (d, *J* = 9.0 Hz, 2H), 5.80 – 5.56 (m, 1H), 5.10 – 4.98

(m, 2H), 4.02 (t, *J* = 6.5 Hz, 2H), 3.89 (s, 3H), 2.17 – 1.98 (m, 2H), 1.86 – 1.72 (m, 2H), 1.60 – 1.52 (m, 2H). **MS** (ESI): calculated for $C_{14}H_{18}O_3$ $[M+H]^+$ m/z = 235.13, found: 235.46.

*4-(hex-5-en-1-yloxy)benzoic acid **50***

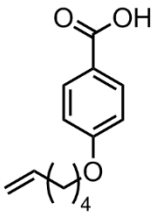

Compound **50** (5.4 g, 22.9 mmol) was dissolved in methanol (60 mL) and sodium hydroxide (2.8 g, 69 mmol) was added. The solution was stirred under reflux overnight and cooled down to room temperature. The solution was dropped in cold acidified methanol (100 mL) and the product was collected by filtration to afford 4-(hex-5-en-1-yloxy)benzoic acid (4.5 g, 20.6 mmol, 90 %) as a white solid. **^{1}H NMR** (400 MHz, $CDCl_3$) δ 8.07 (d, *J* = 9.0 Hz, 2H), 6.95 (d, *J* = 9.0 Hz, 2H), 5.80 – 5.77 (m, 1H), 5.27 – 5.15 (m, 2H), 4.05 (t, *J* = 6.5 Hz, 2H), 2.20 – 2.13 (m, 2H), 1.87 - 1.79 (m, 2H), 1.63 – 1.54 (m, 2H). **MS** (ESI): calculated for $C_{13}H_{16}O_3$ $[M+H]^+$ m/z = 221.27, found: 221.03.

*2-methyl-1,4-phenylene bis(4-(hex-5-en-1-yloxy)benzoate) **51***

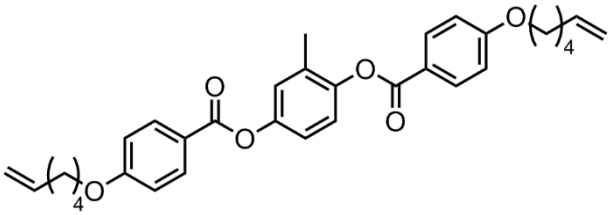

Compound **51** (4.5 g, 20.6 mmol) and methylhydroquinone (1.3 g, 10.3 mmol) were dissolved in dichloromethane (80 mL). Dimethylaminopyridine (252 mg, 2.1 mmol) and dicyclohexylcarbodiimide (4.7 g, 23 mmol) were then added. The mixture was stirred for three days at room temperature. After evaporation of the solvent under reduced pressure, the residue was further purified by column chromatography (silica gel, cyclohexane : dichloromethane, 1 : 1) to afford 2-methyl-1,4-phenylene bis(4-(hex-5-en-1-yloxy)benzoate) (7.6 g, 14.4 mmol, 70 %) as white crystals. $\mathbf{R_f}$ = 0.5 (cyclohexane : dichloromethane, 1 : 1). **^{1}H NMR** (400 MHz, $CDCl_3$) δ 8.16 (d, *J* = 9.0 Hz, 2H), 8.14 (d, *J* = 9.0 Hz, 2H), 7.20 – 7.05 (m, 3H), 6.98 (d, *J* = 9.0 Hz, 2H), 6.97 (d, *J* = 9.0 Hz, 2H), 5.90 – 5.78 (m, 2H), 5.09 – 4.97 (m, 4H), 4.064 (t, *J* = 6.5 Hz, 2H), 4.059 (t, *J* = 6.5 Hz, 2H) 2.19 – 2.11 (m, 4H), 2.15 (s, 3H), 1.90 – 1.79 (m, 4H), 1.65 - 1.55 (m, 4H). **MS** (ESI): calculated for $C_{33}H_{36}O_6$ $[M+H]^+$ m/z = 529.25, found: 529.11.

References

1. Q. Li, G. Fuks, E. Moulin, M. Maaloum, M. Rawiso, I. Kulic, J. T. Foy, N. Giuseppone, *Nat. Nanotechnol.* **2015**, *10*, 161–165.

Appendix B

Characterization of polymers

Poly(ethylene glycol)

α,ω-dihydroxy-(polyethylene glycol)

Gel Permeation Chromatography

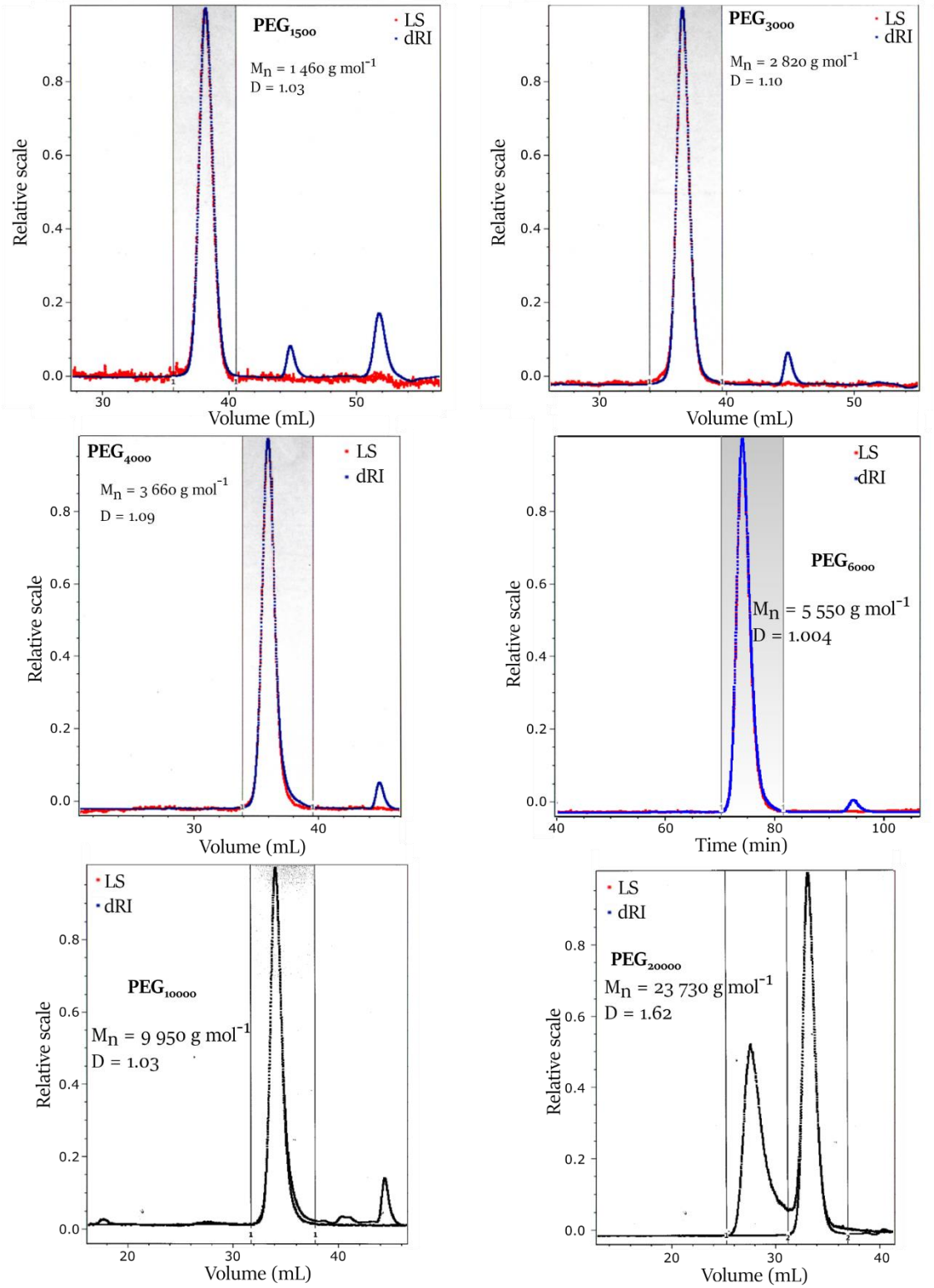

Figure B.1. GPC chromatograms of α,ω-dihydroxy-PEG of different molecular weights.

MALDI-TOF

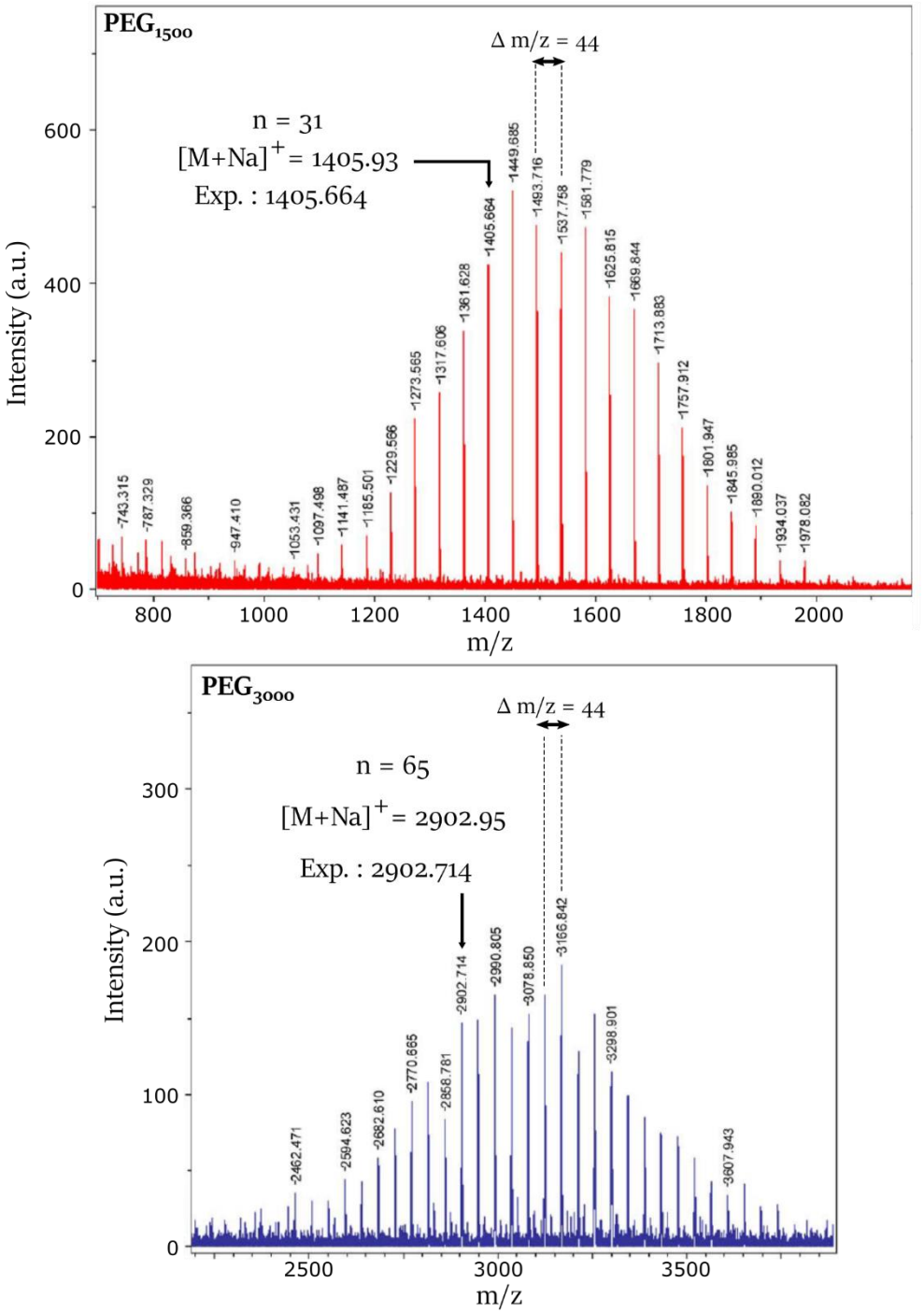

Figure B.2. MALDI-TOF spectra of α,ω-dihydroxy-PEG of different molecular weights.

*α,ω-diazido-(polyethylene glycol) **39**M*

Gel Permeation Chromatography

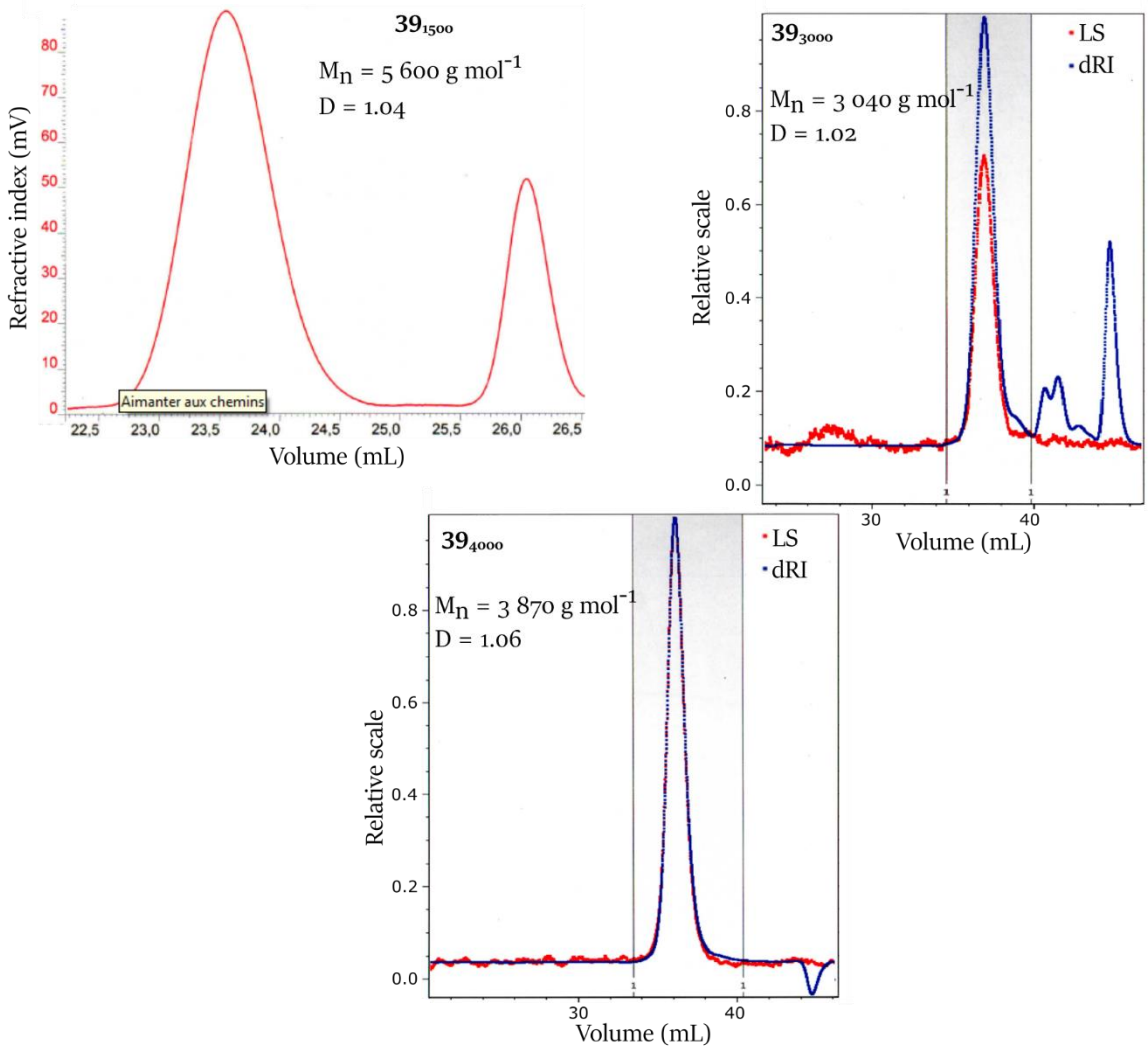

Figure B.3. GPC chromatograms of α,ω-diazido-PEG **39** of different molecular weights.

MALDI-TOF

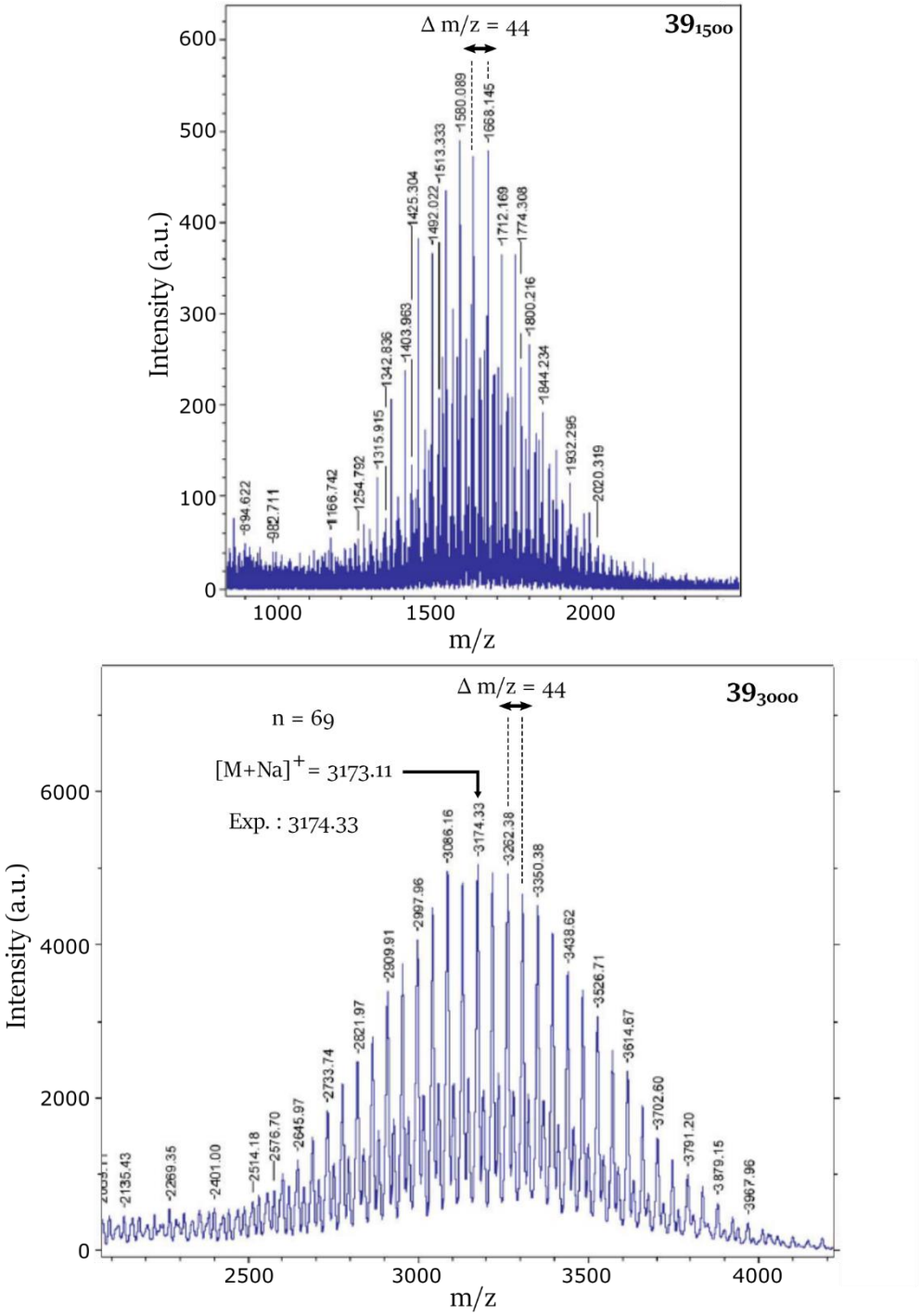

Figure B.4. MALDI-TOF spectra of α,ω-diazido-PEG **39** of different molecular weights.

α,ω-dipropargyl-(polyethylene glycol) 42M

Gel Permeation Chromatography

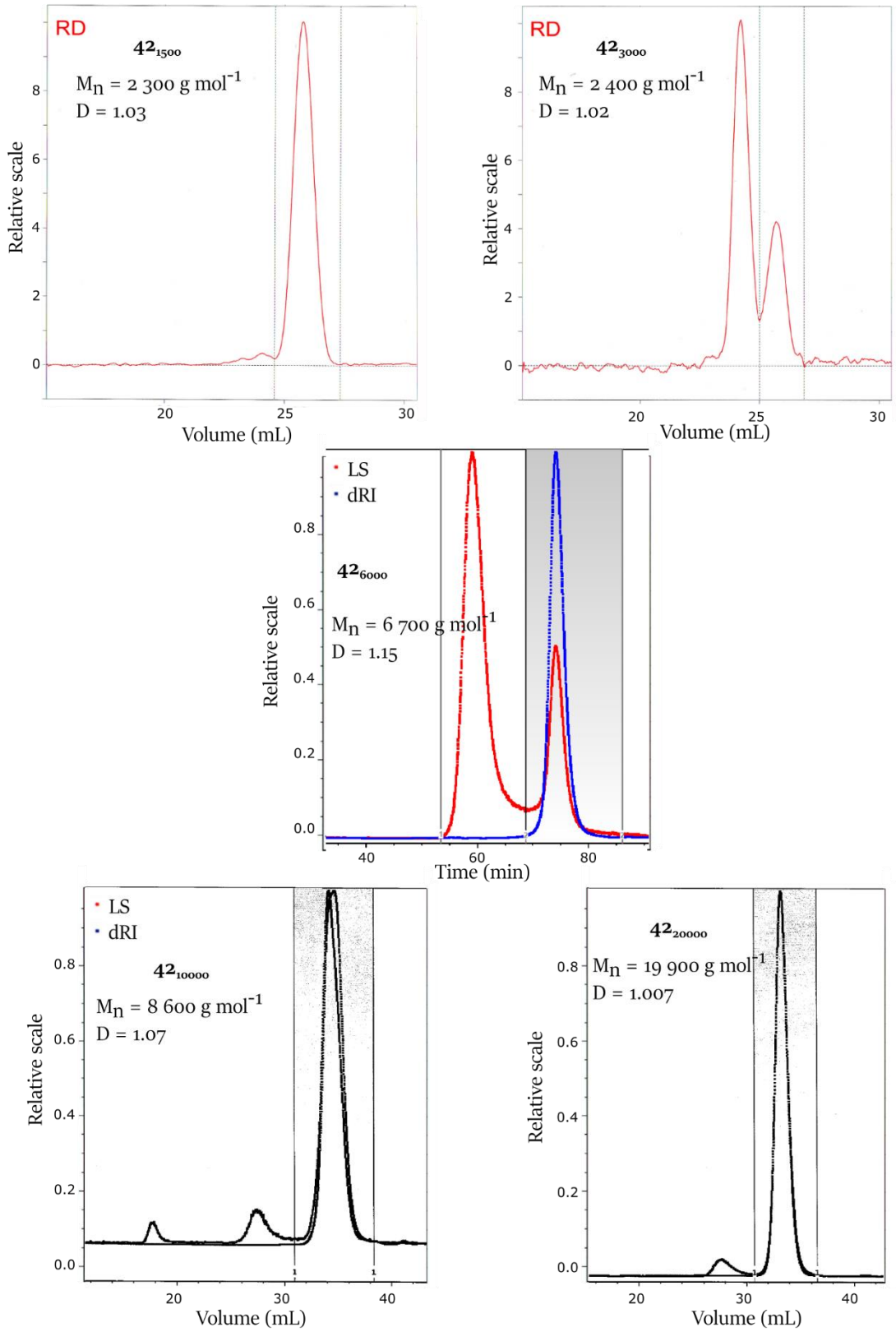

Figure B.5. GPC chromatograms of α,ω-dipropargyl-PEG **42** of different molecular weights.

MALDI-TOF

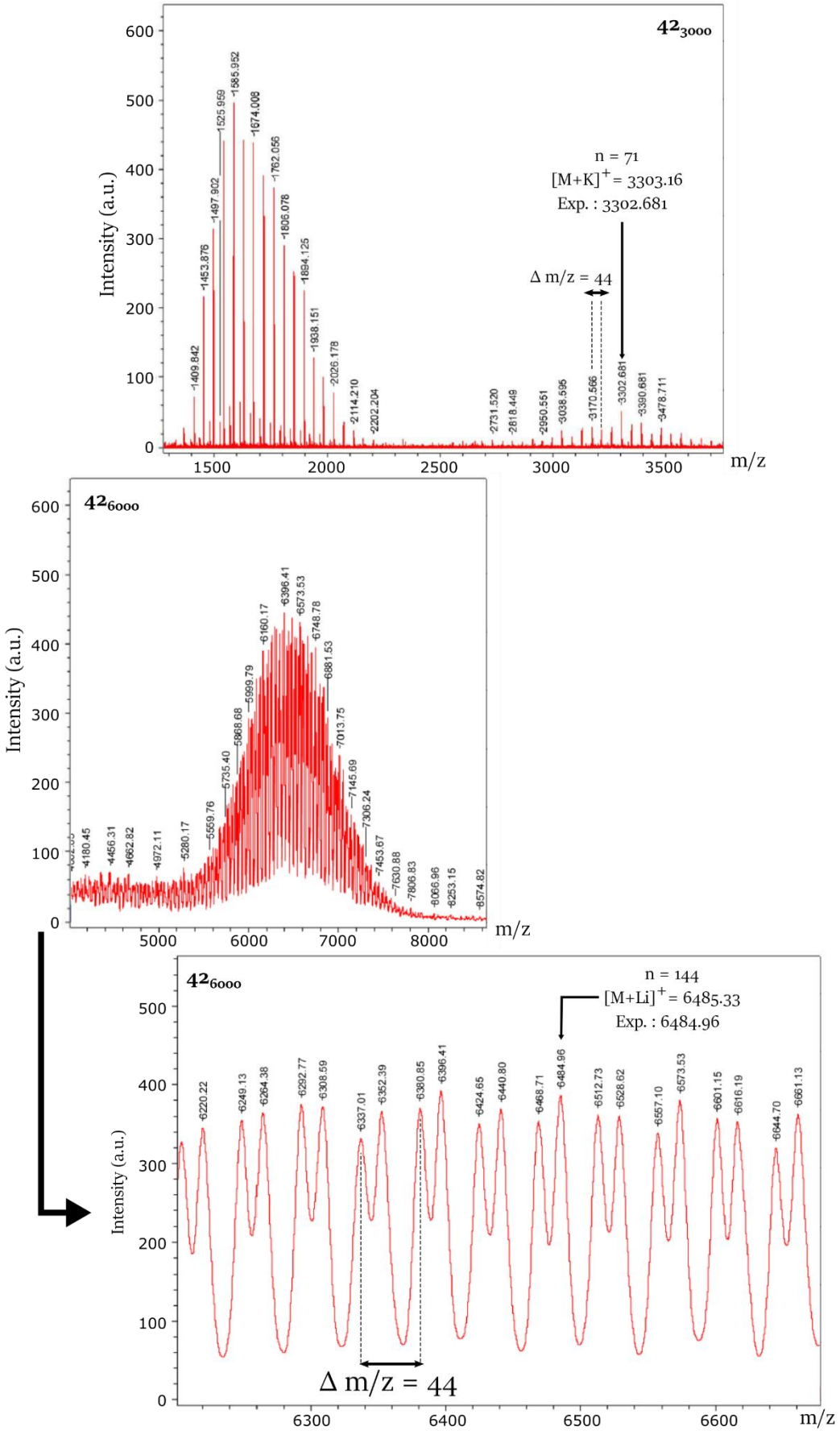

Figure B.6. MALDI-TOF spectra of α,ω-dipropargyl-PEG **42** of different molecular weights.

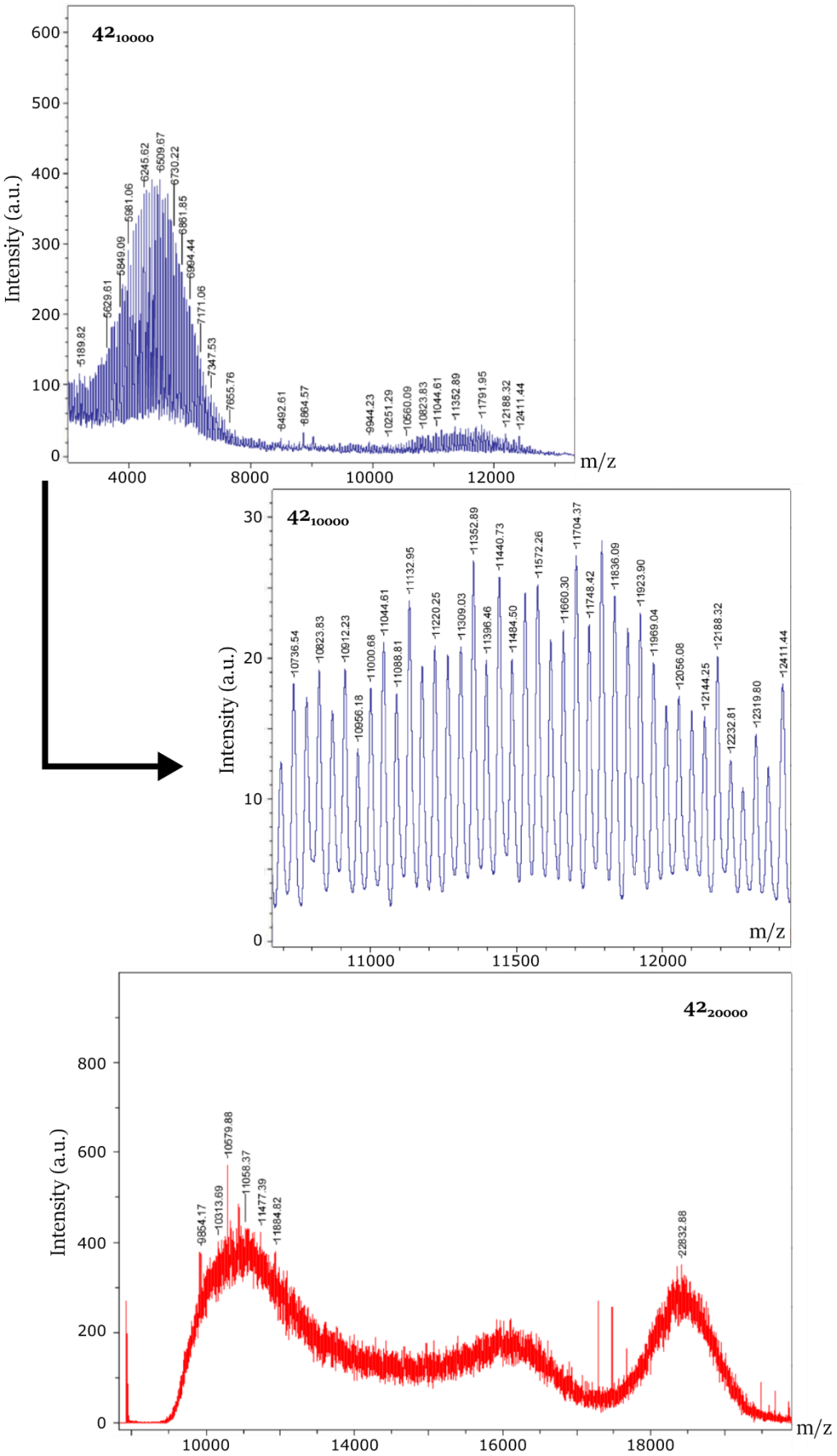

Figure B.6.(continued) MALDI-TOF spectra of α,ω-dipropargyl-PEG **42** of different molecular weights.

Viscometry

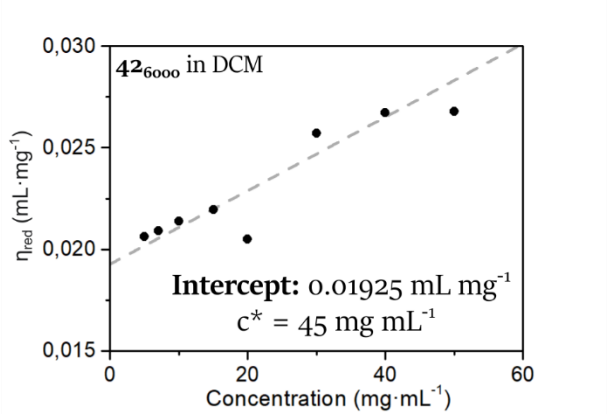

Figure B.7. Evolution of the reduced viscosity η_{red} as a function of concentration of α,ω-dipropargyl-PEG $\mathbf{42_{6000}}$ in dichloromethane.

Poly(3-hexylthiophene) 43

Gel Permeation Chromatography and MALDI-TOF

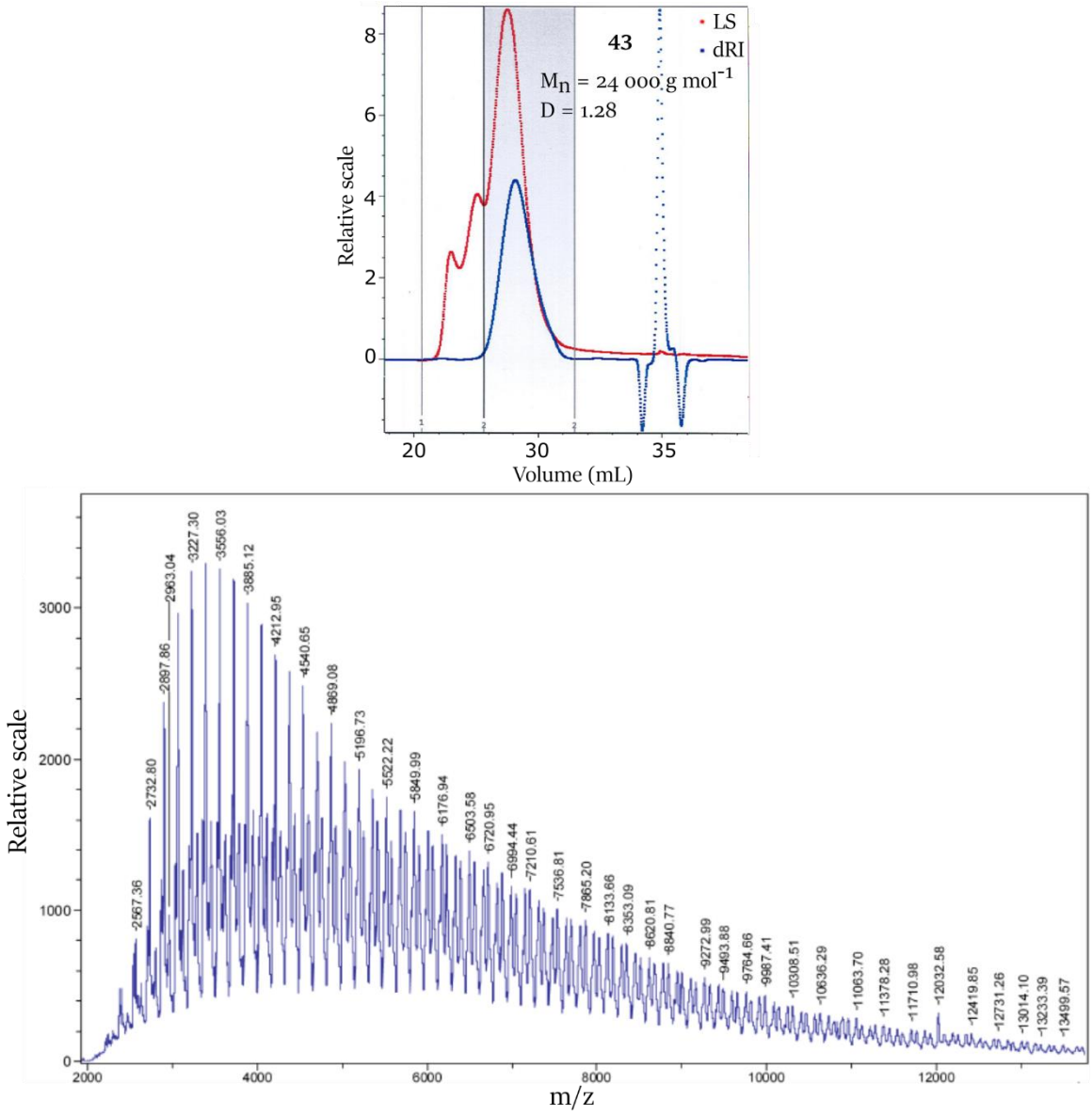

Figure B.8. GPC chromatogram (top) and MALDI-TOF spectrum (bottom) of P3HT **43**.

Poly(N-isopropylacrylamide) 46

Gel Permeation Chromatography

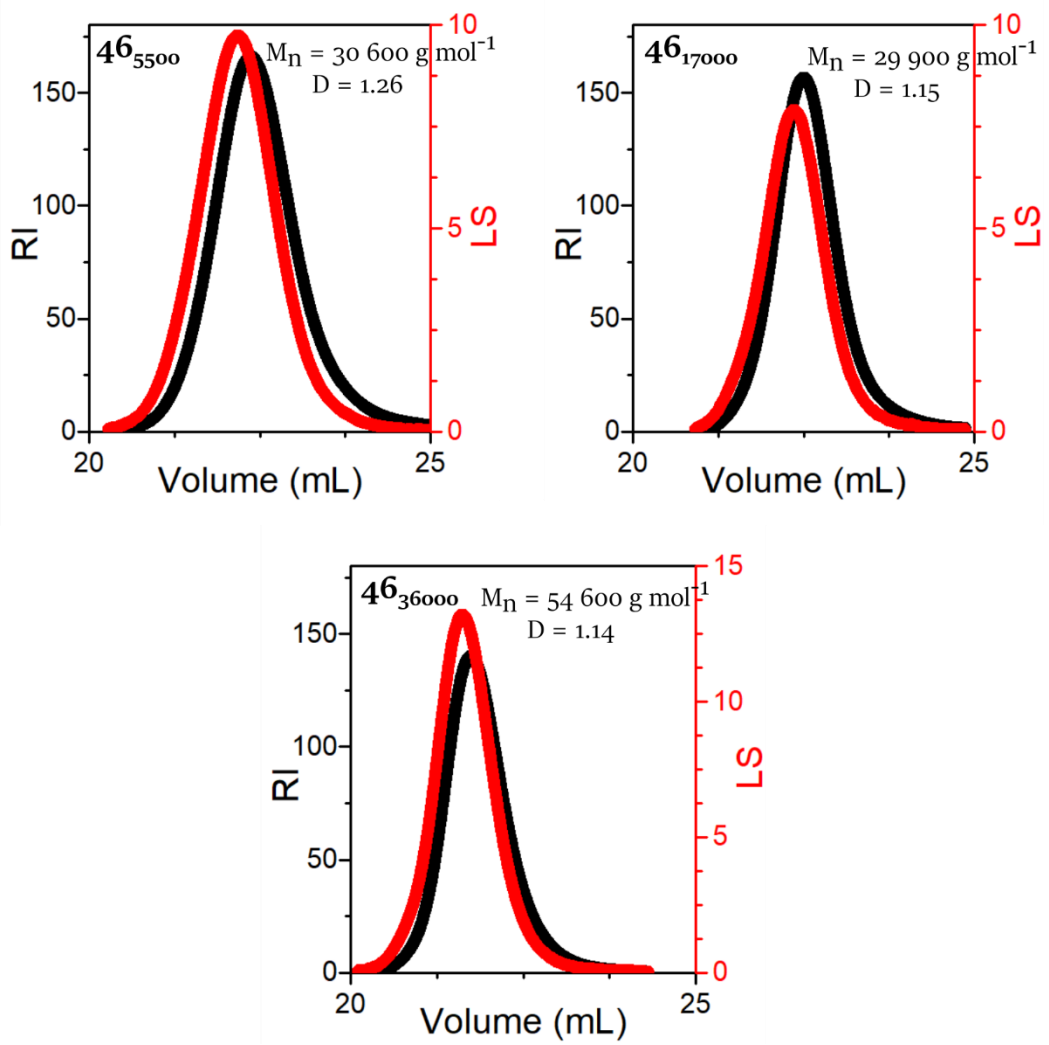

Figure B.9. GPC chromatograms of PNIPAAm **46** with different molecular weights.

α,ω-diazido-poly(dimethylsiloxane) 48

Gel Permeation Chromatography

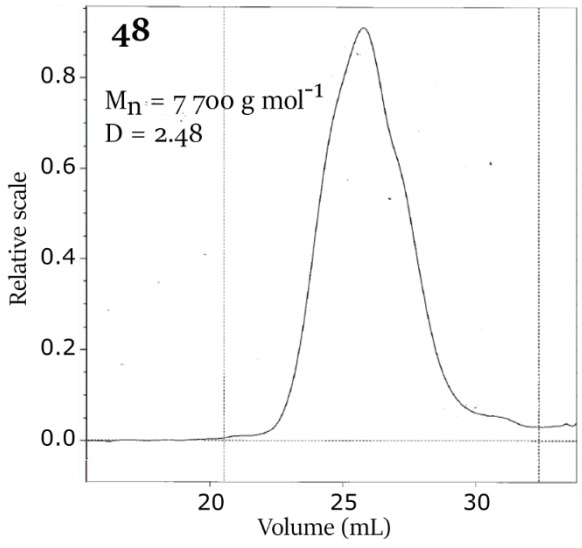

Figure B.10. GPC chromatogram of α,ω-diazido-PDMS **48**.

Appendix C

NMR spectra of key molecular motors

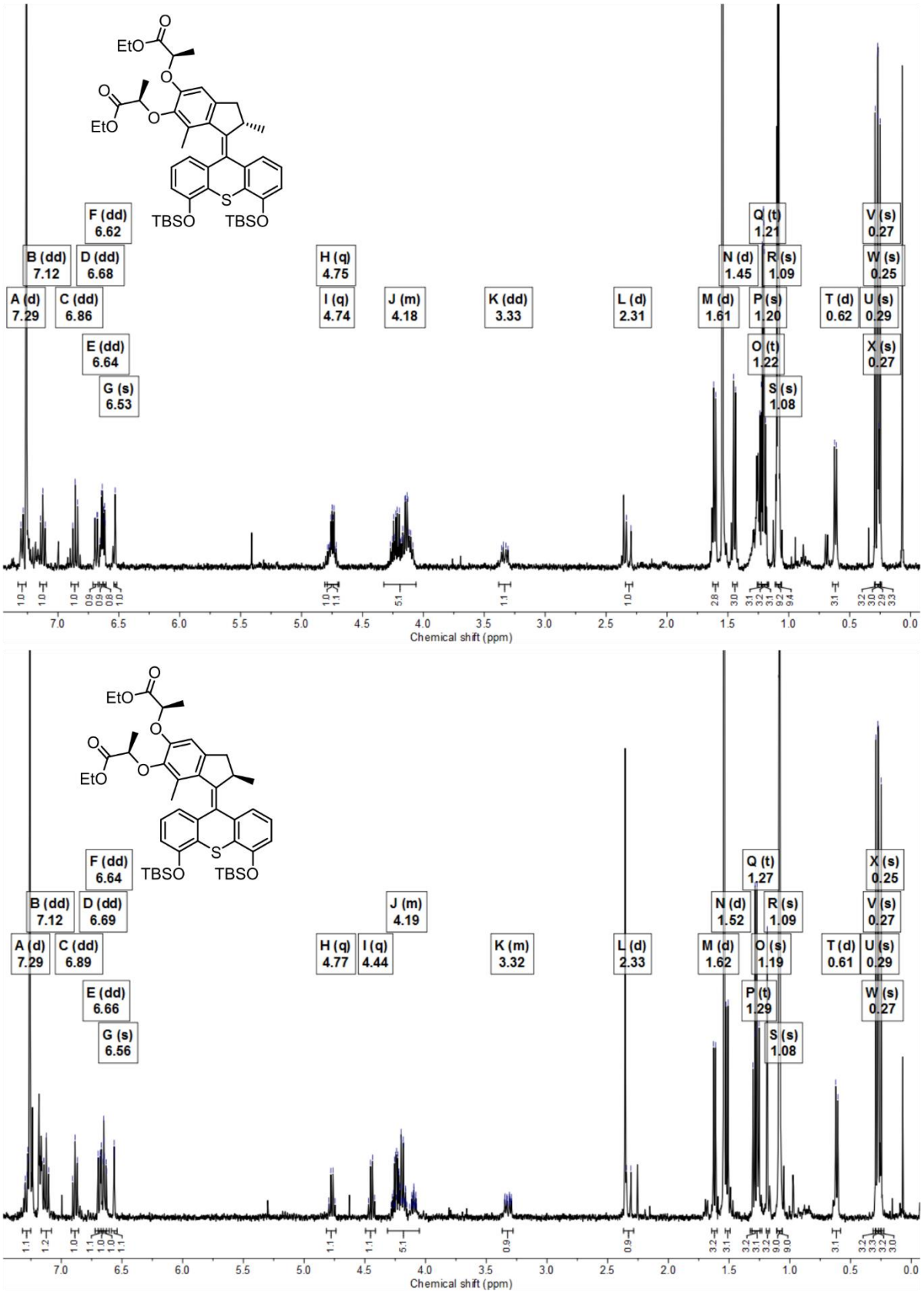

Figure C.1. ^{1}H NMR spectra of diastereoisomers **13**.

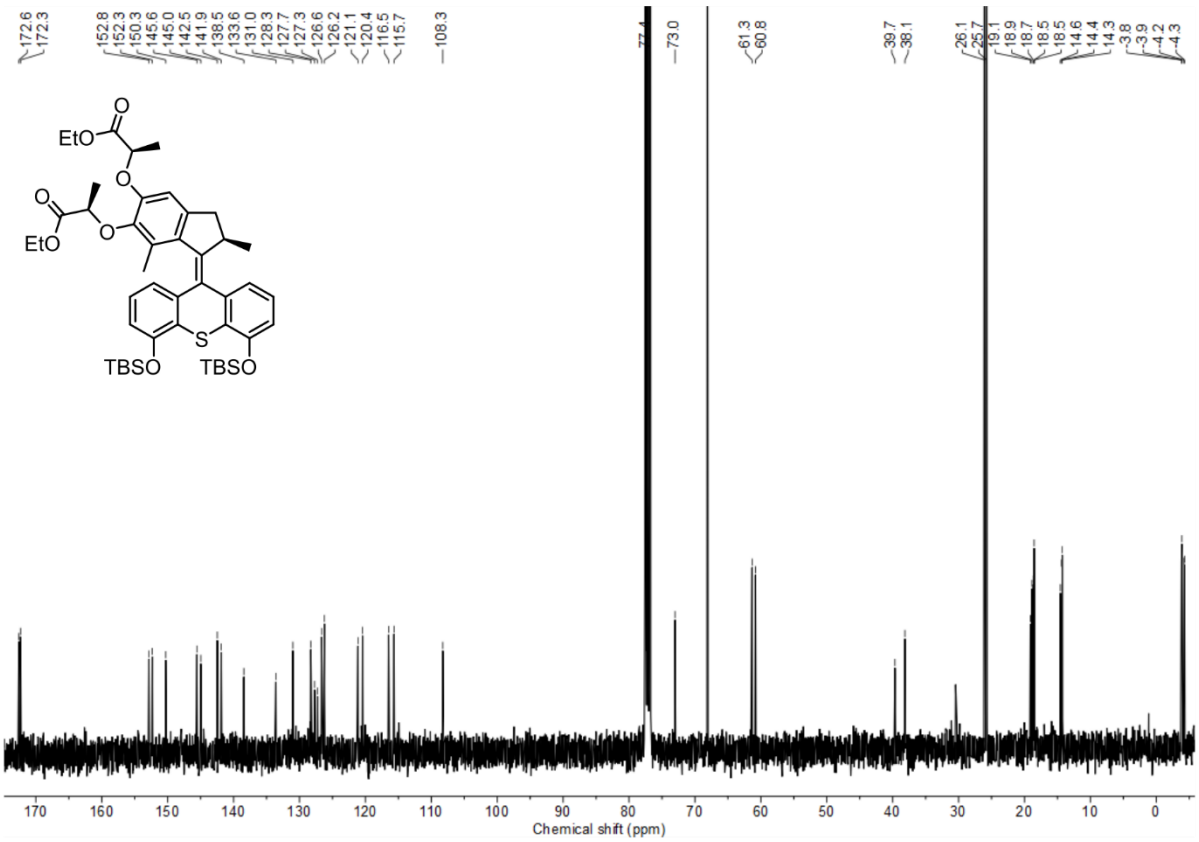

Figure C.2. ^{13}C NMR spectrum of *(R)*-**13**.

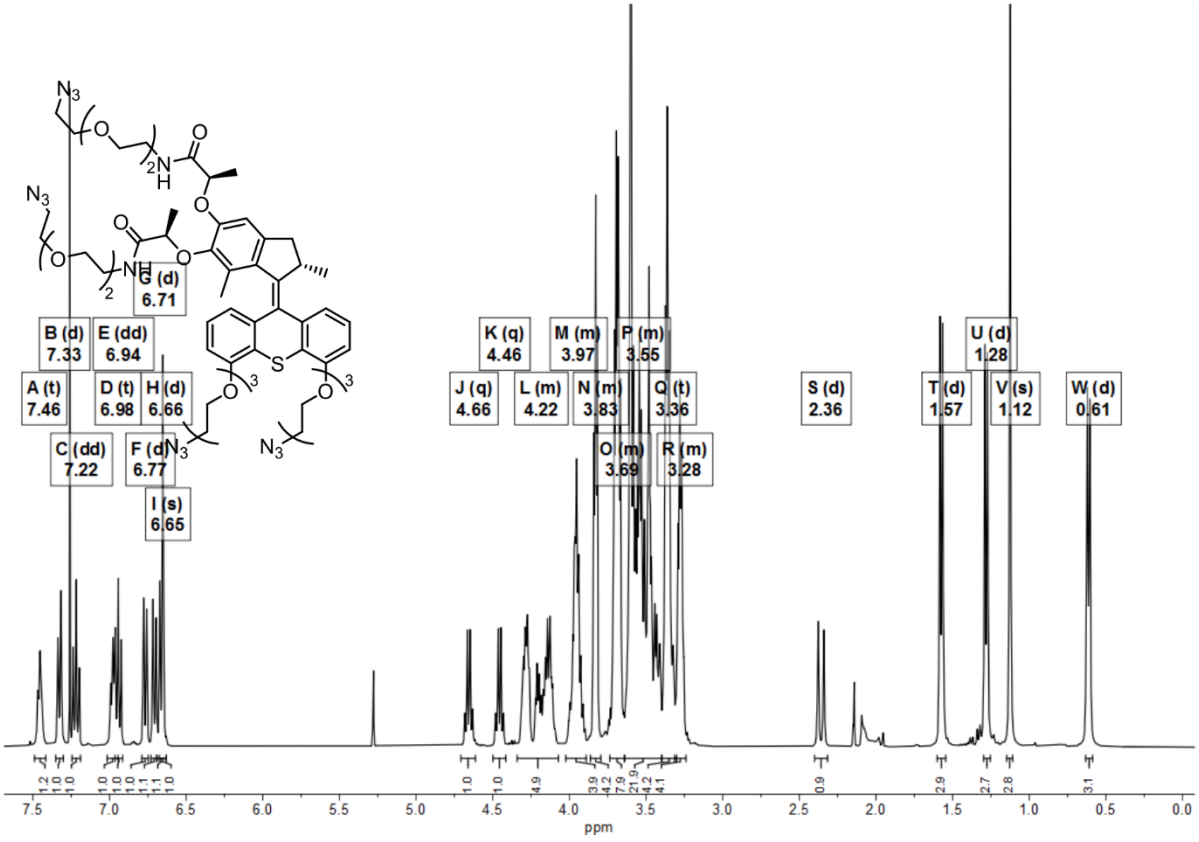

Figure C.3. ^{1}H NMR spectrum of *(S)*-**25**.

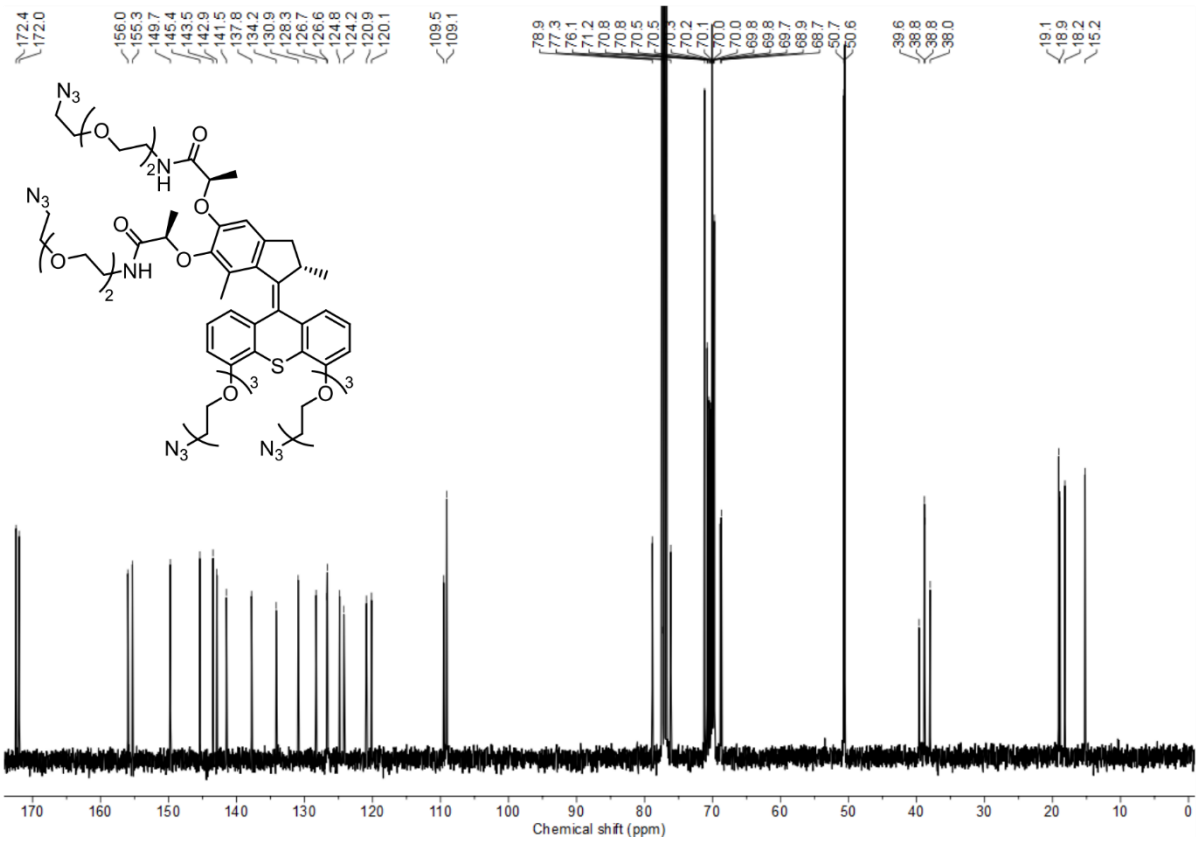

Figure C.4. ^{13}C NMR spectrum of *(S)*-**25**.

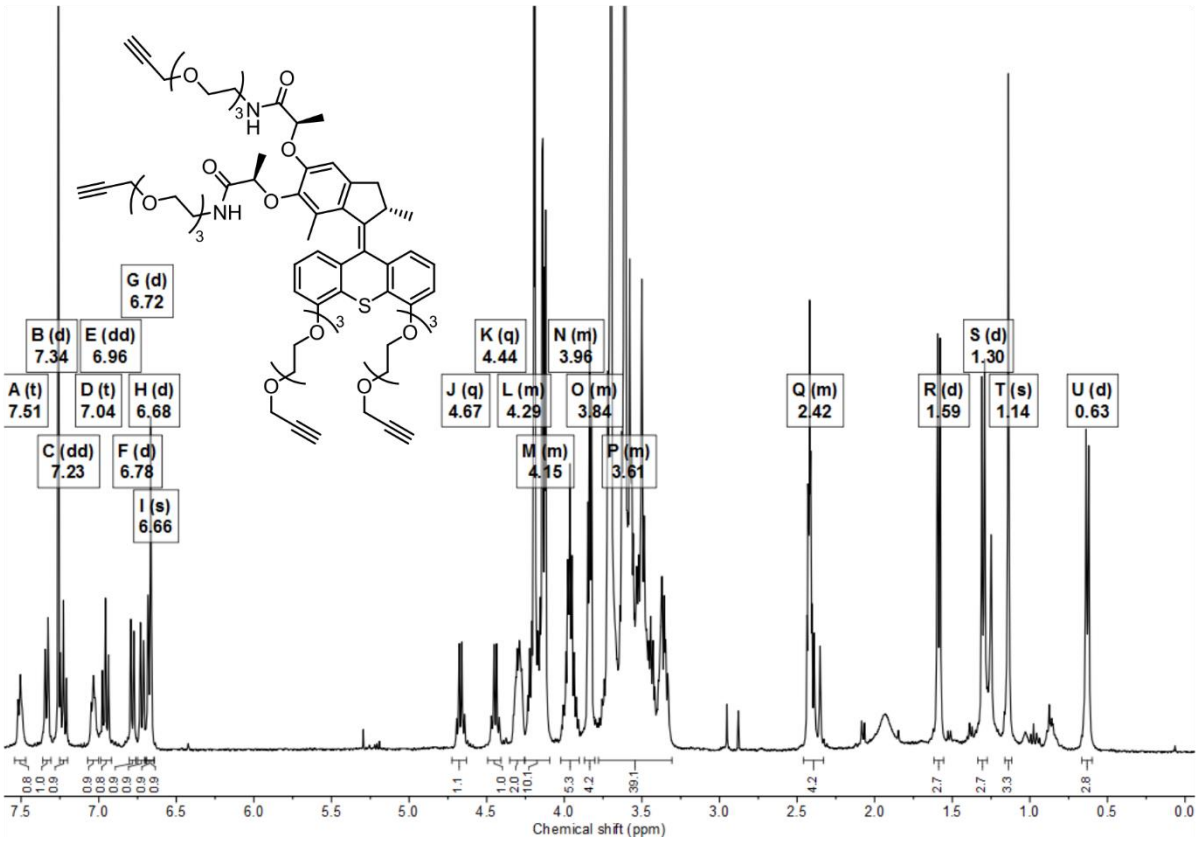

Figure C.5. ^{1}H NMR spectrum of *(S)*-**28**.

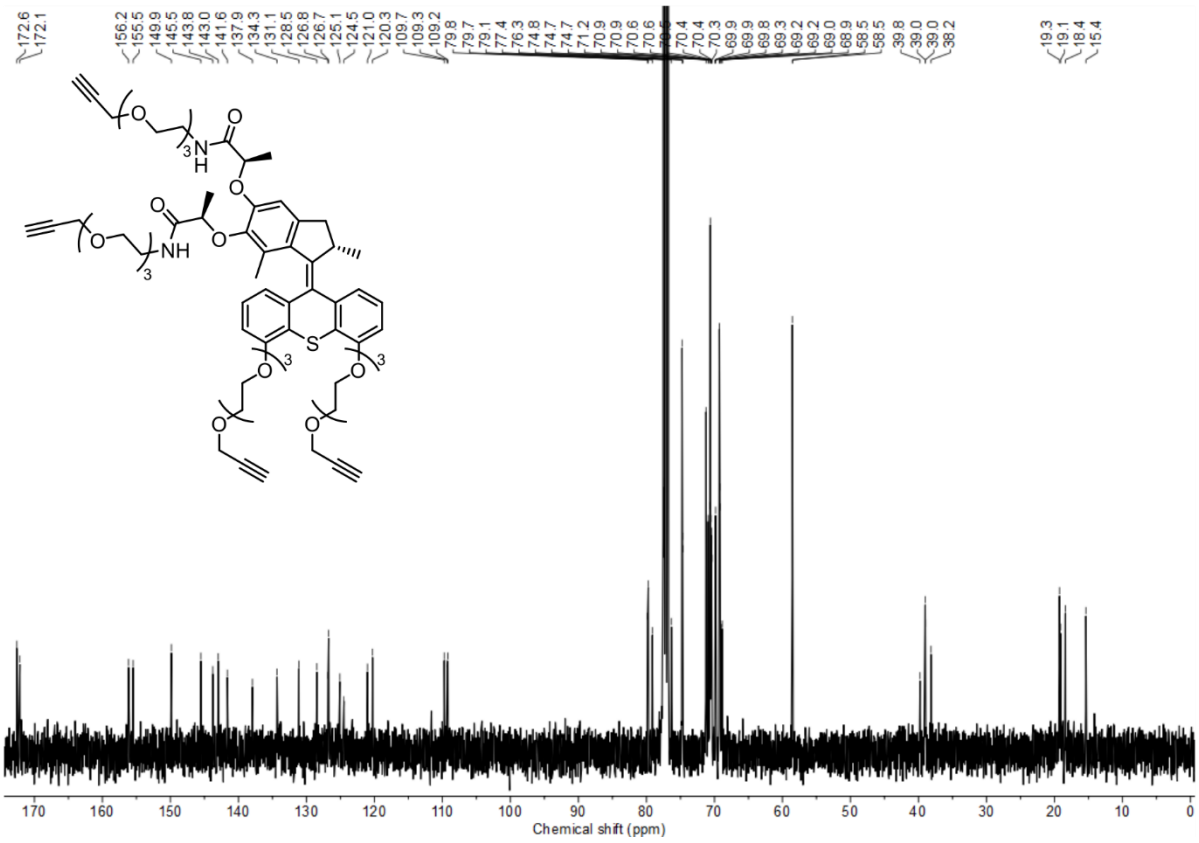

Figure C.6. ^{13}C NMR spectrum of *(S)*-**28**.

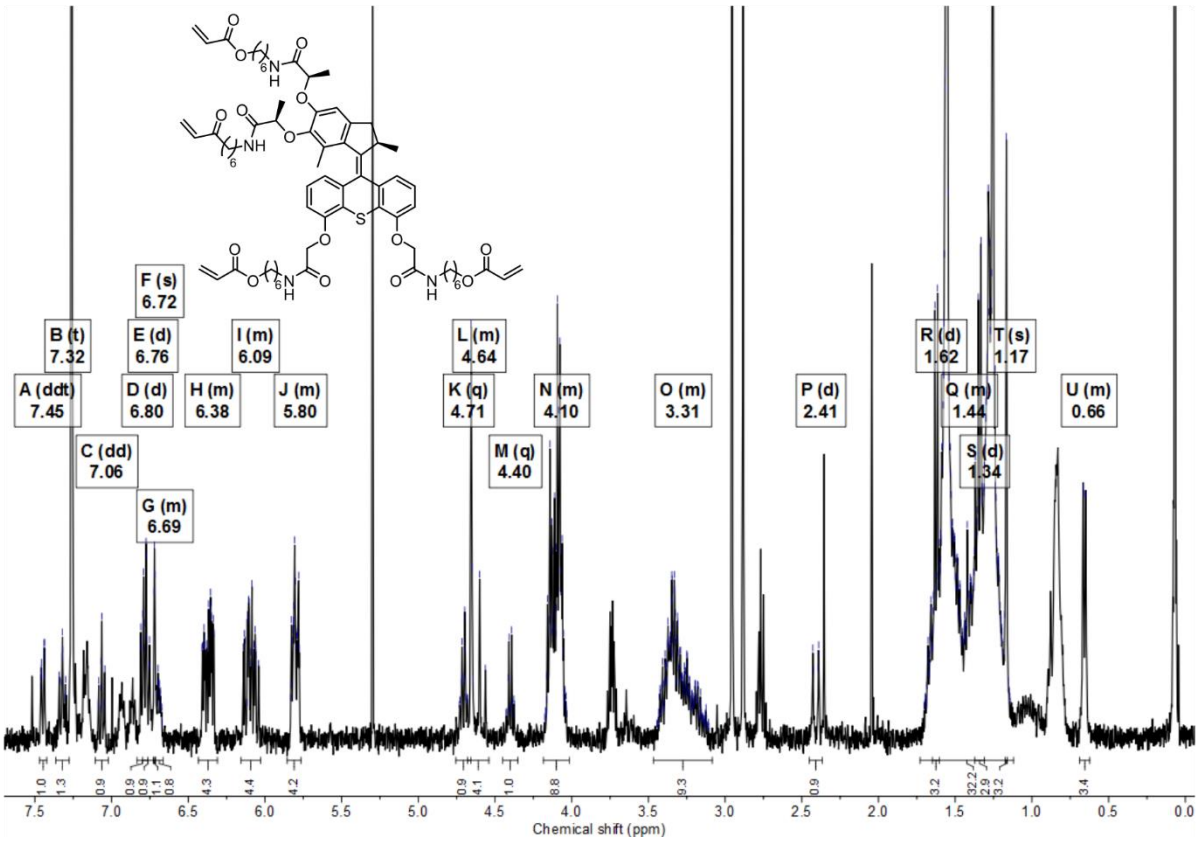

Figure C.7. ^{1}H NMR spectrum of *(R)*-**34**.

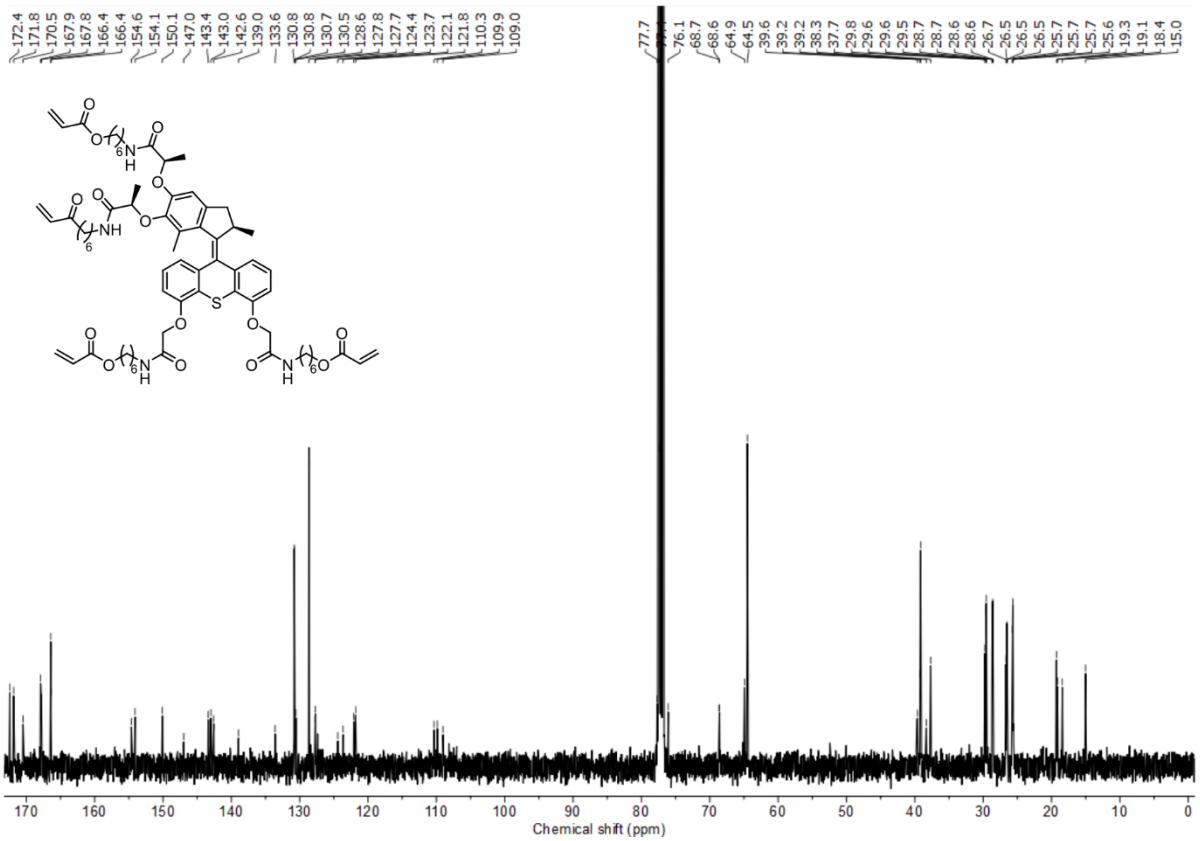

Figure C.8. ^{13}C NMR spectrum of *(R)*-**34**.

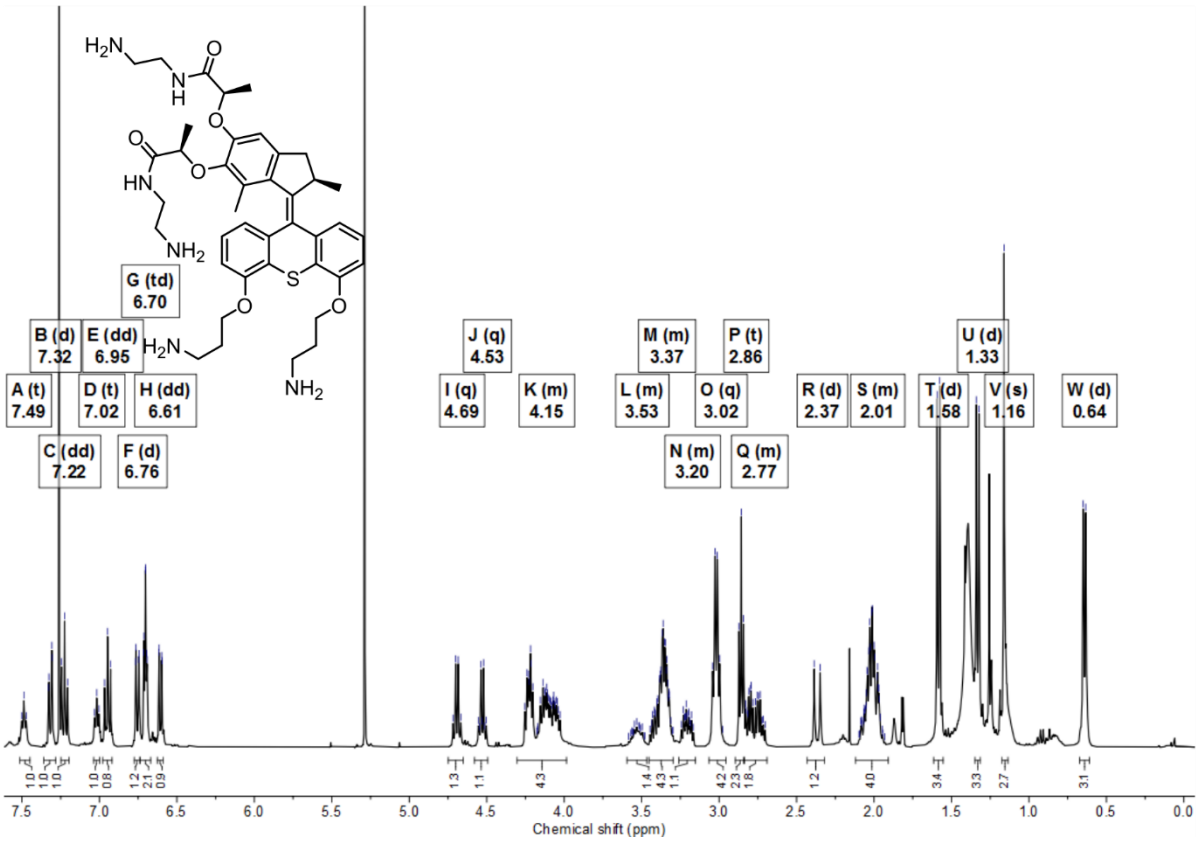

Figure C.9. ^{1}H NMR spectrum of *(R)*-**37**.

« *Odi panem quid meliora*. Ça veut rien dire, mais je trouve que ça boucle bien.»

Loth d’Orcanie

Alexis PERROT

Rationalization of the contractile behavior of light-sensitive polymeric materials based on synthetic molecular motors

Résumé

L'intégration de moteurs moléculaires comme nœuds de réticulation dans des réseaux polymériques permet d'exploiter leur rotation unidirectionnelle nanoscopique pour entraîner un changement de volume macroscopique du matériau. Dans cette thèse, nous avons étudié l'impact de plusieurs paramètres structuraux et environnementaux sur la rotation du moteur, et les conséquences sur la cinétique de contraction de ces réseaux. La topologie du matériau fut gardée constante pour tous les systèmes en les préparant à leurs concentrations de recouvrement respectives. Ainsi, nous avons pu isoler l'influence du solvant, de la température, de l'épaisseur, de la puissance lumineuse et de la masse moléculaire entre nœuds de réticulation. Nous avons également changé la nature chimique du polymère afin de comprendre l'impact de la longueur de persistance. L'utilisation d'autres macromolécules a aussi permis l'obtention du premier exemple de l'actuation d'un élastomère amorphe causée par le mouvement unidirectionnel de moteurs moléculaires, ainsi que le premier exemple de gel physique photosensible, thermiquement réversible, intégrant ces mêmes molécules.

Mots clés : matériaux photosensibles, actionneurs, moteurs moléculaires, gels polymériques

Abstract

The integration of molecular motors as crosslinking agents in polymer networks allows for the exploitation of their nanoscopic unidirectional rotation to trigger a macroscopic volume change of the material. In this thesis, we studied the impact of several structural and environmental parameters on the rotation of molecular motors, and the consequences on the contraction kinetics of these networks. The topology of the material was kept constant by preparing the systems at their respective overlap concentrations. Therefore, we isolated the influence of the solvent, the temperature, the thickness, the light power, and the molar mass between crosslinks. We also changed the chemical structure of the polymers to understand the influence of the persistence length. The use of other macromolecules also led to the first example of an actuating amorphous elastomer caused by the unidirectional motion of molecular motors, as well as the first example of a light-sensitive physical gel, thermally reversible, integrating these molecules.

Keywords : light-sensitive materials, actuators, molecular motors, polymer gels